EXPERIMENTAL AND THEORETICAL INVESTIGATIONS OF MAGNESIUM-CHLORINE CYCLE AND ITS INTEGRATED SYSTEMS

By

HASAN OZCAN

A Thesis Submitted in Partial Fulfillment
of the Requirements for the degree of Doctor of Philosophy
in
Mechanical Engineering

University of Ontario Institute of Technology
Faculty of Engineering and Applied Science

Oshawa, Ontario, Canada

Abstract

This study aims to investigate the feasibility of the Mg-Cl hybrid thermochemical cycle and to develop a more cost and energy effective cycle. There are five key elements of this study: (i) modeling and simulation of the Mg-Cl cycle considering both the ideal reference case and realistic operating conditions; (ii) novel configuration developments of the Mg-Cl cycle through literature review of experimental and theoretical studies on the intermediate reaction steps to identify potential cycle improvement options; (iii) experimental investigations to validate the proposed configurations of the Mg-Cl cycle; (iv) comprehensive thermodynamic and thermoeconomic assessments, and optimization of the Mg-Cl cycle; (v) cycle integration with sustainable energy systems and hydrogen storage options.

Although a simulation study of the conventional Mg-Cl cycle under ideal operating conditions provides an upper limit for an overall performance of the cycle, it is not an actual indicator about the cycle efficiency under actual conditions. In reality, material and energy inputs well beyond the ideal requirements are necessary to overcome thermodynamic inefficiencies and incomplete reactions throughout the intermediate steps, which significantly affects the cycle performance. Specifying these in a practical model is a more conservative and realistic approach for the cycle simulation; addressing these performance-impacting factors leads the development of various feasible cycle options capable of operating at a level comparable to water electrolysis and other hybrid cycles.

The second element of this work develops an additional step to the three-step Mg-Cl cycle for lower power consumption and higher cycle efficiency than the conventional case by considering the literature review of the intermediate cycle steps. This step leads to the integration of two subsequent electrolysis steps, namely dry and aqueous electrolysis of HCl, where the dry HCl electrolysis is a lower power consuming step for hydrogen production than that of aqueous HCl electrolysis; thus, an experimental study is undertaken to capture HCl in dry form. In the light of literature teachings, two experimental procedures are developed to capture HCl from its mixture with steam, and liberate HCl in dry form. The third element experimentally studies several cases to observe HCl capture performance, including testing of the resulting substances in detail using

Thermogravimetric Analysis (TGA), and X-ray diffraction (XRD) tests. Results of the experiments show 30.8% HCl capture by solid MgO particles in a packed bed reactor design with an uncertainty value of $\mp$1.17%. XRD results indicate an optimum reactor temperature of 275ºC to prevent the process from side reactions and undesirable products. Experimental results are adapted to the four-step Mg-Cl cycle to form the final design of the Mg-Cl cycle.

The fourth element of the thesis studies the thermodynamics, thermoeconomics, and optimization of the Mg-Cl cycle. Simulation of the final design utilizes the Aspen plus Software package to account for the thermochemistry of all reactions throughout the cycle. A multi-objective optimization process uses Genetic Algorithm (GA) with the results of the thermodynamic analyses, given on a stream-basis, and the economic assessment to maximize plant efficiency and minimize plant cost. The results of thermodynamic and thermoeconomic analyses for the base design of Mg-Cl cycle give energy and exergy efficiency values of 44.3% and 53%, respectively, an annual plant cost of $458.5 million, and a hydrogen production cost rate of 3.67 $/kg. The multi-objective optimization results indicate an increase in exergy efficiency (56.3%), and decrease in total annual plant cost ($409.3 million). Thermodynamic and thermoeconomic results indicate that the final design of the Mg-Cl cycle shows higher hydrogen cost results than that of the Hybrid-sulfur Cycle (HyS) and shows a similar trend with the hybrid Copper-Chlorine (Cu-Cl) cycle.

Although the main focus of this study is production of hydrogen, it is also crucial to consider the various means of providing energy input for the Mg-Cl cycle and post-treatment of the hydrogen as a consumer product. The final element of this work integrates the Mg-Cl cycle with two different sustainable energy system and hydrogen treatment options: a solar thermal driven supercritical-CO_2 Gas turbine cycle with a 5-stage hydrogen compression plant (System I), and a nuclear heat driven steam Rankine Cycle with a Linde-Hampson Liquefaction plant (System II). Thermodynamic analyses assess and compare the performance of each integrated system, which have resulting energy efficiencies of 16.3% and 18.9%, and corresponding exergy efficiencies of 17.6% and 31.4%, respectively.

Acknowledgements

I cannot express enough gratitude to my supervisor, Prof. Dr. Ibrahim Dincer for giving me this unique opportunity to work in this area, his continuous support, and his horizon expanding advices.

I gratefully acknowledge the financial support by Ministry of National Education of Turkey.

My completion of this thesis could not be achieved without the existing and previous members of Dr. Dincer's research group. I would like to thank Dr. Calin Zamfirescu, Dr. Ahmet Ozbilen, Dr. Rami El-Emam, Dr. Ofelia Jianu, Canan Acar, Janette Hogerwaard and Munur Herdem for their support and assistance for my thesis work.

I would like to thank my friends Ahmet Ozbilen, Hakan Ciloglu, Diniyaer Maimaitijiang, Batuhan Gultepe, and Jason Huang for bearing with me as their housemate. I am also thankful to Ozdemir and Karasu families for treating me as a family member during my stay in Canada.

To my dear wife Sultan, and my son Omer Salih. Their existence has always been my ultimate motivation through my research. Last but not least, if there is any honor in this degree, it belongs to my parents, Fatma and Zafer Isik Ozcan, and my siblings Murat, Huseyin Ersin, Enes, and Talha Emir.

To the unique engineer and designer of the universe, God, the merciful and the compassionate.

Table of Contents

List of Figure Captions

List of Table Captions

Nomenclature

A	Area (m^2)
B	Bias Error
c	Cost per unit of exergy ($/kJ)
$\dot{C}$	Cost rate ($/s)
Cp	Specific heat (kJ/kmolK)
$\overline{ex}$	Specific exergy (kJ/kmol)
$\dot{E}$	Energy rate (kW)
$\dot{Ex}$	Exergy rate (kW)
f	Exergoeconomic factor
F	Faraday constant (C/mol)
h	Specific enthalpy (kJ/kg)
$\bar{h}$	Specific enthalpy (kJ/kmol)
i	Interest rate
k	Kinetic parameter
K	Equilibrium constant
$\dot{m}$	Mass flow rate (kg/s)
n	Equipment lifetime (years)
N	Annual number of operation hours
n_e	Number of electrons exchanged
p	Partial pressure (bar)
P	Precision error, pressure (kPa)
Q	Heat (kJ)
$\dot{Q}$	Heat rate (kW)
R	Universal gas constant (kJ/kmolK)
$\bar{s}$	Specific entropy (kJ/kmolK)
$\dot{S}$	Entropy rate (kW/K)
T	Temperature (°C, K)
tc	Thermocouple
U	Heat transfer coefficient (W/m^2K)

V	Voltage (V) - Volume (m^3)
W	Work (kJ)
$\dot{W}$	Work rate (kW)
Z	Purchased equipment cost ($)
$\dot{Z}$	Cost rate of owning and operating the cycle ($/s)

Greek Symbols

η	Efficiency
θ	Total energy (kJ/kg)
σ	Stefan-Boltzmann Constant ($5.67 \cdot 10^{-8}$ W/m^2K^4)
α	Absorptivity
β	Symmetry factor
ε	Emissivity
ρ	Density (kg/m^3)
φ	Maintenance factor
ψ	Distance (m)
ϵ	Heat exchanger effectiveness

Subscripts and Superscripts

0	Ambient
0	Reference state
00	Chemical equilibrium
a	Anode
aq	Aquaeous
c	Cathode
cap	Capture
ch	Chemical
chl	Chlorination
comp	Compressor
d, dest	Destruction
dec	Decomposition

e	Exit
elec	Electrolyzer
en	Energy
ex	Exergy
f	Fuel
g	Gaseous
gen	Generation
hex	Heat exchanger
hyd	Hydrolysis
i	i^{th}
in	Inlet
k	k^{th}
kin	Kinetic
l	Liquid
lm	Logarithmic mean difference
out	Outlet
p	Product
ph	Physical
R	Reactant
rec	Receiver
s	Solid
sep	Separation
sys	System
t	Turbine
v	Vapor

Acronyms

ABWR	Advanced Boiling Water Reactor
AE	Alkaline Electrolyser
AHWR	Advanced Heavy Water Reactor

ANL	Argonne National Laboratory
ANN	Artificial Neural Network
APWR	Advanced Pressurized Water Reactor
AR	Auto-thermal Reforming
BWR	Boling Water Reactor
CANDU	Canada Deuterium Uranium
CEPCI	Chemical Engineering Plant Cost Index
CERL	Clean Energy Research Laboratory
CRF	Capital Recovery Factor
Cu-Cl	Copper-Chlorine
DTA	Differential Thermal Analysis
EES	Engineering Equation Solver
EPR	European Pressurized Reactor
FWH	Feed Water Heater
GA	Genetic Algorithm
GFR	Gas Fast Reactor
GTA	Greater Toronto Area
HBR	Hydrogen-Bromide
HEEP	Hydrogen Economy Evaluation Program
HTF	Heat Transfer Fluid
HTSE	High Temperature Steam Electrolysis
HyS	Hybrid Sulfur Cycle
IAEA	International Atomic Energy Agency
IGT	Institute of Gas Technology
LASL	Los Alamos Scientific Laboratory
LFR	Lead-cooled Reactor
LHV	Lower Heating Value
LMTD	Logarithmic Mean Temperature Difference
Mg-Cl	Magnesium-Chlorine

MSR	Molten Salt Reactor
NSGA	Non-dominated Sorting Genetic Algorithm
ORC	Organic Rankine Cycle
PEC	Purchase Equipment Cost
PEM	Proton Exchange Membrane
PO	Partial Oxidation
PWR	Pressurized Water Reactor
RCD	Relative Cost Difference
SCWR	Supercritical Water Reactor
SEM	Scanning Electron Microscopy
SFR	Sodium-cooled Reactor
S-I	Sulphur-Iodine
SMR	Steam Methane Reforming
SOEC	Solid Oxide Electrolysis Cell
SOFC	Solid Oxide Fuel Cell
SPECO	Specific Exergy Costing
SPT	Solar Power Tower
SR	Steam Reforming
SRC	Steam Rankine Cycle
TGA	Thermogravimetric Analysis
UNLV	University of Nevada Las Vegas
UOIT	University of Ontario Institute of Technology
VHTR	Very High Temperature Reactor
XRD	X-ray Diffraction

CHAPTER 1: INTRODUCTION

Energy is one the most crucial issues for society, international politics, and the environment. Its finite existence has major effects on mechanisms of decision making and use of fossil fuels has a dominant effect on all aforementioned issues. This results in direct and indirect effects on human activities, most importantly with environmental issues. Since abundancy, cost and ease of fossil fuel utilization are still promising compared to renewable based energy production, phasing out of fossil fuels can be a very challenging issue even if its negative effects are well-known. Therefore, it is of importance to investigate, develop, and commercialize cost and energy effective methods to produce energy in a clean way as an alternative to fossil fuels. Hydrogen is so far the most promising energy carrier alternative to fossil fuels and there are several possible ways to produce it in a sustainable way. Most of these methods are still in the development stage and energy production using these systems cannot currently compete with fossil fuel based applications. However, ongoing research on several methods looks promising and shows the possibility to compete with conventional methods.

1.1 Hydrogen Production

Hydrogen is an energy carrier which is not readily available in nature but can be produced using an energy resource. Hydrogen is an ideal energy carrier because it can be produced from or converted into electricity at relatively high efficiencies. Additionally its raw material is water, it is a renewable fuel, it can be stored in gaseous liquid or metal hydride form, can be converted in other forms of energy efficiently, and most importantly it is environmentally friendly during all processes to utilize hydrogen (Veziroglu and Barbir, 1992). There are several methods to produce hydrogen. These methods can be categorized in six classes, namely electrochemical, thermochemical, photochemical, radiochemical, biochemical and hybrid (involving one or more of first five methods together). Renewable energy resources such as solar, hydro, wind, tidal, biomass, geothermal and nuclear can be used for sustainable hydrogen production (Dincer and Acar, 2015).

Hydrogen can be produced from both primary and secondary energy sources. Commercially applied methods generally consist of fuel processing and the required energy

is provided from primary energy sources. Natural gas reforming and coal gasification are commercially available and are still under research to improve efficiency of existing plants. Biomass based hydrogen production is still under development and not commercially available yet. Hydrogen production from secondary energy resources are exclusively by water electrolysis using electricity. Hydrogen can be produced by secondary energy sources in three ways (Naterer et al., 2013):

- Electrolyzing water at off-peak hours from power plants.
- Providing process heat for high temperature reactors for steam reforming of methane.
- Producing hydrogen through a thermochemical cycle, such as S-I, Cu-Cl and Mg-Cl.

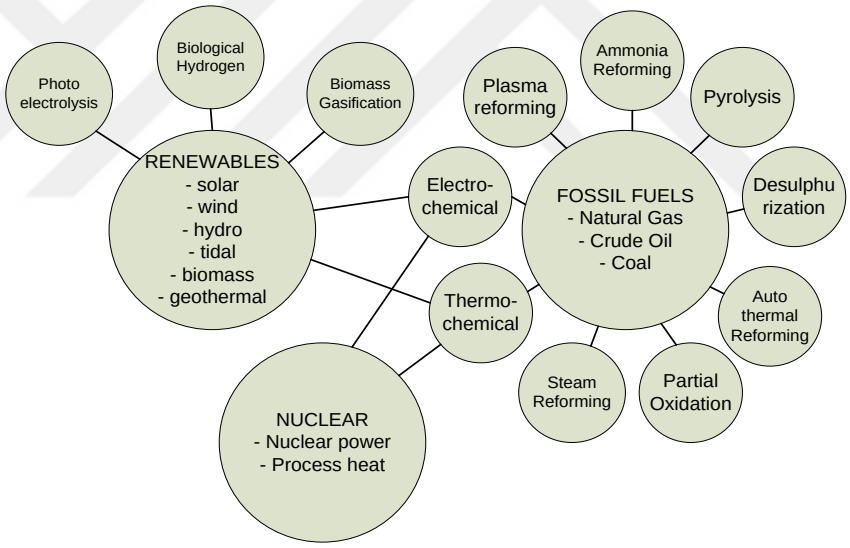

Figure 1.1 Hydrogen production methods (Modified from Holladay et al., 2009; Dincer and Zamfirescu, 2012).

Renewable based electrolytic or thermochemical hydrogen production is the most sustainable method and provides a clean, non-polluting and promising alternatives to fossil fuels. Renewable based hydrogen production is still under research (Dincer and Zamfirescu, 2012). Figure 1.1 shows methods for hydrogen production based on primary, secondary and renewable energy resources.

1.1.1 Hydrogen from Fuel Processing

Hydrogen is produced from hydrogen containing fossil fuels by reforming them into pure or hydrogen rich streams. Fuel processing techniques can be sorted as hydrocarbon reforming, desulphurization of liquid and gaseous fuels, pyrolysis, plasma reforming, aqueous phase reforming and ammonia reforming.

Hydrocarbon reforming has three primary techniques: steam reforming (SR), partial oxidation (PO) and auto thermal reforming (AR). Steam reforming is the most commonly used technique in industry since it has a high H_2/CO ratio and is more convenient for hydrogen production. Although it does not require oxygen for the process and this process can be accomplished at lower temperatures compared to other hydrocarbon reforming techniques, it has the highest emissions (Wilhelm et al., 2001). Partial oxidation converts fossil fuels to hydrogen by partially oxidizing the fuel and provides heat for the process. H_2/CO ratio of this process is lower than that of steam reforming and requires very high reaction temperatures. However this technique decreases desulphurization requirement and no catalyst is required (Balat, 2009). Auto thermal reforming uses partial oxidation to provide heat and steam reforming to increase the hydrogen production resulting with thermally neutral process (Holladay et al., 2009). Although auto thermal reforming has the lowest process temperature compared to SR and PO, it requires oxygen for the process and expensive equipment such as an air separation unit.

Pyrolysis is another hydrogen production technology decomposing hydrocarbons into hydrogen and carbon without using water or air resulting with lower emissions and elimination of secondary reactors. It can work with any kind of organic fuel with lower emissions and without complexity of the plant (Muradov, 2003). Plasma reforming reactions are almost the same with conventional reforming technologies, however when steam is injected with the fuel, H, OH^- and O radicals are formed, creating conditions for both reductive and oxidative reactions. Plasma reforming overcomes limitations of conventional reforming such as cost and deterioration (Biniwale et al., 2004). Note that aqueous phase reforming and ammonia reforming technologies are also types of fuel processing for hydrogen production. Main differences between these reforming technologies are use of different types of fuels and processes. The advantage of aqueous phase reforming is using water in liquid form and elimination of fuel vaporization (Taylor

et al., 2003). Ammonia reforming is primarily used with fuel cell power applications. Although ammonia is easier to transport, its strong odor allows for leakage detection, and it has a higher energy density than methanol. However, its acidic nature may increase irreversibilities and losses through PEM fuel cells (Chachuat et al., 2005).

1.1.2 Hydrogen from Biomass

Biomass can be converted into gaseous, liquid, and solid fuels by several physical, chemical, and biological processes such as gasification, carbonization, pyrolysis, hydrolysis, and biological conversion of all types of organic wastes (Dincer, 2000). Biomass gasification and steam reforming are the most common conversion technologies for biomass. The technology is used in petrochemical processes, namely, obtaining more desirable fuels by reacting solid fuels with steam. Figure 1.2 illustrates a conventional biomass gasification system. For hydrogen production, conventional biomass gasification systems can be employed to increase the hydrogen ratio in the product and a separation process can be used to produce pure hydrogen.

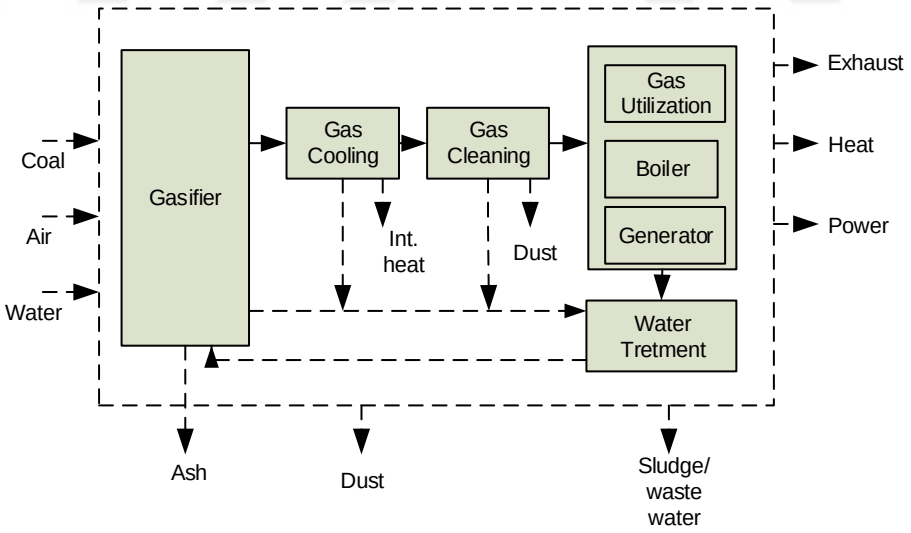

Figure 1.2 Schematic diagram of conventional biomass gasification (Modified from Kalinci et al., 2009).

Interest in biological hydrogen production has substantially increased as it provides sustainable hydrogen production with less waste and emissions. These technologies include: photolytic hydrogen production from water by green algae or cyanobacteria, dark-

fermentative hydrogen production during the acidogenic phase of anaerobic digestion of organic material, photo-fermentative processes, and hydrogen production with water-gas shift. (Holladay et al., 2009; Levin et al., 2004) A multi-stage integrated bio hydrogen system is illustrated in Figure 1.3.

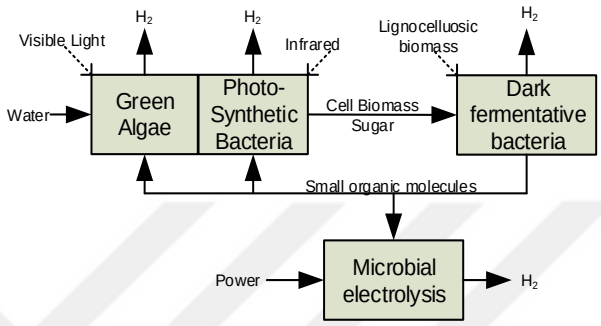

Figure 1.3 Integrated biological hydrogen production unit (Modified from DOE, 2007).

Direct photolysis of water utilizes algae photosynthesis to generate hydrogen and oxygen ions and is inexpensive since water is the only input. However, a significant surface area is required for sunlight absorption and proper oxygen and hydrogen separation is required as these components are produced in a mixed form which could be hazardous in large scale production (Kovacs et al., 2006). Dark fermentation uses primarily anaerobic bacteria on carbohydrate rich substrates in a dark ambient. Here, biomass is used for fermentation and is less expensive than that of glucose and lactose. However, used biomass should be biodegradable for the organisms (Levin et al., 2004). Microbial electrolysis cells use electro-hydro-genesis to directly convert biodegradable material into hydrogen (Call and Logan, 2008). Water-gas-shift is based upon a specific bacteria family which can grow in dark ambient and feeding upon CO. Since it occurs at low temperatures, it is thermodynamically favourable and possesses a high conversion rate compared to other biological hydrogen production technologies. However, it requires an appropriate CO source for production and darkness (Levin et al., 2004). Although all technologies briefly explained about biological hydrogen production above are promising technologies they need further development and investigation. Additionally the hydrogen production rate is relatively slower than other technologies.

1.1.3 Hydrogen from Water Splitting

Hydrogen can be produced using fossil fuels, water, biomass, anthropogenic wastes and hydrogen sulphide. Water is one of the most promising resources for hydrogen production. Water can be split into hydrogen and other products by several technologies. High and low temperature electrolysis, pure and hybrid thermochemical water splitting cycles, photochemical, and radiochemical systems are promising technologies for hydrogen production from water.

Electrolysis

Electrolysis is one of the simplest ways to produce hydrogen from water. It can simply be summarized as conversion of electric power to chemical energy in the form of hydrogen and oxygen as a by-product with two reactions in each electrode; anode and cathode. There is a separator between anode and cathode electrodes which ensures products remain isolated. Electrolysers can be classified in three types: Alkaline water electrolysers (AE), proton exchange membrane electrolysers (PEM) and high temperature electrolysers (Dincer, 2012). A simple representation of electrolysis process and possible resources to produce hydrogen via electrolysis is shown in Figure 1.4.

PEM electrolysers typically use Pt black, iridium, ruthenium, and rhodium electrode catalysts and a Nafion membrane (Turner et al., 2008). Water is introduced and is split into protons and hydrogen; protons travel through a membrane where they are recombined into hydrogen. PEM electrolysers can be coupled to electric power plants, wind turbines, and organic Rankine cycles (ORC). PEM electrolysers are more efficient than alkaline electrolysers (56-73% based on LHV of hydrogen with an 80-95% conversion) but more expensive due to the costly membrane requirements. Figure 1.5 represents polarization performance of various PEM water electrolysis for various current densities. AEs are most commonly used, most mature, and the cheapest way of producing hydrogen from water compared to other electrolysis methods (Turner et al., 2008). AEs are typically composed of electrodes, separators and aqueous alkaline electrolyte of approximately 30 wt% KOH or NaOH (Holladay et al., 2009). Almost 99.7% hydrogen purity and energy efficiency range of 55-90% (higher efficiencies at higher temperatures up to 120 ºC) can be obtained from an AE.

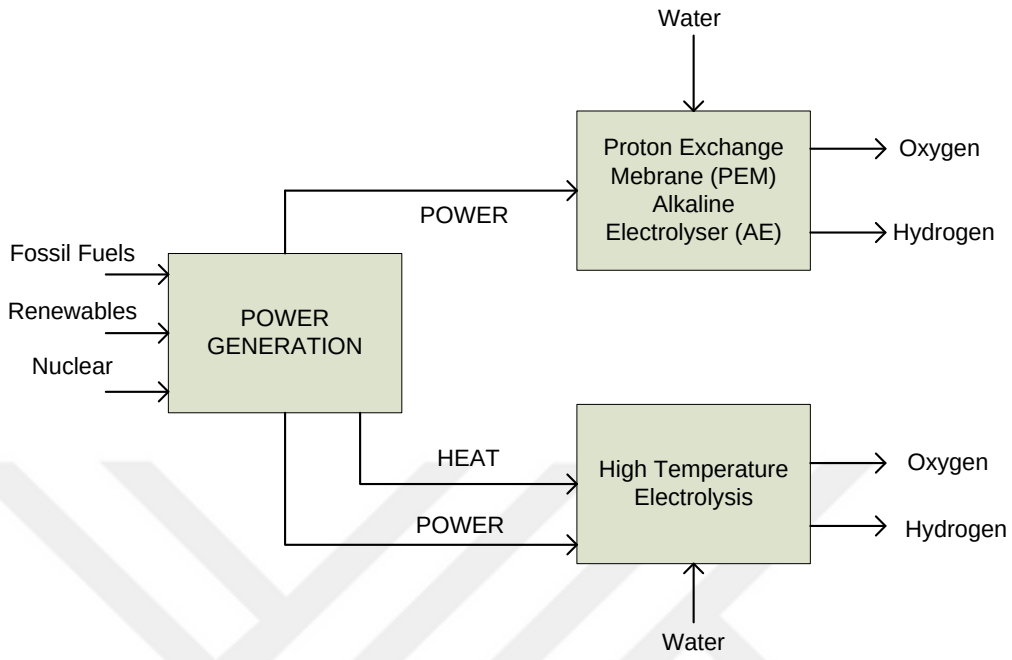

Figure 1.4 System configuration for electrolytic hydrogen production technologies (Modified from Dincer and Zamfirescu, 2012).

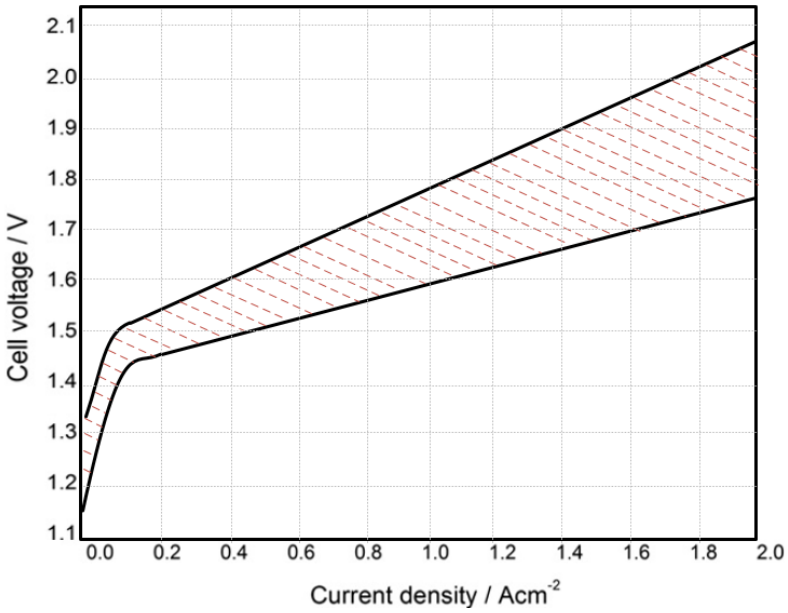

Figure 1.5 Range of water electrolysis voltage at increased current density (Modified from Carmo et al., 2013).

Solid oxide electrolysis cells (SOEC) are used in reverse as solid oxide fuel cells to produce power using gaseous fuels and hydrogen at high temperatures. Proton conducting

SOECs operate at 750-1025 K and oxygen ion conducting SOECs operate at 1000-1300 K. SOECs are not commercially available, however reverse SOECs are widely used in industry with a production of 300 kW. The average efficiency of a SOEC can be achieved up to 65% (Nieminen et al., 2010). High temperature steam electrolysis process can be considered as the reverse process of solid oxide fuel cells where the electrical energy demand can be decreased by around 24% than the conventional water electrolysis at elevated temperatures. A simplified diagram of nuclear based high temperature steam electrolysis process is illustrated in Figure 1.6 by coupling the HTSE process with the power generation cycle.

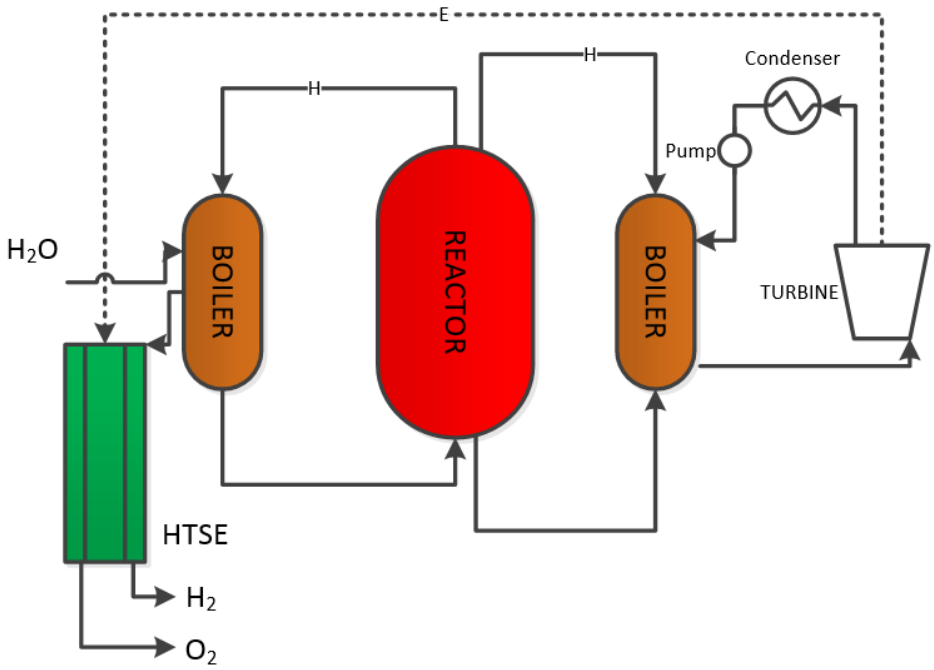

Figure 1.6 Schematic diagram of HTSE process (Modified from Yildiz et al., 2006).

Pure Thermochemical Water Splitting

Thermochemical splitting of water is an alternative to electrolytic splitting of water. This method requires more than one chemical reaction and sums the one step water thermolysis at decreased maximum temperatures. Water splitting at high temperature (thermolysis) is possible at very high temperatures (>2000K) and results in production of oxygen and hydrogen as one input which requires a very challenging separation process (Naterer et al., 2013).

Multi-step thermochemical cycles work at lower maximum temperatures than one step thermolysis through a cyclic process of splitting water. These steps vary from 2 to 6 steps in relation with the chemistry of the substances. Higher number of steps tends to work at lower maximum temperatures. However, the minimum achievable temperature is around 800ºC. A generalized reaction for a three-step thermochemical reaction can be written as follows:

$$H_2O + A \rightarrow 0.5O_2(or\ 0.5H_2) + AH_2(or\ AO) \quad (1.1)$$

$$AH_2(or\ AO) + B \rightarrow 0.5H_2(or\ 0.5O_2) + AB \quad (1.2)$$

$$AB \rightarrow A + B \quad (1.3)$$

Some multi-step thermochemical cycles with maximum temperatures lower than 1273 K are tabulated in Table 1.1 with their efficiencies (considering the efficiencies higher than 50% only).

Hybrid Thermochemical Water Splitting

Hybrid thermochemical cycles can be divided as thermo-electrochemical, thermo-photo-electrochemical, and thermo-radiochemical cycles. Thermo-electrochemical cycles utilize electricity at one of the steps throughout the cycle. Thermo-photo-electrochemical cycles require a photochemical reaction to complete the cycle, and radiochemical reaction is needed for thermo-radiochemical cycles. In this section, we mainly focus on thermo-electrochemical cycles only.

Most thermo-electrochemical cycles have been proposed in order to decrease the Reverse Deacon Reaction temperature by using electrical work lower than water electrolysis to make the cycle a feasible one. Figure 1.7 shows the effect of electrical energy usage on Gibbs energy of thermochemical cycles. Lower temperature cycles tend to consume more electrical work to decrease the Gibbs energy to zero. Low maximum temperatures are one of the most important characteristics of hybrid cycles to utilize heat from relatively low temperature heat sources such as nuclear and solar energy.

Table 1.1 Some selected thermochemical cycles (Selection is based on maximum temperature (<1273K) and efficiency (>50%)).

Cycle	Number of steps	T_{max} (K)	Reactions	η (%)
UNLV*-159	3	1023	$H_2O+SO_2+C_2H_4 \rightarrow C_2H_6+H_2SO_4$ (623K) $C_2H_6 \rightarrow C_2H_4+ H_2$ (1073K) $H_2SO_4 \rightarrow 0.5O_2+ H_2O+SO_2$ (1123K)	58
Mark-2	3	1073	$Mn_2O_3+4NaOH \rightarrow H_2+ H_2O+ 2Na_2OMNO_2$ (1073K) $2MnO_2 \rightarrow 0.5O_2+Mn_2O_3$ (873K) $2H_2O+2Na_2OMnO_2 \rightarrow 4NaOH+2MnO_2$ (373K)	57
Mark-2C	4	1123	$H_2+CO \rightarrow H_2+CO_2$ (773K) $2MnO_2 \rightarrow).5O_2+Mn_2O_3$ (873K) $Mn_2O_3+2Na_2CO_3 \rightarrow 2NaOMnO_2+CO_2+CO$ (1123K) $nH_2O+2Na_2OMnO_2+2CO_2 \rightarrow 2Na_2CO_2nH_2O+2MnO_2$ (373K)	57
LASL*	3	1273	$3H_2O+3Li_2OMn_2O_3 \rightarrow 6LiOH+3Mn_2O_3$ (355K) $6LiOH+2Mn_3O_4 \rightarrow H_2+3Li_2OMn_2O_3+2H_2O$ (973K) $3Mn_2O_3 \rightarrow 0.5O_2+2Mn_3O_4$ (1273K)	56
JULICH*	3	1223	$H_2O+CO \rightarrow H_2+CO_2$ (773K) $H_2SO_4 \rightarrow 0.5O_2+SO_2+H_2O$ (1223K) $CO_2+SO_2+H_2O \rightarrow CO+H_2SO_4$ (623K)	56
UNLV-142	3	1123	$H_2O+CH_4 \rightarrow 3H_2 +CO$ (1100K) $2H_2+CO \rightarrow CH_2OH$ (500K) $H_2SO_4 \rightarrow 0.5O_2+ H_2O+SO_2$ (1123K)	52
IGT*-C7	3	1273	$H_2O+F_2O_3+2SO_2 \rightarrow H_2+2FeSO_4$ (400K) $SO_3 \rightarrow 0.5O_2+SO_2$ (1273K) $FeSO_4 \rightarrow Fe_2SO_3+SO_2+SO_3$ (973K)	51

*IGT: Institute of Gas Technology, LASL: Los Alamos Scientific Laboratory, UNLV: University of Nevada Las Vegas, JULICH: Julich Research Centre.
Source: Naterer et al., 2013

The Hybrid Sulfur (HyS) cycle is one of the simplest thermochemical water splitting processes, including only two reactions (Yan and Hino, 2011). This is the well-known ISPRA Mark-11 cycle and under development by Westinghouse. Figure 1.8 shows the process of HyS cycle with respect to its chemical reactions. The first reaction is the

thermochemical step where decomposition of sulfuric acid is accomplished by providing high-temperature heat at around 900°C. Second step is the SO_2-depolarized water splitting process where it requires electrical work at a temperature range of 80-120°C. Simple water electrolysis theoretically consumes 1.23 V for splitting a mole of water, where HyS cycle needs only 0.158V electrical input. The practical electricity consumption of electrochemical HyS step is around 0.6 V, which makes this system promising compared to other proposed hybrid cycles in terms of electrical work requirement.

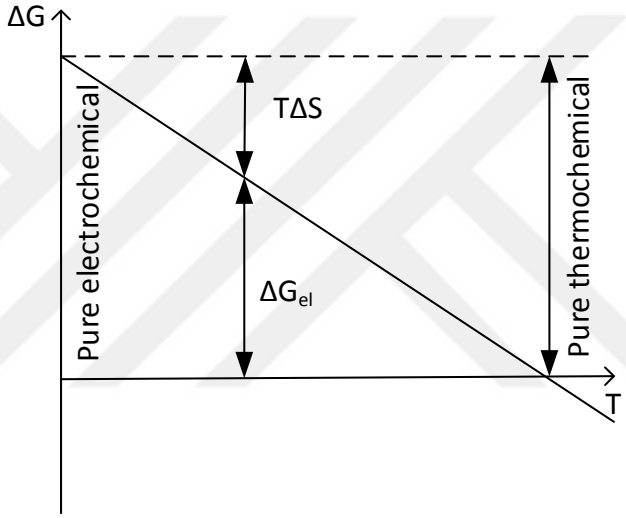

Figure 1.7 Minimization of Gibbs energy using electrical work at lower temperatures (Modified from Yan and Hino, 2011).

The hybrid chlorine cycle (Hallet Air Products) is another two-step process with an electrochemical reaction. Separation of the mixture of oxygen and HCl is a very challenging process, and achieving a reasonable yield of products can be accomplished at and above 850ºC with excess steam (Gooding, 2009). The cycle schematic diagram is illustrated in Figure 1.9. HCl electrolysis theoretically requires 0.99 V for 1 mole of hydrogen production. Since aqueous HCl production is expected from the thermochemical step of the hybrid chlorine cycle, where the electrical requirement increases up to 1.8 V, and it is a mature process. Thus, this cycle may not compete with water electrolysis unless anhydrous HCl is utilized as the electrolysis input.

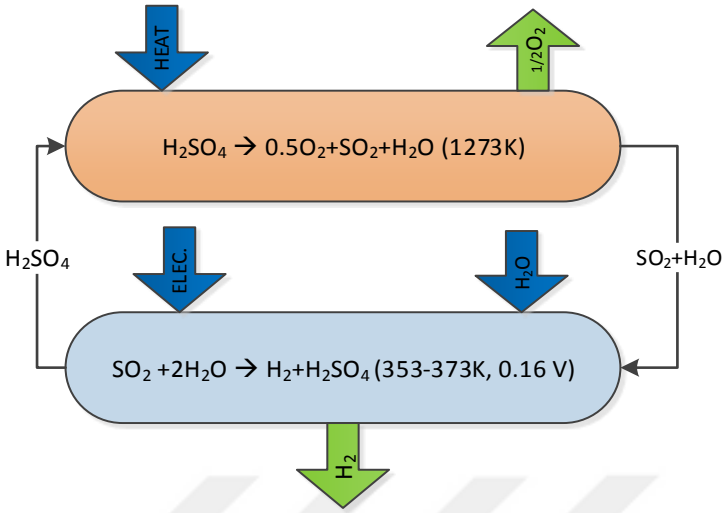

Figure 1.8 Schematic diagram of hybrid sulfur cycle.

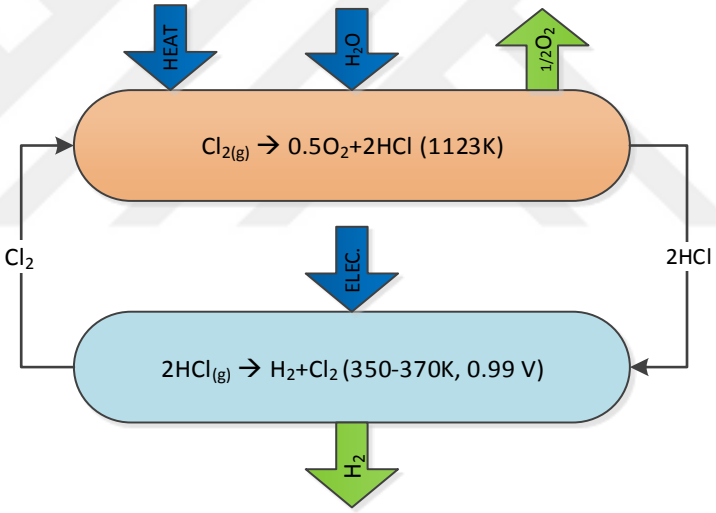

Figure 1.9 Schematic diagram of hybrid chlorine cycle.

Another two step hybrid process has been proposed by Dokiya and Kotera (1976) and it is denoted as CuCl-C cycle by Lewis et al., (2009). The thermochemical step produces HCl and CuCl, where these substances are the inputs for the electrochemical step. Concentration of HCl gas is again an important parameter for lower energy requirement of this step. The theoretical voltage requirement ranges from 0.3 to 1.2 V depending on the concentration of CuCl and HCl, as well as the current density. This cycle is also illustrated in Figure 1.10. Estimated efficiency for this plant is reported as 46%.

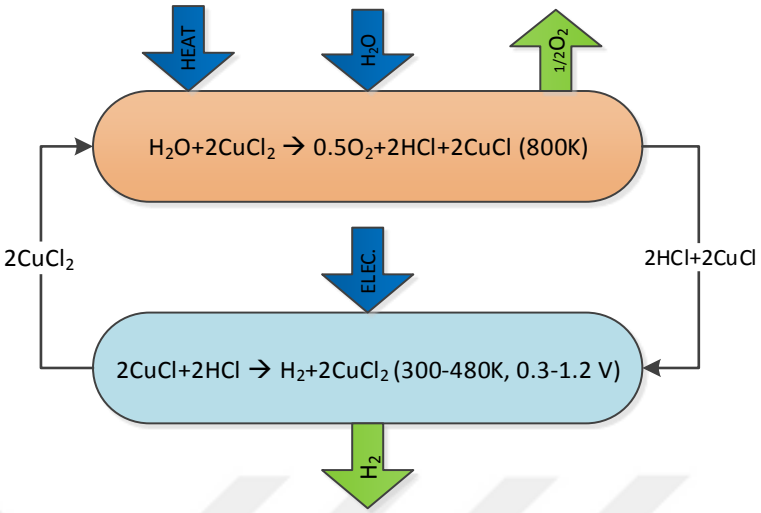

Figure 1.10 Schematic diagram of two-step CuCl-C cycle.

Argonne National laboratory (ANL) studied a three step Cu-Cl cycle which was denoted as CuCl-B by Levis and Masin (2009). The electrochemical reaction is proposed to have a high pressure (~24 bar). This cycle is different than the CuCl-C in terms of products from the hydrolysis step. It is found out that the lower reactor temperature yields Cu_2OCl_2, rather than separate oxygen production as shown in Figure 1.11. Considering a 50% electricity generation efficiency, 45% can be achieved from this three-step hybrid process.

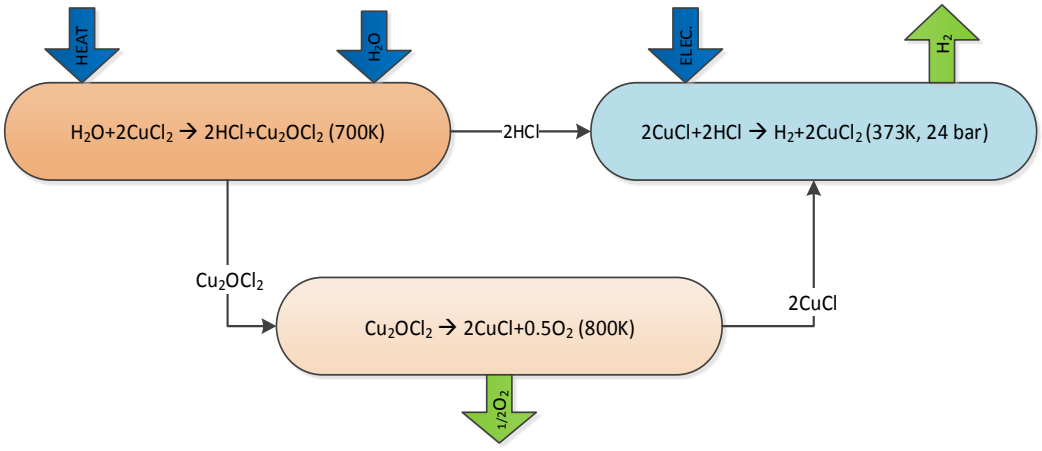

Figure 1.11 Schematic diagram of three-step CuCl-B cycle.

The four-step CuCl hybrid cycle has also been proposed with two options being researched. The first one is the IGT cycle, and the second one is the University of Ontario Institute of Technology (UOIT)'s CuCl cycle (Naterer et al., 2013). The IGT cycle is

denoted as CuCl-A by Lewis and Masin (2009). Figure 1.12 represents both cycles. The main difference between these two cycles is the electrolysis step. The CuCl-A option has a continuous step of recovering CuCl from the hydrogen production step to produce Cu at an electrolysis step. The fourth step of the UOIT CuCl cycle is drying of $CuCl_2$ after the electrolysis step to enhance the performance of the hydrolysis step.

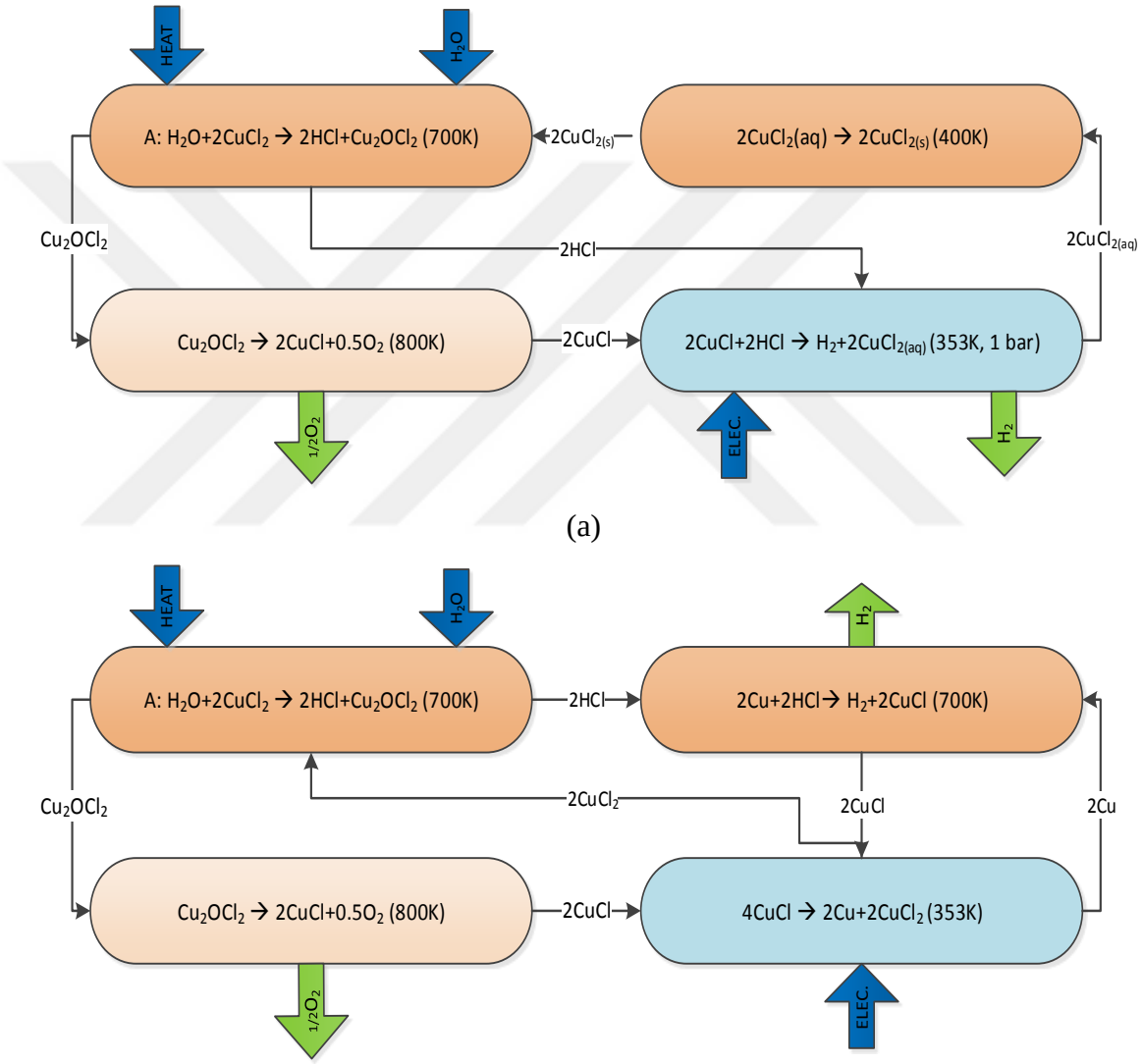

Figure 1.12 Schematic diagrams of four-step CuCl cycle configurations (a) UOIT and (b) CuCl-A.

The expected efficiency of the four-step CuCl cycle is 50%, and it is one of the least electrical work requiring hybrid technologies so far. The electrolysis step is still under

research with various electrochemical cells, but indicates a low voltage requirement at low current densities with a limiting current density. Maturity of the electrochemical step can be accomplished in the upcoming decade to compete with mature electrolysis systems such as water and HCl.

Argonne National Laboratory (ANL) studied the hybrid HBr cycle where the maximum temperature of this cycle is around 770ºC. However, lower theoretical voltage requirement of the electrolysis step can make this cycle a feasible one. Higher current densities increases the practical voltage requirement up to 1.5 V, which is still compatible with conventional water electrolysis. Efficiency of the cycle is relatively low (~30%) due to the high temperature heat requirement for the hydrolysis step. ANL also conducted preliminary work on a three-step Li-N cycle. Theoretical voltage requirement for the electrolysis step is close to that of water electrolysis (~1.2 V) and maximum temperature requirement is 375ºC. This cycle is a good candidate to utilize heat from low temperature energy sources if the electrolysis step is advanced enough to compete with water electrolysis (Levis and Masin, 2009).

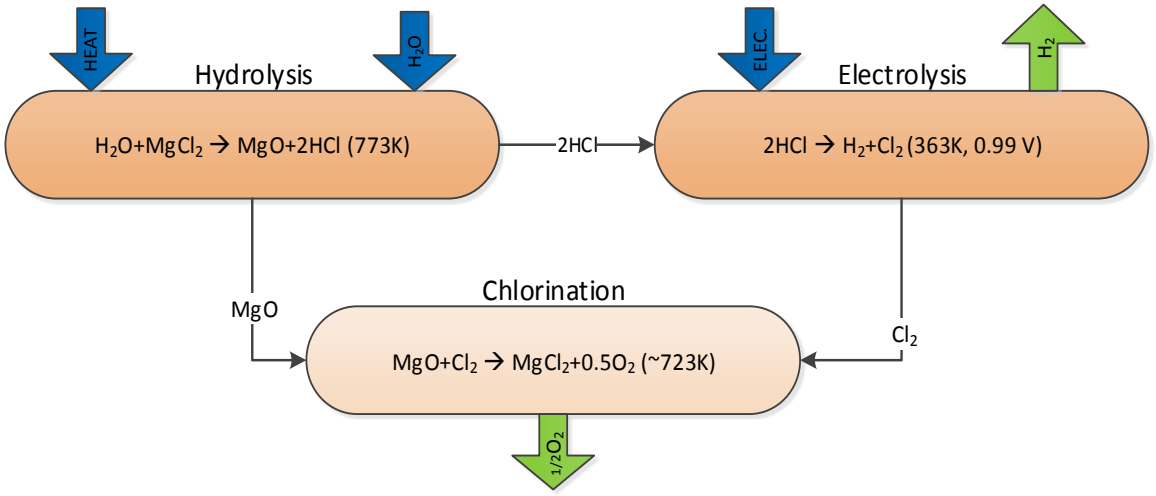

Figure 1.13 Schematic diagram of three-step $MgCl_2$ –MgO cycle.

The hybrid Mg-Cl cycle is another three-step thermo-electrochemical cycle utilizing heat and electrical work to produce hydrogen. Main steps of the cycle are; the hydrolysis of $MgCl_2$, the chlorination of MgO, and the electrolysis of HCl gas. It can be accomplished with two different options, namely $MgCl_2$-MgO, and $MgCl_2$-MgOHCl

cycles as reported by Hesson (1979). Feasible chemical reactions, mature electrolysis technology, and low maximum temperature of the cycle are promising in terms of integrating this cycle with nuclear and solar energy sources. Schematic diagram of the $MgCl_2$-MgO cycle is illustrated in Figure 1.13. ANL studied the hydrolysis step of the cycle with additives and reported promising results for reactant conversion at desired temperatures (Simpson et al., 2006).

One of the main issues with the Mg-Cl cycle is possible steam/HCl mixture after the hydrolysis step. Aqueous HCl electrolysis is also a mature process where up to 1.8 V per mole of hydrogen is required with several solubility issues of oxygen and chlorine gas in water. Thus, the anhydrous HCl production is one of the crucial considerations throughout the cycle in order to make it a feasible one. The electrolysis step can work below 80ºC at atmospheric pressure with both anhydrous and aqueous HCl.

The $MgCl_2$-MgOHCl cycle is also one of the alternative to the ideal cycle where the hydrolysis reaction is exothermic and commences at 240ºC with a full reactant conversion at 300ºC. In order to produce the same amount of hydrogen as in $MgCl_2$-MgO cycle, the stoichiometry of this reaction should be doubled. Figure 1.14 represents the schematic diagram of this cycle. The chlorination reaction produces a mixture of steam and oxygen, where possible problems may occur during the separation process due to solubility of oxygen in water.

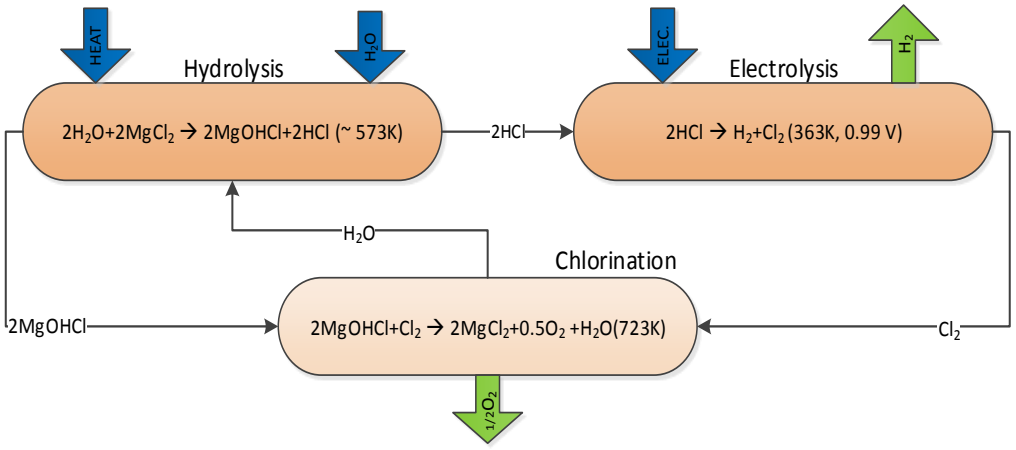

Figure 1.14 Schematic diagram of three-step $MgCl_2$-MgOHCl cycle.

Other Technologies for Water Splitting

There are several other types of water splitting proposed by several researchers and are still under research and development. These proposed technologies are (Grimes et al., 2008):

- Mechano-catalytic water splitting
- Water plasmolysis
- Water magnetolysis
- Water radiolysis

Above technologies are still under development stage and maturity of these processes are considered to be long term.

1.2 Hydrogen Storage and Distribution

Physical and chemical properties of hydrogen result in technical challenges for standard methods of storing hydrogen in pure form. Effective hydrogen storage is one of most critical issues that needs to be addressed to establish a viable hydrogen economy. There are five common ways to store hydrogen:

- Pressurized hydrogen
- Liquefied hydrogen
- Hydrogen storage in solids
- Hybrid storage systems
- Regenerative off-board systems

The high pressure hydrogen storage has been accomplished in a 700 bar system with better volumetric capacity and smaller size of tanks. However, there is still a safety concern due to the very high tank pressures. Materials research has been performed to understand degradation effects to reduce several risks (Ball and Wietschel, 2009).

As an alternative to high pressure storage of hydrogen, liquefaction is particularly attractive. A cooling of 21 K should be provided for liquefaction and 30% of hydrogen LHV is required to provide energy for cryogenic refrigeration. The stored hydrogen evaporates after a certain period of time and 2-3% of evaporation occurs per day (Eberle et al., 2006; Nandi and Sarangi, 1993). A system developed by Linde has decreased the evaporation losses with a cryogenically liquefied air flowing through walls of hydrogen tank. A Linde liquefaction plant is shown in Figure 1.15 (Baker and Shaner, 1978).

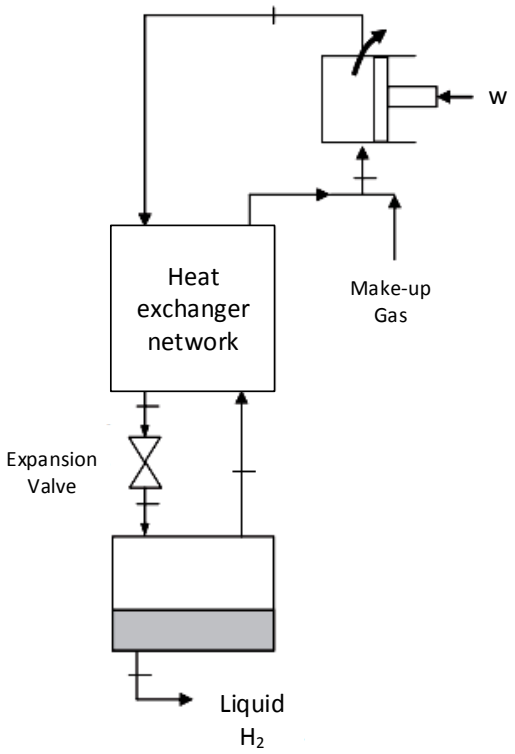

Figure 1.15 Schematic diagram of the Linde-Hampson liquefaction plant (Modified from Dincer and Kanoglu, 2013).

Hydrogen storage can also be accomplished by using metal hydrides with basic bonding mechanisms called chemisorption and physisorption. The main drawback of chemisorption is splitting or recombining hydrogen molecules as they form chemical bonds with the material, and storage with physisorption requires insulated cryovessels. The highest known volumetric hydrogen density is obtained from hydride storage of hydrogen (Mg_2FeH_6). Hydride storage tanks should be kept at elevated pressures to increase gravimetric capacity and operational features of storage systems which are called hybrid storage systems.

There are two main options for hydrogen distribution: delivery of gaseous or liquid hydrogen by trailers and pipeline transportation of hydrogen. The most economic option depends on transport volumes and distances. When considering cost of liquid hydrogen transportation, liquefaction plant costs should be included as well. Hydrogen can also be mixed with natural gas at a delivery point for use in combustion applications. Several

hydrogen distribution options have been studied and reported in the literature. However, the most efficient and inexpensive option is still under debate (Ball and Wietschel, 2009). Ratios of energy losses from storage and transportation for hydrogen can be listed as follows:

- 10-15% for hydrogen compression (200-800 bar)
- 30-50% for hydrogen liquefaction (20.1 K)
- 1.4% per 150 km for pipeline transportation
- 7.5-40% to pump hydrogen for cars at stations

1.3 Energy Sources

Energy requirement of hydrogen production can be provided by fossil fuels, renewable energy sources, nuclear energy, and waste heat. Although almost all types of fossil fuels can be used for hydrogen production, some of the renewable energy sources may not provide enough energy for hydrogen production. Therefore, a down selection in terms of type of energy and grade of heat for renewable energy sources should be performed specific to the hydrogen production process. Thermochemical and thermo-electrochemical water splitting processes require medium to high temperature heat as well as electrical work for hybrid processes. Solar and nuclear energy are two of the sources for hydrogen production via thermochemical water splitting cycles.

1.3.1 Solar Energy

Solar energy is one of the most abundant renewable energy sources, however, it has an intermittent nature. Solar radiation concentration can be accomplished using reflecting or refracting type collectors in order to achieve high temperature heat from solar energy. There are several practical solar thermal plants, providing a wide temperature range in order to produce several forms of energy. Main technologies can be sorted as: heliostat solar power tower, parabolic dish reflector, parabolic trough reflector, linear reflective Fresnel lens, and reflective Fresnel lens. Depending on the technology and the heat transfer fluids, these options can provide heat at levels varying from 250°C to 1250°C. Commonly temperature levels less than 370°C is accepted as low temperature applications. The types of some existing concentrating collectors are shown in Figure 1.16.

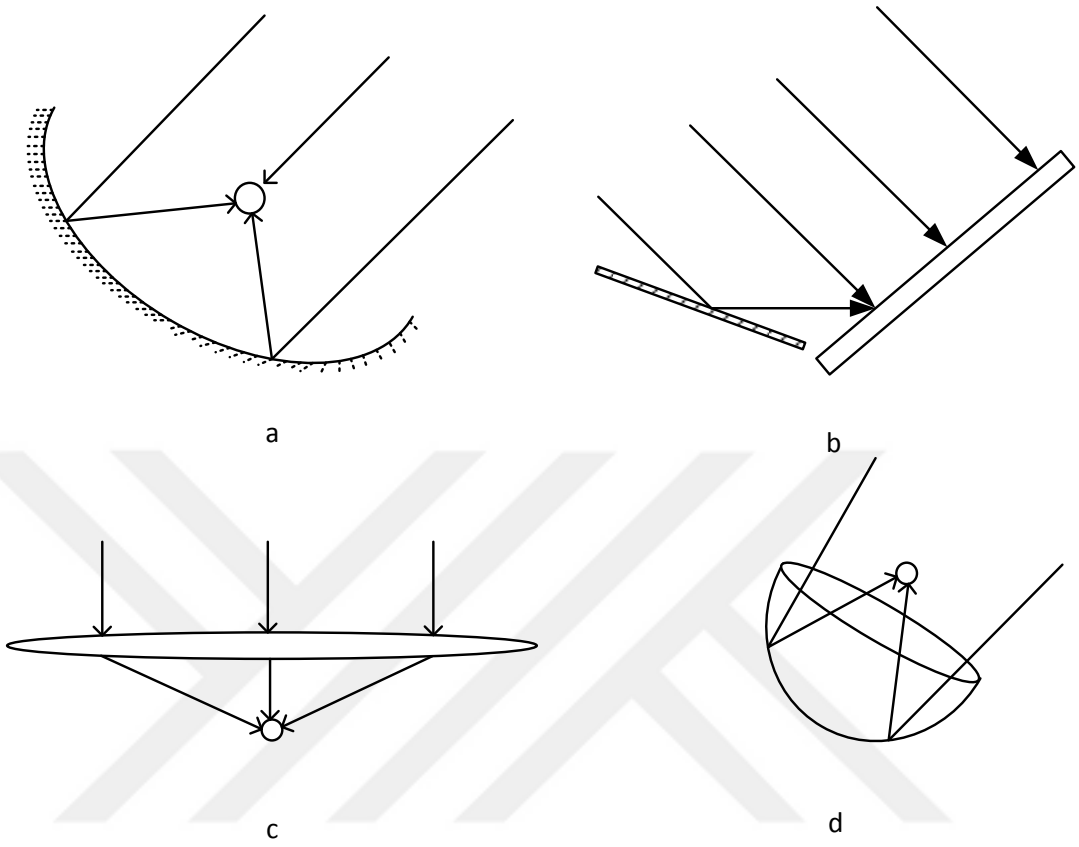

Figure 1.16 Some types of solar concentrators (a) cylindrical parabolic collector, (b) flat-plate collectors with reflectors (c) Fresnel lens collector, and (d) Parabolic dish collector (Modified from Sukathme and Nayak, 2008).

Solar power towers (SPT) which are also named as heliostat fields are used to convert solar irradiation to electricity without using organic fuels. Many sun-tracking mirrors, namely heliostats are used to focus the light on the tower in order to provide high-temperature (~565°C with molten salt storage) heat to heat transfer fluid (HTF). A schematic diagram of single tower heliostat field is shown in Figure 1.17.

Some existing systems use liquid sodium, steam, molten nitrate and air as the heat transfer fluid. Molten nitrate salts are considered as the most promising HTFs since these salts can be stored at higher temperatures to be used when the sun is out, and provides a steady state condition for SPTs (Zhang et al., 2013). Molten salts are less expensive than those of synthetic-oils and batteries when energy storage is considered. The life time, storage efficiencies, and the maximum temperatures are also favorable compared to other options. However, molten salts should be tracked carefully through the system since they

have comparatively higher freezing point (Pacheco and Dunkin, 1996). The upper critical temperature of molten salts is 550-600°C and makes these HTFs suitable for low and medium temperature thermochemical water splitting cycles. SPT systems can be regarded as suitable candidates to provide continuous heat and power supply for medium temperature hybrid thermochemical cycles with energy storage. Use of molten salts is a better option than using steam or other substances with their promising storage characteristics.

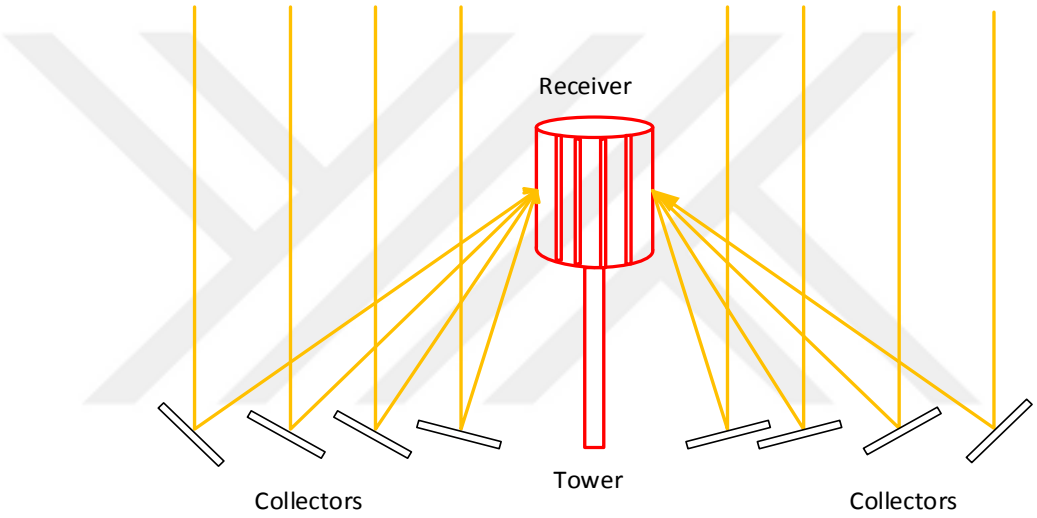

Figure 1.17 A single tower heliostat field.

1.3.2 Nuclear Energy

Although renewable energy sources are good candidates to supply energy needs of the communities in a clean and sustainable way, maturity of renewable based energy plants are still an ongoing process and the intermittent nature of most renewables can be a limiting factor for continuous energy supply. Therefore, nuclear energy is one of the most promising energy supply sources with mature technologies at a very large range of capacities.

Nuclear energy is converted into thermal energy within a fission reaction, and to mechanical energy with conversion units such as a steam Rankine cycle or a gas turbine cycle. Nuclear power plant efficiencies vary from 30-40% depending on the technology used, and generate up to 16% of global electricity demand. Major losses throughout the plant are due to thermal to mechanical energy conversion. It is possible to use the medium

to high temperature thermal energy source to supply heat for some endothermic reaction steps, and heating processes of thermochemical cycles to produce hydrogen (Naterer et al., 2010). Nuclear based hydrogen production can be accomplished by splitting water with aforementioned water splitting methods. Options for nuclear based water splitting for hydrogen production is shown in Figure 1.18.

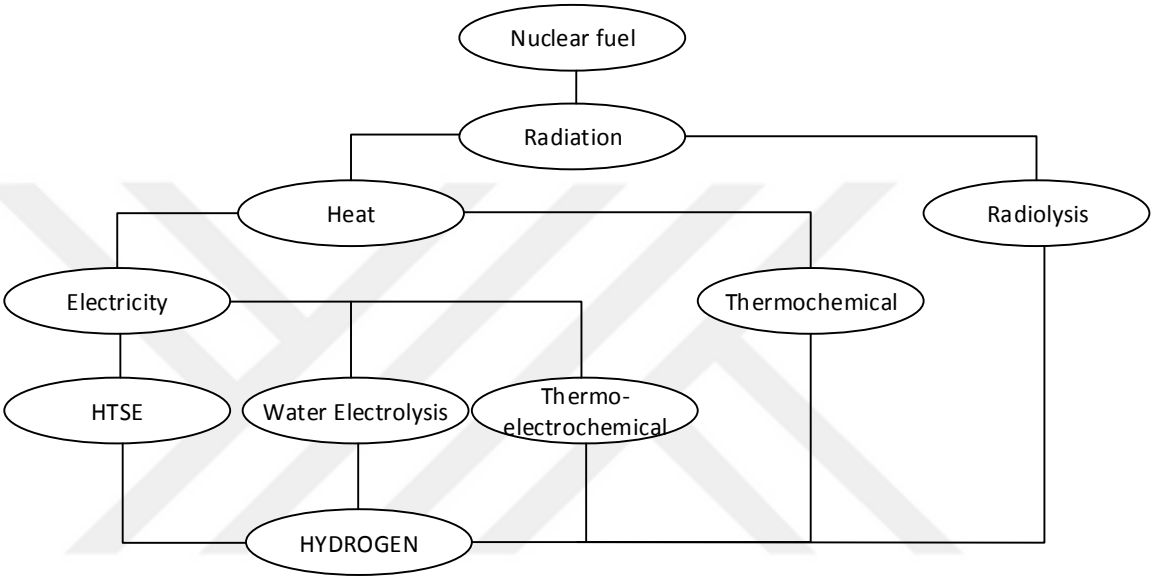

Figure 1.18 Pathways for nuclear hydrogen via water splitting methods.

Nuclear reactors are mainly classified in four generations starting from generation I to IV. First generation reactors are breeder or boiling type, where breeder reactors use either natural uranium or thorium-232 and boiling type reactors are built within a moderator environment to transfer the heat from reactor to a coolant. First generation reactors are not in use today. Second generation reactors include five types of reactors, where AECL (Atomic Energy Canada Limited) reactors belong to this generation. CANDU-6 (Canada Deuterium Uranium) reactors are second generation reactors using heavy water (deuterium) as moderator at ~350ºC, which absorbs less neutrons than light water coolant, and makes natural uranium use possible as fuel. Other reactor types are PWR (water-water reactor), BWR (boiling water reactor) and AGR (advanced gas reactor).

Table 1.2 Some selected nuclear reactors and their hydrogen production routes.

Reactor type	Coolant	Reactor coolant	Reactor size range (MWt)	Hydrogen production route

		temperature (°C)		
Light water reactors (PWR, AP, EPR)	Light water	280-325	2000-4080	Water electrolysis
Heavy-water reactors (CANDU, ACR)	Heavy water	310-319	2000-3200	Water electrolysis
Supercritical water reactor (S-LWR, CANDU, SCWR)	Light water	430-625	1600-2540	Water electrolysis, Thermochemical
Liquid metal fast reactors (SFR, LFR)	Sodium: lead: lead bismuth	500-800	45-3000	Water electrolysis, Thermochemical CH_4 Reforming
Molten salt reactors (MSR)	Salts	750-1000	900-2400	Water&Steam electrolysis, Thermochemical CH_4 Reforming
Gas-fast reactors (GFR)	Helium	850	600-2400	Water&Steam electrolysis, Thermochemical CH_4 Reforming
High-Temp. reactors (HTGR, VHTR)	Helium	750-950	100-600	Water&Steam electrolysis, Thermochemical CH_4 Reforming
Source: Yan and Hino, 2011.				

Generation III reactors are advanced models of generation II reactors with improved efficiency and safety with various designs. This generation reactors can be sorted as follows (Generation IV International Forum, 2014):

- CANDU-6 (Canadian Deuterium Uranium)
- AHWR (Advanced heavy water reactor)
- APWR (Advanced pressurized water reactor)
- ABWR (Advanced boiling water reactor)
- EPR (European pressurized reactor)

Also, Generation IV reactor concepts are mainly defined by six reactor types as follows:

- GFR (Gas fast reactors)
- VHTR (Very high temperature reactor)
- SCWR (Super critical water-cooled reactor)
- SFR (Sodium-cooled fast reactor)
- LFR (Lead-Cooled reactor)

- MSR (Molten salt reactor)

Some reactor types with their coolants, maximum temperatures, capacities, and their routes for hydrogen production are presented in Table 1.2. CANDU-SCWR and MSR reactors are suitable candidates for medium temperature hybrid thermochemical hydrogen production systems and provides a large range of scaled up plants with their extended capacities.

1.4 Motivation

Hydrogen can be produced from both primary and secondary energy sources. Commercially applied methods generally consist of fuel processing and the required energy is provided from primary energy sources such as coal and CH_4. Natural gas reforming and coal gasification are commercially available and are still under research to improve efficiency of existing plants. Biomass based hydrogen production is still under development and not commercially available yet. Hydrogen production from secondary energy resources are exclusively by water electrolysis using electricity. So far, the highest rate of direct hydrogen production is occupied by steam methane reforming. However, renewable based hydrogen production with several types of methods can be good candidates to compete with conventional hydrogen production methods (Dincer and Zamfirescu, 2012).

Pure thermochemical cycles have the disadvantage of high maximum temperatures to split water into hydrogen which makes these cycles challenging in terms of material selection and require a high temperature heat source. Therefore, hybrid thermochemical cycles have been proposed as feasible alternatives to produce hydrogen at lower maximum temperatures with and additional electrical work consumption. Hybrid thermochemical cycles show the potential to be coupled with relatively lower temperature sources than that of pure thermochemical cycles, which makes these cycles good candidates to utilize heat from clean energy sources. The main hybrid thermochemical cycles which are under intensive research, and in the development stage are the Hybrid Sulfur Cycle (HyS) and Copper-Chlorine (Cu-Cl) cycle.

The Mg-Cl cycle is another hybrid thermochemical hydrogen production method which shows promising results in terms of maximum temperature requirement and

electrical work consumption. This cycle can be coupled with several renewable and nuclear energy resources (500-550ºC), and shows lower voltage requirement than that of conventional water electrolysis (1.01 V). However, studies in the literature are generally based on theoretical conditions and lack the assessments of the cycles with various practical considerations. Therefore, this thesis work is devoted to investigation of the Mg-Cl cycle both theoretically and practically, in order to make the Mg-Cl cycle a more feasible method that can compete with other hybrid cycles.

1.5 Objectives

In this thesis, a comprehensive investigation of the Mg-Cl cycle is conducted, its integrated systems are developed and various assessments are performed by using various tools of thermodynamics, thermochemistry and economics, and by conducting experimental research for key reactions of the cycle. Initially, a simulation of the Mg-Cl cycle is conducted to specify origin of inefficiencies and various problems throughout reactions of the cycle. These inefficiencies are analysed using Aspen Plus simulations. Afterwards, novel reactions are adapted to the ideal Mg-Cl cycle in order to overcome existing problems of reactions, where developed reactions are validated with the simulations and literature studies. Finally, an effective cycle is developed with more feasible reactions throughout the cycle and decreased steam requirement of the hydrolysis reactor. Results of Aspen Plus software are transferred to Engineering Equation Software (EES) for thermodynamic assessment and parametric studies.

Further investigation is conducted in order to decrease the electrical work consumption of the cycle by experiments. Since the product of the hydrolysis reactor is a mixture of steam and HCl, this mixture yields to a higher electrolysis power requirement. Therefore, an experimental setup is designed to separate HCl from steam to decrease the electrolysis voltage, which leads to decreased power consumption of the overall cycle. Experimental results are observed with various measurement tools (TGA, XRD and SEM), and these results are adapted to the final design of the Mg-Cl cycle. A MATLAB code is also adapted to determine uncertainty of the experimental results.

Final design of the Mg-Cl cycle is analysed using thermodynamic tools (mass, energy, entropy, and exergy) by considering all components of the cycle, followed by a

comprehensive comparison with other cycle options. Exergoeconomic analysis of the final design is conducted based on the state point information from thermodynamic analysis, and a comparison is made with other hybrid thermochemical cycles in terms of economics. Multi-objective optimization of the final design in also conducted by considering cycle cost and efficiency as objective functions to be enhanced.

Since the required heat and electricity for the Mg-Cl cycle is provided from another energy source, two different integrated systems are developed to provide heat and power for the Mg-Cl cycle, and to store the produced hydrogen. Thermodynamic analyses of both integrated systems are performed to provide a better view of hydrogen production performance using different energy sources and hydrogen storage methods. Several parametric studies are conducted to optimize subsystem efficiencies by considering several system and environmental parameters of both systems.

The main objective of this thesis is to investigate the Mg-Cl cycle by conducting research on individual reactions of the cycle, further development of the cycle by considering novel approaches to enhance thermochemistry of the cycle, and to integrate this cycle to various other thermal systems for a more energy and cost effective plant operation. Available literature studies do not provide adequate information on cycle performances and economics for practical conditions, and it is lacking in experimental investigations. Various thermodynamic assessments in the literature are mainly based on basic theoretical approaches which do not provide detailed performance of the system, and do not indicate any solution for a better performing cycle. Therefore, this thesis work focuses on the Mg-Cl cycle in detail to specify shortcomings of this cycle, and enhance these shortcomings by developing novel methods for a more efficient and cost effective hydrogen production.

Specific objectives of this thesis study can be listed as follows:

1. To simulate and develop various configurations of the Mg-Cl cycle
    - The ideal Mg-Cl cycle is simulated as the reference model, and further investigated considering practical conditions for reactions throughout the cycle.
    - Novel configurations of the Mg-Cl cycle are developed for enhanced hydrogen production performance, cycle thermochemistry, and decreased steam requirement for the hydrolysis reactor.

- Energy and exergy performances of all developed configurations are thermodynamically studied and compared to specify the best performing configuration to be coupled to appropriate energy resources.
- A final configuration of the Mg-Cl cycle is developed with superior thermodynamic performances.

2. To conduct experiments for decreased electrical work consumption of the cycle
    - An experimental setup is built to separate HCl from steam using heterogeneous reactions.
    - Several experiments are performed to observe effects of various reactor parameters on products of the experiments.
    - Experimental uncertainties are determined to obtain errors of the experimental investigation.
    - Samples from experiments are observed using various measurement tools such as TGA, DTA, XRD, and SEM imaging.
    - Experimental results are integrated into the simulation of the final Mg-Cl cycle configuration.
3. To develop Mg-Cl based integrated systems using nuclear and solar energy as energy sources with hydrogen storage.
    - System I: A heliostat solar field integrated with a CO_2 gas turbine to provide heat and power to Mg-Cl cycle. A hydrogen compression plant to store hydrogen from Mg-Cl cycle.
    - System II: A nuclear reactor (SCWR) integrated with a reheat and regeneration type steam Rankine cycle (SRC) to provide heat and power to Mg-Cl cycle. A Linde-Hampson liquefaction plant to store hydrogen from Mg-Cl cycle.
4. To perform analysis and parametric optimization of the Mg-Cl cycle and integrated systems
    - A thermoeconomic model is developed for the exergoeconomic analysis of the Mg-Cl cycle.
    - The Mg-Cl cycle is optimized for enhanced thermodynamic performance and decreased plant cost.

- The amount and origin of irreversibilities throughout proposed systems are investigated.
- Component based thermodynamic analyses of integrated systems and their comparative assessments are conducted.

1.6 Thesis Outline

An organization of the thesis is presented in seven main sections. A comprehensive introduction and background on most of the hydrogen production methods by generally focusing on thermochemical water splitting, as well as motivation and objectives of the thesis are provided in Chapter 1. Chapter 2 focuses on literature review on the Mg-Cl cycle and its individual reactions. Several other recent literature information is provided for system integration and for similar hybrid thermochemical cycles. Information on selected components and property methods from the Aspen Plus database are presented in Chapter 3, where simulated and developed configurations, and system integration of the Mg-Cl cycle are explained in detail. Chapter 4 represents two procedures of experiments with the methodology used with an uncertainty assessment, where detailed analyses and optimization of the Mg-Cl cycle and its integrated systems are presented in Chapter 5. Chapter 6 provides results for simulations, experimental work, and integrated systems, as well as their comprehensive comparison by providing deep information on main and detailed findings from this research. Summary of the results and further recommendations are provided in Chapter 7.

CHAPTER 2: LITERATURE REVIEW

2.1 Introduction

This section provides a large and detailed overview of individual reactions of the Mg-Cl cycle by considering chemistry, thermochemistry, and thermodynamics of the reactions and the overall Mg-Cl cycle. An initial literature review is also provided for recent studies on hybrid thermochemical cycles including possible system integration for the Mg-Cl cycle.

2.2 Thermochemical Water Splitting Cycles

Majority of thermo-electrochemical cycles have been proposed in order to decrease the reverse Deacon reaction temperature by using electrical work lower than required for water electrolysis to make the cycle a feasible one. The hybrid chlorine cycle (Hallet Air Products) has been proposed as a two-step process with an electrochemical reaction. The separation of O_2 and HCl is a very challenging process. Achieving a reasonable product yield can be accomplished at 850ºC with excess steam (Gooding, 2009). The cycle schematic diagram is illustrated in Figure 1.9.

The Hybrid Sulfur (HyS) cycle has been one of the simplest thermochemical water splitting processes as it includes only two reactions (Yan and Hino, 2011). This is the well-known ISPRA Mark-11 cycle under development by Westinghouse. HyS needs a theoretical value of 0.16 V electrical input which significantly decreases the power requirement for hydrogen production. Practical electricity consumption of the electrochemical HyS step is around 0.6 V, making this system promising in comparison to other proposed hybrid cycles in terms of electrical work requirement.

Another two step hybrid process has been proposed by Dokiya and Kotera (1976) which is denoted as the CuCl-C cycle by Lewis and Masin (2009). The thermochemical step produces HCl and CuCl; these substances are the inputs for the electrochemical step. The concentration of HCl gas is again an important parameter of the lower energy requirement of this step. The theoretical voltage requirement ranges from 0.3 to 1.2 V related to the concentration of CuCl and HCl, as well as current density. Argonne National laboratory (ANL) has studied a three step Cu-Cl cycle which is denoted as CuCl-B by Levis

and Masin (2009). The electrochemical reaction has been proposed to have high pressure (~24 bar). This cycle has been different than the CuCl-C in terms of products in the hydrolysis step. It has been discovered that lower reactor temperature yields to Cu_2OCl_2 production rather than separate O_2 production. Considering a 50% electricity generation efficiency, 45% efficiency has been achieved from this three step hybrid process.

ANL has studied the hybrid HBr cycle where the maximum temperature of this cycle is around 770ºC. However, the lower theoretical voltage requirement of the electrolysis step could make this cycle a feasible one. Higher current densities has increased the practical voltage requirement up to 1.5 V, which is still compatible with the conventional water electrolysis. Efficiency of the cycle has been found to be relatively low (~30%) due to the high temperature heat requirement for the hydrolysis step. ANL has also conducted preliminary work on a three-step Li-N cycle. Theoretical voltage requirement for the electrolysis step is close to that of water electrolysis (~1.2 V) and the maximum temperature requirement is 375ºC. This cycle can be regarded a good candidate to utilize heat from low temperature energy sources if the electrolysis step is advanced enough to compete with water electrolysis (Levis and Masin, 2009).

2.3 Magnesium-Chlorine Cycle

Hydrogen production via the Mg-Cl cycle requires individual reaction steps for completion of the cycle. Stoichiometric reactions throughout the cycle have been reported by Funk (1976) with other 70 cycles. The main steps of the cycle, which influence the performance characteristics of the cycle have been previously conducted by many researchers. Since every step of the cycle produces an individual substance, existing literature focuses on the products of these steps rather than integrating these steps to study the Mg-Cl cycle. Reported literature overview for the individual steps are very important to understand the chemistry, kinetics, and thermochemistry of the cycle. The Mg-Cl cycle can run with two different hydrolysis steps. The first one is a low-temperature exothermic reaction to produce MgOHCl and direct chlorination of this substance. Since the produced HCl rate is 1:1, the amount of $MgCl_2$ feed should be 2 moles for 2 moles of steam, which requires additional heating load for larger amounts of steam. The second option has been the high temperature hydrolysis of $MgCl_2$ (Haag, 1977).

2.3.1 $MgCl_2$ Hydrolysis

Due to its high reactivity, it is hard to find magnesium in its free state. It generally forms as chlorides, and due to its desiccant nature, it is found as in various forms with water. Production of anhydrous $MgCl_2$ is important for the sake of hydrolysis in dry form, which requires a couple of reactions at elevated temperatures. During the hydrolysis of $MgCl_2$, Mg may react with both Cl_2 and OH^- which tends to form MgOHCl.

Formation of MgOHCl from the hydrolysis of $MgCl_2$ has first been investigated by Moldenhauer (1906). The thermochemistry of this product has been studied by Kelley (1946). Formation and decomposition of this substance have also been experimentally reported by the aforementioned researchers. It has been investigated that MgOHCl can form in various ratios of the substances it includes, and it has been reported that the lower temperature hydrolysis tends to produce MgOHCl rather than pure MgO particles.

Energy requirements and equilibrium of hydrolysis, decomposition and dehydration of $MgCl_2$ has been reported by Kelley (1946) by deriving required equations and calculating the data for various temperature ranges with possible reactions through all processes. The correlations have been validated with existing experimental results where the theoretical calculations are in good agreement with the experimental results. It has been reported that the dry $MgCl_2$ hydrolysis has two common products, namely MgO and HCl where they might be bonded to or free from each other depending on the temperature.

The recovery and decomposition reactors of $MgCl_2$ particles have developed and studied by Christensen (1946). The decomposition of anhydrous $MgCl_2$ particles has converted into MgO, MgOHCl, or Mg(OH)Cl. Mg(OH)Cl formation has been very slow at lower temperatures (<200°C) and more rapid at temperatures ranging from 450-500°C. Pure MgO production have started from 500°C at the conversion and is very faster at higher temperatures.

Haag (1977) has conducted hydrolysis experiments to decompose $MgCl_2$ into MgO and optionally MgOHCl substances in a fixed bed reactor. 100% conversion of the solid particles into MgO has been succeeded in 60 minutes of residence time by providing steam/Mg ratio of 6 at 550-575ºC. MgOHCl production has occurred at temperatures less than 293ºC with a conversion of more than 90% for a steam/Mg ratio of 11. The major

advantages of forming MgOHCl have been reported as the lower hydrolysis temperature and the capability of utilizing heat from another reaction.

A kinetic analysis for hydrolysis of bioschofite ($MgCl_2 \cdot 6H_2O$) has been conducted by Kirsh et al., (1987). The reaction order, activation energy, and pre-exponential factor of the hydrolysis process have been experimentally determined. Activation energy of the dehydration process has decreased by decreasing the ratio of H_2O molecules to Mg. Kinetic parameters have also been reported considering several experimental measurements mainly using thermo-gravimetric analysis and XRD of the products up to 480ºC.

Thermodynamic properties of aqueous $MgCl_2$ solutions have been studied by Wang and Pitzer (1998). A general model has been developed based on existing experimental results. Heat capacities, freezing and melting points, densities and dilution enthalpies have been evaluated in a temperature range from -33ºC to 350ºC at up to 100 MPa. The Gibbs free energy change for the dissolution reaction has been reported by the researchers by including activities of all individual substances.

Chemistry and thermochemistry of anhydrous $MgCl_2$ have been studied by Kipouros and Sadoway (1987, 2001). A phase diagram for $MgCl_2$-H_2O has been formed considering the mole percent of $MgCl_2$ in water for various temperatures. The reaction heats and equilibrium constants of possible reactions have been specified in order to show all product yields. The researchers have also reported some catalytic substances in order to increase the reaction rates and fully recover reactants throughout the dehydration and the hydrolysis of $MgCl_2$.

The properties of MgOHCl have been determined by Kashani-Nejad et al., (2004). The studied properties have been namely solubility and characteristic absorption peak, and titration results have shown that 95% of MgOHCl has been obtained under 376ºC of hydrolysis temperature with a controlled heating of the reactor.

Kashani-Nejad et al., (2005) have reported that MgO and HCl production occurs without any intermediate step after 376ºC during the hydrolysis of $MgCl_2$. Experiments have been performed to study the controlled dehydration of the $MgCl_2$ and a predominance area diagram has been reported showing the reaction tendencies within various temperature ranges.

Simpson et al., (2006) have experimentally investigated and assessed the conversion of $MgCl_2$ into MgO using silicalite supported catalysts in the hydrolysis reaction of the reverse Deacon reaction. Potential of long term stability and faster reaction kinetics of solid particles have made the reaction a feasible one.

The production of anhydrous $MgCl_2$ particles for electrolytic magnesium production has been studied by Zhou et al., (2006). Ammonium carnallite and salt lake solution has been used to produce anhydrous $MgCl_2$ at 700ºC. The size of the produced particles has been found to be suitable for electrolytic production of magnesium.

An anhydrous $MgCl_2$ production from bioschofite has been extensively studied by Yu-Long et al., (2008). A complex four step decomposition method has been reported to provide a theoretical basis to industrialize the decomposition process. A kinetic study of the decomposition of $MgCl_2$ has also been undertaken by them to evaluate activation energies and the frequency factor of the individual steps of the hydrolysis.

A mechanism for thermolysis of $MgCl_2 \cdot H_2O$ substance has been proposed by Wang and Chen (2011). The results have shown that decreasing the reactivity of $MgCl_2$ to prevent dehydrogenase process is a solution for controlling the hydrolysis of $MgCl_2$. Bakker (2012) has studied pyrohydrolysis of $MgCl_2$ brines into MgO and HCl to add value to effective disposal of waste products of HCl leaching process. It has been concluded that the hydroxichloride method had a smaller amount of energy requirement than pyrohydrolysis of $MgCl_2$.

An ammonium carnallite has been used by Zhang et al., (2012) as the starting material to produce high purity anhydrous $MgCl_2$ particles. Alumina has been used as the covering agent for the $MgCl_2$ where it has prevented it from atmospheric interaction. This method has been reported as beneficial for high purity $MgCl_2$ production.

2.3.2 HCl Electrolysis

A conversion of HCl gas into H_2 and Cl_2 is accomplished by a direct current passing through the solution in an electrolytic process. It is also known as the UHDE process, where a 22% HCl solution is used at 65-80°C. The content of water in the chlorine gas is an unwanted outcome which requires an additional process for dry chlorine. The presence of water also limits the current density. Aqueous HCl electrolysis can also be mass transfer

limited due to diffusivity rates. When the concentration is higher than 22%, electrical work requirement increases, and below 17%, the oxidation violates the electrolysis process. Thus, using anhydrous HCl for electrolysis, one can achieve higher current densities, lower cell voltages, and dry halogen gases as products (Bulan et al., 2006). Dry HCl utilization for electrolysis is still under research and development by many researchers. Aqueous HCl electrolysis is an industrially mature process and is mostly used to recover Cl_2 from waste HCl. Hydrogen is another important product of this process with its high energy content, which is the main aim of the Mg-Cl cycle for hydrogen production.

One of the very first developments for HCl electrolysis has been proposed by Messner (1974) for separation of the produced gases in different compartments of the electrolyser for a longer diaphragm life. At an average temperature of 70°C, 21 vol% steam has been present in Cl_2 and H_2 gases, where the separation process has purified the product gases up to 99.7 vol%.

Balko (1981) has first invented an electrolyser with a unitary membrane electrode structure which utilizes low feed acid concentration in order to decrease the HCl in the produced Cl_2. Lower HCl concentration has prevented the acid boil-off with the chlorine gas. The cell voltage of the electrolyser unit has decreased by 11% when the temperature increased from 35°C to 60°C, where reduced concentration has had tendency to increase the cell voltage of the electrolyser.

A process for aqueous HCl electrolysis has been invented by Minz (1988) where it has been claimed that the maximum conductivity of the HCl can be obtained at 17-22 wt% HCl concentration. The HCl concentration decreases in the cathode region due to transfer of hydration water through the membrane. Therefore, the solution should be replaced in order to sustain a steady operation of the electrolysis unit. Developed systems have prevented direct discharge of low concentration HCl acid, by being charged back to the anode chamber.

A solid-polymer-electrolyte electrolysis cell for oxidation of HCl into Cl_2 gas has been proposed by Eames and Newman (1995). Up to 900 mA/cm^2 has been obtained with a lower open circuit potential. The experiments have been conducted under 2 V in order to prevent O_2 evolution at the anode current collector.

A single membrane cell study for separating Cl_2 from HCl has been conducted with an experimental setup by Johnson and Winnick (1999). It has been resulted that the separation can be accomplished at reasonable voltages with high conversion efficiencies. The experimental operation had advantages such as continuous recycling of Cl_2 since it is fed to the electrolyser in anhydrous form.

Lyke and Tadapudi (2000) have developed a process for aqueous HCl electrolysis with thin film electrodes where high current density at low cell voltage and low HCl outlet concentration is achieved. It has also decreased the possibility of side reaction formation. The cell temperature has varied from 60°C to 90°C in a practical cell voltage ranging from 1.62-1.86 V. 40% of the HCl has been utilized in the cell at 1.66 V and 10 kA/m^2 with traces of O_2 in Cl_2 stream.

Zimmermann et al., (2001) have developed an electrochemical cell utilizing essentially dry HCl gas. The developed cell has possessed higher current densities at considerably lower cell voltages which is comparable with existing technologies. Since the Nafion membrane has changed its characteristics above 120°C, the cell temperature range has been kept between 60-120°C. The cell pressure has also affected the transport characteristics of H_2O.

Water transport in PEM electrolysers to recycle anhydrous HCl has been studied by Motupally et al., (2002). A mathematical model has been developed to characterize water transport across Nafion membranes and to calculate the concentration of liquid hydrochloric acid in contact with the membrane. The electro-osmotic drag parameter has been fairly insensitive to temperature at 80ºC.

Bartling and Winnick (2003) have developed a novel electrochemical membrane to recover chlorine from anhydrous HCl waste. For the proposed single cell design HCl removal efficiencies have exceeded 94% with an almost 100% current efficiency. The formation of gas bubbles, H_2 at the cathode and Cl_2 at the anode have influenced the cell performance and the ohmic polarization. It has been imposed that with minor design modifications and proper cell operation, the proposed configration can be applicable for industrial applications.

Bermashenko and Jorissen (2005) have proposed a high Cl_2 current efficiency up to 97% with $CaCl_2$ added salt in an electrolysis cell. The water and salt transfer through the

membrane, limiting the concentration range of HCl, has been suggested to optimize the operating conditions. A comparable cell voltage performance has been observed from the proposed electrolysis cell.

A method for electrolysis of aqueous HCl has been proposed by Bulan et al., (2006) to predict initial concentration of the solution and the desired current density of the electrolyser. To prevent the electrolyser unit from high energy consumption, the HCl feed has been kept above 5 wt% and below 20 wt%. An optimum concentration of 9 wt% has consumed 1.47 V at the desired current density of the electrolyser.

Mohammadi et al., (2009) have investigated effects of current density, anolyte temperature, O_2 flow rate and anolyte concentration on the cell voltage and the Cl_2 current efficiency of an oxygen reducing membrane. The Taguchi method has been used to design experiments. It has been observed that increasing anolyte concentration and temperature, anolyte and oxygen flow rate have decreased the cell voltage and have increased the Cl_2 current efficiency. The anolyte flow rate and the current density have had the highest contribution to the cell voltage. The oxygen and anolyte flow rate have had the highest contribution on the Cl_2 current efficiency.

An artificial neural network (ANN) model has been developed by Asrafizadeh et al., (2010) to predict further characteristics of the HCl membrane electrolysis. 53 experiments have been conducted to train the test networks where a very close estimated values have been obtained at a reasonable range among the measured values.

Perez-Ramirez et al., (2011) have reviewed catalysts for enhancing the recovered chlorine from HCl electrolysis. Catalytic HCl oxidation has been a more efficient method than HCl electrolysis because the electrical work and the cell cost are lower. High activity and long term lifetime of the HCl oxidation have been supported by Ru and Ti based catalysts. Most of the reported studies have not focused on H_2 production from the HCl cycle and focus on Cl_2 recovery by bonding the hydrogen molecules to catalysts.

Vidakovich-Koch et al., (2012) have reviewed several membrane reactors for chlorine recycling, effects of cell parameters have been comparatively evaluated, and membrane and catalyst selections have been discussed. The major outcome has been the acid equilibrated Nafion membranes had lower conductivity than water equilibrated

membranes and HCl electrolysis might increase the energy demand resulting in deterioration of the catalytic activity.

A fuel cell type reactor for gaseous HCl electrolysis for Cl_2 recovery has been proposed by Kuwertz et al., (2013). Since most practical electrolysis applications have a cell voltage range varying from 1.4 to 2 V, the reported experimental setup has decreased the cell voltage by almost 30%. However, hydrogen production have not been considered because it has been reacted with oxygen gas through the cell.

Tolmachev (2014) has conducted a comprehensive review on electrochemical cells and their applications. A comprehensive comparison on hydrogen-chlorine and hydrogen-bromine fuel cells has been discussed. Corresponding studies in the literature including electrolysis and fuel cell options of various hydrogen-halide cells have been reported.

A recent development on building an electrode, with a high energy density, for non-aqueous electrolytic primary and secondary battery packs has been reported by Hotta et al., (2014). The reverse reaction of the HCl electrolysis has been accomplished using H_2 and Cl_2 in the fuel cell system. A high performance PEM fuel cell working with H_2 and Cl_2 gases has been developed by Anderson et al., (1994) where usage of Cl_2 instead of O_2 has enhanced the power and energy density of the PEMFC with a significant cold start capability.

Thomassen (2005) has proposed three fuel cell systems utilizing H_2 and Cl_2 to produce HCl and electricity: the conventional PEM fuel cell system, a composite system applied for aqueous HCl and Nafion membrane, and a phosphoric acid doped PBI membrane fuel cell system. Stable operation could not be obtained due to the corrosive nature of chlorine and HCl. However, the optimum cell potential has been obtained from PBI, and a water free ambient requirement has been reported for the sake of minimising the corrosion difficulties. Computational simulation of a single hydrogen/chlorine fuel cell has also been conducted by Thomassen et al., (2006). It has been reported that the best cell performance has been obtained at 6 mol/dm^3 at higher operating pressures than the base case.

Gooding (2009) has studied various flow sheets for the hybrid chlorine cycle with a steam/chlorine separation step. A maximum temperature of 850ºC has been required for the reverse Deacon cycle to produce HCl. It has also been concluded that the aquaeous HCl

electrolysis requires 2V practical voltage, and cannot compete with direct water electrolysis at 1.8V.

A commercial hydrogen fuel cell has been employed as a hydrogen-chlorine electrochemical cell with a low precious metal alloy for the chlorine electrode by Huskinson et al., (2012). The galvanic density of the cell has exceeded 1 W/cm^2 which has almost doubled the previous values in the literature. Higher cell pressure has resulted in higher cell potential and power density. The peak power density has been obtained at the highest studied pressure at around 60% voltage efficiency. Another study on the model performance of the same fuel cell for grid-scale electrical energy storage has been proposed by Rugalo et al., (2012).

2.3.3 MgO chlorination

Chlorination of MgO products from hydrolysis is another main reaction to complete the Mg-Cl cycle. Several experimental studies have been conducted to accomplish a full conversion of MgO into $MgCl_2$ particles. Effects of particle size, reactivity, thermal treatment methods and reactor parameters have been studied. Definitions and correlations of the reaction rate for various forms of MgO chlorination methods have been reported. Use of catalysts to enhance reaction rate and conversion have also been extensively studied in the literature.

Ino et al., (1961) have conducted experiments to determine the rate of the MgO chlorination from 25 ºC to 1000ºC, and it has been concluded that the reaction is very slow without using a carbonaceous environment as low temperatures. Charcoal powder addition has provided a complete conversion of MgO into $MgCl_2$ in a shorter time period at 400-500ºC.

The chlorination reaction has been experimentally investigated by Hesson (1979) by measuring the O_2 formation after the reaction. The reaction rate and diffusion coefficients for the reaction have been reported and an optimum temperature range has been determined. Main challenges have been found to be the surface area of the MgO particles and ash layer of $MgCl_2$ on the MgO surface during the reaction. Preparation of the MgO particles also has had a very influential effect on the chlorination process. MgO produced from high temperature $MgCl_2$ hydrolysis has been less reactive and had less

surface area than the MgO produced by $Mg(OH)_2$ decomposition. Titration results have shown that use of MgO prepared from $Mg(OH)_2$ has close to 50% conversion at 643ºC. It has also been suggested that the rate of the reaction can be increased by using a fluidized bed instead of a packed bed reactor.

The reaction orders for chlorination and carbochlorination of MgO particles have been experimentally studied by Kanari and Gaballah (1999). 98% pure MgO powder obtained from $MgCO_3$ calcination has been used for the experiments. Effects of gas flow rate, temperature and partial pressure of gases have been determined. An apparent activation energy of MgO has been found to be 49 kJ/mol between a 425-600ºC.

The production of MgO with calcination of $MgCO_3$ at 600ºC has been studied by Aramendia et al., (2003). The effects of MgO preparation method on its surface and structural properties have been determined. The most successful results have been obtained by using calcination and rehydration of MgO produced from $Mg(OH)_2$.

Over 90% of MgO particles have been converted into $MgCl_2$ when the chlorination agent is taken to be HCl gas. (Ng et al., 2005). The MgO produced from decomposition of MgOHCl has shown better surface and activity characteristics in a chlorination environment compared to direct hydrolysis of $MgCl_2$. Diffusion of HCl into an ash layer of $MgCl_2$ particles has been much better than Cl_2 gas alone, where the conversion rate has been increased for MgO. A numerical model to estimate the shrinkage of MgO particles has also been developed by the researchers which helped evaluate the performance of the hydrochlorination process.

The hydrolysis of $MgCl_2$ tends to form MgOHCl rather than producing MgO and HCl at temperatures around 300ºC. Decomposition of this substance has been required to produce MgO particles in pure form and release the HCl gas for the electrolysis step. The decomposition reaction started at 375ºC and the direct conversion into MgO has been accomplished (Kashani-Nejad et al., 2005). The completion of the decomposition has occurred above 533ºC, where the rate of the reaction can be doubled by proper removal of the produced gas from the reactor by using Argon gas.

The production of $MgCl_2$ from the MgO reaction with HCl has been studied by Eom et al., (2010). A solution of $MgCl_2$ can be produced even at atmospheric conditions. Afterwards, the prepared solution has been mixed with NH_4Cl at the same molar ratio, to

prepare ammonium magnesium chloride solution. Above 200ºC, anhydrous $MgCl_2$ and HCl gas have been produced with a residue of 35%.

2.3.4 Dry HCl Capture

The literature overview for the hydrolysis of $MgCl_2$ at both low and high temperatures superimposes that HCl would be in mixture with steam which would result in aqueous HCl electrolysis requiring high cell potentials during the electrolysis step of the Mg-Cl cycle. Dry HCl capture can be accomplished using a suitable solid metal oxide sorbent which possesses low solubility in water (Seader and Henley, 2006).

$MgCl_2$ is highly desiccant in water where 1 mole of this substance can absorb up to 12 moles of water. The high adsorbance capacity can be utilized to capture water from the steam/HCl mixture. However, there has not been a study showing its characteristics for capturing HCl gas. An ion interaction model to predict solubility of this ternary system has been studied by Ya-Hong et al., (2005). The study has been conducted at 20ºC and has been validated with the experimental studies. A considerably high amount of HCl has bonded with the solid particles at this temperature.

The ternary system HCl-$MgCl_2$-H_2O has been evaluated using Pitzer's ion interaction model by Li et al., (2005) at varying temperatures. The solubility of HCl has been lower at a higher rate of $MgCl_2$ in the ternary system. The ternary system has led to production of $HCl{\cdot}MgCl_2{\cdot}7H_2O$. The resulting data have presented that it might be possible for $MgCl_2$ to absorb more H_2O than HCl with a possible concentrated mixture. Zeng et al., (2007) have predicted the solubility phase diagram for the HCl-$MgCl_2$-H_2O system at 273 K. Higher HCl concentration leads to $HCl{\cdot}MgCl_2{\cdot}7H_2O$ formation. It has been suggested that the HCl concentration should be controlled to prevent double salt formation. Existing studies have not validated any results for the higher temperature absorption of HCl gas, or occurrence of double salts.

MgO solubility in an aquaeous HCl solution has been studied by Urwongse et al., (1980). Higher concentrations have been achieved for highly concentrated HCl solutions at room temperature. An experimental study has been conducted to determine the reaction characteristic of an intermediate step of MgO chlorination in a molten salt reactor (Lamy et al., 2004). The alkalimetric titration results have shown that MgOHCl is formed before

the chlorination of MgO particles with chlorine, and it has reached to a maximum before $MgCl_2$ production. It has been imposed that this intermediate step can play a significant role to absorb HCl from the mixture gas.

Rappold and Luft (1999) have proposed a novel process to capture HCl gas from exhaust emissions using MgO particles as sorbents. The reaction has been conducted at the exhaust gas temperature (120ºC) to validate MgO hydrochlorination. Products have been heated up to 450ºC to form back MgO particles in a steam environment. Partanen et al., (2005a) have studied the absorption of HCl gas in limestone by considering the reaction atmosphere and absorbent characteristics. Several limestone types containing several metal oxides have been determined. The main concerns with this process have been the corrosive nature of $CaCl_2$ at high temperatures and fouling of the boiler. Another study have shown that the Cl/Ca ratio is the most influencing factor to determine the amount of sorbent for practical applications (Partanen et al., 2005b).

2.3.5 Overall System Analysis

Simpson et al., (2006) has been the first to investigate the hydrolysis reaction with additives in the Mg-Cl cycle to study a more feasible reaction. The hydrolysis reaction has been experimentally studied to determine the effect of silicalite support on $MgCl_2$ particles and titration results have shown that silicate addition made the reaction more feasible.

Balta et al., (2012) have conducted energy and exergy analyses of the conventional Mg-Cl hybrid thermochemical cycle for hydrogen generation and examined the respective cycle's thermodynamic efficiencies. A parametric study has been undertaken to investigate the behaviour of the cycle under varying environmental and system parameters. 63.8% energy and 34.86% exergy efficiencies have been obtained from the Mg-Cl hybrid thermochemical cycle. Overall system efficiencies have shown that Mg-Cl cycle can compete with other thermochemical cycles such as the Cu-Cl cycle.

Ozcan and Dincer (2014a) have studied the individual reactions throughout the Mg-Cl cycle to investigate reaction parameters for completion of the reactions. A case study has been performed to specify and study the yields of compounds in the hydrolysis and chlorination steps of Mg-Cl cycle for various temperatures, pressures, and steam/Mg and Cl/Mg ratios. The Aspen Plus simulations and sensitivity analyses have shown that a lower

pressure, a higher temperature and a higher steam/Mg ratio have been required to provide full conversion of reactants in hydrolysis step. On the other hand, a lower temperature, a higher pressure and a higher Cl/Mg ratio have been required to provide full conversion of chlorination reactor reactants. Based on the study results and findings, an option for the complete Mg-Cl cycle has been developed, and efficiency analysis of the cycle has been conducted. Energy and exergy efficiencies of the Mg-Cl cycle have been found to be 37.4% and 47.3%, respectively.

Economic aspects of several hydrogen production cycles have previously been studied by several researchers, including Ozbilen (2013) and Levis and Masin (2009). The Cu-Cl cycle has been studied by them to determine the cost of hydrogen for several plant capacities showing a large range of variations of the hydrogen production cost depending on the cycle configuration. An economic assessment for the HyS cycle has been conducted by Jeong and Kazimi (2009) for an 11 tons of H_2 production resulting in \$3.85/kg H_2. Several other cost assessments are conducted by using International Atomic Energy Agency (IAEA)s Hydrogen Economy Evaluation Program (HEEP) for water electrolysis, S-I, HyS, and HTSE plants (Ozcan et al., 2014; El-emam et al., 2015).

The current literature for the overall system analysis is not adequate to completely evaluate the performance of the Mg-Cl cycle. Preliminary studies are based on either stoichiometry of the reactions or individually studied without integrating them. A complete analysis can be conducted by experimental validations of key reactions and Aspen Plus simulations, which can help to understand the practical heat and power requirements of the cycle.

2.4 System Integration

It is depicted that the Mg-Cl cycle can be integrated to relatively lower temperature heat sources with its flexible maximum temperature range. Solar, geothermal and nuclear sources are the most promising options to become a candidate heat source for the Mg-Cl cycle. However, abundance of geothermal heat sources at higher temperatures (>400ºC) is not at a desired level. Thus, geothermal sources are not discussed in this thesis work. The main input of the Mg-Cl cycle should be a heat and power source. Available subsystems

to manipulate produced hydrogen should also be considered to transfer the product to end user.

A solar based Mg-Cl cycle has been proposed to determine an overall efficiency of the produced hydrogen (Ozcan and Dincer, 2014b). Higher molten salt outlet temperature, higher concentration ratio, and lower solar field area have been suggested to increase solar field efficiency. Such plant would show better performances at lower solar irradiation and higher ambient temperature. However, environmental parameters cannot be controlled and variations on environmental parameters may also affect the plant efficiency. Overall system energy and exergy efficiencies have been found to be 18.8% and 19.9%, respectively considering solar energy as the input. It has been concluded that the Mg-Cl hybrid thermochemical has had comparative advantages such as possessing low maximum temperatures which can be linked to various renewable or nuclear waste energy sources than those of several reported thermochemical cycles. Main challenge of such a cycle have been found to be consumption of relatively higher electrical work and challenging O_2 and Cl_2 separation at the chlorination reactor.

A solar based Mg-Cl cycle has been compared with the steam methane reforming in terms of their environmental impacts by Ozcan and Dincer (2015). The comparison has been made for the same heat source where additional hydrocarbon requirement for SMR unit has also been considered. The SMR unit has shown higher energy and exergy performances and environmental impact indices when these indices have been dependent on thermodynamic efficiencies. However, it has been reported that the Mg-Cl cycle does not emit greenhouse gases compared to the SMR system, which had a 14.4 g/mol H_2 of CO_2 production for 1 mole/s H_2 production. the production of emissions are taken into account due the carbon release from the SMR plant only, and other life cycle costs are not included for both systems studied.

2.5 Main Gaps in the Literature

Individual reactions of the Mg-Cl cycle have been studied by several researchers in order to determine the reactivity of substances, particle size distributions, reaction kinetics and theoretical heat requirements. Overall cycle analyses have also been made by considering stoichiometry neglecting the reaction behaviour of every individual step.

Since $MgCl_2$ generally forms bioschofite at ambient conditions, most of the studies in the literature have focused on controlled dehydration and hydrolysis of this substance. Other possible products which might occur at varying reactor conditions have also been reported by phase diagrams. The information in the literature provides a good background on the chemistry and thermochemistry of hydrolysis of $MgCl_2$ with its tendencies. Existing literature does not provide adequate information on the completion of the 1:1 Mg-steam reaction. The existing thermochemistry shows that full completion can be achieved at 550ºC which is very close to the melting point of $MgCl_2$.

Considering the MgO chlorination process, the available literature is limited with regards to several issues such as the possession of CO_2 production during carbochlorination of MgO particles. Since the main products from the Mg-Cl cycle are supposed to be H_2 and O_2, it leads to a cleaner production of H_2 without emissions. The ash layer thickness of the reacting MgO particles slows down the reaction, which has been studied in a packed bed reactor. It has also been reported that a fluidized bed reactor may lead to better conversion of the MgO particles into $MgCl_2$. When an option of recirculation of unreacted substances is considered, a continuous production of $MgCl_2$ may also be accomplished.

Most of the studies in the literature have focused on Cl_2 recovery and increasing the recovered Cl_2 by way of oxygen reducing agents which tends to reduce the amount of H_2 production. Since the aim of the Mg-Cl cycle is to produce hydrogen as the main product and to feed the produced chlorine back to chlorination process, both products need to be considered individually without reducing any of them. The electrolysis step is feasible and can work at high current densities with a low voltage requirement. Reverse reaction can be accomplished using H_2 and Cl_2 gas at high power densities.

HCl production from the hydrolysis reactor of the Mg-Cl cycle is expected to be in a mixture with steam, thus, separation of steam and HCl is of importance for the sake of lower electrical work requirement of the electrolysis step. A separation step is crucial for anhydrous HCl production from the Mg-Cl cycle. Teachings in the literature impose that aquaeous HCl electrolysis may not be more feasible than conventional water electrolysis in terms of power consumption. Thus, dry HCl capture from hydrolysis reaction is the most crucial part of the system in order to make this cycle a feasible one.

System integration and preparation of produced hydrogen for end user has not been studied for the Mg-Cl cycle. Thus, system development with nuclear and renewable resources should be performed for a complete model. Various configurations of other thermal systems should be integrated into the Mg-Cl cycle to provide required energy and to utilize the products of this cycle. There is also no study performed to investigate the cost of H_2 from the Mg-Cl cycle.

CHAPTER 3: SYSTEMS DEVELOPMENT AND SIMULATIONS

3.1 Simulations

Aspen Plus is a process simulator that predicts the kinetics and thermochemistry of various chemical reactions and physical processes using several databases containing the physical properties of thousands of substances (Martin, 2007). Several unit operation models help simulate small and large scale thermal and chemical systems with following steps:

- Selection and definition of unit operation models
- Unit operations assembly to develop the plant
- Specification of all components involved in the process. This can be performed from the Aspen Plus component database, and with non-database components
- Selection of thermodynamic models for all unit blocks to represent the physical properties of the components and mixtures in the process, including properties that are not given in the Aspen Plus database
- Specification of molar flow rate and thermodynamic conditions of all feed streams
- Specification of the operating conditions of all unit operations
- Model analyses, flow sheeting options, or calculator blocks for sensitivity analyses

A cost and energy effective simulation can also be optimized using the Energy Analyzer option of Aspen Plus. Next subsections briefly defines and discusses unit operation models and various property methods which are of importance for development of the MgCl cycle options.

3.1.1 Unit Operation Model Types

In the Aspen Plus simulation package, unit operation models are used to determine and evaluate thermodynamic, economic, and chemical considerations of several built-in equipments. These unit operation models perform specific functions based on a feed, thermodynamic models and operating conditions. Blocks used in the simulation are described in next sections (Aspen Plus, 2003).

Reactors

There are several reactor blocks in Aspen Plus software package for simulation of reactions in different ways. In order to simulate a known stoichiometric reaction where yields are not taken into account, stoichiometric type (RStoic) reactors can be used. These reactors can be a good selection to determine reaction heats and thermodynamic properties of input and outputs of the reaction.

For a reaction with negligible reaction kinetics which can be a one or more phases can be simulated using several built in reactor models (Rgibbs, REquil and Ryield). Here, RGibbs type reactor aims to minimize the Gibbs free energy of the reaction which is a promising built-in reactor type to find out reaction conditions in a feasible way. For a known yield of a reaction at a specific reaction condition, RYield type reactors can be conveniently used to determine thermochemical and thermodynamic properties of inlet and outlet streams, as well as the corresponding reaction heat.

RBatch, RCstr and RPlug reactor types give practical results by considering both stoichiometry and experimentally derived kinetics of a reaction. These rigorous reactors can be used for reactions which are experimentally studied with obtained kinetic parameters. Other details of all built-in reactor types and user models can be found in user guides of Aspen Plus software.

Heat Exchangers

Several built-in heat exchanger types in Aspen Plus software provide flexibility of appropriate heat exchanger selection based on the phase and the substance under study. Shell & Tube, plate, and air cooled heat exchangers can determine the heat duty of the heat exchanger with a given inlet and outlet condition, or change in the thermodynamics of a stream for a given heat duty. It is also possible to retrieve several heat exchanger parameters for further heat transfer analyses. Types of built-in heat exchangers in Aspen Plus are: HeatX (shortcut rating), MHeatX (heat transfer between hot and cold streams), HxFlux (calculation of driving force and LMTD), Hetran (Designing shell & tube heat exchangers), and Aerotran (design of air cooled exchangers). It is also possible to simulate a heat exchanger network by using energy Analyser option of Aspen Plus software.

Pressure Changers

Pumps are used to increase pressure of a liquid or even a slurry by selecting the suitable component. Pump performance, pressure, and power curves can be retrieved from selected pumps. Gas compression is made using compressor models in Aspen Plus software. A specification of compression operation conditions should be made to determine compressor efficiencies and these values can be taken from manufacturer data. Expansion valve and turbines are also built-in pressure manipulating components in Aspen Plus, thus, power production and thermopysical data of streams are calculated.

Mixers and Splitters and Separators

Mixer (stream mixer), FSplit (stream splitter) and SSplit (Substream splitter) type equipments are used in Aspen Plus software. Mixing and splitting devices can merge or split stream, work and heat. There are several types of separators as well as distillation columns in Aspen Plus to help users simulate various industrial separation processes. Based on the specifications made by the user, combinations and separation of a feed stream, and phase separation of any reaction product can be accomplished by even taking the water decant into account. Molar vapor fraction, pressure, heat duty and temperature may be required to fix the thermodynamic conditions of the separation process.

3.1.2 Property Methods

Physical property methods can be sorted in three main sections; ideal property methods, equation-of-state property methods, and activity coefficient property methods. These methods are used to determine thermodynamic (fugacity, enthalpy, entropy, Gibbs free energy and volume) and transport (viscosity, conductivity, diffusion coefficient and surface tension) properties of the substance under study.

Ideal Property Methods

There are two ideal property methods (IDEAL and SYSOP0) using Ideal gas law, Raoult's law, and Henry's law to determine properties of gases when the user require ideal gas properties.

***Equation-of-State Property methods*.**

These methods determine thermodynamic and transport properties by blending several equation-of-state methods such as Lee-Kessler-Plocker, Peng-Robinson, Redlich-Kwong-Soave methods. These methods can be used for most real gases.

Activity Coefficient Property Methods

This method includes built-in liquid phase activity coefficient methods and vapor phase fugacity coefficient methods. UNIFAC, UNIQUAC, WILSON, NRTL, ELECNRTL, and B-PITZER types are some of the major methods with their several modifications in Aspen Plus software.

Selection of the property method is generally dependent on the substances and phases used in the simulation. Thus, selection of the property method is of importance for realistic and true results. Since the Mg-Cl cycle includes all three phases of studied substances, NRTL and extended version of this method (ELECNRTL) are used to determine properties of the substances on the cycle. This method is useful when electrolytes are present in the simulation. H_2O-HCl and H_2O-HCl-$MgCl_2$ systems are available at ELECNRTL method which makes this method the most feasible one among others (Aspen Plus, 2003).

3.2. Mg-Cl Cycle Configurations

The Mg-Cl cycle can be simulated by considering all individual chemical reactions throughout the cycle using the hydrolysis step as the main influencing reaction. Reactions are simulated using the Rgibbs reactor, where heaters are used for temperature manipulators through streams. However, the majority of these reactions are already known with their existing kinetics. Thus, this data is also taken into consideration for the yields. Ryield type reactors are used for this case for known conversions such as the chlorination step. There are several exothermic reactions throughout the cycle. These reactions are assumed to be isothermal for the sake of preventing any interruption of the reaction rates. Thus, Ryield type reactors are adapted considering existing experimental data from the literature. Initially three options are evaluated with respect to their heat requirements. The first option is taken to be the high temperature hydrolysis of $MgCl_2$ into MgO and HCl gas (Mg-Cl-A). The second option is relatively lower temperature hydrolysis of $MgCl_2$ into

solid MgOHCl particles and HCl gas, where two unit moles of $MgCl_2$ should be fed into the hydrolysis reactor in order to obtain the same amount of HCl gas as in the first option (Mg-Cl-B). A novel fourth step is introduced in the third configuration with a decomposition step of MgOHCl into MgO and HCl gas (Mg-Cl-C). All options are designed to produce 3600 kmol/h of H_2, and net heat requirements of these configurations are determined by considering the exothermic reactions as isothermal. A final design is then modified to further decrease the electrical work requirement of the cycle with dry HCl capture. This cycle is still considered as the Mg-Cl-C cycle with an additional separation process to capture HCl by using a metal oxide in two successive reactions, namely HCl capture and decomposition reaction.

Table 3.1 Different configurations of the Mg-Cl cycle.

Cycle	Max. Temperature (ºC)	Reactions	Comments
Mg-Cl-A	537	H: $MgCl_2 + H_2O \rightarrow MgO + 2HCl_{aq}$ C: $MgO + Cl_2 \rightarrow MgCl_2 + 1/2O_2$ E: $2HCl_{aq} \rightarrow Cl_2 + H_2$ $(1.8\,V)$	HCl production occurs in mixture with steam. MgO from hydrolysis is less reactive with chlorine and low particle surface area. The only endothermic reaction is hydrolysis.
Mg-Cl-B	500	H: $2MgCl_2 + 2H_2O \rightarrow 2MgOHCl + 2HCl_{aq}$ C: $2MgOHCl + Cl_2 \rightarrow 2MgCl_2 + H_2O + 1/2O_2$ E: $2HCl_{aq} \rightarrow Cl_2 + H_2$ $(1.8\,V)$	For the same amount of HCl production, stoichiometry of hydrolysis should be doubled. The only endothermic reaction is chlorination.
Mg-Cl-C	450	H: $MgCl_2 + H_2O \rightarrow MgOHCl + HCl_{aq}$ D: $MgOHCl \rightarrow MgO + HCl_g$ C: $MgO + Cl_2 \rightarrow MgCl_2 + 1/2O_2$ E: $2HCl \rightarrow Cl_2 + H_2$ $(1.4 - 1.8V)$	The only endothermic reaction is the decomposition step with higher heat requirement. A gas removing agent is required to separate HCl from MgO surface. Half of the HCl can be produced in dry form.

The electrolysis step of all options has been calculated with a calculator block in Aspen Plus by assuming all of the HCl gas is converted into H_2 and Cl_2. Electrical work requirements are calculated based on their practical voltage requirements as mentioned in the literature review. For a logical comparison between the flowsheets, actual steam requirements are adapted in the simulation. This directly influences the heat requirements of individual components, as well as the system performance. Electrolysis steps are

simulated with Rstoich type reactors with separators and work requirements are determined with a calculator block. All three configurations are presented in Table 3.1 with definitions for comparison.

3.2.1 $MgCl_2$-MgO Cycle (Mg-Cl-A)

The first option is considered to be the conventional three step cycle with a direct high temperature hydrolysis step as given in Table 3.1. Rgibbs type reactor models are adapted in the Aspen Plus simulations to determine the heat requirement of the cycle for comparison. The flow sheet of the Mg-Cl-A cycle is shown in Figure 3.1. For this option, the hydrolysis reaction temperature is kept at 537ºC, which is the optimum temperature to fully convert $MgCl_2$ into MgO.

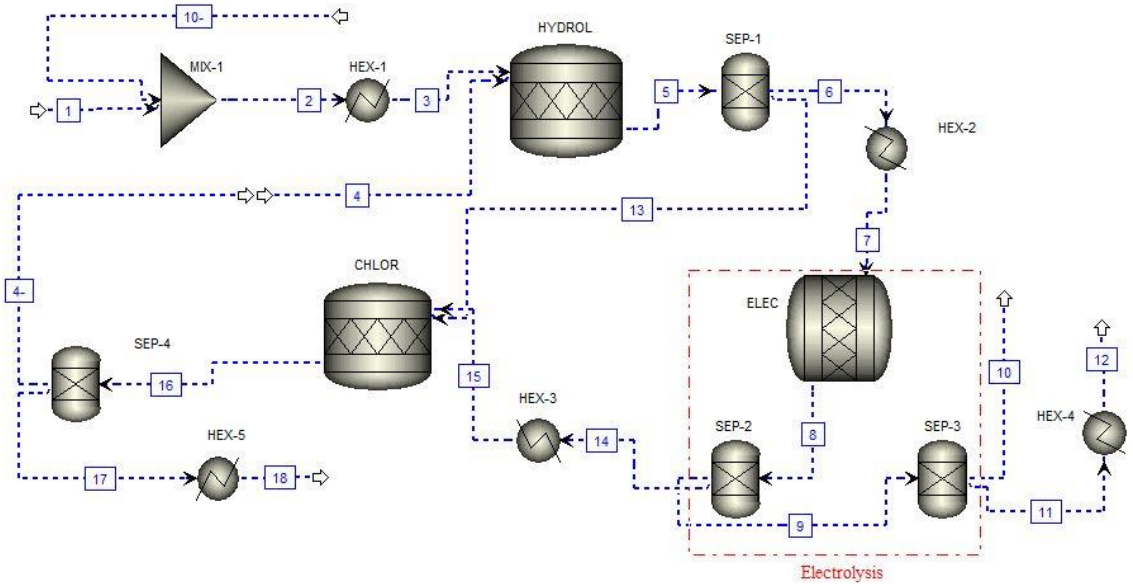

Figure 3.1 Aspen flow sheet for the Mg-Cl-A cycle.

Water is heated up to hydrolysis temperature at 17:1 steam/Mg molar ratio. This value is based on the experimental study of Haag, (1979) for a fixed bed reactor. A previous Rstoic model is used to determine the reaction heat and validated with previously reported values by Kelley (1945). MgO is separated from the gas and is sent directly for chlorination, where HCl gas is cooled down to 70ºC for the electrolysis step. Cl_2 gas from electrolysis is heated up to the desired temperature for chlorination step and reacted with

MgO under stoichiometric conditions. Produced O_2 gas is cooled to ambient temperature and the cycle is completed.

3.2.2 $MgCl_2$-MgOHCl Cycle (Mg-Cl-B)

As reported in the literature overview section, MgOHCl is produced from lower temperature hydrolysis of $MgCl_2$ at temperatures starting from 230ºC to 300ºC. For this option, water is superheated to a relatively lower temperature than the first option to form HCl gas and MgOHCl as in Table 3.1. A basic Aspen Plus simulation for the low temperature hydrolysis reaction is conducted to make a rough comparison for the actual steam requirements of both high- and low-temperature reactions. A previous study showed that Rgibbs type reactor shows full conversion at a 3.1:1 steam/Mg ratio for the high temperature hydrolysis at vacuum pressures (Ozcan and Dincer, 2014a). This value decreases to 1.8:1 when low-temperature hydrolysis is considered. This rate is simply adapted to the simulation with experimental results and resulted in 11:1. Since all comparisons are based on 3600 kmol/h hydrogen production, the amounts of the reactants should be doubled, which would require higher amounts of steam.

The produced MgOHCl is heated to a desired chlorination temperature, namely 500ºC, and directly reacts with chlorine gas from the electrolysis step. The chlorination reaction between MgOHCl and Cl_2 gas has not been experimentally studied previously, thus, Rgibbs reactor results are directly adapted in the simulation. This reaction might be more feasible than the direct reaction of MgO with Cl_2 since it is reported that HCl existence during the chlorination step shows a good conversion of MgO into $MgCl_2$ (Ng et al., 2005). Since the reaction produces oxygen and steam in gaseous form, oxygen gas is in mixture with the steam and provides high amount of internal heating while it is cooled to ambient temperature. The separation process of oxygen and steam can also be considered as an easy process since the solubility of O_2 in water is not too high (~8 mg/L at 50ºC). The Aspen flow sheet for the Mg-Cl-B cycle is shown in Figure 3.2.

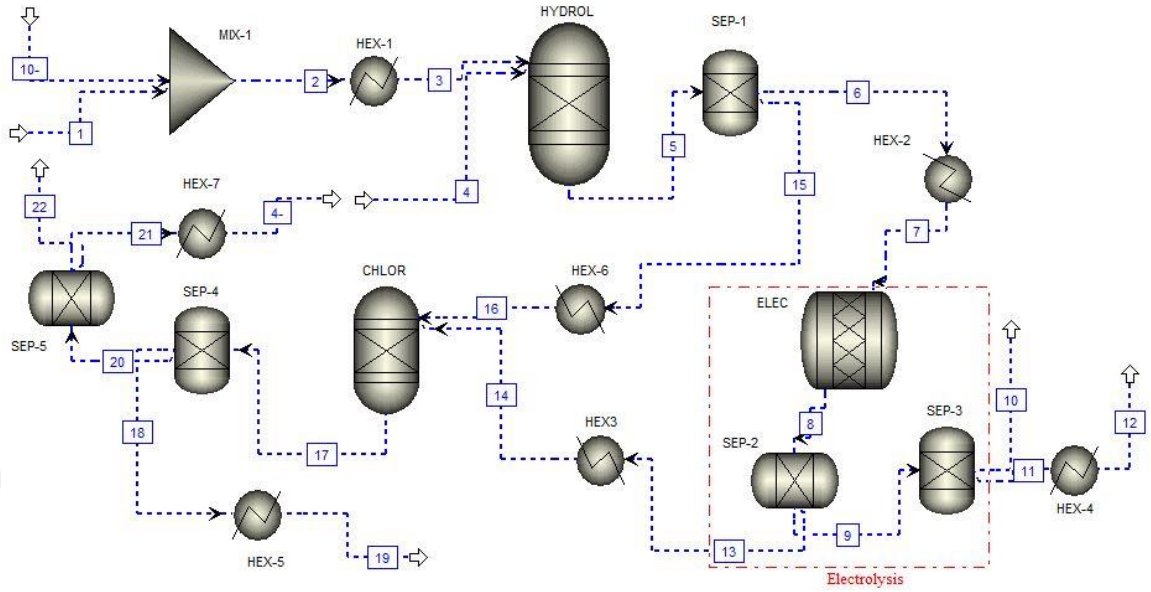

Figure 3.2 Aspen flow sheet for the Mg-Cl-B cycle.

3.2.3 Four-Step Mg-Cl Cycle (Mg-Cl-C)

As the last alternative, a fourth step is introduced to decompose MgOHCl in order to recover the remaining HCl without a need for a higher steam requirement. This step is developed for the following reasons:

- It is possible to obtain dry HCl gas by decomposing MgOHCl which lead to dry HCl electrolysis. Considering the practical voltage requirements, this option directly reduces the electrical work consumption by 11.2%.
- The stoichiometry to produce same amount of H_2 as in the Mg-Cl-B option can be reduced from two to one, by capturing the HCl gas in the decomposition step.
- MgO produced from high temperature hydrolysis is less reactive with the Cl_2 gas and has less surface area for proper reaction than hydrolysis of $Mg(OH)_2$. However, experimental studies showed that fine MgO can be produced from decomposition of MgOHCl which would enhance the reactivity of MgO with the chlorine gas.
- The only endothermic reaction is decomposition of MgOHCl, and the maximum temperature of the reaction can be reduced to 450ºC by using an inert gas to remove HCl gas from the surface of MgO particles. This also leads to a very fast conversion

of the reactant into the desired product. The lower maximum temperature provides this option to link this cycle to lower temperature heat sources.

The stability and decomposition kinetics of the MgOHCl substance has been studied by Kashani-Nejad (2006) and it is concluded that the removal of HCl with an inert gas increases the reaction rate significantly, by only removing the produced gas from the surface of MgO particles. This reaction occurs at 376ºC, and a minimum of 533ºC is needed to fully decompose into HCl and MgO. The Aspen flow sheet for this option is shown in Figure 3.3 with stream information.

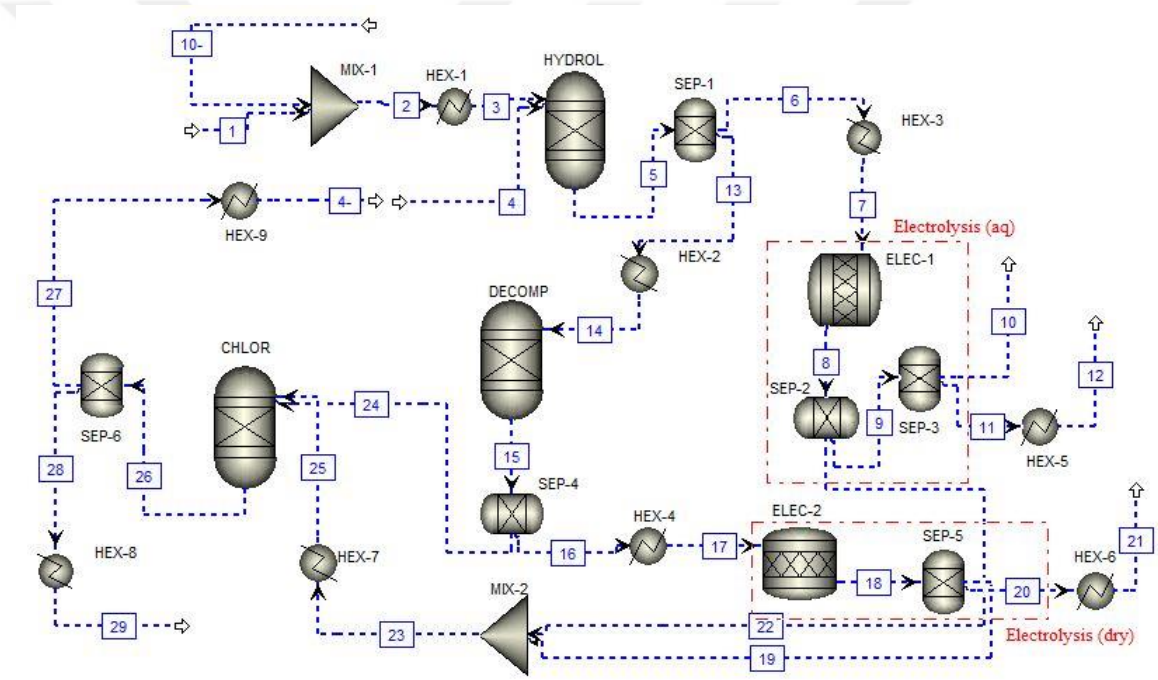

Figure 3.3 Aspen flow sheet for the four-step Mg-Cl-C cycle.

The hydrolysis step is set to 280ºC to form MgOHCl where the reactor temperature for decomposition step is set to 450ºC. The required steam for the hydrolysis step is same as the Mg-Cl-B cycle and it is set to 11:1. A preheating process is considered to bring the MgOHCl temperature to the lower limit of decomposition (376ºC). Argon gas is used as the inert gas to remove the HCl gas from the MgO surface and is adapted in the simulation with varying flow rates. Produced HCl gas is utilized in the dry HCl electrolysis process where the steam/HCl mixture from the hydrolysis step is cooled to electrolysis temperature for aqueous HCl electrolysis. The temperature of decomposition and chlorination is

assumed to be equal, where an additional heat exchanger is required to cool down the $MgCl_2$ from the chlorination step. Both the hydrolysis and chlorination steps are exothermic, and the only endothermic reaction is decomposition of MgOHCl. Cl_2 gas from both electrolysis paths is mixed and heated up to chlorination temperature.

3.2.4 Four-Step Mg-Cl Cycle with HCl capture

The flowsheet of the four-step Mg-Cl cycle with HCl capture is shown in Figure 3.4. A separation process to absorb HCl gas from the mixture can make this cycle more efficient and compatible. Thus, a modified four-step Mg-Cl cycle is considered with dry HCl capture. It is roughly estimated that capturing all of the HCl from the steam mixture can lead this cycle to consume 22.3% less electrical work than the three-step options and 12.4% less work from the four-step option. HCl capture can make this cycle more feasible than all other options and can be competitive with existing hybrid thermochemical cycles and the water electrolysis.

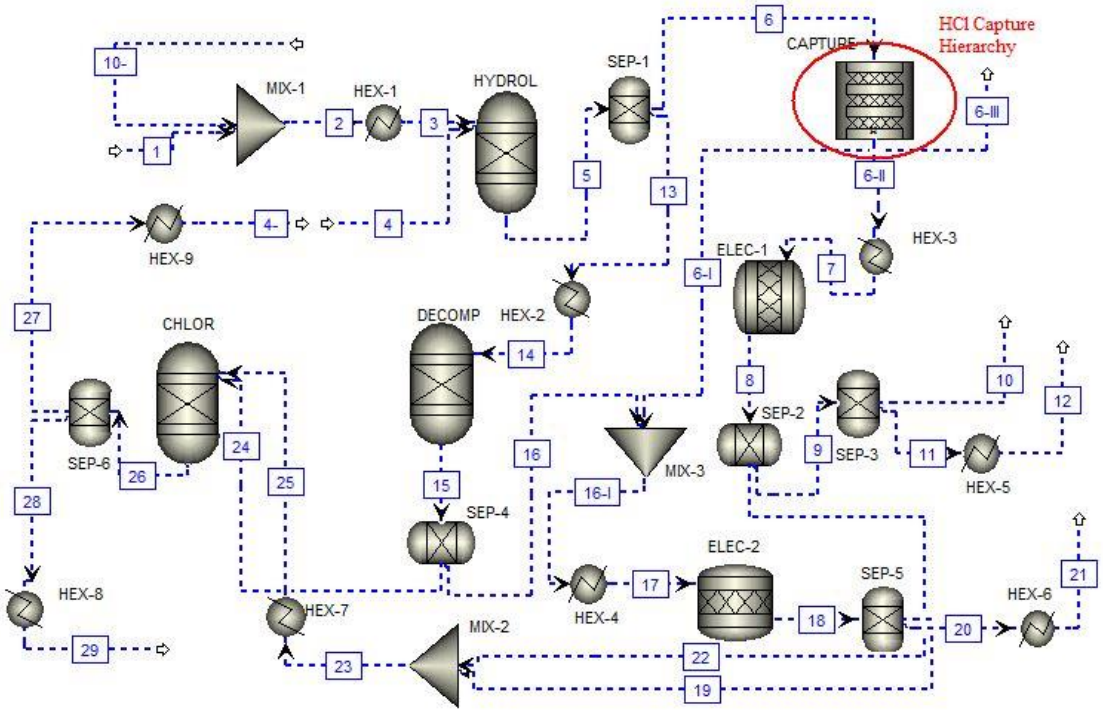

Figure 3.4 Aspen flow sheet for the four-step Mg-Cl-C cycle with HCl capture.

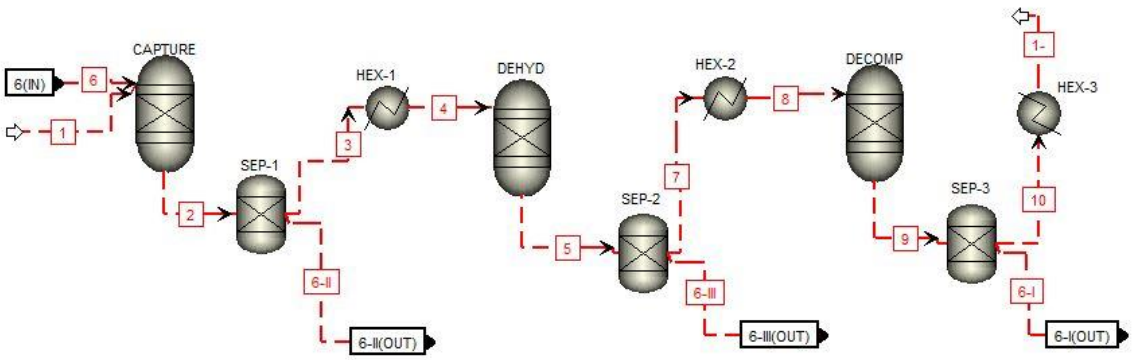

Figure 3.5 Aspen flowsheet of the HCl capture hierarchy.

The unique difference of this final design from the four-step option is adaptation of a possible separation process to capture HCl from the mixture after the hydrolysis step. The captured HCl is mixed with the HCl gas from the decomposition step to increase the amount of the dry HCl gas from the H_2 production at a low voltage. The remaining stream after the separation process is either in mixture or with a low content of HCl with high amount of steam. Based on the amount of captured HCl, this stream can be scrubbed and sent back to hydrolysis reactor or utilized for aqueous HCl electrolysis. However, the aqueous HCl electrolysis step is included in this option by considering the molarity of HCl gas in steam. The Aspen flowsheet of the separation process is illustrated in Figure 3.5. The hydrochlorination of MgO has tendency to produce several Mg- based hydrates. Thus, a second reactor is adapted to dehydrate Mg- based hydrates, and a final reactor is adapted to recover MgO, and to liberate HCl gas.

3.3 Systems Development

A system integration is crucial for evaluation of the overall production of a desired product where several subsystems are integrated related to their source requirements. The Mg-Cl cycle requires electrical and thermal energy to accomplish the H_2 production, and the produced H_2 from this cycle is at ambient conditions. Therefore, other subsystems such as H_2 liquefaction and compression should be considered to provide H_2 ready for the end user. Since the maximum temperature requirement of the Mg-Cl cycle is known with the existing literature and the simulation results, suitable sources to compensate this requirement should

be selected. A supercritical water reactor (SCWR) and a heliostat solar field are selected as energy sources, and two integrated systems are then proposed as follows:

- System I: A solar heliostat-based integrated system with hydrogen compression for co-production of hydrogen and electricity with thermal energy storage
- System II: A nuclear-based integrated system with hydrogen liquefaction for co-production of electricity and hydrogen

The first system includes a heliostat solar field to provide high temperature heat to the Mg-Cl cycle, a supercritical CO_2 (sCO_2) Brayton Power cycle, and a thermal energy storage system. This system is designed specifically to produce 1 kmol/s hydrogen from the Mg-Cl cycle. High temperature heat from the solar collectors are transferred to heat requiring components of the Mg-Cl cycle and the Brayton cycle. System II differs from the first system in terms of energy source, power producing subsystem, and hydrogen treatment. Here, a suitable nuclear plant is selected to provide adequate heating and electrical work requirement for the subsystems. A steam Rankine power plant is selected as the power generation unit which is a common practice for conventional power generation from nuclear energy. Produced hydrogen (1 kmol/s) is liquefied in a liquefaction plant based on the Linde-Hampson plant. Figure 3.6 represents brief layouts of the developed integrated systems. Both systems are common with hydrogen production subsystem, where they all include the energy source, the power production, and the hydrogen storage subsystems.

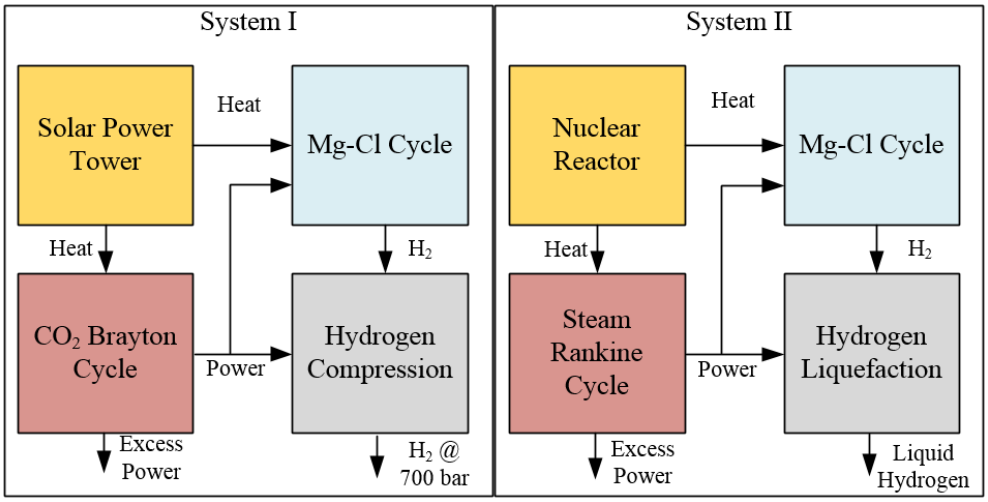

Figure 3.6 Layout of the system integration.

3.3.1 System I: Solar Based Mg-Cl Cycle with Hydrogen Compression

A detailed schematic diagram of the studied system is illustrated in Fig. 3.7 with state points. All subsystems are evaluated by considering following state points:

- 1-5: Solar plant
- 6-33: Mg-Cl cycle
- 34-45: Supercritical CO_2 Brayton cycle
- 46-59: Hydrogen compression plant

The solar data for the solar plant is taken for Greater Toronto Area (GTA) by considering daily and annual data. Molten salt storage is considered for the system in order to run the system without source feed interruptions when the sun is out. However, it is possible that the temperature of stored molten salt may not be high enough to run the Mg-Cl cycle. Thus, the analysis of the system is based on a specific month and time of a year, where the grade of the heat is adequate for the cycle. The solar heat from the receiver is transferred to two consecutive heat exchangers to provide enough heat for the Mg-Cl and the sCO_2 Brayton cycles. CO_2 is selected as the working fluid for the Brayton cycle because of its superior properties at the supercritical region. The precooled working fluid is compressed to the high pressure side by a two-stage intercooled compressor system. A regenerator is adapted to the system to recover excess heat of the expanded fluid with a reasonable approach temperature. The high temperature and high pressure working fluid is obtained by the solar heat exchanger and expanded into low pressure side to generate power.

The produced power and heat from the solar subsystem are provided to run the Mg-Cl cycle to produce hydrogen at four consecutive steps. After the internal heat recovery is accomplished, the heating process at required temperature level is supplied by the heat exchanger of the solar plant. The produced hydrogen from the Mg-Cl cycle is compressed up to 700 bar by using a five-stage compression plant with intercooling where the required compression power is compensated by the sCO_2 Brayton cycle. The compressed hydrogen shows ~38 kg/m^3 density value, which would make the transportation of this product easier and cost effective.

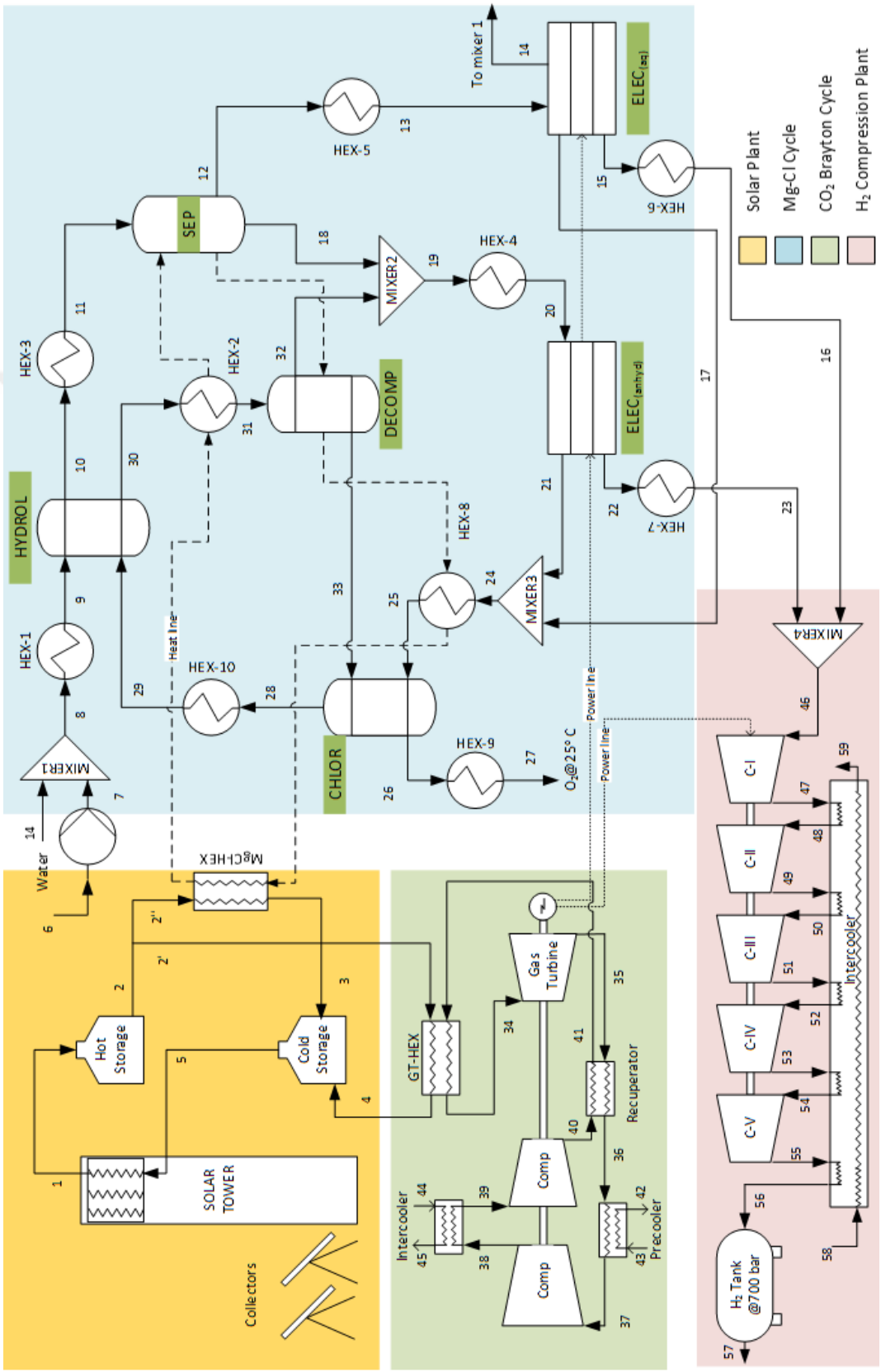

Figure 3.7 Detailed schematic diagram of system I

3.3.2 System II: Nuclear Based Mg-Cl Cycle with Hydrogen Liquefaction

A detailed schematic diagram of system II with state points is illustrated in Figure 3.8. Here, following state point ranges are used to evaluate thermodynamic properties of subsystems for system performance and cost assessment:

- 1-16: Nuclear Rankine cycle
- 17-43: Mg-Cl cycle
- 44-61: Linde-Hampson plant

A CANDU-SCWR is used as the main energy source for the Mg-Cl cycle and the Rankine cycle. The Rankine cycle is modeled with regeneration and reheating for enhanced cycle performance. The nuclear heat is used to superheat steam at high pressure and steam is first expanded to an assumed extraction pressure. Here, the stream is split in two with a ratio (f_1) which is than determined by writing the balance equation for the regenerator. The remaining steam is further expanded to another assumed expansion pressure, and reheated in the nuclear reactor. Same procedure for expansion is followed by providing a fraction of stream for open feed water heater (FWH). Finally steam is extracted to an assumed vacuum pressure, and then condensed. After the first pump, water is mixed with steam from second turbine for heat recovery purposes, and the mixture is assumed to be in liquid form. The fraction of stream splitting (f_2) is calculated based on energy balance of FWH. Further pumping is provided by second pump, and heat is gained from the regenerator. It is important that the heat supplying stream for the regenerator is again at condensed form and ready to be pumped at the boiler pressure. A mixing chamber is used to mix all streams which are then fed to the nuclear reactor. One of the main issues to be pointed out is assumptions for extraction pressures. A simple optimization process for optimum extraction pressures are carried out for maximized cycle energy and exergy efficiencies.

In this system, the external heat requirement of the Mg-Cl is also compensated by the nuclear reactor with a simple heat exchanger at a desired temperature range. The heat from this reactor is then provided to heat requiring components of the Mg-Cl cycle. Since the produced hydrogen is at ambient conditions, storage is considered to be hydrogen liquefaction.

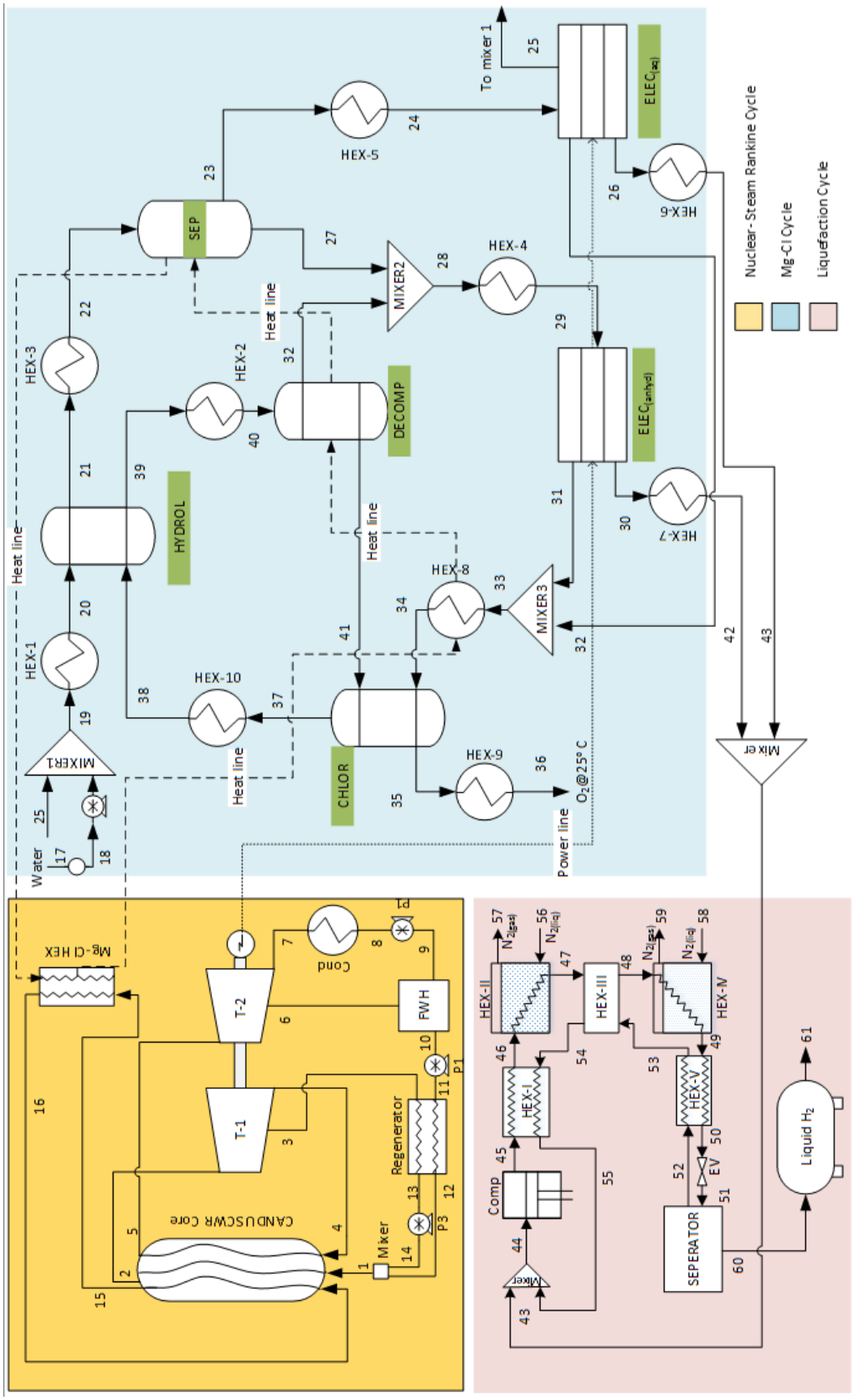

Figure 3.8 Detailed schematic diagram of system II

The hydrogen liquefaction process is relatively more energy intensive than the hydrogen compression, however, the density of liquid hydrogen is almost ~1120 kg/m^3 and it is 29 times higher than that of compressed hydrogen at 700 bar. Thus, a Linde-Hampson liquefaction plant with a secondary nitrogen cooling is considered for hydrogen storage. Since both plants are developed to produce 1 kmol/s hydrogen, an initial assumption is made based on the amount of produced liquid hydrogen. The power consumption of the plant and nitrogen cooling process is then determined based on the produced liquid hydrogen. Hydrogen from the Mg-Cl cycle and the remaining hydrogen from liquefaction is mixed and compressed to a specific pressure. An initial internal cooling is made using the recycling hydrogen from the separator, and a two-stage cooling of hydrogen is made using nitrogen as a secondary heat transfer fluid. Heat exchanging processes decrease the temperature of hydrogen to its critical point, and hydrogen liquefaction is accomplished with the expansion valve. Liquefied hydrogen is then stored for transportation in a storage tank.

CHAPTER 4: EXPERIMENTAL APPARATUS AND PROCEDURES

Since the electrolysis of HCl in anhydrous form requires less electrical work, a process for separation of HCl from H_2O is one of the most crucial steps of the Mg-Cl cycle for better system performance and less electricity consumption. The aqueous HCl electrolysis may also lead to possible problems such as wet hydrogen and chlorine production requiring an additional downstream separation, oxygen evolution at anode, and high current densities etc. $MgCl_2$ has a highly desiccant nature where 1 mole of this substance can absorb up to 12 moles of water depending on the reaction conditions. The interaction between $MgCl_2$ and H_2O with their thermochemical data and reaction conditions are given in Figure 4.1, and corresponding chemical reactions are as follows:

$$MgCl_2 \cdot 6H_2O_{(s)} \leftrightarrow MgCl_2 \cdot 4H_2O_{(s)} + 2H_2O_v \quad (4.1)$$

$$MgCl_2 \cdot 4H_2O_{(s)} \leftrightarrow MgCl_2 \cdot 2H_2O_{(s)} + 2H_2O_v \quad (4.2)$$

$$MgCl_2 \cdot 2H_2O_{(s)} \leftrightarrow MgCl_2 \cdot H_2O_{(s)} + H_2O_v \quad (4.3)$$

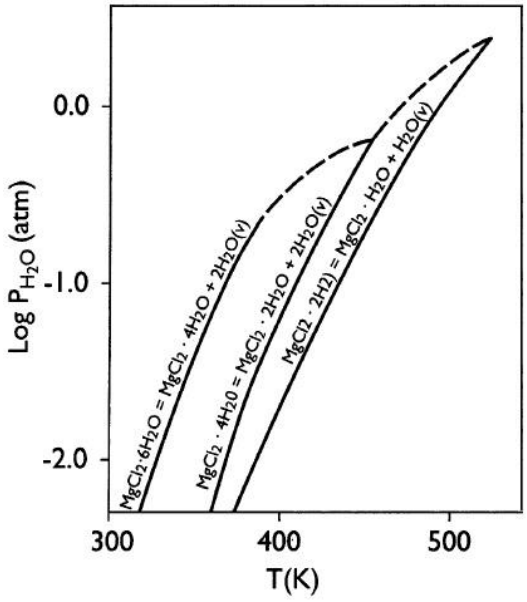

Figure 4.1 Temperature effect on the $MgCl_2 \cdot 6H_2O$ dehydration process (Modified from Kipouros and Sadoway, 2001).

Reactions in Eqs. 4.1 - 4.3 can occur in both directions with exothermic hydration processes. The temperature of the reaction should be increased at higher molar ratio of $MgCl_2$ in the hydrate. It also tends to produce oxides and/or hydroxides at elevated temperatures. It is also expected that this substance can absorb HCl. However, tendency of $MgCl_2$ to absorb either more H_2O or HCl is not a well-known process even if solubility of these binary and ternary systems have been reported before (Ya-Hong et al., 2005). Thus, a preliminary experimental process is designed and conducted to determine if higher molarity HCl solution can be obtained from hydration of $MgCl_2$ with aqueous HCl. The expected form of the $MgCl_2$ hydrate from the experiment is as follows:

$$MgCl_2 + HCl_{aq} \rightarrow MgCl_2 \cdot nH_2O \cdot mHCl + HCl_g \quad (4.4)$$

Another reaction to capture HCl from the mixture can be achieved by using metal oxides. The influence of intermediate MgOHCl production from $MgCl_2$ hydrolysis leads us to use of this solid substance as an HCl sorbent. Its solubility in water is very low and possesses high tendency to bond with HCl gas with an intermediate reaction as follows (Kelley, 1945; Rappold and Luft, 1999):

$$MgO + HCl \leftrightarrow MgOHCl \quad (4.5)$$

$$MgOHCl \leftrightarrow MgO + HCl \quad (4.6)$$

$$MgO + 2HCl \leftrightarrow MgCl_2 + H_2O \quad (4.7)$$

Both types of reactions are experimentally studied and further explanations are given in proceeding subsections.

4.1. $MgCl_2$ Hydration Experiment

Since it is expected that the steam/HCl mixture is in molar ratio of 10 after the hydrolysis step, its molarity corresponds to 5.5 M in liquid form, and this value is used as the reference for the experiments. A stock solution of 11-12 M HCl is diluted into 5.5 M acid by adding deionized water into the solution by following the recommendation of the manufacturer (Sigma-Aldrich, 2014). A 50 ml solution is prepared and vacuumed in a syringe. The same amount of the solution is prepared to use as a reference solution in a flask. An Oaklon 2700 type pH meter is used for pH measurements. Calibration of the pH meter is made by using

three buffer fluids at 4.01, 7.0, and 10.01 pH values, resulting in 99.4% precision. The prepared solution is measured with the calibrated pH meter, where it is initially expected to be -0.74. Since the stock solution does not provide a precise range for molarity, the final solution is adjusted by using either deionized water or stock solution until the pH value is at the desired level.

Considering the stoichiometry, 0.46 mol dry $MgCl_2$ is precisely weighed under the nitrogen environment in a glove box corresponding to the required amount of the solution stock. A preliminary experiment is conducted in order to evaluate the characteristics of the reaction in a vertical vessel. The solution stock in the syringe pump is connected to a valve at the top of the reaction vessel, allowing the control of the solution feed rate into the reactor. The top and the bottom of the reactor are sealed with largely perforated plastic stoppers, where porous distributors are also located in the reactor to form a bed for the powder and for better distribution of the solution through the powder. A ten minutes of solution feed into reactor is considered by also taking the residence time into account. As soon as the solution passes through the distributor, a very fast reaction at the top of solid particles occurred resulting in a solidification of the powder.

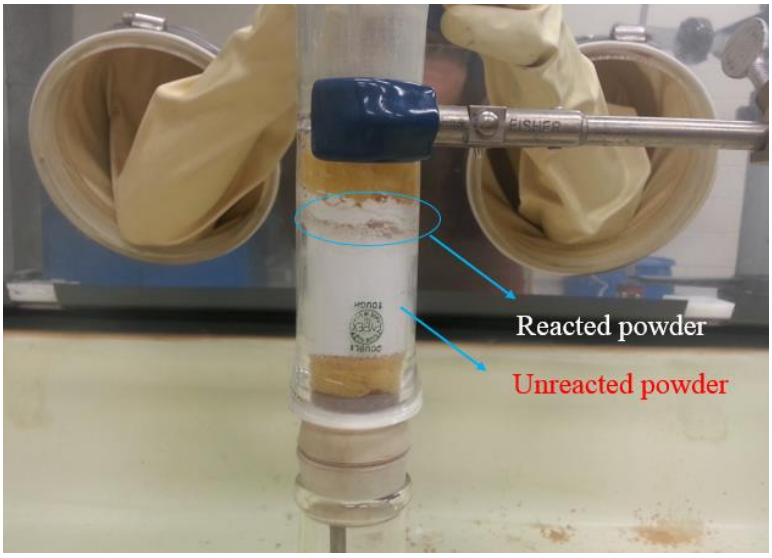

Figure 4.2 Image of immediate solidification of $MgCl_2$ with the HCl solution in the reaction flask.

The formed and saturated product at the top did not let the remaining solution pass through the powder and stopped the reaction as seen in Figure 4.2. Thus, a mixer is used to locate holes on the solidified product. Another fast reaction occurred with the collected solution resulting in a very fast temperature increase up to 36ºC after mixing. This resulted in release of some solution in gaseous form in the glove box ambient and failed to pass through the lower side distributor.

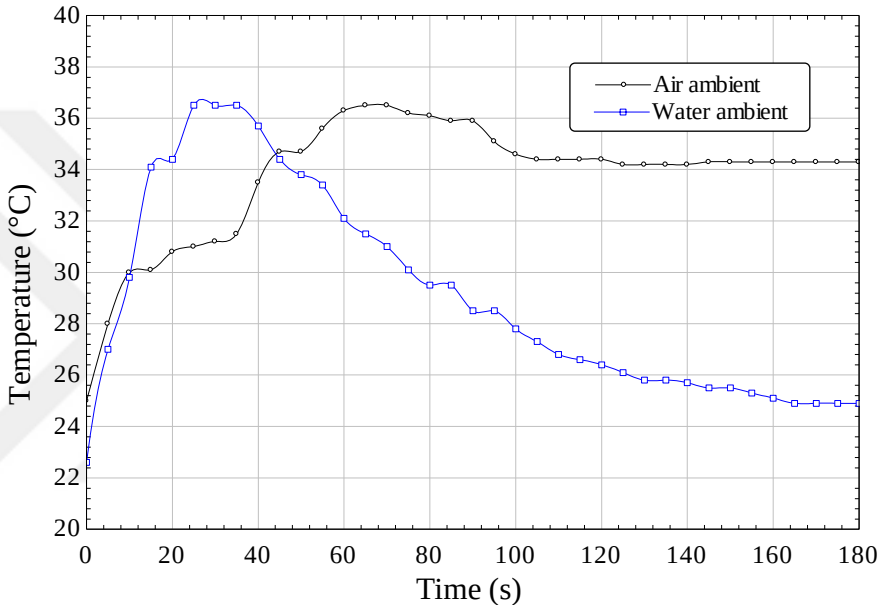

Figure 4.3 Temperature variations of the reactor at water and air ambient conditions.

Considering the preliminary test, the final setup for the HCl - $MgCl_2$ reaction is modified and designed to get better results. As soon as the reactor is kept under air ambient, the temperature of the reactor does not decrease to desired value and this results in release of more HCl gas from the solution. Thus, the reactor is kept under 20ºC to decrease the gas release. Figure 4.3 shows the change of the reactor temperature by time when the reactor is kept under air and water ambient. In both cases, the reaction temperature immediately increases up to 36ºC where this increase is faster for the water covered reactor. In three minutes, the water covered reactor temperature decrease down to its start point, where the air covered reactor remains at the peak temperature. Thus, the reactor vessel is covered with a water ambient for better observation of the reaction.

The final design of the reactor considers capturing of the gaseous HCl in another flask for further measurement with lower amounts of $MgCl_2$ powder. For the final setup. 0.05 moles of the powder is fed in the bed of the reaction vessel and corresponding amount of HCl is slowly interacted with the powder at a specified rate. The unreacted solution is collected at the bottom flask, where the gaseous HCl is transferred to another flask filled with NaOH solution. Final experimental design is shown in Figure 4.4.

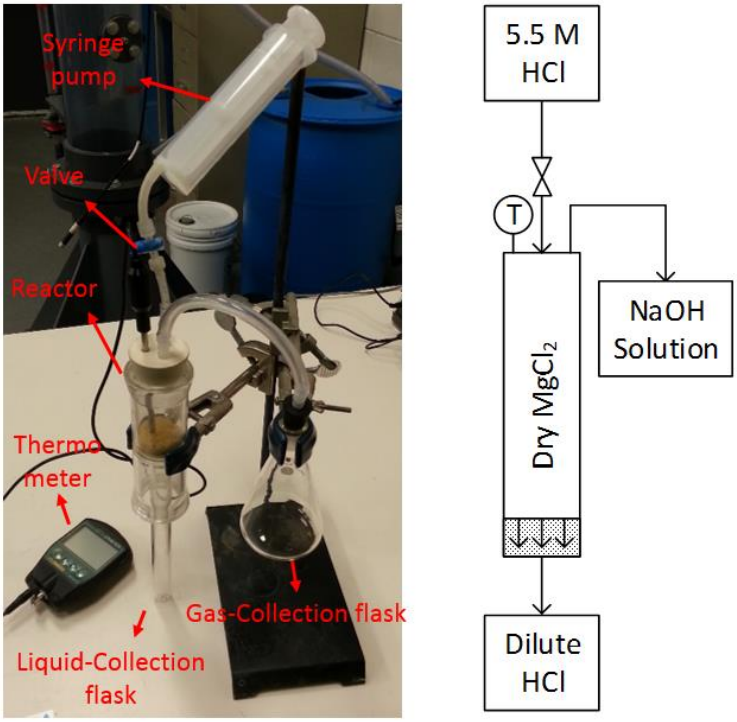

Figure 4.4 Preliminary experimental setup and its schematic diagram for the $MgCl_2$ hydration experiment.

4.2. Hydrochlorination Experiment

The reaction in Eqs. 4.6, and 4.7 have been studied by Kashani-Nejad (2005), where a very good conversion has been achieved at elevated temperatures with better reaction kinetics. The intermediate reaction (Eq. 4.5) has been studied by Lamy (2001) by bubbling the gas in a molten salt and let it react at MgO surface. This reaction can be considered as an HCl adsorbing agent and recovery of MgO particles can be achieved with another decomposition step at elevated temperatures.

Considering the literature information, there is also another possibility to capture HCl from the steam mixture in dry form by using MgO particles. However MgO particles have the potential to react with HCl and steam with the following chemical reactions:

$$MgO + 2HCl \leftrightarrow MgCl_2 + H_2O \quad (4.8)$$

$$MgO + H_2O \leftrightarrow Mg(OH)_2 \quad (4.9)$$

$$MgO + HCl \leftrightarrow MgOHCl \quad (4.10)$$

The simulation of individual reactions of the MgO particles under the steam/HCl mixture may lead to several side products. The dry $MgCl_2$ formation is almost impossible at low temperatures due to its desiccant nature. Thus, initially reaction characteristics are observed using the Rgibbs reactor of Aspen Plus software. Possible products from the MgO hydroxichlorination are simulated to be $Mg(OH)_2$, MgOHCl, $MgCl_2$, $MgCl_2{\cdot}6H_2O$, $MgCl_2{\cdot}4H_2O$, $MgCl_2{\cdot}2H_2O$, and $MgCl_2{\cdot}H_2O$. No traces of MgOHCl has been observed until 120ºC, and the main products remain as $Mg(OH)_2$ and hexahydrate of $MgCl_2$. Formation of MgOHCl initiates slightly at 125ºC and starts decomposing into HCl and MgO after 250ºC. Mol fractions of the possible products from this reaction are illustrated in Figure 4.5.

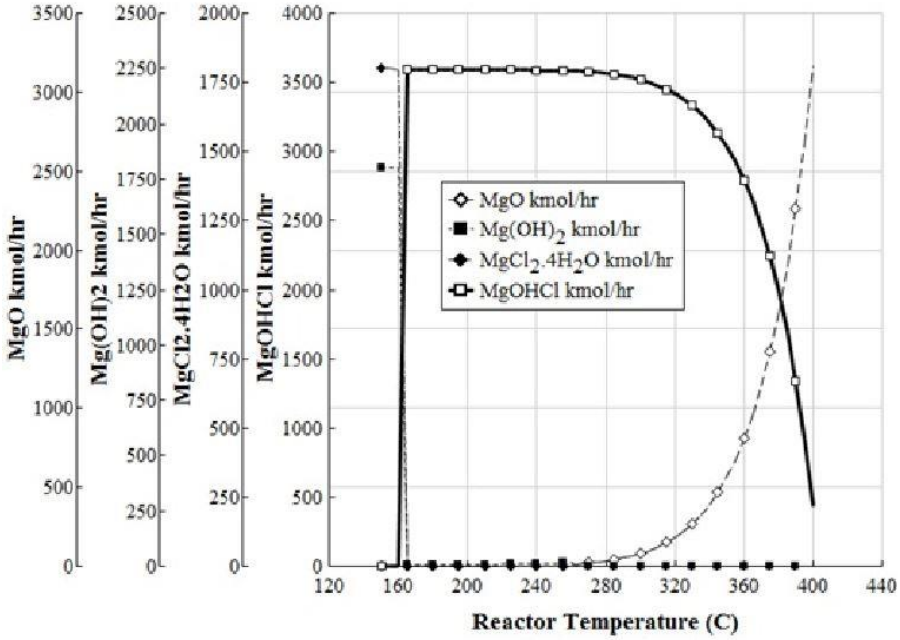

Figure 4.5 Variations of product mol fractions with the reactor temperature for 1 kmol/s MgO feed and 5.5 M HCl from hydrolysis.

The reaction in (4.10) tends to produce $MgCl_2$ starting from 120ºC in one of its hydrated forms. A black box analysis shows that MgOHCl production is likely to start from 150ºC. The stoichiometric requirement of $MgCl_2$ formation is two, and this ratio is only one for MgOHCl formation. Thus, it is appropriate to consider the experimentation at various HCl feed ratios. Since the reproduction of MgO from $MgCl_2$ requires a vast amount of steam, the reaction (4.8) is considered as an unwanted side reaction. The formed $Mg(OH)_2$ can be decomposed into H_2O and MgO at 332ºC. A controlled dehydration process can be made at this temperature range without jeopardizing possible HCl/steam mixture in the decomposition reaction of MgOHCl.

The HCl capture experiment is conducted in a semi-batch reactor by feeding HCl and N_2 at a specific rate into the reactor filled with MgO powder. 5.5. M HCl is prepared from a 12 M stock solution by following the producer suggestions. For 1:1 stoichiometry, 25 mL HCl is fed to reactor filled with 5.04 g of MgO powder. Unreacted gases are collected in a 200 mL NaOH solution. This solution is prepared by adding deionized water on 20 g of solid NaOH pellets. The corresponding pH value for 0.5 M NaOH solution is 12.70. Prepared solution is measured with a calibrated pH meter to verify the solution molarity. MgO particles are weighed on a Metler Toledo weighing device, and distributed into the reactor homogeneously. High purity nitrogen is selected as the inert gas and fed into reactor by bubbling in the HCl solution with a controlled flow. Used chemicals and their supplier information are given in Table 4.1.

Table 4.1 Chemicals and supplier information.

Substance	**Specifications**	**Supplier**
HCl solution	(37% wt%)	Sigma-Aldrich
NaOH pellets	White pellets	Fischer Scientific
AgNO3	0.995-1.005 M	Fischer Scientific
MgO	>99% pure, -325 mesh	Sigma-Aldrich
Buffer solutions	pH 4-7-10 (∓0.01)	Omega

The schematic diagram of the experiments are illustrated in Figure 4.6. The HCl stock is preheated up to 145ºC to prevent possible condensation in the piping before reaching the reactor. The preheater utilizes the temperature at around the reactor temperature in order to assure the gases enter the reactor at the desired temperature. The

temperature of the reactor is kept constant by a Digi-Sense temperature controller which is connected with the heating tapes and the *J* type thermocouple which is located in the reactor. A Pyrex type cylindrical glass reactor is used for the experiments. Since the heating tape temperature at the reactor surface might go up to 500ºC, it might result in a failed reactor. Thus, a metal sheet is covered around the reactor by providing an empty space between the glass reactor and the metal sheet. The metal sheet is then covered by the heating tape and the high temperature insulation material to decrease the heat dissipation to fume hood ambient. When the reactor temperature is cooler than the desired temperature, the temperature controller assures to keep the reactor temperature at the desired level. The pressure of the reactor is also measured to prevent the reactor from instant pressure changes. Thus, a vane is located to relieve possible overpressures during the experiment. For this purpose, a Vernier gas pressure sensor is used in connection with a data logger. An air cooled pre-cooler is used to cool gases after the reaction, where a condenser is also considered to form aquaeous HCl before entering the NaOH solution. The inert gas is again bubbled in the NaOH solution to assure the reaction of HCl in the NaOH solution. The change in the pH of the NaOH solution is measured with an Oakton Ion-2700 pH meter throughout the experiment to validate the formation of NaCl. The image of the experimental setup is shown in Figure 4.7 with detailed component explanations.

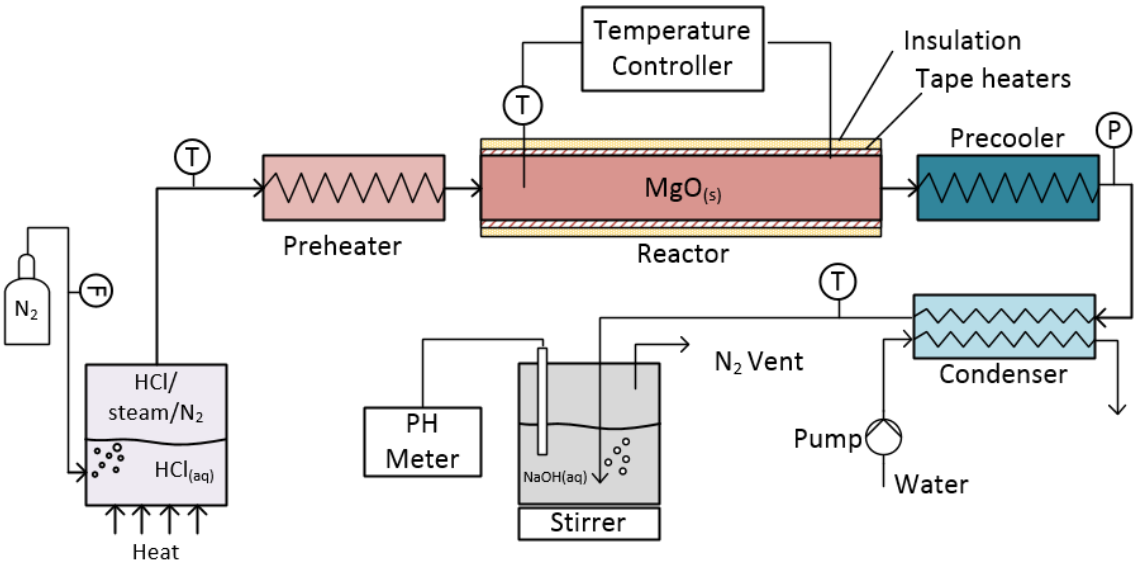

Figure 4.6 Schematic diagram of the hydrochlorination experimental setup.

Experiments are conducted by changing various system parameters. Since the most influential factor is expected to be the reactor temperature, a 25ºC increase is considered from 150 ºC to 275ºC. Recirculation of the gaseous constituents would also influence the corresponding heterogeneous reaction. Thus, the molar ratio of Cl/Mg is varied from one to two, respectively, and the flow rate of the inert gas is considered in two different ranges to evaluate effects of interaction time of the solid-gas reactions. A total of 24 experiments are conducted by considering all aforementioned variables. Table 4.2 shows the range of variables and their levels. The experiments are also repeated twice to get an average value for better reading of the measurements in accordance with the uncertainty assessment.

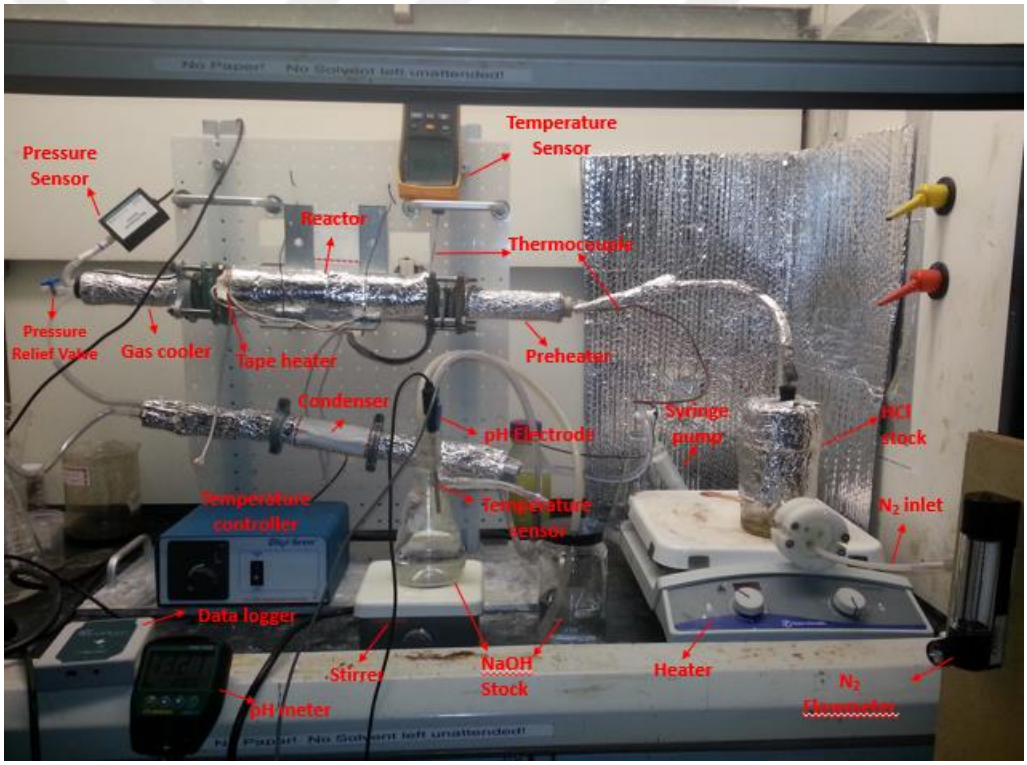

Figure 4.7 Final experimental setup.

Table 4.2 Experimental procedure with the parameters and their ranges.

Varied parameter	Range	Level
Reaction temperature	150 ºC -275 ºC (25ºC step)	6
N_2 flow rate	10-20 (mL/min)	2
Cl/Mg ratio	1-2	2
Total number of experiments		24

The final NaOH solution has a larger volume and lower pH values as expected. The volume change and the pH meter reading would give a general idea on how much Cl^- ions are captured in the reactor. However, this type of measurement can be misleading due to additional water inlet into the solution. Therefore, the precipitation titration method is selected to measure the amount of Cl^- ions in the solution. For this purpose 1 M $AgNO_3$ is selected as the precipitating agent. The reaction between the silver cation and the chlorine halide is as follows:

$$Ag^+ + Cl^- \rightarrow AgCl_s \tag{4.11}$$

where the reaction between $AgNO_3$ and NaCl is:

$$AgNO_3 + NaCl \rightarrow AgCl_s + NaNO_{3_{aq}} \tag{4.12}$$

Use of the pH meter is a very promising and accurate way to determine the completion of the titration without any need of indicators. The start of the rapid pH change indicates that the reaction is complete. Thus, calibration and accuracy of the pH meter is of importance. Calibration of the pH meter has been done by considering the supplier suggestions using three buffer fluids at pH 4, 7, and 10 with 99.9% accuracy. The final calibration also resulted in more than 99% accuracy.

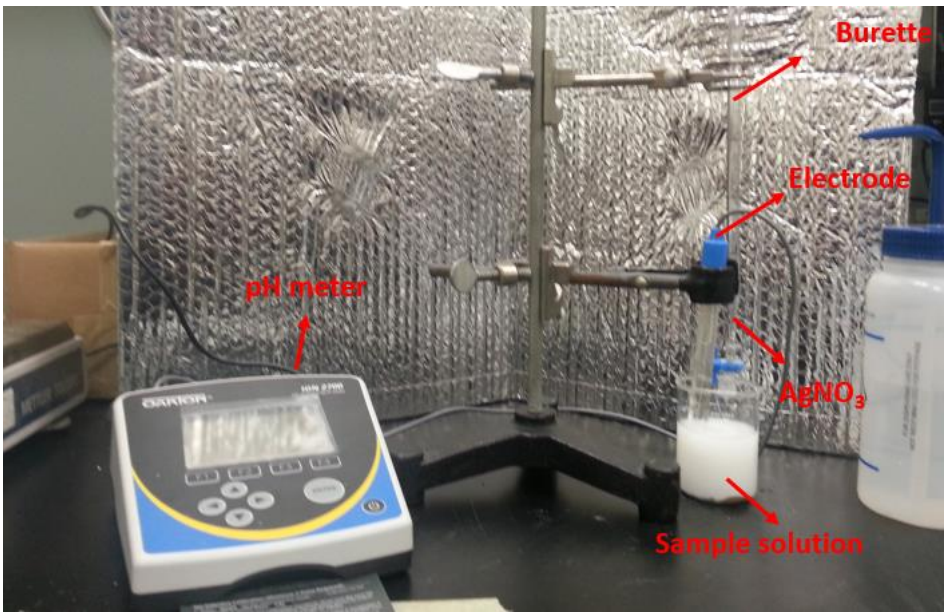

Figure 4.8 Precipitation titration experimental setup.

The precipitation titration experimental setup is shown in Figure 4.8. To validate the accuracy of this measurement technique, 10 mL of 1M NaCl solution is prepared with deionized water. The molar amount of the NaCl in the solution corresponds to 0.01 mol. Thus, it is known that 0.01 mol of $AgNO_3$ is required to complete the precipitation test, which corresponds to 10 mL. The rapid change started to occur when all $AgNO_3$ is fed into NaCl solution. The observation of the pH change is shown in Figure 4.9. A very accurate indication is obtained with the pH meter observations which is more convenient than use of indicators.

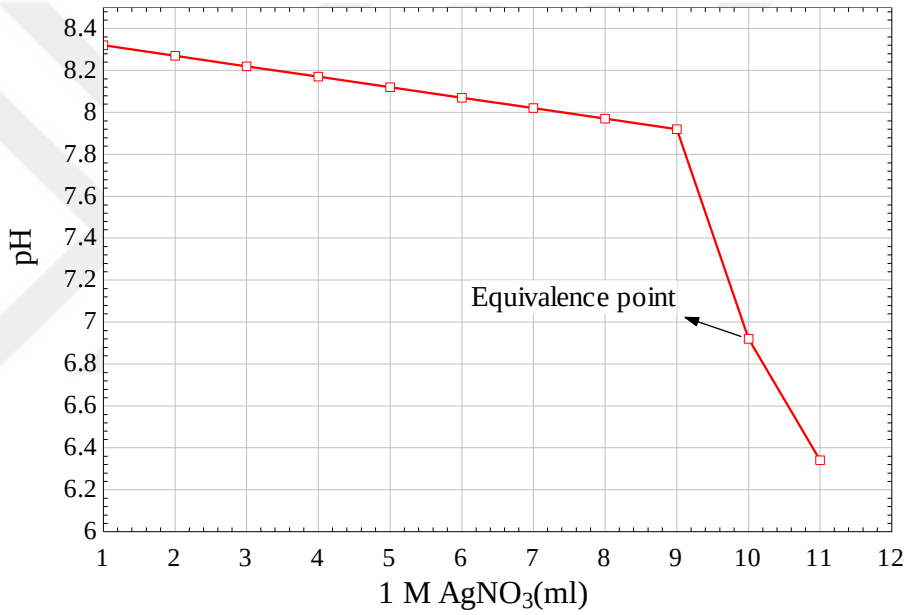

Figure 4.9 pH change in the NaCl solution with $AgNO_3$ addition.

The following procedure is applied to the precipitation titration experiment for measurement of resulting samples from each experiment:

- 5 mL sample of the NaCl/NaOH solution is measured in a volumetric flask.
- Deionized water is added in the sample until the pH of the solution is lower than 10 to prevent AgOH formation.
- The burette is filled with 1 M $AgNO_3$ solution, and droplets are carefully added into the solution by mixing the sample solution.
- All pH values are recorded at every step to see the pH changes of the sample solution.
- The $AgNO_3$ feed is stopped when a rapid change in pH is observed.

- The amount of $AgNO_3$ feed is measured from the burette which corresponds to amount of Cl^- ions in the sample solution.
- The molar amount of Cl^- ions are balanced with the total amount of the NaOH stock.
- The total amount of HCl is calculated in the NaOH solution
- Determination of the total HCl capture by the MgO particles is made by the difference of HCl amount in the 5.5 M HCl and the NaOH solution.

The precipitation titration experiment is a promising method to evaluate the captured HCl by the MgO particles. However it does not provide adequate information on which form the HCl agent is captured. Thus, an initial measurement is made using the thermogravimetric analysis (TGA) which helps determine amounts of captured species on the surface of MgO particles. The characteristics of the reacted solid particles are also evaluated using the XRD tests. This type of testing provides useful information on the form of captured HCl, as well as intensity of desired products.

4.3. Experimental Uncertainties

Uncertainty analysis of an experiment is crucial to determine the effect of device accuracies, and their bias and precision errors (Pope, 2012). Calculation of the experimental uncertainty is based on the bias and precision errors and it is defined as follows:

$$U_i = (B_i^2 + P_i^2)^{0.5} \tag{4.13}$$

Here, *B* stands for bias error and *P* stand for precision error. Table 5.3 represents the bias and precision errors of all devices effecting the measurements in the experiments. Bias and precision errors are calculated based on the partial derivatives of the varying parameters and corresponding device errors. The varied parameters in the experiments are reactor temperature, *Cl/Mg* ratio, and N_2 flow rate. Here errors for reactor temperature is considered twice due to use of both thermocouple and temperature controller. Corresponding equations for uncertainty are as follows:

$$B_{HCL}^2 = \left(\frac{\partial HCl}{\partial T}\right)^2 B_t^2 + \left(\frac{\partial HCl}{\partial T}\right)^2 B_{tc}^2 + \left(\frac{\partial HCl}{\partial N}\right)^2 B_N^2 + \left(\frac{\partial HCl}{\partial CM}\right)^2 B_{CM}^2 \tag{4.14}$$

$$P_{HCL}^2 = \left(\frac{\partial HCl}{\partial T}\right)^2 P_t^2 + \left(\frac{\partial HCl}{\partial T}\right)^2 P_{tc}^2 + \left(\frac{\partial HCl}{\partial N}\right)^2 P_N^2 + \left(\frac{\partial HCl}{\partial CM}\right)^2 P_{CM}^2 \quad (4.15)$$

where *T*, *N*, *CM*, *t*, and *tc* stand for temperature, flow rate, Cl/Mg ratio, thermocouple and temperature controller, respectively. Partial derivatives of the variables are calculated from a correlated equation obtained from experimental results which is a function of all variables. A code is modified in order to determine uncertainty of the HCl capture experiments, using MATLAB software (Jianu, 2013). Modified MATLAB code is provided in Appendix A.

Table 4.3 Relative errors and accuracies related to measurement devices.

Variable	Device	Accuracy	Range	Reference value	Relative bias error	Relative precision error
T	Digi-Sense temperature controller	∓0.4ºC	Up to 1000 ºC	350 Cº	0.0011	$4.0 \cdot 10^{-4}$
	Omega J-type thermocouple	∓1ºC	-190 to 1000ºC	300 ºC	0.016	0.005
CM	Oakton Ion-2700 pH meter	∓0.002	-1 to 15	7.5	0.0014	-
N	Omega direct read flowmeter FL-2500	∓0.065 L	0.01 to 1.3 L/min	0.1 L/min	0.0013	$3.4 \cdot 10^{-4}$
V_s	Mettler Toledo ML3002E	∓0.01 g	0.01 to 3200 g	2500 g	$4.0x10^{-6}$	-

CHAPTER 5: ANALYSES AND OPTIMIZATION

5.1 Fundamental Concepts

Thermodynamic and thermoeconomic analyses of any system are based on the thermopysical and the chemical properties of individual streams throughout the studied system. Therefore, mass, energy, entropy, and exergy balances of any component are required to determine efficiencies, inefficiencies, exergy destructions, and the cost of the component. Following subsection provides brief information for model development.

5.1.1 Thermodynamic Analysis

The mass, energy, entropy and exergy balances are required in the first step of the exergy analysis to determine the heat input/output, entropy generation rate, exergy destructions, and energy and exergy efficiencies. The mass balance equation for a steady-state condition is as follows (Dincer and Zamfirescu, 2014):

$$\sum \dot{m}_{in} = \sum \dot{m}_{out} + \frac{\mathrm{d}m_{CV}}{\mathrm{d}t} \tag{5.1}$$

Here, the second definition at the right side is cancelled when the flow is steady. Energy balance of a system can be defined by considering all forms of energy within a system:

$$\Delta E_{sys} = m\Delta e_{sys} = m\left[\left(u_{out} + \frac{1}{2}v_{out}^2 + gz_{out}\right) - \left(u_{in} + \frac{1}{2}v_{in}^2 + gz_{in}\right)\right] \tag{5.2}$$

where *u* stands for internal energy, *v* is velocity of the corresponding flow, *g* is gravity and *z* is height. Energy of a non-flowing thermodynamic system is defined as

$$e = u + \frac{1}{2}v^2 + gz \tag{5.3}$$

The total energy of a flowing matter can be defined as sum of non-flow energy and flow work:

$$\theta = e + Pv \tag{5.4}$$

The energy balance of an open system can now be defined as follows:

$$\sum_{in} \dot{m}\theta + \sum \dot{Q}_{in} + \sum \dot{W}_{in} = \sum_{out} \dot{m}\theta + \sum \dot{Q}_{out} + \sum \dot{W}_{out} + \left[\frac{\mathrm{d}(me)}{\mathrm{d}t}\right]_{sys} \tag{5.5}$$

where the fourth definition at the right side is cancelled when the flow is steady. When kinetic and potential energies are cancelled, the sum of internal energy and the flow work correspond to enthalpy of the individual stream.

The heat transfer for a chemical process is basically the difference between enthalpies of products and reactants of a reaction and is determined with the following expression:

$$Q = H_P - H_R = \sum n_p\left(\bar{h}_f^\circ + \bar{h} + \bar{h}^\circ\right)_p - \sum n_R\left(\bar{h}_f^\circ + \bar{h} + \bar{h}^\circ\right)_R \quad (5.6)$$

where *n* refers to molar amount, and corresponding *h* values are molar enthalpy of formation, molar enthalpy of state, and reference enthalpy, respectively. Enthalpy of formation and reference enthalpy values can be found in thermochemical tables of various databases, where enthalpy of state is calculated based on temperature of the reaction with various empirical correlations. Supposing that the reactants of the reaction under study are *A*, and *B*, and products are denoted as *C*, and *D*; the specific heat of the reaction is expressed as follows (Kelley, 1945):

$$Cp_i = a_i + b_i T + c_i T^{-2} \quad (5.7)$$

where *a*, *b* and *c* are empirically calculated constants. The specific heat for the individual reaction depends on the specific heats of the individual components of the reaction, and defined as follows:

$$\Delta Cp = Cp_c + Cp_d - Cp_a - Cp_b = a + bT + cT^{-2} \quad (5.8)$$

Empirically developed constants are determined by finding the difference of the products and reactants in a general form. The corresponding reaction heat can be calculated in terms of temperature with the standard heat of the reaction as follows:

$$\Delta H = \int \Delta Cp \mathrm{d}T = \Delta H_0 + aT + \frac{b}{2}T^2 - \frac{c}{T} \quad (5.9)$$

The entropy balance of an open system can be expressed in rate form as sum of entropy input and generated entropy, and is equal to sum of entropy of output and change of control volume entropy as follows:

$$\sum \dot{S}_{in} + \dot{S}_{gen} = \sum \dot{S}_{out} + \frac{\mathrm{d}S_{sys}}{\mathrm{d}t} \quad (5.10)$$

If there is heat transfer across the boundary of a control volume, then the balance equation becomes:

$$\sum_{in} \dot{m}s + \sum_{in} \int \frac{\mathrm{d}\dot{Q}}{T} + \dot{S}_{gen} = \sum_{out} \dot{m}s + \sum_{out} \int \frac{\mathrm{d}\dot{Q}}{T} + \left[\frac{\mathrm{d}S}{\mathrm{d}t}\right]_{CV} \quad (5.11)$$

which can further be simplified by considering a steady and adiabatic process:

$$\sum_{in} \dot{m}s + \dot{S}_{gen} = \sum_{out} \dot{m}s \quad (5.12)$$

When the entropy difference of a reaction is required for a chemical process, it can be calculated using Gibbs free energy and reaction heat as follows:

$$\Delta S = \frac{\Delta H - \Delta G^0}{T} = a + alnT + bT - \frac{c}{2}T^{-2} - I \quad (5.13)$$

where ΔG^0 is determined with the following expression:

$$\Delta G^0 = \int \frac{\Delta H}{T^2} \mathrm{d}T = \Delta H_0 - aTlnT - \frac{b}{2}T^2 - \frac{c}{2T} + IT \quad (5.14)$$

where *I* corresponds to irreversibility, and can be determined from total entropy generation and ambient temperature. For the known values of standard heat of reaction and *I*, temperature is the ultimate variable to calculate the free energy of the reaction.

Gibbs free energy is also related with the equilibrium constant (*K*) as follows:

$$\Delta G^0 = -RTlnK \quad (5.15)$$

where *K* is defined as the rate of activities of the products and reactants as follows:

$$K = \frac{\alpha_c \alpha_d}{\alpha_a \alpha_b} \quad (5.16)$$

The activities of the gaseous and liquid reactants and products are assumed to be equal to their partial pressures, depending on the reference pressure. Thus, the equilibrium constant can be defined as

$$K = \left(\frac{p_c p_d}{p_a p_b}\right) \frac{1}{p^0} \quad (5.17)$$

where p^o is the reference pressure considered for calculation and for its effects on the behaviour of the reaction. Calculations and the amount of the produced components are based on the Gibbs free energy of the reactions. In order to obtain a favorable reaction in terms of pressure and temperature of the reactions, determination of the molar percentages of the produced gaseous components should be conducted. Specific heat equations for some of the required substances through the Mg-Cl cycle are tabulated in Table 5.1.

Table 5.1 Specific heat equations for some substances.

Substance	Specific heat equation (cal/mole°C)
$MgO_{(s)}$	$10.86 + 1.197 \cdot 10^{-3}T - 2.087 \cdot 10^{5}T^{-2}$
$MgCl_{2(s)}$	$18.9 + 1.42 \cdot 10^{-3}T - 2.06 \cdot 10^{5}T^{-2}$
$MgCl_{2(l)}$	22.1
$MgCl_2H_2O_{(s)}$	$21.75 + 19.45 \cdot 10^{-3}T$
$MgOHCl_{(s)}$	$13.40 + 14.47 \cdot 10^{-3}T$

The exergy content of a non-flow system is sum of all forms of exergy, and flow exergy is sum of non-flow exergy and flow work as expressed below:

$$Ex_{nf} = Ex_{ph} + Ex_{kin} + Ex_{pot} + Ex_{ch} \quad (5.18)$$

$$Ex_f = Ex_{nf} + (P - P_0)V \quad (5.19)$$

The physical exergy of any stream is expressed as

$$Ex_{ph} = (U - U_0) + P_0(V - V_0) - T_0(S - S_0) \quad (5.20)$$

Here, *U*, *V*, and *S* are internal energy, volume, and entropy of a closed system, respectively. Kinetic and potential energies are associated directly with work, which remains the same in exergy definition as expressed in energy balance definitions.

The chemical exergy of a system is expressed as

$$Ex_{ch} = \sum n_i(u_i^0 - u_i^{00}) \quad (5.21)$$

where u_i^0 is chemical potential of i^{th} component in thermomechanical equilibrium and u_i^{00} is the chemical potential of i^{th} component in chemical equilibrium. Standard chemical exergy values of various chemical substances can be found elsewhere (Kotas, 2013; Dincer and Rosen, 2012). Table 5.2 represents standard chemical exergy values of some substances used in the Mg-Cl cycle.

Table 5.2 Standard chemical exergy of species in Mg-Cl cycle.

Substance	**($\overline{ex}_{ch}^0$) (kJ/kmol)**	**Substance**	**($\overline{ex}_{ch}^0$) (kJ/kmol)**
$H_2O_{(g)}$	11,710	$HCl_{(g)}$	85,950
$H_2O_{(l)}$	3,120	$O_{2(g)}$	3,970
$MgCl_{2(s)}$	151,860	$Cl_{2(g)}$	11,7520
$MgO_{(s)}$	59,170	$H_{2(g)}$	23,8490
Source: Kotas, 2013			

For a control volume, exergy balance of a system can now be expressed as

$$\sum_{in}\left[\dot{W} + \dot{m}ex + \dot{E}x^Q\right] = \sum_{in}\left[\dot{W} + \dot{m}ex + \dot{E}x^Q\right] + \frac{\mathrm{d}Ex}{\mathrm{d}t} - \frac{P_0(\mathrm{d}V_{CV})}{\mathrm{d}t} + \dot{E}x_d \quad (5.22)$$

$\dot{E}x_d$ is the exergy destruction and its associated with the entropy generation rate as follows:

$$\dot{E}x_d = T_0\,\dot{S}_{gen} \quad (5.23)$$

$\dot{E}x^Q$ is exergy associated with the corresponding heat transfer:

$$\dot{Ex}^{Q} = (1 - \frac{T_0}{T})\dot{Q} \tag{5.24}$$

It should be noted that the second and the third definitions in Eq 5.22 are cancelled when the system is steady flow. One can now perform efficiency assessments based on energy and exergy of any system by simply considering inputs and outputs to and from the system. Energy and exergy efficiencies are expressed in a general form as follows:

$$\eta_{en} = \frac{Useful\ output}{Total\ input}$$
$$\eta_{ex} = \frac{\dot{Ex}_{useful}}{\dot{Ex}_{in}} = 1 - \frac{\dot{Ex}_{d}}{\dot{Ex}_{in}} \tag{5.25}$$

5.1.2 Exergoeconomic Analysis

Economics of a plant in connection with second law of thermodynamics is a promising and precise tool to evaluate costs related to thermodynamics of the plant. Cost analyses itself may not be a good indicator on understanding the economics of a plant. Thus exergoeconomic analysis is offered by Tsatsoronis and Moran (1997). The cost rate $\dot{C}$ (\$/h) of a stream is the main variant for exergoeconomic assessment and its explained as follows:

$$\dot{C} = c\ \dot{Ex} \tag{5.26}$$

where *c* stands for cost per unit of exergy.

The component related cost ($\dot{Z}$) includes life cycle phases of construction and operation of components and expressed as follows:

$$\dot{Z} = \frac{Z_k CRF \varphi}{3600N} \tag{5.27}$$

where Z_k is the purchase cost of k^{th} component, *CRF* is capital recovery factor, φ is maintenance factor (~1.06) and *N* is the annual operating hours. Here, Z_k of a component is calculated from various correlations derived by considering the type of component by the study estimate method (Turton et al., 2009). Given correlations for purchase cost are generally explained with a cost index, which should be updated using the chemical engineering plant cost index (CEPCI) (Vatavuk, 2002). The correlations are used as in Turton et al., (2009), which are than updated to 2014 values using the following definition:

$$C_1 = C_2(\frac{CEPCI_1}{CEPCI_2}) \tag{5.28}$$

The plant cost index for the year 2001 is 394, where this index is 575.7 for 2014 (December final) (Chemical Engineering Journal, 2015). Thus, the CEPCI factor is taken to be 0.684 to update the costs of components.

The CRF is dependent on interest rate (i) and total life time (n) of the system:

$$CRF = \frac{i(1-i)^n}{(1+i)^n-1} \tag{5.29}$$

and general cost rate balance is:

$$\dot{C}_p = \dot{C}_f + \dot{Z} \tag{5.30}$$

Here subscripts p and f stand for product and fuel, respectively. Now, a general definition for cost balance of any thermal system in steady-state form can be expressed as

$$\sum_e \left(c_e \dot{E}x_e\right)_k + c_{w,k}\dot{E}x_{w,k} = c_{q,k}\dot{E}x_{q,k} + \sum_i \left(c_i \dot{E}x_i\right)_k + \dot{Z}_k \tag{5.31}$$

where subscripts e, w, q, and i stand for exit, work, heat and inlet, respectively. Using the exergy destruction rates of any component, it is possible to define cost of destruction as follows:

$$\dot{C}_{dest} = c_f \dot{E}x_{dest} \tag{5.32}$$

It is necessary to derive auxiliary equations to calculate unknowns of a cost balance for a component, which requires additional exergy balances of the individual components by considering products and fuels of the component. These formulations can be made using fuel (F) and product (P) rule, in which it is possible to formulate (n_e-1) equations when there are (n_e) streams exiting from the individual component (Lazzaretto and Tsatsaronis, 2006).

The principles of fuel and product should be interpreted to formulate auxiliary equations properly. The F principle dictates that specific cost of an exergy removal from a fuel stream must be equal to average cost of the same stream entering to upstream components. It should be noted that auxiliary costing equation from the F principle is not required when inlet-outlet exergy difference is not considered as fuel. As for the P rule, each exergy unit associated with the product is denoted as c_p. Thus, ($n_{e,p}$-1) equations can be formulated with the P rule. Total formulated equations with the fuel and product rules will be equal to (n_e-1) equations to evaluate costs of components (Lazzaretto and Tsatsaronis, 2006).

After formulation of the equations, the required steps for specific exergy costing (SPECO) method is completed. It is also crucial to evaluate performances of individual components using an exergoeconomic factor (*f*), which helps determine major cost sources:

$$f = \frac{\dot{Z}}{\dot{Z}+c_f \dot{E}x_{dest}} \tag{5.33}$$

Relative cost difference (RCD) is also a helpful tool to determine component based cost comparison of the system:

$$RCD = \frac{c_p - c_f}{c_f} \tag{5.34}$$

5.1.3 Optimization Study

Multi-objective optimization is conducted to maximize the Mg-Cl cycle performance and to minimize cost of the system. Since most of the world problems depend on many parameters, optimization of these systems by considering a single objective does not provide precise results with respect to other objectives to be optimized (Deb, 2001). For a system to be optimized with multiple (*K*) objectives, minimization of objectives can be defined (Konak et al., 2006). In a solution space of *x* and for an *n*-dimensional decision variable:

$$x = \{x_1, x_2 \dots x_n\} \tag{5.35}$$

It is necessary to determine an *x** vector to minimize:

$$z(x*) = \{z_1(x*), \dots z_K(x*)\} \tag{5.36}$$

The search space *x* is restricted with specified constraints of the system studied:

$$g(x*) = b_j \;\; for\; j = 1, \dots m \tag{5.37}$$

A decision for the optimization can be made for both minimization and maximization. However this selection should be at the same direction for all objective functions. Thus, if a minimization study is conducted and one of the objectives is to be maximized, this objective functions can be multiplied by negative one (-1). Among all feasible solutions, the most dominant solution is the Pareto optimal solution. For a determined Pareto optimal set, all corresponding objective function values are called the Pareto front.

There are several methods of optimization which can be adapted to solve multi-objective optimization problems. Genetic Algorithms (GA) are one of the most promising

optimization methods (Holland, 1975). In the GA, the solution vector (x) is defined as a chromosome, and collection of chromosomes form a population. Generation of new solutions are accomplished by crossover and mutation, where crossover is forming of new solutions from two chromosomes called 'parents'. It is expected that the offspring inherits good genes from the parents to optimize the population. Mutation is generally applied at gene level, which helps the population remain in the local optima by setting a mutation rate between zero and one, so that the offspring will not be very different than their parents. The GA optimization can be accomplished with the following steps:

- Initiate a population
- Select random parents from the population
- Crossover
- Mutation
- Reproduction of new population from the children population
- Stop evolution

Multi-objective optimization can be made using the GA by finding a set of non-dominated solutions in a single run (Konak et al., 2006). Here, a general method can be defined as weight-based GA, where a user defined weight factor is used to minimize all objective functions in a single objective problem:

$$\min z = w_1 z_1'(x) + \cdots . w_k z_k'(x) \tag{5.38}$$

Here, defining the weight factor is a challenging process through the optimization process. However, this is a simple and useful tool to solve multi-objective problems. There are several other modifications for multi-objective GA optimization, and can be found elsewhere (Talbi, 2009; Konak, 2006). The optimization of the Mg-Cl is conducted using the multi-objective non-dominated sorting GA (NSGA) algorithm in MATLAB software. The objectives functions are defined by using Artificial Neural Network (ANN) application of MATLAB software package by considering Levenberg-Marquart algorithm as a default option (MATLAB, 2014).

5.2 Analysis of Mg-Cl cycle

This section provides details of the thermodynamic and economic evaluation of the Mg-Cl cycle with state point information.

5.2.1 Thermodynamic Analysis

In this section, detailed thermodynamic analysis of the modified four-step Mg-Cl cycle is presented. State point information is taken from Figure 3.4. Mass, energy, entropy and exergy balances of the components of the Mg-Cl cycle are tabulated in Table 5.3. For the cycle itself energy and exergy efficiencies are defined by following definitions which consider oxygen and hydrogen streams as useful outputs from the cycle, and the water, heat and work as input:

$$\eta_{en} = \frac{\dot{E}_{12}+\dot{E}_{21}+\dot{E}_{29}}{\dot{E}_{1}+\dot{Q}_{in}+\dot{W}_{elec1}+\dot{W}_{elec2}} \tag{5.39}$$

$$\eta_{ex} = \frac{\dot{E}x_{12}+\dot{E}x_{21}+\dot{E}_{29}}{\dot{E}x_{1}+\dot{Ex}^{Q}_{in}+\dot{W}_{elec1}+\dot{W}_{elec2}} \tag{5.40}$$

Thermal energy input to the system is provided for heat requiring reactions and heat exchangers at their required temperature grades. Internal heat utilization is conducted based on pinch point analysis, and amount of external heat requirement and its grades are calculated. Thus, the sum of the required external heat is taken as input to the system, and thermal exergy content of this heat is considered for the exergy efficiency calculations. The same procedure is applied to other flowsheet options of the Mg-Cl cycle.

Detailed information on subscripts, superscripts and special notations are provided in the nomenclature. Exergy destruction rates of components are determined from exergy balance equations where the total is sum of exergy destructions of considered components. It is also possible to calculate exergy destructions by multiplying entropy generation rates with the ambient temperature for most cases. Above explanations are used as the base for the Mg-Cl cycle where they are also used for the exergoeconomic evaluation.

Electrolysis of anhydrous HCl is also modeled by using the information in the literature work (Eames and Newman, 1995). Initially, utilization of the HCl gas is taken into consideration with the following utilization factor definition:

$$u = 1 - \frac{m_a x_{HCL}}{m_a^0 x_{HCL}} \tag{5.41}$$

where *x* refers to mole fraction of HCl gas, and subscript *a* stands for anode. A water-flux index is developed by Eames and Newman (1995), in which it is aimed to determine the water flux between the electrode surface and membrane. However, this parameter is

assumed to be zero for this thesis work. Thus, differential balances of anode and cathode gas stream compositions are defined as follows:

$$x_{HCl} = \frac{x_{HCl}^{o}(1-u)}{1-0.5x_{HCl}^{0}u} \tag{5.42}$$

$$x_{Cl2} = \frac{x_{Cl2}^{o}+\frac{x_{HCl}^{0}u}{2}}{1-0.5x_{HCl}^{0}u} \tag{5.43}$$

$$x_{H2} = \frac{x_{H2}^{o}+\frac{x_{HCl}^{0}u}{2}}{1-0.5x_{HCl}^{0}u} \tag{5.44}$$

Table 5.3 Mass, energy, entropy and exergy balances of the four step Mg-Cl cycle

Component	Balance Equations
Hydrolysis	$\dot{m}_3 + \dot{m}_4 = \dot{m}_6 + \dot{m}_{13}$ $\dot{E}_3 + \dot{E}_4 = \dot{E}_6 + \dot{E}_{13} + \dot{Q}_{hyd}$ $\dot{S}_3 + \dot{S}_4 + \dot{S}_{gen} = \dot{S}_6 + \dot{S}_{13} + \frac{\dot{Q}_{hyd}}{T_r}$ $\dot{E}x_3 + \dot{E}x_4 = \dot{E}x_6 + \dot{E}x_{13} + \dot{E}x^{Q} + \dot{E}x_{dest}$
Decomposition	$\dot{m}_{14} = \dot{m}_{16} + \dot{m}_{24}$ $\dot{E}_{14} + \dot{Q}_{dec} = \dot{E}_{16} + \dot{E}_{24}$ $\dot{S}_{14} + \frac{\dot{Q}_{dec}}{T_r} + \dot{S}_{gen} = \dot{S}_{16} + \dot{S}_{24}$ $\dot{E}x_{14} + \dot{E}x^{Q} = \dot{E}x_{16} + \dot{E}x_{24} + \dot{E}x_{dest}$
Chlorination	$\dot{m}_{24} + \dot{m}_{25} = \dot{m}_{27} + \dot{m}_{28}$ $\dot{E}_{24} + \dot{E}_{25} = \dot{E}_{27} + \dot{E}_{28} + \dot{Q}_{chl}$ $\dot{S}_{24} + \dot{S}_{25} + \dot{S}_{gen} = \dot{S}_{27} + \dot{S}_{28} + \frac{\dot{Q}_{chl}}{T_r}$ $\dot{E}x_{24} + \dot{E}x_{25} = \dot{E}x_{27} + \dot{E}x_{28} + \dot{E}x^{Q} + \dot{E}x_{dest}$
Separation	$\dot{m}_6 = \dot{m}_{6-I} + \dot{m}_{6-II} + \dot{m}_{6-III}$ $\dot{E}_6 + \dot{Q}_{dec} = \dot{E}_{6-I} + \dot{E}_{6-II} + \dot{E}_{6-III}$ $\dot{S}_{6-I} + \frac{\dot{Q}_{dec}}{T_r} + \dot{S}_{gen} = \dot{S}_{6-I} + \dot{S}_{6-II} + \dot{S}_{6-III}$ $\dot{E}x_6 + \dot{E}x^{Q} = \dot{E}x_{6\_I} + \dot{E}x_{6-II} + \dot{E}x_{6\_III} + \dot{E}x_{dest}$
Electrolysis (aq)	$\dot{m}_7 = \dot{m}_9 + \dot{m}_{22}$ $\dot{E}_7 + \dot{W}_{elec1} = \dot{E}_9 + \dot{E}_{22}$ $\dot{S}_7 + \dot{S}_{gen} = \dot{S}_9 + \dot{S}_{22}$ $\dot{E}x_7 + \dot{W}_{elec1} = \dot{E}x_9 + \dot{E}x_{22} + \dot{E}x_{dest}$
Electrolysis (dry)	$\dot{m}_{18} = \dot{m}_{19} + \dot{m}_{20}$ $\dot{E}_{18} + \dot{W}_{elec2} = \dot{E}_{19} + \dot{E}_{20}$ $\dot{S}_{18} + \dot{S}_{gen} = \dot{S}_{19} + \dot{S}_{20}$ $\dot{E}x_{18} + \dot{W}_{elec2} = \dot{E}x_{19} + \dot{E}x_{20} + \dot{E}x_{dest}$
Hex-1	$\dot{m}_2 = \dot{m}_3$ $\dot{E}_2 + \dot{Q}_{hex1} = \dot{E}_3$ $\dot{S}_2 + \frac{\dot{Q}_{hex1}}{T_{hex1}} + \dot{S}_{gen} = \dot{S}_3$ $\dot{E}x_2 + \dot{E}x^{Q} = \dot{E}x_3 + \dot{E}x_{dest}$

Hex-2	$\dot{m}_{13} = \dot{m}_{14}$ $\dot{E}_{13} + \dot{Q}_{hex2} = \dot{E}_{14}$ $\dot{S}_{13} + \frac{\dot{Q}_{hex2}}{T_{hex2}} + \dot{S}_{gen} = \dot{S}_{14}$ $\dot{E}x_{13} + \dot{E}x^{Q} = \dot{E}x_{14} + \dot{E}x_{dest}$
Hex-3	$\dot{m}_{6-II} = \dot{m}_{7}$ $\dot{E}_{6-II} = \dot{E}_{7} + \dot{Q}_{hex3}$ $\dot{S}_{6-II} + \dot{S}_{gen} = \dot{S}_{7} + \frac{\dot{Q}_{hex3}}{T_{hex3}}$ $\dot{E}x_{6-II} = \dot{E}x_{7} + \dot{E}x^{Q} + \dot{E}x_{dest}$
Hex-4	$\dot{m}_{16-I} = \dot{m}_{17}$ $\dot{E}_{16-I} = \dot{E}_{17} + \dot{Q}_{hex4}$ $\dot{S}_{16-I} + \dot{S}_{gen} = \dot{S}_{17} + \frac{\dot{Q}_{hex4}}{T_{hex4}}$ $\dot{E}x_{16-I} = \dot{E}x_{17} + \dot{E}x^{Q} + \dot{E}x_{dest}$
Hex-5	$\dot{m}_{11} = \dot{m}_{12}$ $\dot{E}_{11} = \dot{E}_{12} + \dot{Q}_{hex5}$ $\dot{S}_{11} + \dot{S}_{gen} = \dot{S}_{12} + \frac{\dot{Q}_{hex5}}{T_{hex5}}$ $\dot{E}x_{11} = \dot{E}x_{12} + \dot{E}x^{Q} + \dot{E}x_{dest}$
Hex-6	$\dot{m}_{20} = \dot{m}_{21}$ $\dot{E}_{20} = \dot{E}_{21} + \dot{Q}_{hex6}$ $\dot{S}_{20} + \dot{S}_{gen} = \dot{S}_{21} + \frac{\dot{Q}_{hex6}}{T_{hex6}}$ $\dot{E}x_{20} = \dot{E}x_{21} + \dot{E}x^{Q} + \dot{E}x_{dest}$
Hex-7	$\dot{m}_{23} = \dot{m}_{25}$ $\dot{E}_{23} + \dot{Q}_{hex7} = \dot{E}_{25}$ $\dot{S}_{23} + \frac{\dot{Q}_{hex7}}{T_{hex7}} + \dot{S}_{gen} = \dot{S}_{25}$ $\dot{E}x_{23} + \dot{E}x^{Q} = \dot{E}x_{25} + \dot{E}x_{dest}$
Hex-8	$\dot{m}_{28} = \dot{m}_{29}$ $\dot{E}_{28} = \dot{E}_{29} + \dot{Q}_{hex8}$ $\dot{S}_{28} + \dot{S}_{gen} = \dot{S}_{29} + \frac{\dot{Q}_{hex8}}{T_{hex8}}$ $\dot{E}x_{28} = \dot{E}x_{29} + \dot{E}x^{Q} + \dot{E}x_{dest}$
Hex-9	$\dot{m}_{27} = \dot{m}_{4}$ $\dot{E}_{27} = \dot{E}_{4} + \dot{Q}_{hex9}$ $\dot{S}_{27} + \dot{S}_{gen} = \dot{S}_{4} + \frac{\dot{Q}_{hex9}}{T_{hex9}}$ $\dot{E}x_{27} = \dot{E}x_{4} + \dot{E}x^{Q} + \dot{E}x_{dest}$

All equations listed in Table 5.3 are used to determine concentrations of the substances which leads to determining the partial pressures at the exit of the electrochemical cell. Considering the hydrogen production from the cell, current density with the Butler-Volmer expression can be assumed for the cathode reaction as follows:

$$i = k_a p_{HCl}^{o} \exp\left(\frac{\alpha_a FV}{RT}\right) - k_c p_{H_2}^{0\ 0.5} \exp\left(-\frac{\alpha_c FV}{RT}\right) \quad (5.45)$$

Here, the kinetic parameters (k_a and k_c) are reduced to one parameter as follows:

$$i = p_{HCl}^{o} \exp\left(\frac{\alpha_a FV}{RT}\right) - \frac{k_c}{k_a} p_{H_2}^{0\ 0.5} \exp\left(-\frac{\alpha_c FV}{RT}\right) \quad (5.46)$$

where k_c/k_a can be calculated using the available thermodynamic data, or can be taken from existing tabulated data as a function of temperature. The unknowns, *p*, *F*, *V*, *R*, and *T* refer to partial pressure, Faraday's constant, cell voltage, universal gas constant, and the cell temperature, respectively. Apparent transfer coefficients (α_a and α_c) are taken to be 0.5, by considering the symmetry factor as 0.5. This relation is derived from the following expression for symmetry factor:

$$\alpha_a = 1 - \alpha_c \ ; \ \alpha_c = \beta \quad (5.47)$$

As for the aquaeous HCl electrolysis, a practical cell voltage requirement is taken into account to determine the required power for the electrolysis cell. Table 5.4 presents assumptions and range of variations for the four-step Mg-Cl cycle with required input to the system for thermodynamic and economic analyses.

5.2.2 Exergoeconomic Analysis

An exergoeconomic analysis of the Mg-Cl cycle is conducted by determining the cost rates of individual streams using component cost balance equations in connection with auxiliary equations. Since there will be a known number of exiting streams (n_e) from the components, (n_e-*1*) equations are required to determine cost rate of streams. These auxiliary equations are formed using fuel and product rules as mentioned in previous sections.

Fuel and product definitions for individual components are given in Table 5.5. The cost balance equations of individual components are provided as follows:

- **Hydrolysis reactor**

$$\dot{C}_3 - \dot{C}_2 + \dot{Z}_{hyd} = \left(\dot{C}_6 + \dot{C}_{13}\right) - \left(\dot{C}_3 + \dot{C}_4\right) \quad (5.48)$$

$$\frac{\dot{C}_3}{\dot{E}x_3} = \frac{\dot{C}_2}{\dot{E}x_2} \quad (5.49)$$

$$\frac{\dot{C}_6}{\dot{E}x_6} = \frac{\dot{C}_{13}}{\dot{E}x_{13}} \quad (5.50)$$

Table 5.4 Assumptions and system parameters used for the Mg-Cl cycle.

Variable	Unit	Range of Variations
Maximum temperature	ºC	450-550
Approach temperature	ºC	10-20
Decomposition temperature	ºC	450
Electrolysis temperature	ºC	70
Steam/Mg ratio	-	11-22
Aquaeous electrolysis voltage	V	1.8
Anhydrous electrolysis voltage	V	Eq. 7.46
Current density	kA/m^2	5
HCl utilization ratio	%	100
Symmetry factor	-	0.5
Decomposition inert gas flow rate	kmol/s	0.5-2
Cost of thermal energy	$/kWh	0.032
Cost of electricity	$/kWh	0.09
Interest rate	%	2.5-7.5
Equipment life time	Years	15-25
Plant capacity factor	%	85
Capital recovery factor	-	1.06

Table 5.5 Fuel and product definitions for individual components of the Mg-Cl cycle.

Component	Fuel	Product
Hydrolysis	$\dot{E}x_3 - \dot{E}x_2$	$(\dot{E}x_6 + \dot{E}x_{13}) - (\dot{E}x_3 + \dot{E}x_4)$
Decomposition	$\dot{E}x_{14} - \dot{E}x_{13} + \dot{E}x^Q_{dec}$	$(\dot{E}x_{16} + \dot{E}x_{24}) - \dot{E}x_{14}$
Electrolysis (aq)	$\dot{W}_{elec,aq}$	$(\dot{E}x_{11} + \dot{E}x_{22}) - \dot{E}x_7$
Electrolysis (dry)	$\dot{W}_{elec,dry}$	$(\dot{E}x_{19} + \dot{E}x_{20}) - \dot{E}x_{17}$
Separation	$\dot{E}x^Q_{sep}$	$(\dot{E}x_{6-I} + \dot{E}x_{6-II}) - \dot{E}x_6$
Chlorination	$\dot{E}x_{25} - \dot{E}x_{23}$	$(\dot{E}x_{27} + \dot{E}x_{28}) - (\dot{E}x_{24} + \dot{E}x_{25})$
Hex-1	$\dot{Ex}^Q{}_{hex1} + (\dot{E}x_{6-II} + \dot{E}x_7)$	$\dot{E}x_3 - \dot{E}x_2$
Hex-2	$\dot{E}x_{28} - \dot{E}x_{29}$	$\dot{E}x_{14} - \dot{E}x_{13}$
Hex-3	$(\dot{E}x_{6-II} - \dot{E}x_7)$	$\dot{Ex}^Q{}_{hex3}$
Hex-4	$(\dot{E}x_{16-1} - \dot{E}x_{17})$	$\dot{Ex}^Q{}_{hex4}$
Hex-5	$(\dot{E}x_{11} - \dot{E}x_{12})$	$\dot{Ex}^Q{}_{hex5}$
Hex-6	$(\dot{E}x_{20} - \dot{E}x_{21})$	$\dot{Ex}^Q{}_{hex6}$
Hex-7	$\dot{Ex}^Q{}_{hex7} + (\dot{E}x_{27} - \dot{E}x_4)$	$\dot{E}x_{25} - \dot{E}x_{23}$
Hex-8	$(\dot{E}x_{28} - \dot{E}x_{29})$	$\dot{Ex}^Q{}_{hex8}$
Hex-9	$(\dot{E}x_{27} - \dot{E}x_4)$	$\dot{Ex}^Q{}_{hex9}$

- **Decomposition reactor**

$$c_{th}\dot{E}x_{dec}^{Q} + \dot{Z}_{dec} = \left(\dot{C}_{16} + \dot{C}_{24}\right) - \dot{C}_{14} \quad (5.51)$$

- **Chlorination reactor**

$$\dot{C}_{25} - \dot{C}_{23} + \dot{Z}_{chl} = \left(\dot{C}_{27} + \dot{C}_{28}\right) - (\dot{C}_{24} + \dot{C}_{25}) \quad (5.52)$$

$$\frac{\dot{C}_{23}}{\dot{E}x_{23}} = \frac{\dot{C}_{25}}{\dot{E}x_{25}} \quad (5.53)$$

- **Aquaeous electrolysis**

$$c_{el}\dot{W}_{elec1} + \dot{Z}_{elec1} = \left(\dot{C}_{10} + \dot{C}_{11} + \dot{C}_{22}\right) - \dot{C}_{7} \quad (5.54)$$

$$\frac{\dot{C}_{10}}{\dot{E}x_{10}} = \frac{\dot{C}_{11}}{\dot{E}x_{11}} \quad (5.55)$$

- **Anhydrous electrolysis**

$$c_{el}\dot{W}_{elec2} + \dot{Z}_{elec2} = \left(\dot{C}_{19} + \dot{C}_{20}\right) - \dot{C}_{17} \quad (5.56)$$

$$\frac{\dot{C}_{19}}{\dot{E}x_{19}} = \frac{\dot{C}_{20}}{\dot{E}x_{20}} \quad (5.57)$$

- **Separation**

$$c_{th}\dot{Ex}^{Q}{}_{sep} + \dot{Z}_{sep} = \left(\dot{C}_{6-I} + \dot{C}_{6-II} + \dot{C}_{6-III}\right) - \dot{C}_{6} \quad (5.58)$$

$$\frac{\dot{C}_{6-I}}{\dot{E}x_{6-I}} = \frac{\dot{C}_{6-II}}{\dot{E}x_{6-II}} \quad (5.59)$$

- **Mixer-1**

$$\dot{C}_{10} + \dot{C}_{1} = \dot{C}_{2} \quad (5.60)$$

- **Mixer-2**

$$\dot{C}_{19} + \dot{C}_{22} = \dot{C}_{23} \quad (5.61)$$

- **Mixer-3**

$$\dot{C}_{16} + \dot{C}_{6-I} = \dot{C}_{16-I} \quad (5.62)$$

- **Hex-1**

$$c_{th}\dot{Ex}^{Q}{}_{hex1} + \dot{Z}_{hex1} = \dot{C}_{3} - \dot{C}_{2} \quad (5.63)$$

$$\frac{\dot{C}_3}{\dot{E}x_3} = \frac{\dot{C}_2}{\dot{E}x_2} \tag{5.64}$$

- **Hex-2**

$$c_{th}\dot{Ex}^{Q}{}_{hex2} + \dot{Z}_{hex2} = \dot{C}_{14} - \dot{C}_{13} \tag{5.65}$$

$$\frac{\dot{C}_{13}}{\dot{E}x_{13}} = \frac{\dot{C}_{14}}{\dot{E}x_{14}} \tag{5.66}$$

- **Hex-3**

$$c_{cw}\dot{Ex}^{Q}{}_{hex3} + \dot{Z}_{hex3} = \dot{C}_{6-II} - \dot{C}_7 \tag{5.67}$$

$$\frac{\dot{C}_{6-II}}{\dot{E}x_{6-II}} = \frac{\dot{C}_7}{\dot{E}x_7} \tag{5.68}$$

- **Hex-4**

$$c_{cw}\dot{Ex}^{Q}{}_{hex4} + \dot{Z}_{hex4} = \dot{C}_{16-I} - \dot{C}_{17} \tag{5.69}$$

- **Hex-5**

$$c_{cw}\dot{Ex}^{Q}{}_{hex5} + \dot{Z}_{hex5} = \dot{C}_{11} - \dot{C}_{12} \tag{5.70}$$

- **Hex-6**

$$c_{cw}\dot{Ex}^{Q}{}_{hex6} + \dot{Z}_{hex6} = \dot{C}_{20} - \dot{C}_{21} \tag{5.71}$$

- **Mixer-1**

$$\dot{C}_{19} + \dot{C}_{22} = \dot{C}_{23} \tag{5.72}$$

- **Hex-7**

$$c_{th}\dot{Ex}^{Q}{}_{hex7} + \dot{Z}_{hex7} = \dot{C}_{25} - \dot{C}_{23} \tag{5.73}$$

- **Hex-8**

$$c_{cw}\dot{Ex}^{Q}{}_{hex8} + \dot{Z}_{hex8} = \dot{C}_{28} - \dot{C}_{29} \tag{5.74}$$

- **Hex-9**

$$c_{cw}\dot{Ex}^{Q}{}_{hex9} + \dot{Z}_{hex9} = \dot{C}_{27} - \dot{C}_4 \tag{5.75}$$

It should be noted that the cost flow rate of water inlet to the system (state 1) is taken to be zero, cost of electricity is assumed to be 0.09$/kWh, and cost of thermal energy is 0.032$/kWh (DOE, 2010) and normalized to 2014 values. Stream exergy values are taken from Aspen Plus results, and corresponding thermal exergy values are calculated using the thermodynamic results of components. Cost balance equations form a matrix of *27x27* system and can then be solved.

The purchase equipment costs of the components are calculated based on Eq (5.27). In this equation Z_k is defined for the k^{th} component of the cycle, and it is calculated with various correlations which are defined in terms of their key parameters. Initially purchase equipment costs (PEC) of reactors can be defined as in Turton et al., (2009):

$$\log_{10} Z_R = 3.4974 + 0.4485 \log_{10} V_R + 0.1074(\log_{10} V_R)^2 \tag{5.76}$$

The above equation can be applied to any reactor in the system. Here, one of the main issues is the amount of required reactors which is calculated based on the resident time of the reactors:

$$N_r = \frac{\dot{V}_{vapor} t_r}{V_R} \tag{5.77}$$

where t_r is residence time and $\dot{V}_{vapor}$ is volumetric flow rate of vapor into the reactor, and N_r is the number of reactors. The residence times of individual reactions are taken based on the literature data (Kashani-Nejad, 2005). The reactor volumes can also be assumed based on industrial applications or can be calculated from a known reaction with known volume flow rate of vapor and residence time. It should be noted that, the PEC of separation process is taken as the sum of reactor and heat exchanger costs from the hierarchy, and they are adapted to the main system. Thus, the reaction characteristics of separation process reactors are also taken into account throughout the exergoeconomic analysis.

The cost of the electrolysis cell components are provided by Gorensek et al., (2009), and these parameters are used to calculate an approximate PEC for both dry and aquaeous electrolysis steps:

$$Z_{elec} = 1230 A_{cell} \tag{5.78}$$

where A_{cell} is the electrochemical cell area, which can be calculated using the current density and voltage of one cell.

The area of a heat exchanger can be calculated using the logarithmic mean temperature difference (LMTD) method, which leads to calculate a reasonable area of a heat exchanger. The LMTD method is as follows:

$$\Delta T_{lm} = \frac{\left((T_{H,i} - T_{C,o}) - (T_{H,o} - T_{C,i})\right)}{\ln\left(\frac{(T_{H,i} - T_{C,o})}{(T_{H,o} - T_{C,i})}\right)} \tag{5.79}$$

Here, subscripts *i*, *o*, *H*, and *C* correspond to in, out, hot, and cold, respectively. Area is now a function of mean temperature difference, heat transfer rate, and overall heat transfer coefficient as follows:

$$\mathrm{A} = \frac{\dot{Q}}{\mathrm{U}\Delta\mathrm{T}_{\mathrm{lm}}} \tag{5.80}$$

All heat exchangers with gas and liquid phases are considered to be shell-tube heat exchangers. The heat exchangers which are manipulating temperatures of solid particles are taken to be Bayonet type exchangers. For shell-tube heat exchangers PEC correlation is given as

$$\log_{10} Z_{s-t} = 4.3247 + 0.3030 \log_{10} A + 0.1634 (\log_{10} A)^2 \tag{5.81}$$

and for the Bayonet type exchangers, PEC is defined as

$$\log_{10} Z_b = 4.2768 + 0.0495 \log_{10} A + 0.1431 (\log_{10} A)^2 \tag{5.82}$$

All the above correlations are based on 2001 data, which are updated using CEPCI index as mentioned in previous subsections. Cost of the separators and mixers are not included in the exergoeconomic assessment, however, an auxiliary cost has been considered for the analysis. The EES software is used to calculate cost flow rates of the Mg-Cl cycle in connection with the auxiliary equations.

5.2.3 Optimization of Mg-Cl cycle

The thermodynamic and thermoeconomic optimization of the Mg-Cl cycle is conducted using the multi-objective NSGA optimization method of MATLAB software. It is aimed

to minimize the cost and maximize the exergy efficiency of the cycle. Thus, there are two objective functions as follows:

$$\eta_{ex} = \frac{\dot{E}x_{12}+\dot{E}x_{21}+\dot{E}x_{29}}{\dot{E}x_{1}+\dot{Q}_{in}+\dot{W}_{elec1}+\dot{W}_{elec2}} \tag{5.83}$$

$$\dot{C}_{tot} = \dot{Z} + \dot{C}_{dest} \tag{5.84}$$

Here, constraints are also taken into consideration for a feasible search space during optimization, which would lead to a more suitable solution space. The main performance influencing parameters in the cycle are the hydrolysis temperature, the steam to magnesium ratio, the decomposition temperature, and the inert gas flow rate of the decomposition reactor. Ranges of constraints are listed as follows:

- Hydrolysis temperature: $250℃ \leq T_{hyd} \leq 300℃$
- Steam/Mg ratio: $8 \leq S/Mg \leq 18$
- Decomposition temperature: $450℃ \leq T_{dec} \leq 500℃$,
- Inert gas flow rate: $3{,}600\ kmol/h \leq \dot{m}_{inert} \leq 7{,}200\ kmol/h$

The above listed parameter ranges have influence on the cycle performance characteristics as well as heating and cooling rates and size of the components which affect both cost and performance. Optimum values are obtained for minimized cost and maximized exergy efficiency.

5.3 Analysis of Integrated Systems

In this section, thermodynamic analyses of proposed systems are provided with the support of required balance equations and auxiliary tools to model all subsystems.

5.3.1 System I

The first system consists of four main subsystems in which the Mg-Cl cycle analyses are provided before. Thus, methodology and modeling of the remaining subsystems are given in this subsection.

Solar Cycle Subsystem

There are several factors to determine the optical efficiency of a heliostat plant. These factors can be listed as follows; the cosine efficiency, shadowing factor, intercept factor,

mirror reflectivity and attenuation factor (Al-Suleiman and Atif, 2015). Basic definitions to determine the field characteristics are based on Figure 5.1. The characteristic diameter is explained as follows (Collado, 2009):

$$DH = \sqrt{1 + wr^2}LH \tag{5.85}$$

Here, *DH* is heliostat diagonal, and the characteristic diameter, *DM*, is then defined as

$$DM = DH + d_{sep} \tag{5.86}$$

where *wr* is width/height ratio, *LH* is heliostat height, and d_{sep} is security distance. The radial distance in between heliostat rows are:

$$\Delta R_{min} = DMcos30^{o} \tag{5.87}$$

and the azimuthal increment as

$$\Delta\alpha z_1 = 2\sin^{-1}\left(\frac{DM}{2R_1}\right) \cong \frac{DM}{R_1} \tag{5.88}$$

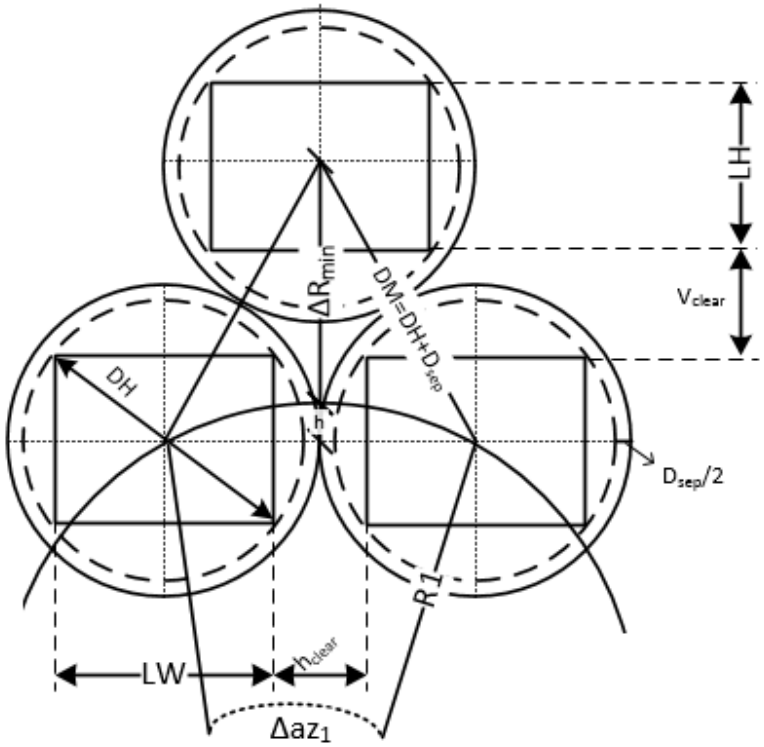

Figure 5.1 Radial and azimuthal spacing of heliostat field (Modified from Atif and Al-Suleiman, 2014).

Here, R_1 is taken to be the radius of first ring of the field. Increased ring numbers bring a higher distance between heliostats, which requires another definition for azimuthal increment for newer zones on the field:

$$\Delta\alpha z_i = \frac{\Delta\alpha z_{i-1}}{2} \tag{5.89}$$

The number of heliostats can now be calculated with the following definition for odd and even rows, respectively:

$$N_{hel,o} = \frac{2\left(\Psi_{max} - \frac{\Delta\alpha z}{2}\right)}{\Delta\alpha z} + 1 \tag{5.90}$$

$$N_{hel,e} = \frac{2\Psi_{max}}{\Delta\alpha z} + 1 \tag{5.91}$$

where Ψ_{max} stands for distance between last heliostat and north axis. The net optical efficiency of the field can now be explained as follows:

$$\eta_{opt} = \rho \cos w \, f_{at} f_{sb} f_{itc} \tag{5.92}$$

where subscripts *at*, *sb*, and *itc* stand for attenuation factor, shading and blocking factor, and intercept factor, respectively. Here, all parameters except for the attenuation factor are dependent on the co-ordinates and time, where the attenuation factor is dependent from time. The law of specular reflection is used to determine the cosine factor as follows:

$$\cos w = \hat{d}_{sun} \bullet \hat{d}_n \tag{5.93}$$

where $\hat{d}_{sun}$ is unitary sun vector and $\hat{d}_n$ is unit normal to heliostat surface. The attenuation factor is:

$$f_{at} = 0.99321 - 0.0001176 S_{rec} + 1.97 \cdot 10^{-8} S_{rec}^2 \quad if\ S_{rec} \leq 1000m \tag{5.94}$$

and

$$f_{at} = e^{(-0.0001106 S_{rec})} \quad if\ S_{rec} \geq 1000m \tag{5.95}$$

S_{rec} stands for slant distance from receiver to heliostat. Shading and blocking factor, as well as the intercept factor can be found elsewhere (Collado, 2009). In addition to optical losses, radiation and convective heat transfer losses should also be included to determine thermal efficiency of the receiver. Radiation losses are determined by the following equation

$$Q_{rad} = F_{view} A \varepsilon \sigma T_R^4 \tag{5.96}$$

where σ is Stefan-Boltzmann constant, A is receiver area, ε is emissivity factor of the receiver and F is shape factor. Here T_r stands for the receiver temperature. Convection losses and the corresponding convective heat transfer coefficient are defined as follows:

$$Q_c = A\mathrm{h_c}(T_R - T_0) \tag{5.97}$$

$$\mathrm{h_c} = 0.557 \cdot 10^{-6} \left(\frac{T_R - T_0}{H_t}\right)^{0.25} \tag{5.98}$$

Here H_t is the solar tower height. Finally, thermal efficiency of the receiver can be calculated with the flowing definition:

$$\eta_{th} = \frac{\alpha \eta_{opt} I A_h - (Q_{rad} - Q_c)}{\eta_{opt} I A_h} \tag{5.99}$$

where α is absorptivity, I is solar radiation, A_h is heliostat area. Total heat input to the field is also calculated by multiplying heliostat area, solar radiation and optical efficiency.

Table 5.6 Assumptions and data for the heliostat field analyses (Modified from Suleiman and Atif, 2015).

Variable	Symbol	Unit	Value
Latitude (Toronto)	ϕ	-	43.67 ºN
Heliostat height	LH	m	12.2
Heliostat height	LW	m	12.2
Tower optical height	THT	M	203.33
Total Number of heliostats	-	-	12722
Receiver diameter	DR	m	22.43
Receiver size	LR	m	25.21
Emissivity	ε	-	0.85
Absorptivity	α	-	0.95
Reflectivity	ρ	-	0.84
Solar irradiation	I	W/m^2	850
Std. Dev. of sun shape error	α_{sun}	mrad	2.51
Std. Dev. of tracking error	α_{tr}	mrad	1.53
Std. Dev. of surface error	α_{sl}	mrad	2

The thermal efficiency of the field is the same as the energy efficiency. The exergy efficiency of the central receiver system can be calculated with a simple multiplication of thermal exergy values of received heat to total heat input as follows:

$$\eta_{ex} = \frac{Q_{rec}(1-T_0/T_{sun})}{Q_{in}(1-T_0/T_{sun})} \tag{5.100}$$

where T_{sun} is the sun temperature and taken to be ~ 5700 K, and Q_{rec} is the receiver heat, which is the remaining heat after radiative and convective losses. This model is performed using the EES software to validate the results taken from SAM software by using the solar data for Toronto, ON. Assumptions and solar data for the solar field is given in Table 7.6.

CO_2 Gas Turbine Subsystem

The CO_2 gas turbine is modeled with recuperation and intercooling for enhanced cycle performance. The main output from the cycle is the turbine power in which the general energy and exergy efficiency definitions can be made simply by an output-input relation. Considering the state point information in Figure 3.7, one can form efficiency definitions as follows:

$$\eta_{en} = \frac{\dot{W}_{net}}{\dot{m}_{CO2}\eta_{hex}(h_{34}-h_{41})} \tag{5.101}$$

$$\eta_{ex} = \frac{\dot{W}_{net}}{\dot{E}x_{2\prime}-\dot{E}x_4} \tag{5.102}$$

The denominator in the energy efficiency definition is equal to the net power rate from the turbine, however, detailed information is given for a suitable definition of the power output in connection with the state point information. Here, subscripts *t*, *is*, and *hex* stand for turbine, isentropic, and heat exchanger, respectively. These efficiency values are assumed to be 90% for turbine and isentropic efficiencies, and 85% for the heat exchanger effectiveness. The net power output is calculated by subtracting the compression work of the supercritical fluid as follows:

$$\dot{W}_{net} = \dot{W}_t - \dot{W}_{c1} - \dot{W}_{c2} \tag{5.103}$$

One of the main issues with modeling the cycle is to determine the temperature gradient through the recuperator. For this purpose, a balance equation for this component is written as follows:

$$h_{41} - h_{40} = h_{35} - h_{36} \quad (5.104)$$

which provides a reasonable enthalpy value for the exiting stream from recuperator by assuming an approach temperature (10K). This parameter is an important influence on the cycle performance and considered as a variable during the analysis. Necessary assumptions are provided in Table 5.7.

Table 5.7 Input data and assumptions for the CO_2 Gas Turbine cycle.

Variable	Symbol	Unit	Range
Turbine inlet temperature	TIT	K	800-1100
Approach Temperature	ΔT_{app}	K	10-30
Pressure ratio	P_r	-	1.5-4.5
Compressor efficiency	η_c	-	0.85
Turbine efficiency	η_{gt}	-	0.92
Cooling water temperature	T_c	K	300

The mass, energy, entropy and exergy balances of the cycle components are presented in Table 5.8. The corresponding equations are adapted in the EES software to determine quantity and locations of irreversibilities throughout the cycle (Klein, 2008).

Hydrogen Compression Subsystem

Since the produced hydrogen from the Mg-Cl cycle is assumed to be a real gas, compressibility factor of the hydrogen should be taken into account. (Ozsaban et al., 2012). For a given thermodynamic condition, the specific heat ratio is calculated as

$$k = \frac{C_p}{C_v} \quad (5.105)$$

where *Cp* and *Cv* are specific heats at constant pressure and constant volume, respectively. The polytropic exponent is then calculated based on an assumed polytropic efficiency (90%) as follows:

$$\frac{n}{n-1} = \frac{k}{k-1}\eta_p \quad (5.106)$$

The pressure ratio for each compression stage is simply the ratio of the high and low pressure side of the individual compressor in connection with the stage number (*y*) as follows:

$$r_p = \left(\frac{P_e}{P_i}\right)^{\frac{1}{y}} \tag{5.107}$$

Table 5.8 Balance equations for the CO_2 gas turbine system.

Component	Balance Equations
GT-Hex	$\dot{m}_{2'} = \dot{m}_4; \dot{m}_{41}+\dot{m}_{34}$ $\dot{E}_{41} + \dot{E}_{2'} = \dot{E}_4+\dot{E}_{34}$ $\dot{S}_{41} + \dot{S}_{2'} + \dot{S}_{gen} = \dot{S}_{34}+\dot{S}_4$ $\dot{E}x_{41} + \dot{E}x_{2'} = \dot{E}x_{34}+\dot{E}x_4 + \dot{E}x_{dest}$
Turbine	$\dot{m}_{34} = \dot{m}_{35}$ $\dot{E}_{34} = \dot{E}_{35}+\dot{W}_t$ $\dot{S}_{34} + \dot{S}_{gen} = \dot{S}_{35}$ $\dot{E}x_{34} = \dot{E}x_{35}+\dot{W}_t + \dot{E}x_{dest}$
Compressor I	$\dot{m}_{37} = \dot{m}_{38}$ $\dot{E}_{37}+\dot{W}_{c1} = \dot{E}_{38}$ $\dot{S}_{37} + \dot{S}_{gen} = \dot{S}_{38}$ $\dot{E}x_{37}+\dot{W}_{c1} = \dot{E}x_{38} + \dot{E}x_{dest}$
Compressor II	$\dot{m}_{39} = \dot{m}_{40}$ $\dot{E}_{39}+\dot{W}_{c2} = \dot{E}_{40}$ $\dot{S}_{39} + \dot{S}_{gen} = \dot{S}_{40}$ $\dot{E}x_{39}+\dot{W}_{c2} = \dot{E}x_{40} + \dot{E}x_{dest}$
Recuperator	$\dot{m}_{40} = \dot{m}_{41}; \dot{m}_{35} = \dot{m}_{36}$ $\dot{E}_{40} + \dot{E}_{35} = \dot{E}_{41}+\dot{E}_{36}$ $\dot{S}_{40} + \dot{S}_{35} + \dot{S}_{gen} = \dot{S}_{41}+\dot{S}_{36}$ $\dot{E}x_{40} + \dot{E}x_{35} = \dot{E}x_{41}+\dot{E}x_{36} + \dot{E}x_{dest}$
Intercooler	$\dot{m}_{38} = \dot{m}_{39}; \dot{m}_{44} = \dot{m}_{45}$ $\dot{E}_{38} + \dot{E}_{44} = \dot{E}_{39}+\dot{E}_{45}$ $\dot{S}_{44} + \dot{S}_{38} + \dot{S}_{gen} = \dot{S}_{45}+\dot{S}_{39}$ $\dot{E}x_{44} + \dot{E}x_{38} = \dot{E}x_{45}+\dot{E}x_{39} + \dot{E}x_{dest}$

The compressor outlet temperature is related to polytropic exponent and pressure ratio:

$$T_e = r_p^{\frac{n-1}{n}} T_i \tag{5.108}$$

Since an intercooling process is adapted after every compression stage, the inlet temperature of any compressor is assumed to be at ambient conditions. The compressibility factor can be defined by thermopysical properties of hydrogen at the corresponding condition with the following definition:

$$\rho = \frac{100P}{ZRT} \tag{5.109}$$

where ρ is density of hydrogen, and R is the universal gas constant. The compressibility factor for a specific state is defined as

$$Z = 1 + \left(0.018041 - \frac{9.860848}{RT} - \frac{39429.61}{RT}\right)\rho + \left(0.00018 + \frac{0.93433}{RT}\right)$$
$$- \frac{0.93433\alpha}{RT}\rho^5 - \frac{24939\rho^2}{RT}(1 + \lambda\rho^2)e^{(-\lambda\rho^2)} \quad (5.110)$$

Here, the values α and λ can be found elsewhere (Ozsaban et al., 2012). The average compressibility factor can be calculated by calculating the compressibility factor at inlet and outlet conditions of any compressor. Actual work requirement of all compressors can be defined by one equation (Brown, 1997):

$$\dot{W}_{act} = \frac{\sum_{i=1}^{y} \frac{\dot{m}_{h2} Z n R_{h2} T_0 (r_p^{\frac{n-1}{n}} - 1)}{n-1}}{\eta p} \quad (5.111)$$

It is now possible to define energy and exergy efficiencies by considering main inputs and outputs to/from the subsystem:

$$\eta_{en} = \frac{\dot{E}_{H2}}{\dot{W}_{act}} \quad (5.112)$$

$$\eta_{ex} = \frac{\dot{E}x_{H2}}{\dot{W}_{act}} \quad (5.113)$$

The range of variations for the assumed data of the hydrogen compression subsystem is presented in Table 5.9.

Finally the overall efficiency assessment of system I is calculated by considering compressed hydrogen from compression subsystem, and oxygen from the Mg-Cl cycle:

$$\eta_{en,sI} = \frac{\dot{E}_{h2,c} + \dot{E}_{o2}}{\eta_{opt} I A_h} \quad (5.114)$$

$$\eta_{ex,sI} = \frac{\dot{E}x_{h2,l} + \dot{E}x_{o2}}{\dot{E}x^{Q_{solar}}} \quad (5.115)$$

Table 5.9 Input data for the hydrogen compression subsystem.

Variable	Symbol	Unit	Range
Compressed hydrogen	H_2	kg	2
Hydrogen inlet pressure	P_{in}	bar	1-100
Hydrogen compression pressure	P_{out}	bar	150-850
Compression stage	y	-	3-5
Pressure ratio	r_p	-	2.5-4

5.3.2 System II

Since the nuclear Rankine cycle is considered as one subsystem where the SCWR reactor is used as the boiler of the Rankine cycle, modeling of two subsequent subsystems are presented in this subsection.

Nuclear Steam Rankine Cycle Subsystem

The steam Rankine cycle is designed as a 4-stage-turbine system with extraction of some heat in order to provide reheating before boiling the stream where boiler of the cycle is taken to be the SCWR. The ratio of stream *3* is defined as f_1 and remaining is sent for reheating $(1-f_1)$. As for the second extraction, this ratio is defined as $(1-f_1)f_2$ and remaining as $(1-f_1)(1-f_2)$. The energy balance of feed water heater is used to calculate f_2 as follows (Klein and Nellis, 2011):

$$(1-f_1)f_2\dot{m}_w h_6 + (1-f_1)(1-f_2)\dot{m}_w h_9 = (1-f_1)\dot{m}_w h_{10} \tag{5.116}$$

Dividing the equation by $(1-f_1)m_w$:

$$f_2 h_6 + (1-f_2)\dot{m}_w h_9 = h_{10} \tag{5.117}$$

The ratio of steam extracted from the first turbine is calculated using the energy balance of the regenerator as follows:

$$f_1 h_3 + (1-f_1)h_{11} = f_1 h_{13} + (1-f_1)h_{12} \tag{5.118}$$

At the beginning of the analysis of the steam power plant, the highest pressure and the condensing pressure are set to constant values, and extraction pressures of the turbines are guessed. After obtaining energy and exergy efficiencies of the system, these values are optimized by maximizing energy and/or exergy efficiency. Constraints for the optimization and equations to calculate the optimized fraction of the extraction pressures (y_1, y_2, y_3) are defined as follows:

$$P_2 > P_3 > P_4 > P_6 > P_7 \tag{5.119}$$

subjected to

$$P_3 = P_2 - y_1(P_2 - P_7) \tag{5.120}$$

$$P_5 = P_3 - y_2(P_3 - P_7) \tag{5.121}$$

$$P_6 = P_5 - y_2(P_5 - P_7) \tag{5.122}$$

The energy and exergy efficiencies of the Rankine cycle are defined as follows:

$$\eta_{en,RC} = \frac{\dot{W}_{turbines} - \dot{W}_{pumps}}{\dot{Q}_b + \dot{Q}_{rht}} \tag{5.123}$$

$$\eta_{en,RC} = \frac{\dot{W}_{turbines} - \dot{W}_{pumps}}{E\dot{x}_1 + E\dot{x}_4 - E\dot{x}_{R2} - E\dot{x}_{R5}} \tag{5.124}$$

The balance equations required to determine component based characteristics of the SRC system are tabulated in Table 5.10.

Table 5.10 Balance equations for the SRC subsystem.

Component	Balance Equations
Reactor	$\dot{m}_1 = \dot{m}_2; \dot{m}_4 + \dot{m}_5$ $\dot{E}_1 + \dot{E}_4 + \dot{Q}_{in} = \dot{E}_2 + \dot{E}_5$ $\dot{S}_1 + \dot{S}_4 + \dot{S}_{gen} + \frac{\dot{Q}_{in}}{T_r} = \dot{S}_2 + \dot{S}_5$ $\dot{Ex}_1 + \dot{Ex}_4 + \dot{Ex}^{Q_{in}} = \dot{Ex}_2 + \dot{Ex}_5 + \dot{Ex}_{dest}$
Turbine I	$\dot{m}_2 = \dot{m}_3 + \dot{m}_4$ $\dot{E}_2 = \dot{E}_3 + \dot{E}_4 + \dot{W}_{t1}$ $\dot{S}_2 + \dot{S}_{gen} = \dot{S}_3 + \dot{S}_4$ $\dot{Ex}_2 = \dot{Ex}_3 + \dot{Ex}_4 + \dot{W}_{t1} + \dot{Ex}_{dest}$
Turbine II	$\dot{m}_5 = \dot{m}_6 + \dot{m}_7$ $\dot{E}_5 = \dot{E}_6 + \dot{E}_7 + \dot{W}_{t2}$ $\dot{S}_5 + \dot{S}_{gen} = \dot{S}_6 + \dot{S}_7$ $\dot{Ex}_5 = \dot{Ex}_6 + \dot{Ex}_7 + \dot{W}_{t2} + \dot{Ex}_{dest}$
FWH	$\dot{m}_6 + \dot{m}_9 = \dot{m}_{10}$ $\dot{E}_6 + \dot{E}_9 = \dot{E}_{10}$ $\dot{S}_6 + \dot{S}_9 + \dot{S}_{gen} = \dot{S}_{10}$ $\dot{Ex}_6 + \dot{Ex}_9 = \dot{Ex}_{10} + \dot{Ex}_{dest}$
Regenerator	$\dot{m}_{11} = \dot{m}_{12};\ \dot{m}_3 = \dot{m}_{13}$ $\dot{E}_{11} + \dot{E}_3 = \dot{E}_{12} + \dot{E}_{13}$ $\dot{S}_{11} + \dot{S}_3 + \dot{S}_{gen} = \dot{S}_{12} + \dot{S}_{13}$ $\dot{Ex}_{11} + \dot{Ex}_3 = \dot{Ex}_{12} + \dot{Ex}_{13} + \dot{Ex}_{dest}$
Condenser	$\dot{m}_7 = \dot{m}_8$ $\dot{E}_7 = \dot{E}_8 + \dot{Q}_{out}$ $\dot{S}_7 + \dot{S}_{gen} = \dot{S}_8 + \frac{\dot{Q}_{out}}{T_c}$ $\dot{Ex}_7 = \dot{Ex}_8 + \dot{Ex}^{Q_{out}} + \dot{Ex}_{dest}$
Pumps	$\dot{m}_i = \dot{m}_o$ $\dot{E}_i + \dot{W}_c = \dot{E}_o$ $\dot{S}_i + \dot{S}_{gen} = \dot{S}_o$ $\dot{Ex}_i + \dot{W}_c = \dot{Ex}_o + \dot{Ex}_{dest}$

Hydrogen Liquefaction Subsystem

The Linde-Hampson liquefaction plant is designed to liquefy all the hydrogen from the Mg-Cl cycle. Thus, liquefied hydrogen rate is set to a constant value and determination of the total mass flow of hydrogen is made based on this assumption. For this purpose, the yield of the liquid hydrogen should be known (Nandi and Sarangi, 1992) and can be calculated by solving below equations:

$$y = (h_{53} - h_{49})/(h_{53} - h_{60}) \tag{5.125}$$

and

$$h_{46} = h_{45} - (1 - y)(h_{55} - h_{54}) \tag{5.126}$$

$$h_{55} = h_{54} + \epsilon_{hex}(h_{55'} - h_{54}) \tag{5.127}$$

$$h_{48} = h_{47} - (1 - y)(h_{54} - h_{53}) \tag{5.128}$$

$$h_{54} = h_{53} + \epsilon_{hex}(h_{54'} - h_{53}) \tag{5.129}$$

$$h_{53} = h_g + \epsilon_{hex}(h_{53'} - h_g) \tag{5.130}$$

$$h_{50} = h_{49} - (1 - y)(h_{52} - h_g) \tag{5.131}$$

$$h_{51} = h_{50} \tag{5.132}$$

where ϵ_r is the heat exchanger effectiveness factor and states with indices are values for effectiveness of 1. For an assumed yield, it is possible to calculate enthalpy values of streams which leads to determination of the compression power requirement for both hydrogen and nitrogen. The work requirement of nitrogen is assumed to be 7760 kJ/kg N_2. The amount of nitrogen requirement is calculated based on the enthalpy difference of heat exchangers II and IV and the mass flow rate of the hydrogen in the cycle.

The assumptions and ranges of variations for the liquefaction cycle, as well as for the SRC subsystems are provided in Table 5.11. Since the main inputs to the cycle are hydrogen and power for compression of nitrogen and hydrogen, these amounts are taken to be the denominator for performance calculations.

Table 5.11 Assumptions and system parameters for the system II subsystems.

Variable	Symbol	Unit	Range
SRC system			
Turbine inlet temperature	TIT	K	750-900
High pressure side	P_h	bar	90-110
Turbine efficiency	η_t	%	85
Pump efficiency	η_p	-	80
Approach temperature	ΔT_{app}	ºC	10-15
Initial extraction pressure fraction	y	-	0.5
Liquefaction System			
Operating pressure	P_h	bar	7.5-15
N_2 bath temperature	-	K	65-75
Heat exchanger effectiveness	ϵ	-	0.85-1
Hydrogen liquefaction temperature	-	K	23

The main output from the system is liquid hydrogen. Thus, energy and exergy efficiencies of the cycle can be determined as follows (Kanoglu and Dincer, 2002):

$$\eta_{en,LH} = \frac{\dot{E}_{h2,l}}{\dot{E}_{H2,g}+\dot{W}_{c,H2}+\dot{W}_{c,N2}} \tag{5.133}$$

$$\eta_{ex,LH} = \frac{\dot{E}x_{h2,l}}{\dot{E}x_{H2,g}+\dot{W}_{c,H2}+\dot{W}_{c,N2}} \tag{5.134}$$

Finally, overall efficiency assessment of system II is performed by considering liquid hydrogen from the Linde-Hampson cycle, and oxygen from the Mg-Cl cycle, and calculated for energy and exergy efficiencies as follows:

$$\eta_{en,sII} = \frac{\dot{E}_{h2,l}+\dot{E}_{o2}}{\dot{Q}_b+\dot{Q}_{rht}+\dot{Q}_{mgcl}} \tag{5.135}$$

$$\eta_{ex,sII} = \frac{\dot{E}x_{h2,l}+\dot{E}x_{o2}}{\dot{E}x^{Q_b}+\dot{E}x^{Q_{rht}}+\dot{E}x^{Q_{mgcl}}} \tag{5.136}$$

The balance equations of the liquefaction cycle are tabulated in Table 5.12 in order to evaluate component based characteristics of the cycle.

Table 5.12 Component based balance equations for the Linde-Hampson hydrogen liquefaction plant.

Component	Balance Equations
Compressor	$\dot{m}_{44} = \dot{m}_{45}$ $\dot{E}_{44}+\dot{W}_c = \dot{E}_{45}$ $\dot{S}_{44} + \dot{S}_{gen} = \dot{S}_{45}$ $\dot{E}x_{44}+\dot{W}_c = \dot{E}x_{45} + \dot{E}x_{dest}$
Hex-1	$\dot{m}_{45} = \dot{m}_{46};\ \dot{m}_{54} = \dot{m}_{55}$ $\dot{E}_{45} + \dot{E}_{54} = \dot{E}_{46}+\dot{E}_{55}$ $\dot{S}_{45} + \dot{S}_{54} + \dot{S}_{gen} = \dot{S}_{46}+\dot{S}_{55}$ $\dot{E}x_{45} + \dot{E}x_{54} = \dot{E}x_{46}+\dot{E}x_{55} + \dot{E}x_{dest}$
Hex-2	$\dot{m}_{46} = \dot{m}_{47};\ \dot{m}_{56} = \dot{m}_{57}$ $\dot{E}_{46} + \dot{E}_{56} = \dot{E}_{47}+\dot{E}_{57}$ $\dot{S}_{46} + \dot{S}_{56} + \dot{S}_{gen} = \dot{S}_{47}+\dot{S}_{57}$ $\dot{E}x_{46} + \dot{E}x_{56} = \dot{E}x_{47}+\dot{E}x_{57} + \dot{E}x_{dest}$
Hex-3	$\dot{m}_{47} = \dot{m}_{48};\ \dot{m}_{53} = \dot{m}_{54}$ $\dot{E}_{47} + \dot{E}_{53} = \dot{E}_{48}+\dot{E}_{54}$ $\dot{S}_{47} + \dot{S}_{53} + \dot{S}_{gen} = \dot{S}_{48}+\dot{S}_{54}$ $\dot{E}x_{47} + \dot{E}x_{53} = \dot{E}x_{48}+\dot{E}x_{54} + \dot{E}x_{dest}$
Hex-4	$\dot{m}_{48} = \dot{m}_{49};\ \dot{m}_{58} = \dot{m}_{59}$ $\dot{E}_{48} + \dot{E}_{58} = \dot{E}_{49}+\dot{E}_{59}$ $\dot{S}_{48} + \dot{S}_{58} + \dot{S}_{gen} = \dot{S}_{49}+\dot{S}_{59}$ $\dot{E}x_{48} + \dot{E}x_{58} = \dot{E}x_{49}+\dot{E}x_{59} + \dot{E}x_{dest}$
Hex-5	$\dot{m}_{49} = \dot{m}_{50};\ \dot{m}_{52} = \dot{m}_{53}$ $\dot{E}_{49} + \dot{E}_{52} = \dot{E}_{50}+\dot{E}_{53}$ $\dot{S}_{49} + \dot{S}_{52} + \dot{S}_{gen} = \dot{S}_{50}+\dot{S}_{53}$ $\dot{E}x_{49} + \dot{E}x_{52} = \dot{E}x_{50}+\dot{E}x_{53} + \dot{E}x_{dest}$
Separator	$\dot{m}_{51} = \dot{m}_{52} + \dot{m}_{60}$ $\dot{E}_{51} = \dot{E}_{52} + \dot{E}_{60}$ $\dot{S}_{51} + \dot{S}_{gen} = \dot{S}_{52} + \dot{S}_{60}$ $\dot{E}x_{51} = \dot{E}x_{52} + \dot{E}x_{60} + \dot{E}x_{dest}$

CHAPTER 6: RESULTS AND DISCUSSION

6.1 Simulation Results

The Mg-Cl cycle is comprehensively studied using Aspen Plus software package with its extended library to evaluate chemical and physical properties of all substances present in the cycle. Preliminary studies are conducted to determine the reaction conditions for better performing reactors with better yields.

6.1.1 Reactor Simulation Results

Direct formation of pure MgO and HCl gas has been the main motivation of the hydrolysis step. In order to yield the desired products from this reaction, it is of importance to heat up the reactants before entering the reactor up to the desired temperature in order to prevent possible side reactions. The desired reaction is as follows:

$$MgCl_2 + H_2O \leftrightarrow MgO + 2HCl \tag{6.1}$$

The hydrolysis reaction at high (>550ºC) temperatures leads to higher amount of HCl production. Since the melting point of $MgCl_2$ is around 700ºC, it is not appropriate to utilize higher temperatures at the reference pressure. Lower pressure is beneficial to obtain higher amount of product gas at a lower temperature; for instance 100 kPa reference pressure leads to 86% HCl yield at 500ºC. However, it is well known that sustaining vacuum pressure for high temperature processes is very challenging, thus, keeping the reference pressure at reference conditions is more appropriate. The variations of the molar ratios of reaction gases are plotted in Figure 6.1 at various pressures and reaction temperatures. Another option for higher HCl molar ratio at lower temperatures can be considered is the steam/Mg ratio. Higher steam/Mg ratio helps increase the production of HCl at lower temperatures.

The magnesium-chloride hydrolysis is the main step for forming HCl gas for hydrogen production in the Mg-Cl cycle. There are several reactions occurring during the hydrolysis of the $MgCl_2$. Possible expected products from the hydrolysis step are formations of MgOHCl, MgO, HCl, and traces of $MgCl_2$ and MgO bonds with hydroxides. One of the chemical reactions occurring at relatively lower temperatures (<300ºC) is given as follows:

$$MgCl_{2(s)} + H_2O_{(g)} \rightarrow Mg(OH)Cl_s + HCl_g \quad (6.2)$$

This reaction is exothermic and generally occurs during controlled dehydration of $MgCl_2$ hydrates. Figure 6.2 represents the formation of HCl gas at varying reaction temperatures. It is suitable to keep this reaction at a specific reaction condition for better yields. The solid product of this reaction can then be decomposed into another solid and a gas substance with the following reaction

$$Mg(OH)Cl_s \leftrightarrow MgO_s + HCl_g \quad (6.3)$$

This reaction reaches to completion at ~800K and the HCl conversion is completed at 1 bar of reference pressure. Since the temperature of the overall decomposition needs high temperature, pressure of the reaction ambient can be manipulated for the sake of lower temperature decomposition. A higher reference pressure allows the reaction complete at lower temperatures. For instance, 200 kPa reference pressure leads the reaction to complete at ~770 K. The change of HCl partial pressure at varying pressure and temperature conditions is plotted in Figure 6.3.

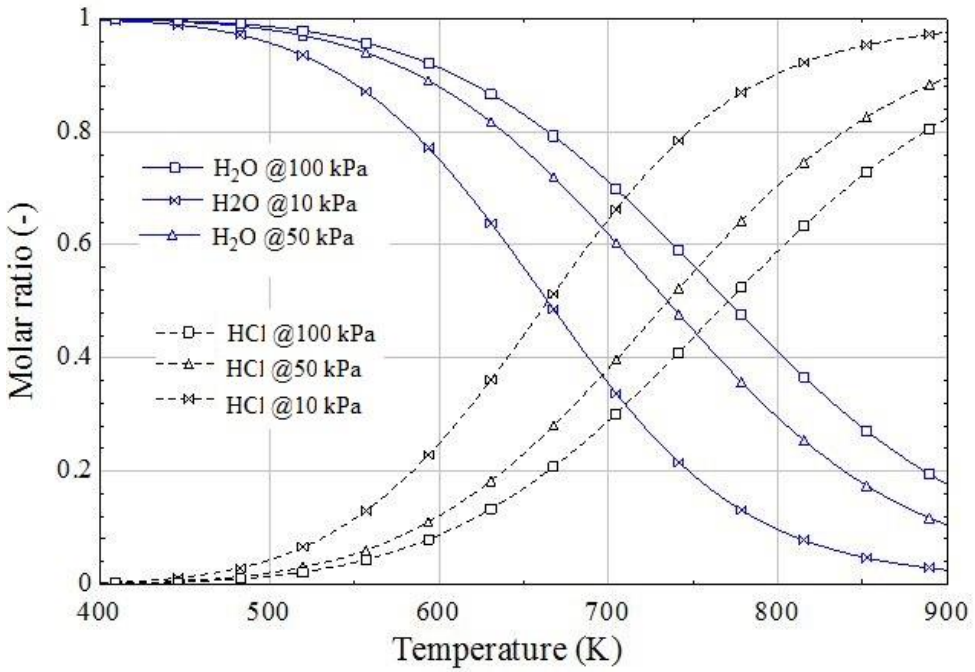

Figure 6.1 HCl formation at various reaction pressure and temperature for direct $MgCl_2$ hydrolysis.

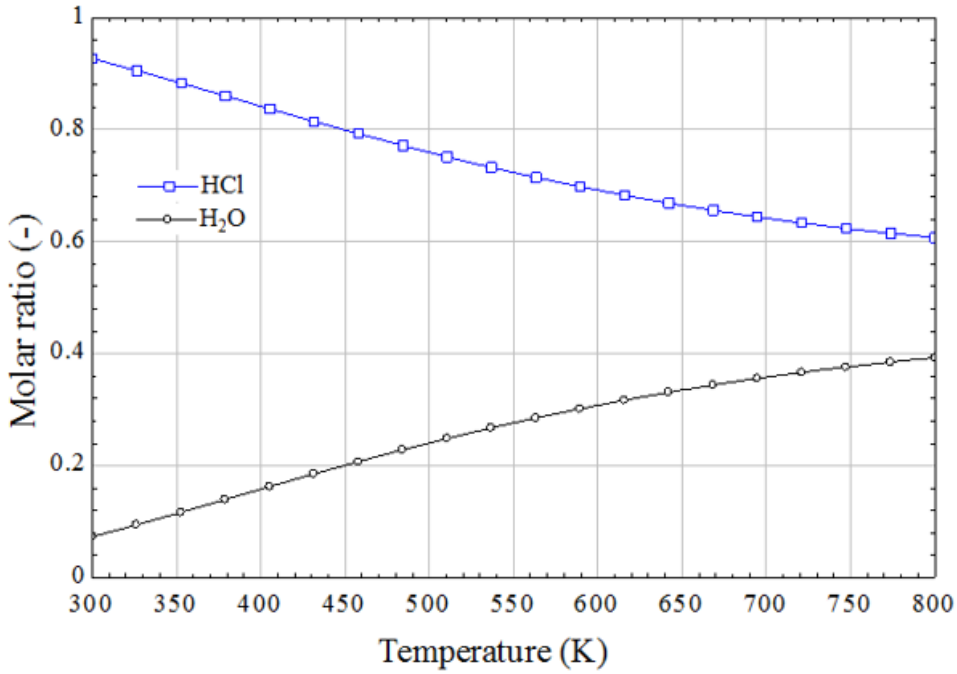

Figure 6.2 Variations of molar fractions of HCl and H_2O in MgOHCl formation reaction.

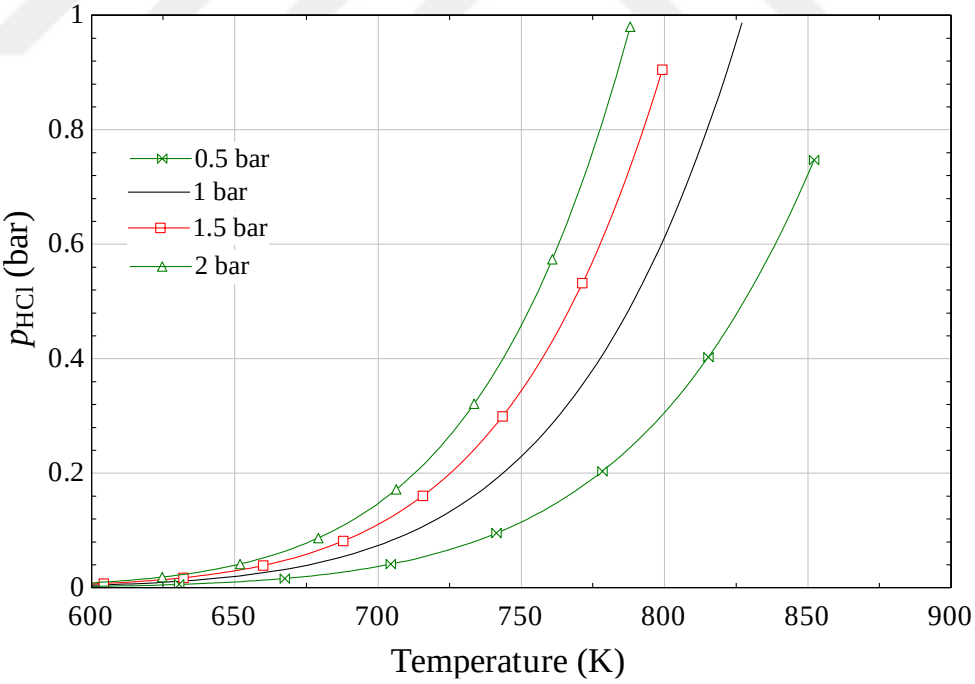

Figure 6.3 Produced HCl from MgOHCl decomposition.

Aforementioned reactions are individually presented, Thus, a total model should also be given for the possible products of $MgCl_2$ hydrolysis at several reaction conditions.

An Rgibbs type reactor is used by involving all possible products from reaction (8.1) in order to determine the interaction of the reactions. A 1 kmol/s solid reactant is fed into the Rgibbs reactor and variance of product amounts at various reactor parameters are observed. Simulation results for the hydrolysis step is shown in Figures 6.4 and 6.5 for solid and gas substances, respectively. These results are in good agreement with previously defined experimental results (Kashani-Nejad, 2005). The MgOHCl production shows the highest rate between 250-300ºC and starts converting into pure MgO particles slowly at 380ºC. The complete reaction can be obtained at a steam/Mg ratio of 1.9 for the MgOHCl production.

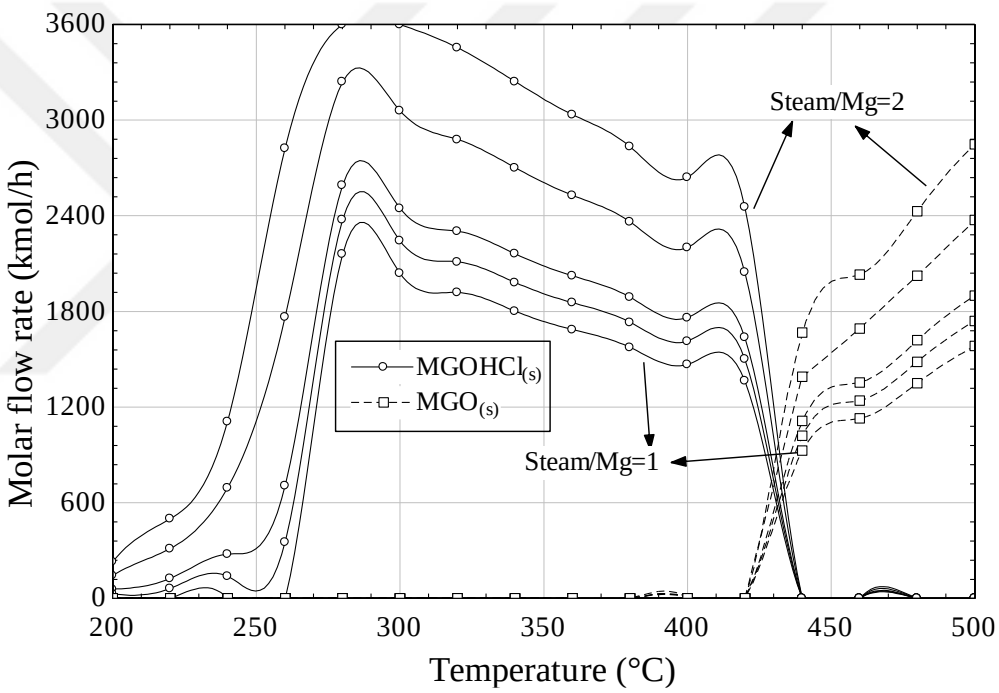

Figure 6.4 Reaction temperature and steam/Mg ratio influence on mole flow of solid products.

Previously, the steam/Mg ratio of 3.1 is specified for full conversion of $MgCl_2$ as reported in a previous work of the researchers (Ozcan and Dincer, 2014b). In order to react 1 kmole/s of $MgCl_2$ with full conversion, 3.1 kmol/s water is heated up to 537ºC. It should be noted that previously conducted experimental results show that the steam requirement is higher than the obtained results from Aspen Plus software and these results are used for the final design. MgOHCl production would require less amount of steam than that of direct MgO production. Thus, keeping the hydrolysis step at lower temperature to produce

MgOHCl, and decomposing this product in a separate reactor can lead to a less steam requiring cycle. It is also imposed that the reactivity of MgO is dependent on how the MgO is produced. The decomposed MgOHCl results in fine MgO with superior particle size, which significantly increases the reaction surface of the solid particles.

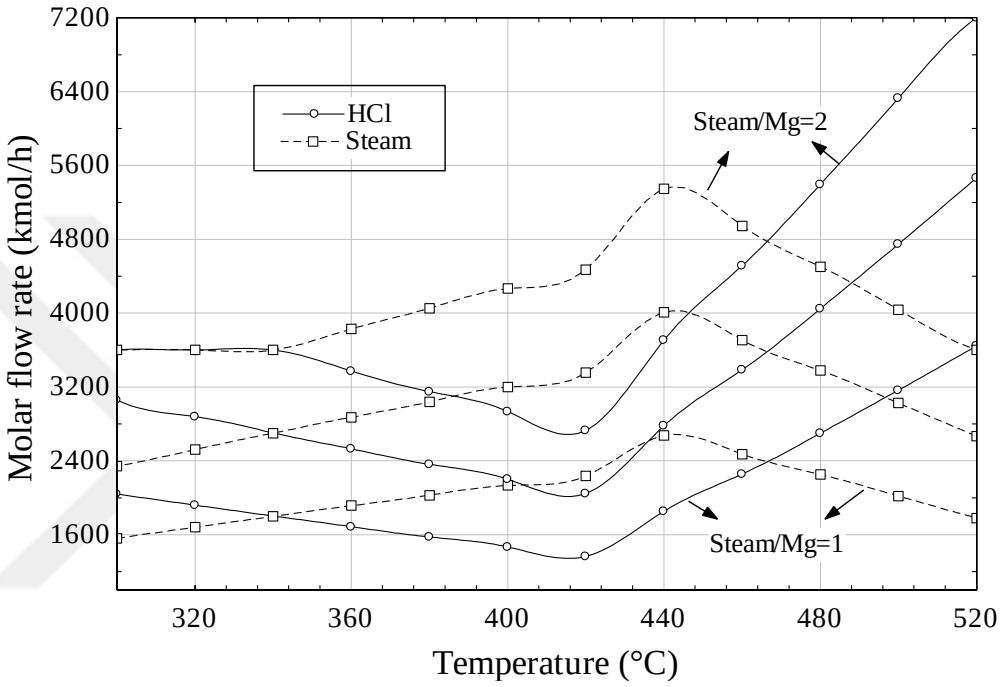

Figure 6.5 Reaction temperature and steam/magnesium ratio influence on molar flow of gaseous products.

The simulations of the decomposition step lead to production of $MgCl_2$ instead of MgO due to the reaction of produced HCl gas with produced MgO particles. Thus, it is crucial to remove the produced HCl gas from the surface of the solid particles with an inert gas. The high temperature reaction leads to a complete decomposition of MgOHCl particles. Inert gas effect on the rate of this reaction has been studied by Kashani-Nejad (2006), and the rate of the reaction is doubled by removing HCl gas from solid particle surface. Increase in inert gas flow leads to double the rate of the reaction. An inert gas at elevated pressures (i.e., Argon or Nitrogen) should be considered as the gas removing agent for the decomposition reaction.

The effects of decomposition reactor temperature and inert gas flow rate are parametrically studied and illustrated in Figures 6.6 and 6.7. At a constant 450ºC reactor temperature gas flow rate effect on MgO production is plotted in Figure 6.6. Argon gas is

selected as the inert gas which is also a favorable option as a carrier gas for the electrolysis step, and all of the MgOHCl is converted into fine MgO at gas/solid ratios higher than 1.7. Considering a constant gas flow rate and keeping it at 1 kmol/s, the reactor temperature effect is also plotted in Figure 6.7. Complete conversion of MgOHCl is accomplished at 480ºC. The inert gas flow is a very important parameter for the decomposition step to remove the HCl gas from the surface of the MgO particles in order to prevent $MgCl_2$ and steam formation due to possible reaction of MgO and HCl at higher temperatures. This variable is also a decision maker for the maximum temperature selection of the cycle. Additional inert gas compression energy and recovery of the inert gas from the electrolysis step should be considered for the overall analysis and assessment of this cycle.

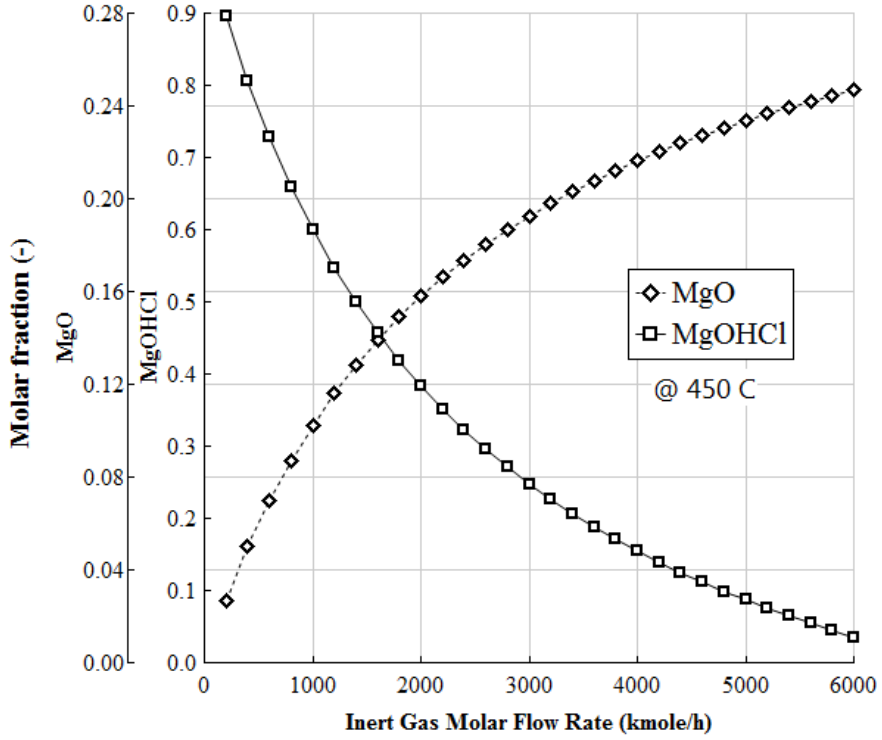

Figure 6.6 Effect of inert gas amount on products of MgOHCl decomposition reaction.

In the conventional Mg-Cl cycle, produced MgO from the hydrolysis reactions is reacted with the chlorine gas from the electrolysis step. This reaction is slightly exothermic and spontaneous at ambient temperature. Thus, kinetics of this reaction should also be considered in order to determine the range of temperature for faster production of the

desired substances. The Gibbs minimization method appears to be in good agreement with the thermochemistry data of this reaction.

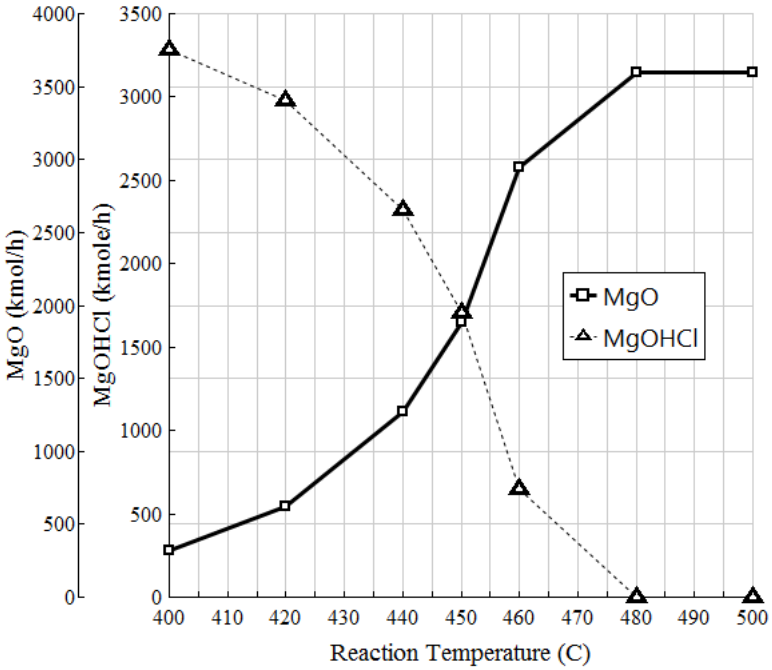

Figure 6.7 Effect of the reaction temperature on products of MgOHCl decomposition reaction at certain inert gas feed.

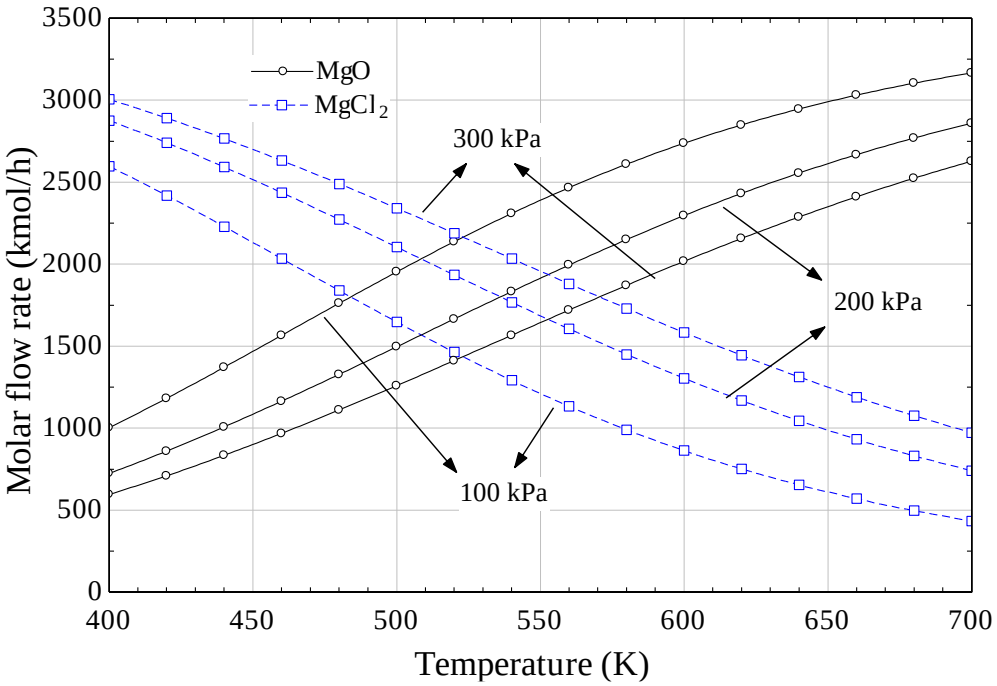

Figure 6.8 $MgCl_2$ production at varying chlorination reactor pressures and temperatures.

Figure 6.8 shows the conversion of solid particles with the chlorination reaction temperature. It is expected that higher chlorine/magnesium ratio is required to completely convert the MgO particles into $MgCl_2$, however, production rate of these two agents are one (Cl_2:MgO=1), and additional use of chlorine is not an option. As reported in the literature, the chlorination reaction at higher or elevated temperatures does not result in completion of the reaction, and hence, several other additives have been explored to complete the reaction such as carbo-chlorination (Kipouros and Sadoway, 2001). However, the reactions occur at very high temperatures with carbon containing substances. Thus, this reaction can be run at a fluidized bed by recirculating unreacted MgO particles without additives. Considering the MgCl-B cycle, the agent to be chlorinated is MgOHCl itself. The chlorination of this substance can be made with the following reaction, as mentioned in Table 3.1, as follows:

$$2Mg(OH)Cl_{(s)} + Cl_{2(g)} \rightarrow 2MgCl_{2(s)} + H_2O_g + \frac{1}{2}O_{2(g)} \quad (6.4)$$

This reaction is endothermic and requires ~51kJ heat per mole of MgOHCl at high temperatures up to 550ºC. This reaction might be feasible in terms of chlorination, however the additional heat requirement drastically increases and results in lower efficiency of the cycle. Since a decomposition process is not conducted for the MgOHCl substance, it results in less HCl for electrolysis and hydrogen production decreases for the same amount of heat input. Thus, the stoichiometry of the Mg-Cl-B cycle should be doubled for the same amount of hydrogen production. There has been no experimental study for this specific reaction, where the material behaviours and reaction kinetics are unknown. Figure 6.9 shows the variance of product mole flow rates at various reactor temperatures.

The hydro-chlorination of MgO particles with HCl gas is also another reported technique for better conversion of MgO particles into $MgCl_2$ and kinetic and experimental analysis of this reaction have been studied by Kashani-Nejad (2005). This reaction is the reverse reaction of the high temperature hydrolysis reaction, where almost 95% conversion can be succeeded at 650ºC. In the chlorination, the ash layer at the surface of reacting particles prevents the reaction. Therefore MgO particles produced directly from high temperature hydrolysis are drastically less reactive and have less surface area than decomposition of MgOHCl (Kashani-Nejad, 2005). Since the HCl gas is the main product

of hydrolysis and decomposition steps and used to produce hydrogen, it cannot be used as a reactant for the Mg-Cl cycle. However, produced MgO particles from MgOHCl decomposition step are more favorable than the ones from high temperature hydrolysis of $MgCl_2$ in terms of particle size and reactivity.

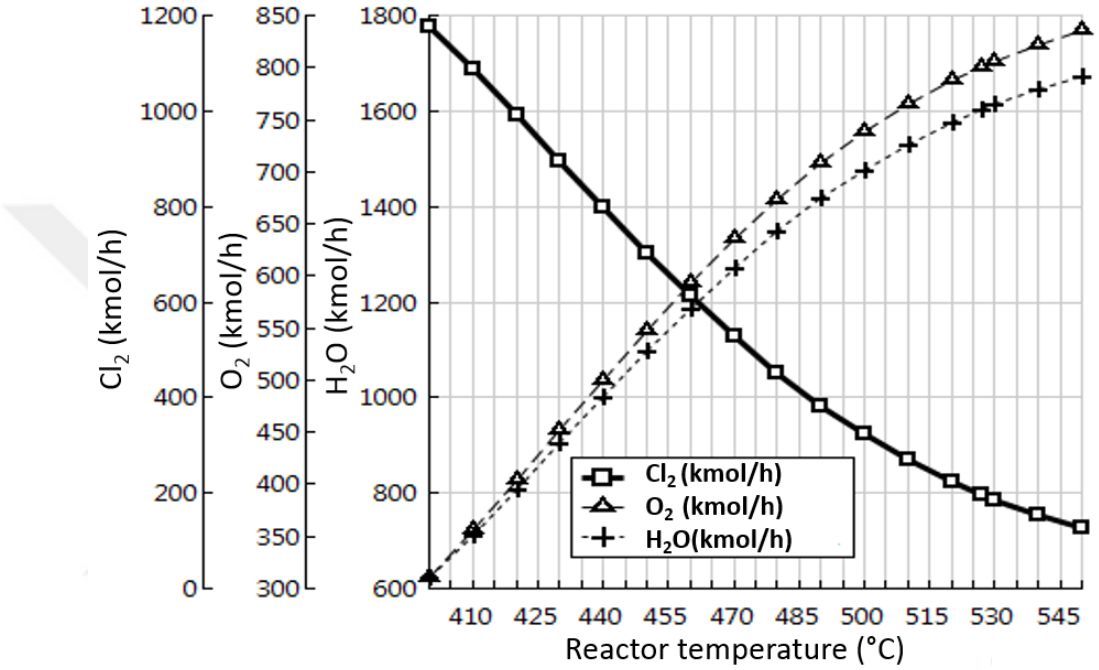

Figure 6.9 Effect of the reactor temperature on products of the reaction in Eq (6.4).

6.1.2 HCl Electrolysis Results

Ideally, the electrolysis of HCl (0.99 V) can save up to 18% electrical work compared to water electrolysis (1.23 V). However, practical aqueous HCl electrolysis needs ~1.8V at 5kA/m^2 current density, and it is a mature technology. This amount can be reduced to 1.4V by anhydrous HCl electrolysis process. Change in the equilibrium cell potential of HCl electrolysis by HCl conversion ratio is presented in Figure 6.10. Cell voltage requirement increases up to 10% with full conversion and the changes are proportional and slightly higher at every 50K increase.

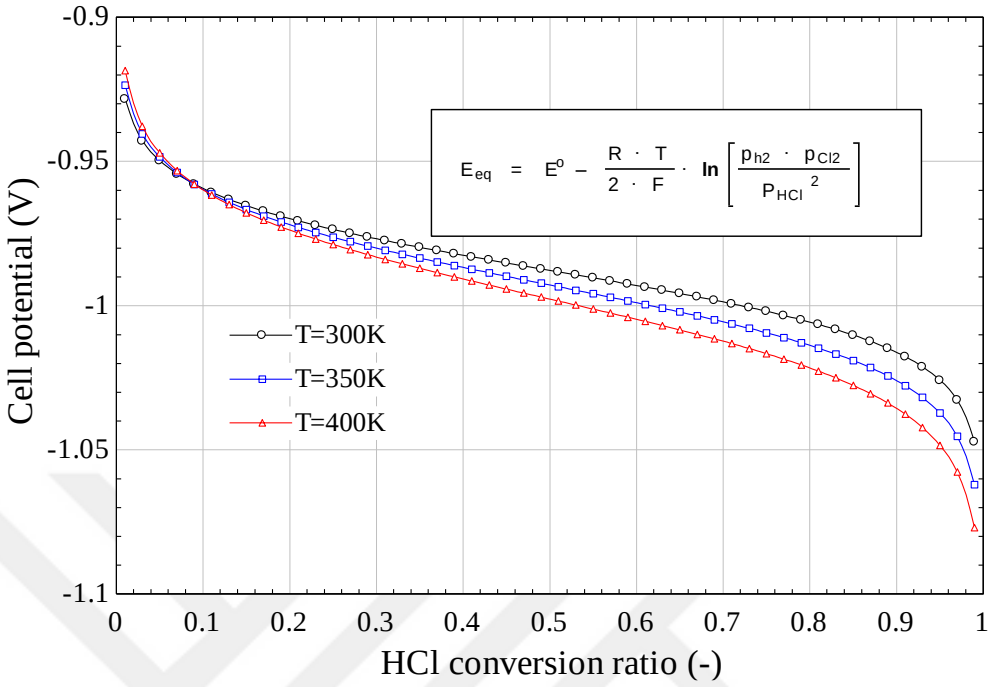

Figure 6.10 Theoretical voltage requirement of the HCl electrolysis for varying cell temperature and HCl conversion ratios.

The electrolysis of aqueous HCl has some major issues in terms of solubility of chlorine gas, and oxygen evolution. Thus, one should consider generating pure HCl gas in order to make the Mg-Cl cycle a feasible one. HCl concentration in water and cell temperature has influential effects on cell voltage as well. Lowest O_2 solubility can be obtained at high cell temperature and low concentration, as seen in Figures 6.11 and 6.12. These aforementioned parameters are key decision mechanisms for selection of electrolysis cell conditions. For the sake of lower O_2 solubility and cell voltage, cell temperature is selected as 80ºC (Alkan et al., 2005). Since the concentration of HCl may vary with the required steam for the hydrolysis reaction, oxygen solubility cannot be kept at a minimum. However, it is possible to decide on the cell temperature for better yield of hydrogen at specific cell conditions to keep the O_2 solubility at a minimum.

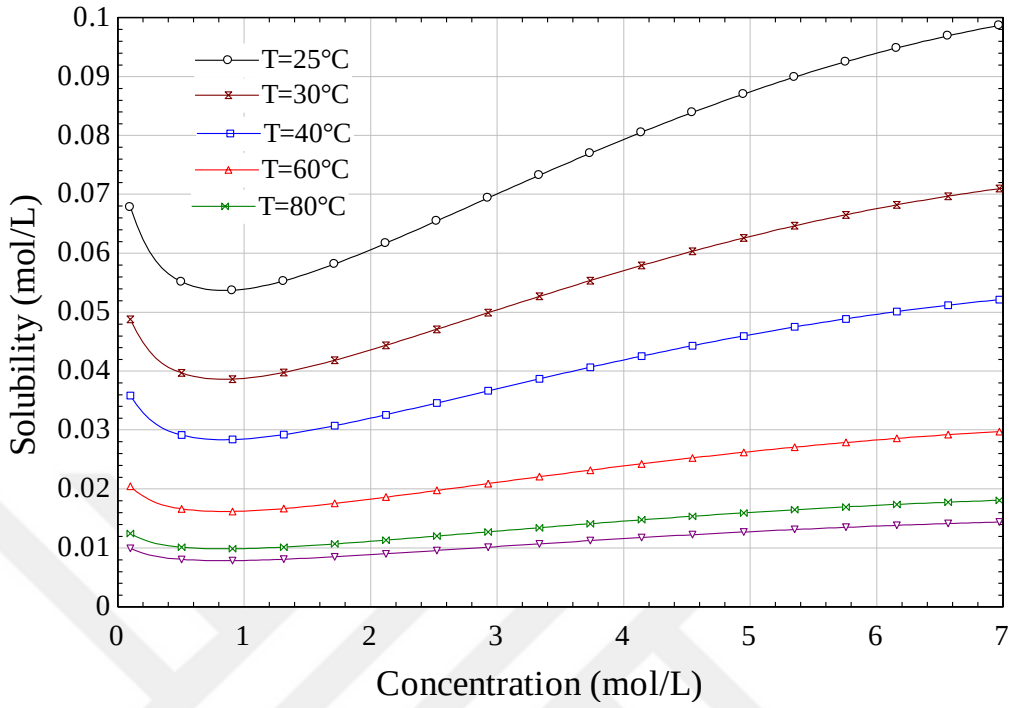

Figure 6.11 Concentration and cell temperature effect on the oxygen solubility through the aquaeous HCl electrolysis.

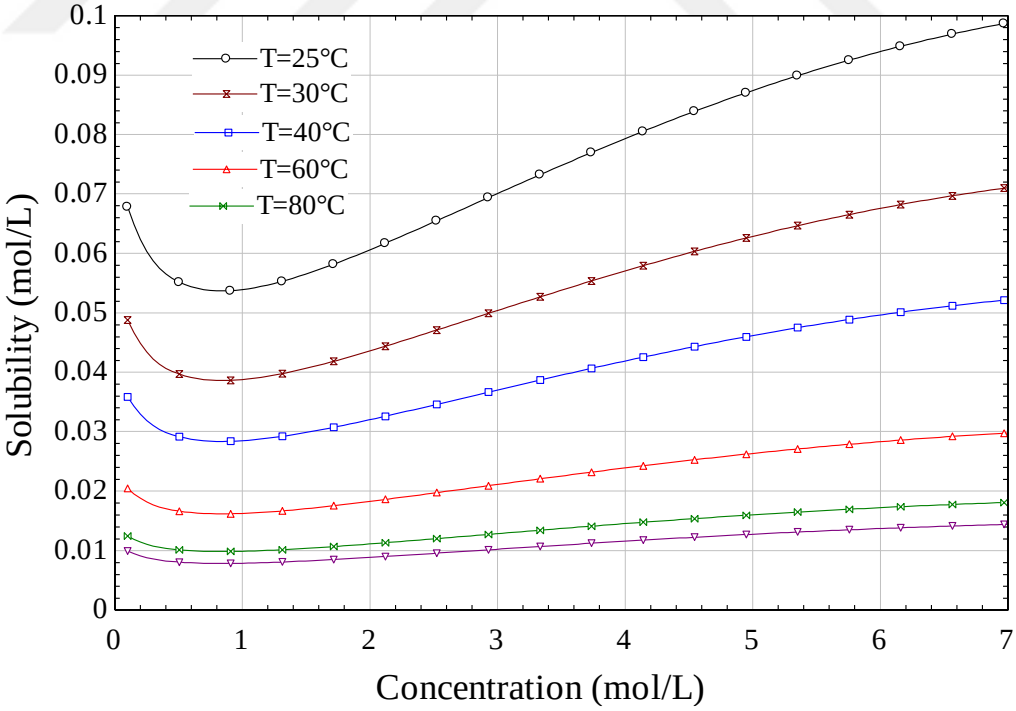

Figure 6.12 Temperature and concentration effect on the oxygen solubility through the aquaeous HCl electrolysis.

The electrochemical model for the dry HCl electrolysis has been studied and reported by Eames and Newman (1995). While the thermodynamic model is integrated with the experimental and kinetic data by taking into account the losses throughout the electrochemical cell. The proposed model is applied to dry HCl electrolysis by also considering the hydrogen production from the cell. The HCl feed is assumed to be 100% dry and all other parameters are simplified in order to result in a simpler current density calculation. Change of the current density at varying cell voltages are presented in Figure 6.13. Since the partial pressure of HCl is an influential factor on the current density of the cell, lower partial pressures, and consequently higher utilization in the cell results in very low current densities regardless of the applied voltage. However, the current density shows a similar trend up to 80% HCl utilization. The change in current density slows down after 1.6 V of applied voltage, where a limiting current density around 420-450 mA/cm^2 can be observed from the model. The models proposed by Motupally et al.,, (2001) show higher limiting current densities than that of the present model.

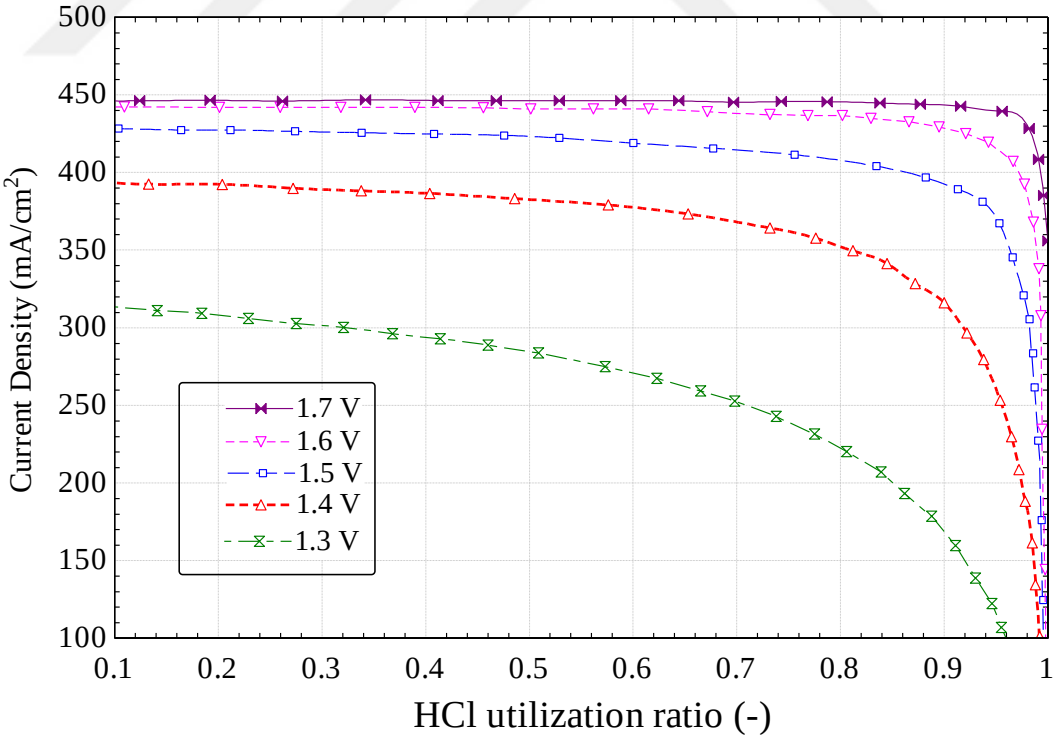

Figure 6.13 Effect of applied voltage and HCl utilization ratio on the current density of the electrochemical cell (Model taken from Eames and Newman (1995)).

Finally, a comparative representation of some hydrogen producing electrolysis methods can be made as shown in Figure 6.14. Both the theoretical and practical values are given in order to provide a prediction on the feasibility of the processes. As for the CuCl-HCl electrolysis process, there have been several reports in the range for the theoretical voltage at various HCl concentration ratios. Thus, these values are not reported in the figure.

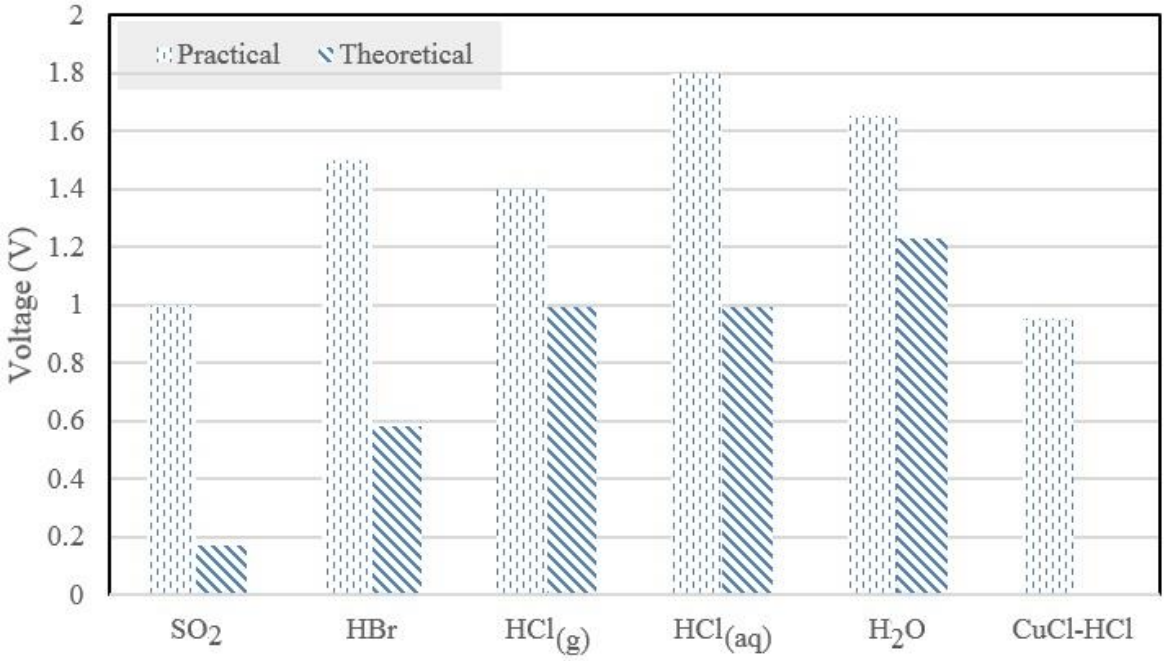

Figure 6.14 Comparison of voltage requirements of several electrolysis methods for hydrogen production (at 5 kA/m^2).

6.1.3 MgCl-A Cycle Results

The Aspen Plus results for the conventional Mg-Cl-A cycle are summarized in Tables 6.1 and 6.2. The results are given for 1 kmol/s hydrogen production from the electrolysis step. Excess water from electrolysis step is fed back to hydrolysis reactor by mixing with the external water input. Main inputs to the system are water, various grades of heat, and electrical work for the electrolysis process. In the efficiency assessment, water input and oxygen output are not included due to their negligible energy contents compared to heat and work requirements. The main output of the system is hydrogen at 25ºC, respectively.

Table 6.1 State point information for the Mg-Cl-A cycle.

State	Stream	$\dot{n}$ kmol/s	T (°C)	$\bar{h}$ (kJ/kmol)	$\bar{s}$ kJ/kmolK	$\overline{ex}_{ph}$ (kJ/kmol)	$\overline{ex}_{tot}$ (kJ/kmol)	$\dot{Ex}$ (MW)
1	H_2O	1	25.00	-285820	-163.14	-241790	3120	3.09
2	H_2O	17	67.36	-282640	-153.15	-238610	3120	55.91
3	H_2O	17	537.00	-223430	-8.78	-223430	11710	331.78
4	$MgCl_2$	1	537.00	-601120	-88.55	-840490	151860	168.92
5	Mix	19	537.00	-226700	-3.81		-	
6	H_2O/HCl	18	537.00	-207180	-0.51	-		388.63
7	H_2O/HCl	18	70.00	-259290	-128.19			289.47
8	Mix	18	70.00	-249290	-129.34	-		
9	H_2/H_2O	17	70.00	-264620	-139.88			
10	H_2O	16	70.00	-282440	-152.57	-238410	3120	53.05
11	H_2	1	70.00	1302	4.17	-240698	238490	238.55
12	H_2	1	25.00	1	0.11	-241999	238490	238.46
13	MgO	1	537.00	-577990	-63.35	-695680	59170	69.26
14	Cl_2	1	70.00	1485	4.82	-160225	117520	117.60
15	Cl_2	1	537.00	18473	35.94	-143237	117520	125.31
16	Mix	1.5	537.00	-395350	-48.60		-	
17	O_2	0.5	537.00	16173	31.29	16173	3970	5.41
18	O_2	0.5	25.00	-8	0.09	-8	3970	1.97

Considering the excess steam requirement of 17 for the conventional cycle, the boiling of a large amount of water is the most energy consuming process. However, the potential of recovering this energy by internal heat recovery, and low grade heat requirement makes it easier to provide energy for this process. Table 6.2 represents the energy balance of the conventional Mg-Cl cycle.

Table 6.2 Energy balance calculation results of the Mg-Cl-A cycle.

Component	Process	Temperature (°C)	$\Delta\bar{H}$ (kJ/mol H_2)	$\dot{W}$ (MW)
Hydrolysis	$MgCl_2$ hydrolysis	537	92.21	-
Chlorination	MgO Chlorination	537	-33.5	-
Electrolysis	$HCl_{(aq)}$ electrolysis	70	-	347.35
Hex-1	Water superheating	537	1006.4	-
Hex-2	HCl cooling	70	-937.9	-
Hex-3	Cl_2 heating	537	16.98	-
Hex-4	H_2 cooling	25	-1.3	-
Hex-5	O_2 cooling	25	-8.1	-
Total			310.85	347.35

The calculation of energy contents is performed through energy balance, considering internal heat recovery from exothermic heat exchanging components with a

heat exchanger effectiveness of 85%. Here, the chlorination reactor also shows an exothermic trend. However, this heat is not utilized as an internal heat recovery agent in order to keep the reaction at elevated temperatures, and to keep it as an isothermally driven one. The total heat requirement of this cycle results in 310.85 MJ/kmol H_2. Here it should also be noted that the heat requiring components at high temperatures are only the hydrolysis reactor and the chlorine heating exchanger. Even if the Hex-1 shows the highest heat requirement, this heat can be supplied at around the phase change temperature of water. The electrolysis power requirement is calculated based on 1.8 V requirement and results in 347.35 MW for 1 kmol/s H_2 production.

The energy efficiency of the Mg-Cl-A cycle is calculated to be 36.8% where it is drastically lower than that of theoretical calculations made under stoichiometric conditions, where previous studies reported up to 52% for the conventional cycle (Ozcan and Dincer, 2014a; 2014b). Use of excess water and consideration of practical voltage for the electrolysis cell are main efficiency reducing factors. The exergy efficiency of the cycle is also calculated by considering the exergy rate of state 12, in Table 6.1. Here, the exergy content of water input and oxygen output are also included in the calculations, where it is calculated as 44.1%. Compared to exergy efficiency values in the previous studies for stoichiometry (68%), almost 35% reduction is observed. Another important issue to be pointed out is that the energy consumption of this cycle is higher than that of conventional water electrolysis. Since most thermo-electrochemical cycles are proposed to be better performing and less power consuming alternatives than those for water electrolysis, the Mg-Cl-A cycle is not a feasible alternative based on a more practical analysis.

6.1.4 MgCl-B Cycle Results

The literature studies show that another option for the Mg-Cl cycle can be simulated by using a low temperature hydrolysis reaction. However, for the same amount of hydrogen production, stoichiometry and the required steam should be doubled. Simulation results for state point information and the energy balance of the Mg-Cl-B cycle are presented in Tables 6.3 and 6.4. The main difference between the option A and B are the hydrolysis step of the cycle. The hydrolysis reaction for option B requires lower temperatures than that of direct $MgCl_2$ hydrolysis as in option A, and this reaction is exothermic.

Table 6.3 State point information for the Mg-Cl-B cycle.

State	Stream	$\dot{n}$ kmol/s	T (ºC)	$\bar{h}$ (kJ/kmol)	$\bar{s}$ kJ/kmolK	$\overline{ex}_{ph}$ (kJ/kmol)	$\overline{ex}_{tot}$ (kJ/kmol)	$\dot{E}x$ (MW)
1	H_2O	1	25	-285820	-163.142	-33.773	3086.227	3.086
2	H_2O	22	67.8	-282600	-153.04	175.890	3295.89	72.509
3	H_2O	22	280	-233040	-22.9991	2433.74	14143.74	311.162
4	$MgCl_2$	2	280	-621940	-119.425	5438.501	157298.5	314.597
5	Mix	23	280	-268400	-31.5061			
6	H_2O/HCl	21	280	-218920	-15.5103		14322.06	300.763
7	H_2O/HCl	21	70	-262630	-131.78		13810.47	290.019
8	Mix	21	70	-254090	-132.826			
9	H_2/H_2O	20	70	-267290	-141.779			
10	H_2O	19	70	-282440	-152.569	195.502	3315.502	62.994
11	H_2	1	70	1301.857	4.171019	57.3860	238547.4	238.547
12	H_2	1	25	0.987862	0.107765	-32.633	238457.4	238.457
13	Cl_2	1	70	1484.522	4.822405	569247.4	628417.4	628.417
14	Cl_2	1	537	18473.2	35.93761	7792.224	125312.2	125.312
15	MgOHCl	2	280	-787930	-199.462	3209.706	148329.7	296.659
16	MgOHCl	2	537	-776180	-182.004	9757.192	154877.2	309.754
17	Mix	3.5	537	-405020	-46.3679			
18	O_2	0.5	537	16173.08	31.29298	16174.96	20144.96	10.072
19	O_2	0.5	25	-7.95734	0.088981	-32.592	3937.408	1.968
20	Mix	3	537	-475220	-61.9581			
21	$MgCl_2$	2	537	-601120	-88.5468	17056.94	168916.9	337.833
22	H_2O	1	537	-223430	-8.7809	7806.704	19516.7	19.5167

The chlorination reaction for of MgOHCl is a highly endothermic one, and results in steam production at high temperature in mixture with oxygen. The separation process of these substances might be challenging and can prevent reuse of the steam in the cycle. Thus, an additional drying process for water separation from oxygen would be required, in order to recirculate the water content after chlorination. For the reaction chain inside the reactor, one can guess that a possible MgOHCl decomposition is initially required to liberate HCl gas first. This may cause mixture of HCl in the outlet stream. However, previous information for reaction kinetics of MgO and HCl shows that this reaction is more feasible and faster than MgO chlorination with a very good conversion of MgO into $MgCl_2$ (Kashani-Nejad 2005).

Table 6.4 Energy balance calculations results of the Mg-Cl-B cycle.

Component	Process	Temperature (°C)	$\Delta\bar{H}$ (MJ/kmol H_2)	$\dot{W}$ (MW)
Hydrolysis	$MgCl_2$ hydrolysis	280	-35.6	-
Chlorination	MgOHCl Chlorination	537	116.3	-
Electrolysis	$HCl_{(aq)}$ electrolysis	70	-	347.35
Hex-1	Water superheating	280	1040.8	-
Hex-2	HCl cooling	70	-817.8	-
Hex-3	Cl_2 heating	537	16.98	-
Hex-4	H_2 cooling	25	-1.3	-
Hex-5	O_2 cooling	25	-8.1	-
Hex-6	MgOHCl heating	537	23.5	
Hex-7	$MgCl_2$ cooling	280	-41.7	
Total			459.02	347.35

The energy balance results of the cycle show a relatively higher energy requirement than that of the Mg-Cl-A, mainly due to energy intensive phase change process for larger amount of required water. The endothermic reactor of this cycle also requires 20.5% more heat than the hydrolysis reaction of the Mg-C-A cycle at elevated temperatures. Energy and exergy efficiencies of this option are 30% and 37.7%, respectively. Considering the electrolysis process, the practical voltage requirement is at the same range of the Mg-Cl-A cycle and highly energy intensive. In the thermodynamic point of view, the Mg-Cl-B cycle does not show any promising performance either for heat requirement or power consumption. However, further investigations can be made to enhance cycle performance and reduce energy requirements by capturing the HCl in dry form, developing less steam requiring hydrolysis reactor configurations, and by investigating temperature dependence and reaction characteristics of the MgOHCl chlorination process.

6.1.5 MgCl-C Cycle Results

The newly developed four-step Mg-Cl cycle is named as the Mg-Cl-C cycle as mentioned previously. The main idea behind the four-step option is to capture HCl in dry form with an additional step to decompose MgOHCl into solid and gas substances at elevated temperatures. Table 6.5 and 6.6 represent the state point information and the energy balance for the four-step cycle.

Table 6.5 State point information for the Mg-Cl-C cycle.

State	Stream	$\dot{n}$ kmol/s	T (°C)	$\bar{h}$ (kJ/kmol)	$\bar{s}$ kJ/kmolK	$\overline{ex}_{ph}$ (kJ/kmol)	$\overline{ex}_{tot}$ (kJ/kmol)	$\dot{Ex}$ (MW)
1	H_2O	1	25	-285820	-163.142	-33.773	3086.227	3.086
2	H_2O	11	65.9	-282750	-153.471	154.298	3274.298	36.017
3	H_2O	11	280	-233040	-22.9991	2433.744	14143.74	155.581
4	$MgCl_2$	1	280	-621940	-119.425	5438.501	157298.5	157.298
5	Mix	12	280	-266930	-31.1178			
6	H_2O/HCl	11	280	-219570	-15.8138		13762.5	151.387
7	H_2O/HCl	11	70	-263540	-132.758	-	13192	145.112
8	Mix	11	70	-255400	-133.775		-	-
9	H_2/H_2O	10.5	70	-268010	-142.293		-	-
10	H_2O	10	70	-282440	-152.569	195.502	3315.502	33.155
11	H_2	0.5	70	1301.857	4.171019	57.386	238547.4	119.273
12	H_2	0.5	25	0.987862	0.107765	-32.633	238457.4	119.228
13	MgOHCl	1	280	-787930	-199.462	3209.706	148329.7	148.329
14	MgOHCl	1	450	-780160	-187.201	7326.017	152446	152.446
15	Mix	2	450	-331050	-16.4064	-	-	-
16	HCl	1	450	-79812.6	36.14458	4729.485	90679.49	90.679
17	HCl	1	70	-91027.6	14.17917	60.197	86010.2	86.01
18	Mix	1	70	1406.357	10.28291	-	-	-
19	Cl_2	0.5	70	1484.522	4.822405	75.877	117595.9	58.797
20	H_2	0.5	70	1301.857	4.171019	57.386	238547.4	119.273
21	H_2	0.5	25	0.987862	0.107765	-32.633	238458.4	119.229
22	Cl_2	0.5	70	1484.522	4.822405	75.877	117595.9	58.797
23	Cl_2	1	70	1484.522	4.822405	75.877	117595.9	117.595
24	MgO	1	450	-582290	-68.9573	7459.278	66629.28	66.629
25	Cl_2	1	500	17097.69	34.19978	6934.588	124454.6	124.454
26	Mix	1.5	500	-397800	-51.694	-	-	-
27	$MgCl_2$	1	500	-604170	-92.4003	15155.3	167015.3	167.015
28	O_2	0.5	500	14926.99	29.71871	6072.696	10042.7	5.021
29	O_2	0.5	25	-7.95734	0.088981	-32.592	3937.408	1.968

This cycle can be considered as a mixture of options A and B in terms of reactions throughout the cycle. The hydrolysis reaction is the same as option B, and the chlorination reaction is the same as option A. The main differing part of the cycle is the decomposition of MgOHCl in a separate reactor. Electrolysis is made in two different cells, one for aqueous and one for anhydrous HCl, coming from different streams. Here the only endothermic reaction is the decomposition reaction with a relatively high heat requirement

(118.1 MJ/kmol H_2). Reactivity of MgO with chlorine has been previously reported to be low when it is produced from direct hydrolysis of $MgCl_2$. MgO from $Mg(OH)_2$ and MgOHCl decomposition shows significantly higher reactivity than the previously mentioned chlorination method. Thus, this cycle is also promising in terms of achieving better reaction kinetics in the most challenging process of the cycle. A complete experimental study to hydrolyze $MgCl_2$ in to MgOHCl, decompose MgOHCl into MgO and HCl, and chlorination of MgO can be conducted in a future work.

Table 6.6 Energy balance calculations of the Mg-Cl-C cycle.

Component	Process	Temperature (ºC)	ΔH (MJ/kmol H_2)	$\dot{W}$ (MW)
Hydrolysis	$MgCl_2$ hydrolysis	280	-17.82	-
Chlorination	MgO Chlorination	500	-31.51	-
Decomposition	MgOHCl Decomposition	450	118.1	-
Electrolysis$_{(aq)}$	$HCl_{(aq)}$ electrolysis	70	-	173.67
Electrolysis$_{(dry)}$	$HCl_{(dry)}$ electrolysis	70	-	135.08
Hex-1	Water superheating	280	546.8	-
Hex-2	MgOHCl heating	450	7.8	-
Hex-3	$HCl_{(aq)}$ cooling	70	-483.8	-
Hex-4	$HCl_{(dry)}$ cooling	70	-11.2	-
Hex-5	H_2 cooling	25	-0.65	-
Hex-6	H_2 cooling	25	-0.65	-
Hex-7	Cl_2 heating	500	15.61	-
Hex-8	O_2 cooling	25	-7.46	-
Hex-9	$MgCl_2$ cooling	280	-17.8	-
Total			244.98	308.75

Since the required steam is lower than direct hydrolysis at elevated temperatures, energy requirement for water superheating is significantly lower than the previous options, and recovery potential is also higher due to internal heat exchanging process. Using the same method for the previous options, a total external heat requirement for this cycle is found to be 244.98 MJ/kmol H_2, which is 21.3% lower than the option A, and almost 47% lower than that of the option B. Electrical work requirement is also lower than previous two options due to lower voltage requirement of dry HCl electrolysis. Electrical wok consumption of option C is 11.2% lower than the previous options and it also shows lower voltage requirement than that of water electrolysis by 3.1%. The calculated energy and exergy efficiencies are 43.7% and 52%, respectively.

6.1.6 Efficiency Comparison of Cycle Configurations

A simple comparison between all cycles and the previous theoretical calculation results can be made by matching heat and power loads of the cycles as well as their efficiencies. Figure 6.15 shows the energy load comparison of the cycles. The theoretical cycle is calculated using the Aspen Plus results for required excess steam and theoretical voltage requirement for HCl electrolysis as in Ozcan and Dincer (2014a). A previous research has been conducted to optimize the maximum cycle temperature by manipulating the excess steam rate into hydrolysis reactor. The heat and power requirement remains the lowest compared to practical applications of the cycle. The highest requirement belongs to Mg-Cl-B cycle due to double stoichiometry and a very high steam requirement. The energy requirement of the four-step cycle is the lowest among all considered cycles with the same internal heat recovery assumption. This energy requirement can be further decreased with more efficient reactor configurations which would lead to a less steam requirement to convert solid reactants into desired products. Lower stream requirement is also favorable for electrolysis of HCl at higher concentrations. However, for this mature technology, optimum concentration of HCl in the aqueous electrolysis is around 18-22%, which corresponds to a steam/HCl molar ratio of 10-11. If the electrolysis is desired to be made at gaseous phase, higher concentrations can be beneficial with higher utilization of HCl in more compact cells. However, this is not a known procedure and further studies should be conducted.

Comparison of energy and exergy efficiencies shows that the four-step option is also promising in terms of system performance having the potential to be further enhanced by further studies (Figure 6.16). Since the power consumption of this cycle is lower than the direct water electrolysis, further studies should be conducted for various configurations of the four-step cycle. The four-step cycle carries the potential to be more than 55% efficient with proper HCl electrolysis at the desired voltage values. Since one of the major energy consuming devices is the aqueous electrolysis step, a proper dry HCl capturing process can be a promising option for reduced power consumption of the cycle. The HCl capturing process can be another energy intensive process which is expected to contribute to the total thermal energy of the cycle.

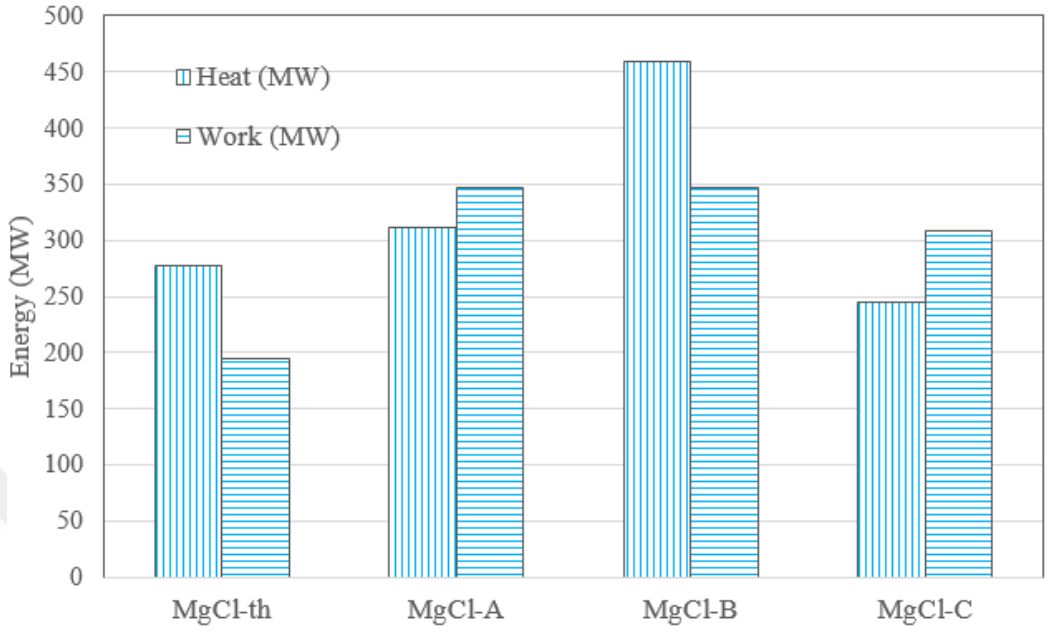

Figure 6.15 Energy load comparison of the Mg-Cl cycle options (*th*: theoretical calculations with Aspen yields).

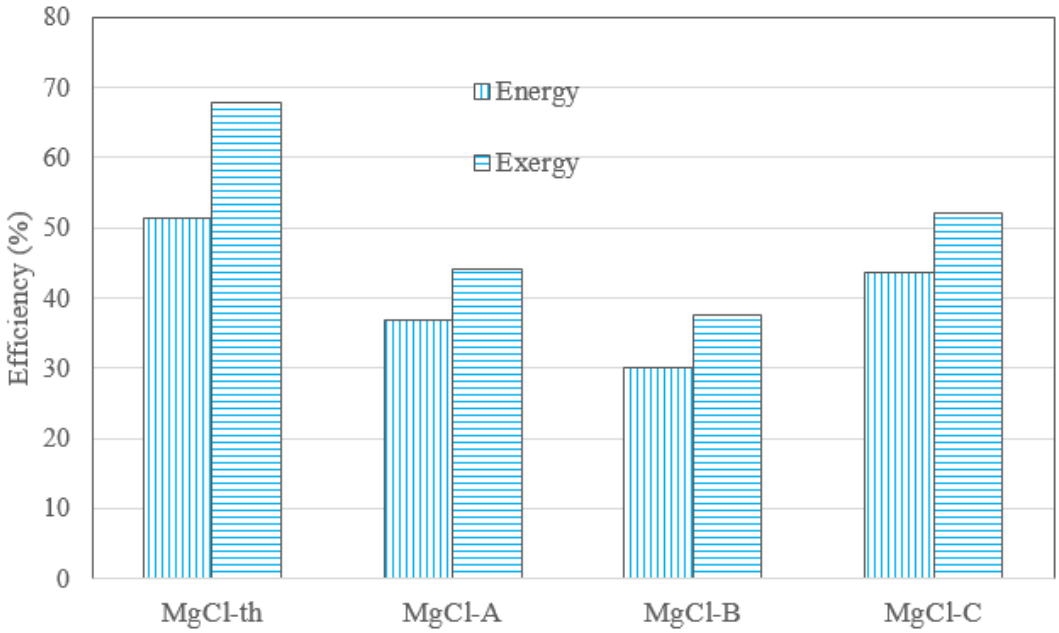

Figure 6.16 Efficiency comparison of the Mg-Cl cycle options (*th*: theoretical calculations with Aspen yields).

Exergy efficiency values for all cycles are calculated based on thermal exergy input. Thus, the heat exchanger effectiveness and the maximum cycle temperature are two main parameters influencing cycle efficiencies. Thermal exergy input to all cycles are strongly

influenced by the sink and source temperatures. Higher reference temperature and lower maximum temperature result in better exergetic efficiencies. However, manipulation of both parameters are not suggested due to their uncontrollable nature. Chemical reactions occur at a specific temperature range for the best possible yield, and changing this parameter would only vary the thermal exergy input, but changes in energy content of the streams cannot be kept constant. Variations of these parameters and their effects on exergy efficiencies are illustrated in Figure 6.17.

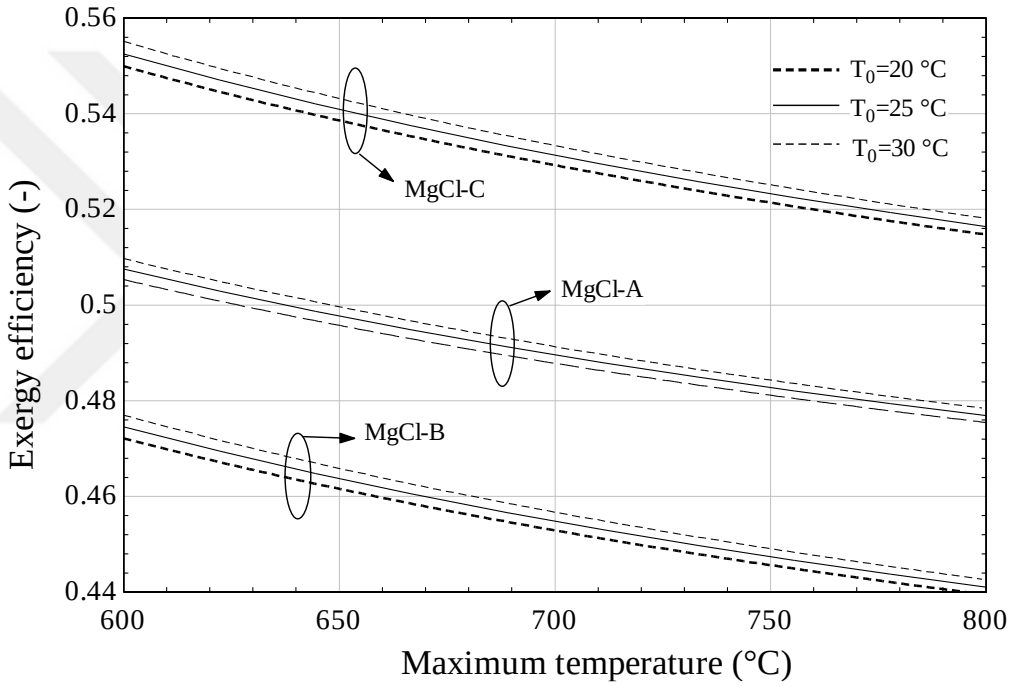

Figure 6.17 Effect of the cycle maximum temperature and ambient temperature on the exergy efficiencies.

Since all calculations are made based on a heat exchanger effectiveness assumption, effect of this parameter is also shown in Figure 6.18. As an expected outcome, increase of this factor has a significant effect on efficiencies. In a perfect case with full internal heat recovery within all cycles, up to 36% increase in the energy efficiency and 25% increase in the exergy efficiency can be observed. It should be noted that the Mg-Cl-B cycle is the one most effected by the heat exchanger effectiveness factor due to high heat loads of the cycle.

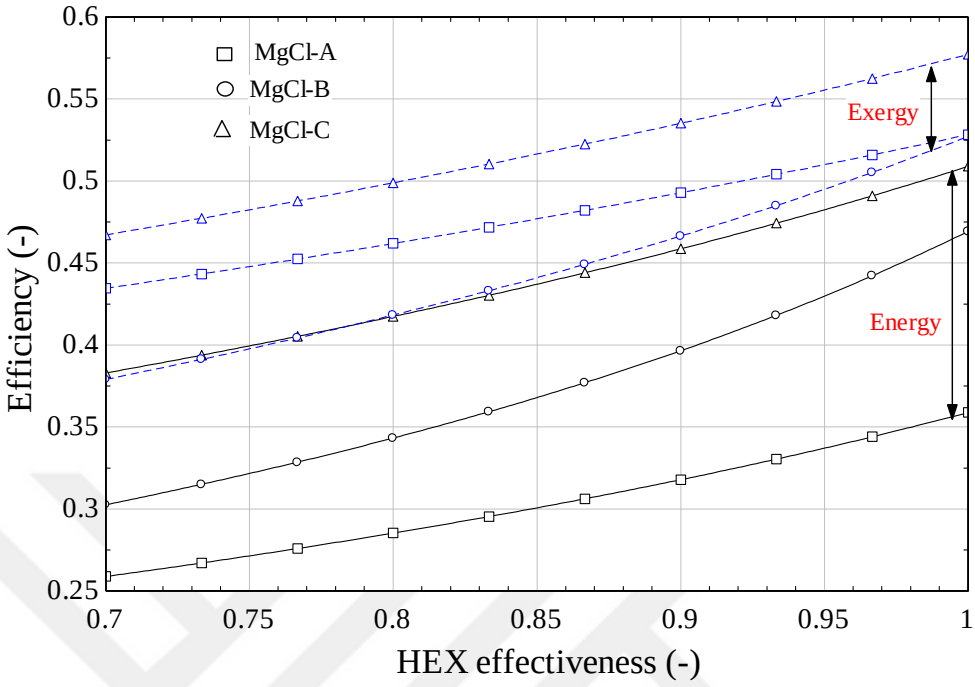

Figure 6.18 Effect of the heat exchanger effectiveness on cycles efficiencies.

6.2 Experimental Results

The main motivation of experimental studies is to capture HCl in dry form for reduced power consumption from the electrolysis step of the four-step Mg-Cl cycle. With known chemistry of the Mg based oxides and chlorides, two experimental procedures are developed. The first method is to capture HCl using $MgCl_2$, and the second method is HCl capture using MgO. This section provides a comprehensive discussion on the results from both experiments.

6.2.1 $MgCl_2$ Hydration Experiment Results

A specified amount of pure $MgCl_2$ particles are weighed in a glove box under nitrogen environment, where the experiments are conducted under the same condition. Prepared solid samples are placed among distributor layers in a vertical reactor. 5.5 M HCl is fed to the reactor at a constant rate using a syringe pump considering the residence time. The first challenge encountered is the rapid formation of $MgCl_2$ hydrates. Solidified powder did not let the liquid feed react with the remaining powder in the reactor. Thus, a better interaction of liquid-powder is provided by locating adequately large holes from top layer to bottom

layer where all of the powder could react with the liquid feed. Figure 6.19 shows unreacted and reacted powder through the experiment.

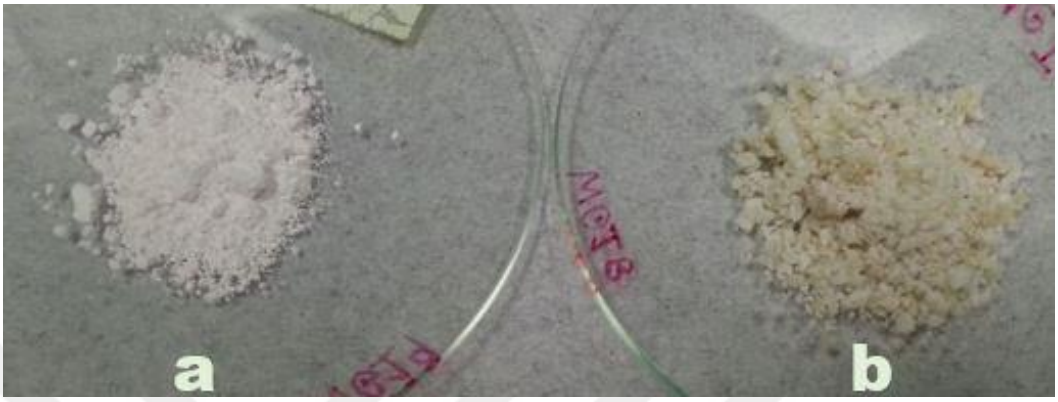

Figure 6.19 Image of (a) pure $MgCl_2$ and (b) reacted particles (with an expected chemical structure of $MgCl_2 \cdot nH_2O \cdot mHCl$)

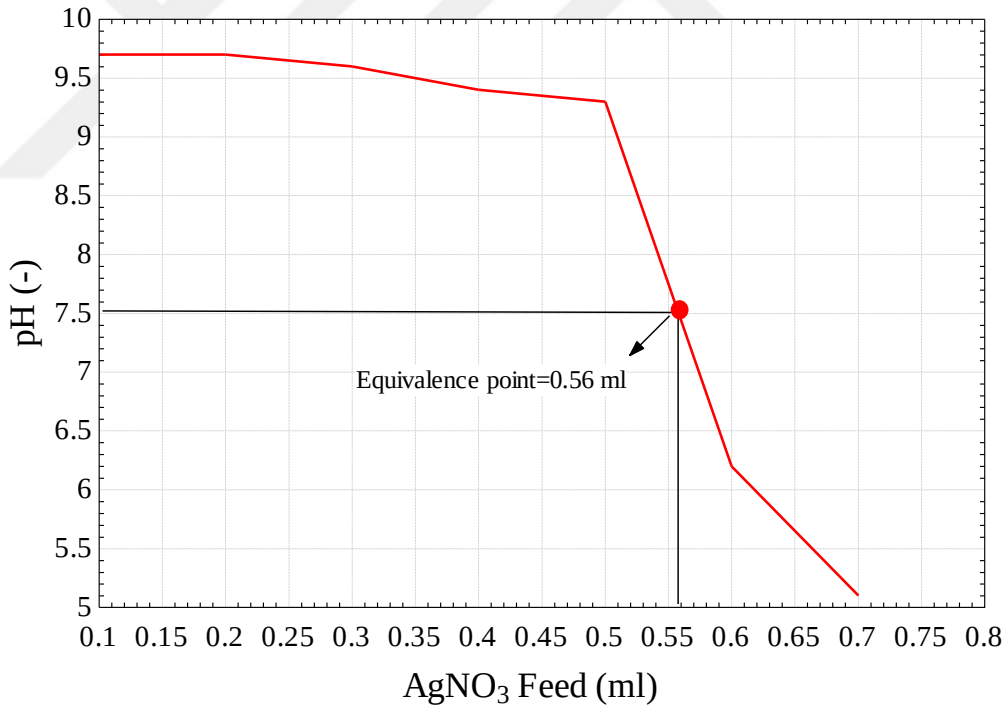

Figure 6.20 Precipitation titration result for the collected sample at the bottom of the reaction vessel.

The liquid collected in the NaOH solution is first analysed with a pH meter where the results are found to be misleading due to captured H_2O by the powder, and produced H_2O from reaction of NaOH and HCl. Thus, precipitation titration method is used to analyse the HCl content of the liquid. Figure 6.20 shows the titration result of a 5 ml sample

reacted with 1M $AgNO_3$. Rapid change in the pH of the solution is observed at 0.56 ml of $AgNO_3$ feed to the NaCl solution, which corresponded to ~4.2M solution. The molar amount of captured Cl^- ions corresponds to 0.021 moles in 5 ml sample, which means only 0.006 moles are captured by $MgCl_2$ for every 5 ml feed. Considering a 5.5M feed, the amount of captured HCl is not at a promising rate. In addition, HCl is captured by $MgCl_2$ with H_2O which makes this procedure meaningless. Since the method does not seem to be promising, no more tests have been conducted to determine the structure of the solid product from the reaction vessel.

6.2.2 Hydrochlorination Experiment Results

As mentioned in the analysis of the four-step Mg-Cl cycle, HCl gas is in mixture with steam after the hydrolysis reactor, and it leads to aqueous HCl electrolysis resulting in a higher voltage requirement. Another solid-gas reaction option is considered by using MgO as the HCl capturing agent. The thermochemistry and kinetics studies in the literature superimpose that the high temperature reaction of MgO and HCl leads to production of $MgCl_2$. However, there have not been a specific study on what products would be observed at lower temperature reaction of these substances when HCl is in mixture with steam.

TGA/DTA Results

In order to initiate the experiments, a simple mixing process has been applied at ambient temperature under fume hood. Pure MgO is mixed with 5.5 M HCl, and the mixture is stirred until all solid particles are reacted with the liquid. The sample was than analysed using thermogravimetric and differential thermal analysis (TG/DTA). A Hitachi-STA 7300 TGA/DTA device with uncertainty values of 0.2 µg for TGA, and a 0.06 µV for DTA is used for testing the sample under nitrogen environment. A random 16.5 mg wet sample is first heated up to 120ºC and the temperature is kept at this rate around 20 minutes for a fully dried sample, as shown in Figure 6.21. In a total of 30 minutes, the sample lost 43.7% of its weight which corresponds to the unreacted water and HCl content.

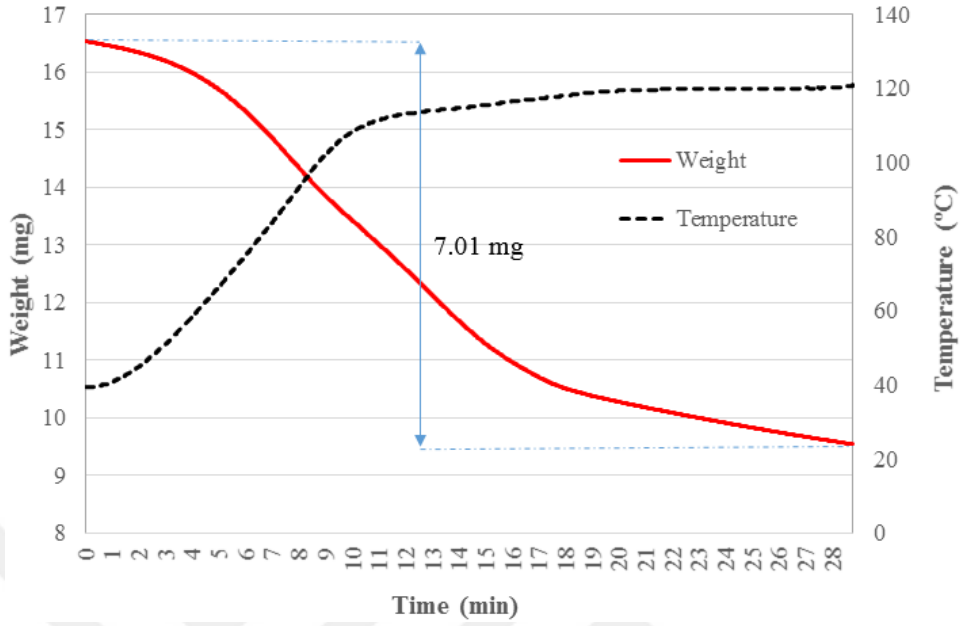

Figure 6.21 Variations of temperature and weight of the sample until 120ºC at 10ºC/min heating rate.

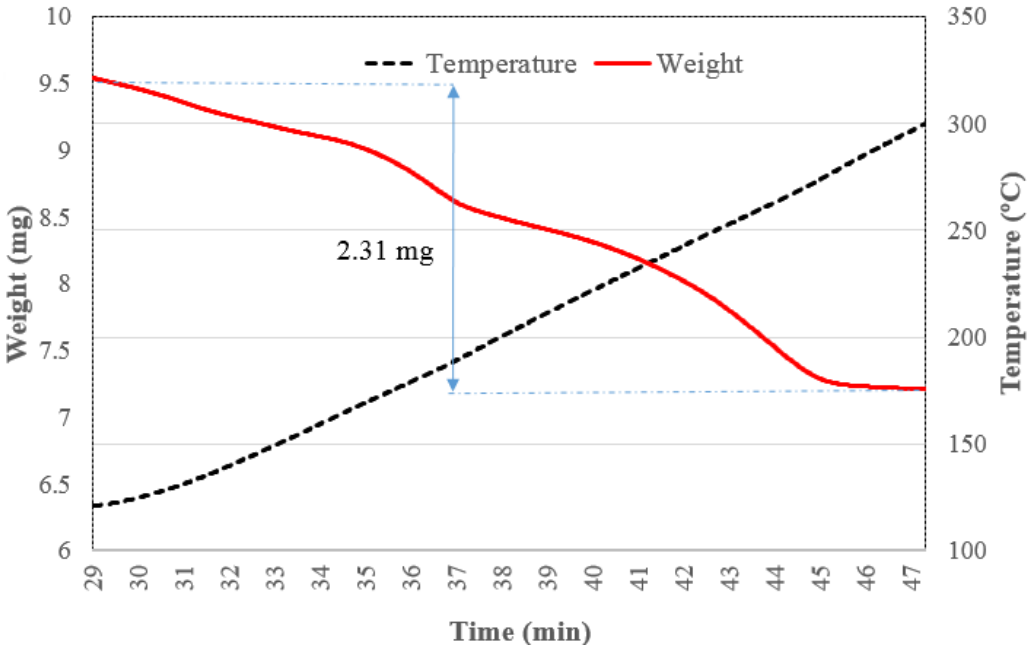

Figure 6.22 Variations of temperature and weight of the sample and 120 and 350ºC at 10ºC/min heating rate.

The dried sample is further heated to 350ºC with a heating rate of 10ºC/min. Here, $MgCl_2$ hydrates are dehydrated and around 14.4% weight loss is observed. Change in the weight of the sample and temperature by time is illustrated in Figure 6.22. The weight

change stopped at around 260ºC, which means that all hydrates of $MgCl_2$ are liberated, and the temperature of the device is not adequate to liberate gases from $Mg(OH)_2$ and MgOHCl. This finding can be regarded as a breakthrough on deciding the reactor temperature of the experimental setup to prevent any side reactions due to $MgCl_2$ hydrates. Further heating is made up to 500ºC in order to separate H_2O from $Mg(OH)_2$ and HCl from MgOHCl. As shown in Figure 6.23, temperature of the device was held at 350ºC for $Mg(OH)_2$ dehydration. However, weight loss is observed to be only ~2%. This result is due to lower tendency of $Mg(OH)_2$ production than that of MgOHCl and $MgCl_2 \cdot 6H_2O$ at ambient conditions. The result for decomposition of MgOHCl is in good agreement with the literature work, where decomposition of this substance starts at around 376ºC and a total decomposition is accomplished at 450ºC in 15 minutes. 33.4% of the sample corresponds to HCl gas captured at the surface of MgO.

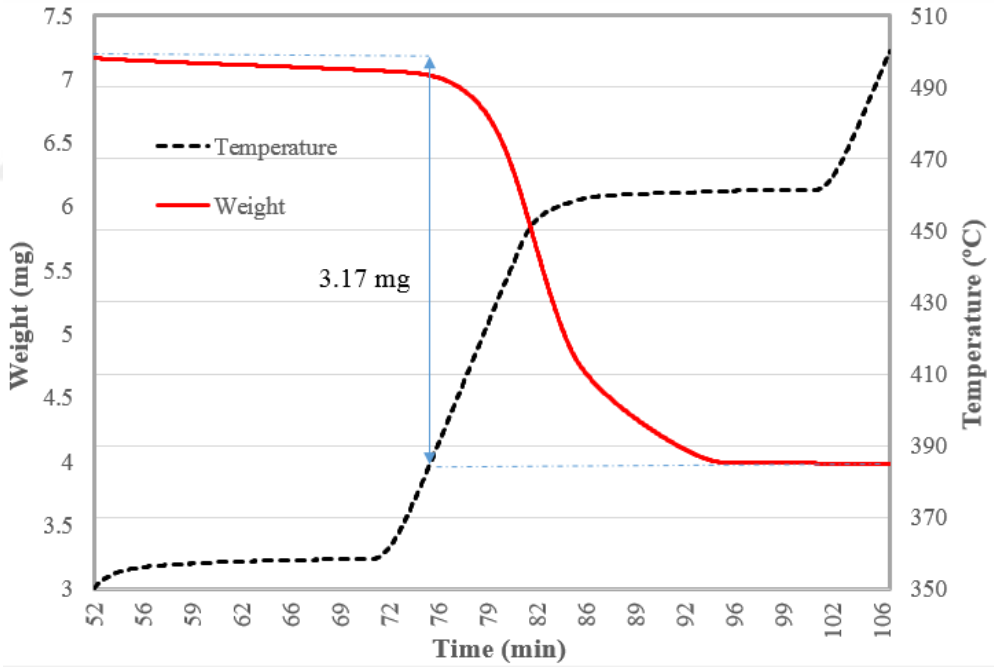

Figure 6.23 Variations of temperature and weight of the sample until 500ºC by holding the temperature constant at 450ºC for 20 minutes.

The next observation could be made by using DTA results, where one can see the endothermic and exothermic reactions throughout the heating process and an approximate estimation can be made on which reactions might occur during heating of the sample. It is possible to see various DTA peaks pointing out dehydration of $MgCl_2$ hydrates as

mentioned in Figure 6.24. Since it is not the main focus of the research, there have been no specific work to determine which peak belongs to which reaction, however, it can be observed that the last peak belongs to the endothermic MgOHCl decomposition. A final interpretation can be made with temperature range selection for the experimental setup. Reaction of the MgO particles with the HCl solution generally leads to high amounts of $MgCl_2$ hydrates production which are regarded as unwanted side reactions. Thus, the reactor temperature should be kept above 150ºC, at least to prevent hydrate formations.

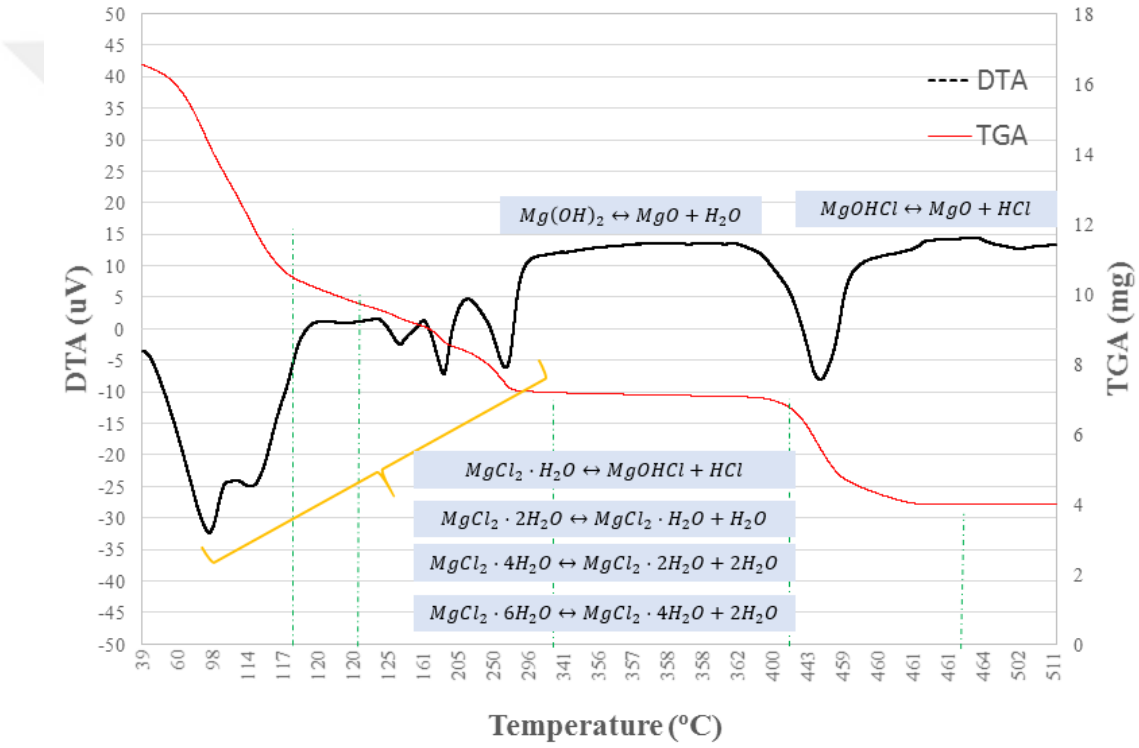

Figure 6.24 DTA/TGA comparison of the sample with possible reactions.

Results of Hydrochlorination Experiments

The HCl capture experiments are conducted in two steps. The first step is the main setup for the reaction of HCl and MgO, where the second step is the precipitation tests to measure the HCl content of the final sample. Precipitation results from the sample is then used to calculate the captured HCl by the MgO particles in the reactor. Thus, the input HCl amount should be known. For this purpose, instead of continuous gas feeding to the reactor, a known amount is fed until it is totally finished in the flask. Figures 6.25-6.29 represent the

variations of captured HCl by temperature at different conditions considering a 95% confidence interval. All measurements show acceptable R-squared values which are more than 83.6%. Since it is mentioned before, the Cl/Mg ratio and the nitrogen flow rate are other observed factors. Thus, these three factors and their effects are in connection and their relations can be correlated using experimental results for uncertainty assessment. Up to 20% of HCl can be captured at elevated temperatures with an increase of ~19% for 125ºC increase at a specified Cl/Mg ratio and nitrogen flow rate. The equation of the experimental results for Figure 6.25 is as follows with an R-squared value of 96.5%:

$$HCl_{cap} = 12.29exp^{0.0017T} \quad (6.5)$$

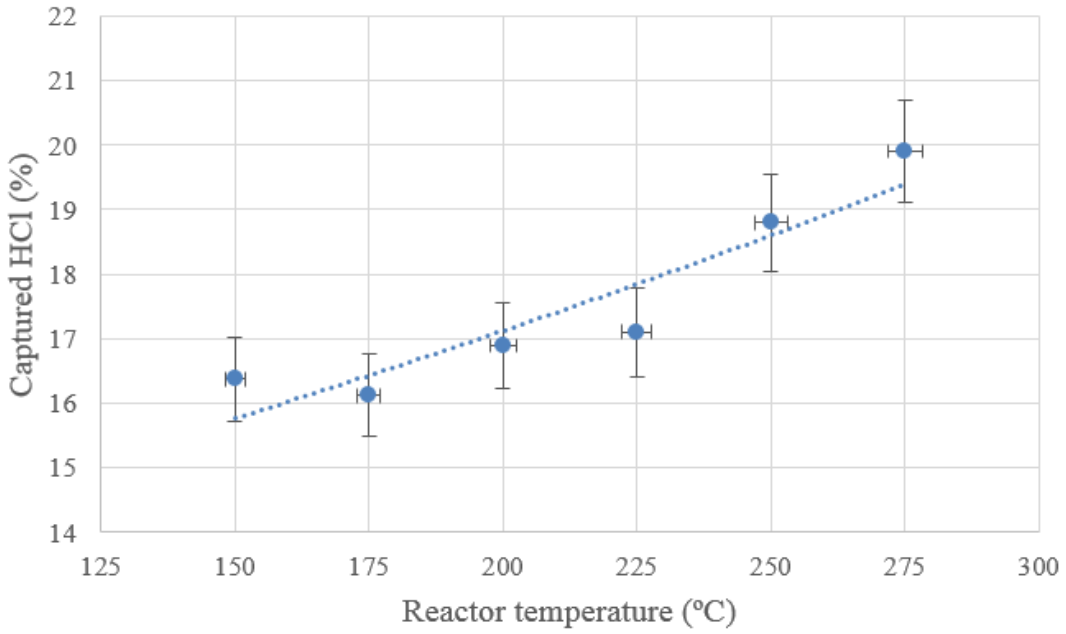

Figure 6.25 Effect of temperature on captured *HCl for* $Cl: Mg = 1,\ \dot{n} = 10\ mL/min.$

Increased nitrogen flow rate also increases the energy required for heating the gas input and decreases the amount of captured HCl. This is possibly due to higher velocity of the gas through the reactor resulting in less reaction between the gas and solid particles and is illustrated in Figure 6.26. Almost three point percent decrease in captured HCl is observed at higher nitrogen flow rate. The equation for the results shown in Figure 6.26 is as follows with an R-squared value of 91.3%:

$$HCl_{cap} = 10.104exp^{0.0018T} \quad (6.6)$$

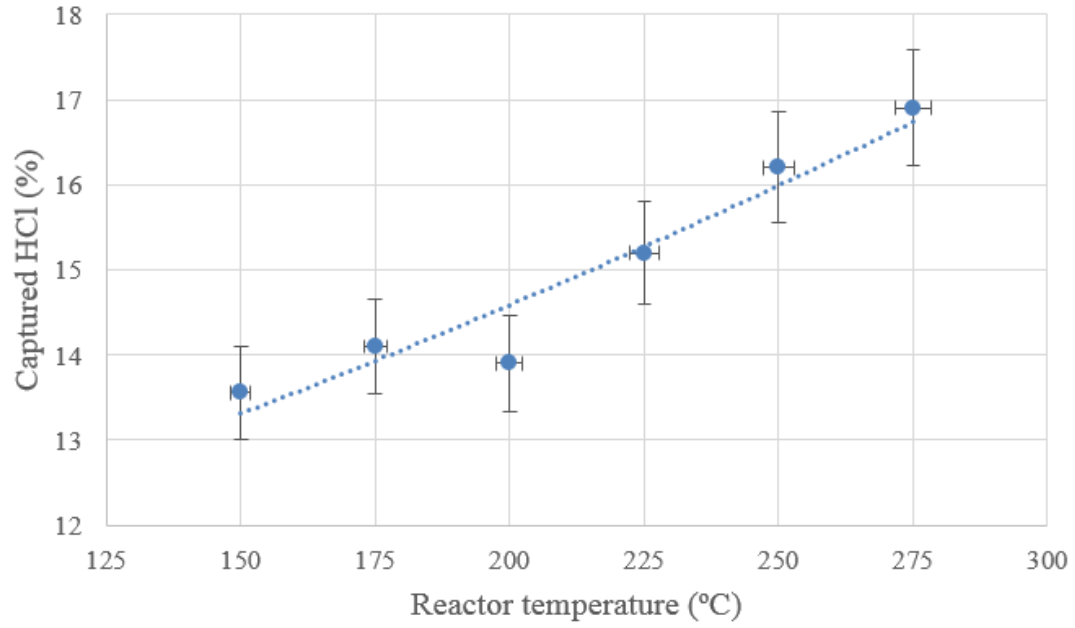

Figure 6.26 Effect of temperature on captured HCl for $Cl{:}\,Mg = 1,\ \dot{n} = 20$ mL/min.

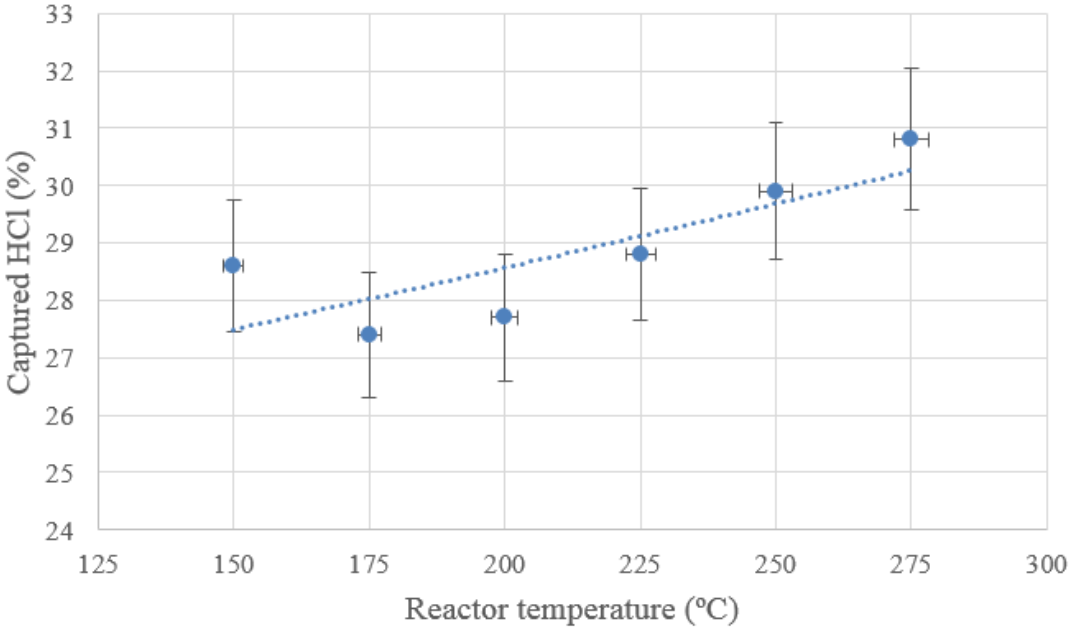

Figure 6.27 Effect of temperature on captured HCl for $Cl{:}\,Mg = 2,\ \dot{n} = 10$ mL/min.

Increased Cl/Mg Ratio is a booster for captured HCl. Here the amount of MgO is kept constant and the HCl is doubled at the same molarity. This change can be regarded as similar to the reaction time, namely, increased amount of HCl requires more time to completely finish in the feed. In addition, time of the reaction for *Cl/Mg=1* is around 65

minutes, where time of the reaction for doubled HCl is around 115 minutes. For the case of 275ºC, amount of captured HCl increases almost by 34% compared to the same flow rate at *Cl/Mg=1*. The trendline of the captured HCl does not show a very significant change as shown in Figure 6.27; the equation for this set of experiments has an R-squared value of 94.6% and is as follows:

$$HCl_{cap} = 24.503exp^{0.0008T} \tag{6.7}$$

Increased nitrogen flow rate does not drastically decrease the amount of captured HCl compared to the previously given results for *Cl/Mg=1*. Up to 29% HCl is captured for this case as presented in Figure 6.28. Higher nitrogen flow rate is not a feasible option due to decreasing residence time of the gas inside the reactor, and requires more energy to heat up the nitrogen gas. Minimized use of inert gas might be a better option for increased of residence time and captured HCl. The equation for the trendline of Figure 6.28 has an R-squared value of 86.7% and is given as follows:

$$HCl_{cap} = 24.714exp^{0.0005T} \tag{6.8}$$

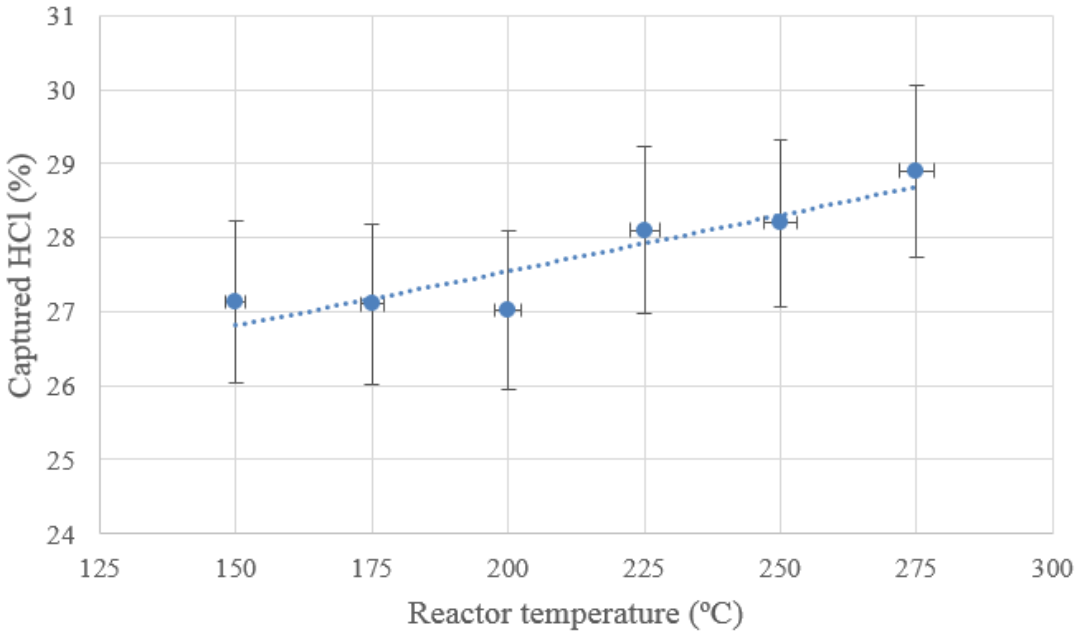

Figure 6.28 Effect of temperature on captured HCl for $Cl{:}\,Mg = 2,\ \dot{n} = 20$ mL/min.

Since the Equations 6.5-6.8 are only functions of temperature, a relationship can be correlated in order to form a final equation where the captured HCl is a function of all three

varied parameters. For this purpose, nitrogen flow rate is first kept constant at 10 ml/min, and the relation between Eqs 6.5 and 6.7 is obtained as follows:

$$HCl_{cap,\dot{n}=10} = 4.52exp^{CM^{0.757}+4.62\cdot10^{-3}exp^{-CM^{0.8105}}T} \quad (6.9)$$

where *CM* refers to Cl/Mg ratio. The correlation for 20 ml/min is obtained as

$$HCl_{cap,\dot{n}=20} = 3.717exp^{CM^{0.9216}+4.89\cdot10^{-3}exp^{-CM^{1.1896}}T} \quad (6.10)$$

Both correlations show more than 98% of R-squared values and present a very good agreement with the experimental results. Figure 6.29 shows the effect of Cl/Mg ratio on captured HCl at different reactor temperatures, using Eqs 6.9 and 6.10. A significant increase in the captured HCl can be observed at higher Cl/Mg ratios.

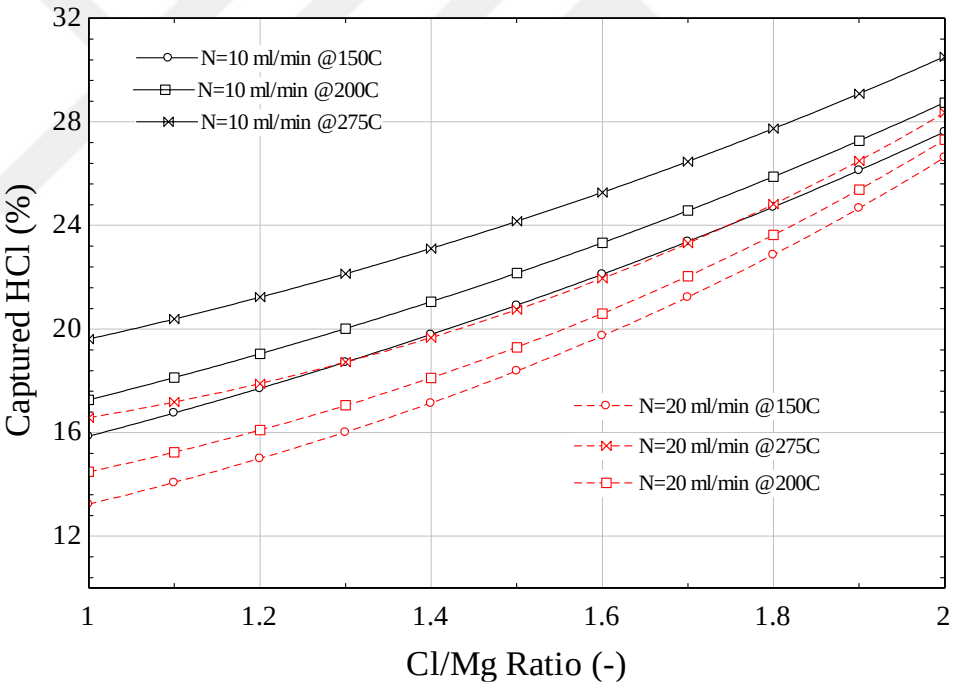

Figure 6.29 Effect of Cl/Mg ratio on captured HCl.

The final equation, where HCl capture ratio is a function of all three parameters, is correlated using Eqs 6.9 and 6.10 as follows:

$$HCl_{cap,f} = 20.29exp\left(-N^{0.1766}+CM^{\left(0.1688\exp N^{0.1766}\right)}+1.433\cdot10^{-3}exp^{\left(N^{0.0683}-CM^{0.1259exp\,N^{0.2701}}\right)}T\right) \quad (6.11)$$

A validation of the present model with experimentally measured data is illustrated in Figure 6.30 by considering Eq 6.11, and it presents a very good agreement with experimental results. This equation can now be used to calculate uncertainties through the experiments. Partial derivatives of all three variables are calculated using Eq 6.11, with corresponding bias and precision errors of the measurement devices. Since the calculated partial derivatives are quite long, they are not presented within the text. The calculation of partial derivatives with relative errors of the measurement devices results in $\mp$1.17% uncertainty. Relative errors of the devices are significant contributors to uncertainty of the results, thus it is of importance to select high accuracy devices while conducting experiments. Use of the weighing device for the solid particles measurement in the reactor is another factor which may contribute to total uncertainty. Thus, relative errors of this device are also included in the calculations. Results for partial derivatives at some selected rates are presented in Table 6.7.

Table 6.7 Partial derivatives of the variables at all steps of the experiments.

CM (-)	$\dot{n}$ **(mL/min)**	**T (ºC)**	$\frac{\partial HCl}{\partial T}$	$\frac{\partial HCl}{\partial N}$	$\frac{\partial HCl}{\partial CM}$
1	10	150	0.02693	-0.3881	8.737
		175	0.0281	-0.3993	8.547
		200	0.02932	-0.4108	8.323
		225	0.03059	-0.4225	8.064
		250	0.03192	-0.4345	7.767
		275	0.0333	-0.4466	7.429
	20	150	0.02379	-0.1833	7.947
		175	0.02489	-0.1892	7.572
		200	0.02603	-0.1951	7.146
		225	0.02723	-0.2013	6.664
		250	0.02848	-0.2075	6.124
		275	0.02979	-0.2139	5.519
2	10	150	0.02209	-0.2198	15.35
		175	0.02254	-0.2476	15.26
		200	0.02299	-0.2765	15.16
		225	0.02345	-0.3065	15.05
		250	0.02393	-0.3376	14.93
		275	0.02441	-0.3698	14.8
	20	150	0.0133	-0.02171	20.53
		175	0.01346	-0.03978	20.33
		200	0.01363	-0.05829	20.12
		225	0.0138	-0.07727	19.91
		250	0.01398	-0.09672	19.68
		275	0.01415	-0.1166	19.45

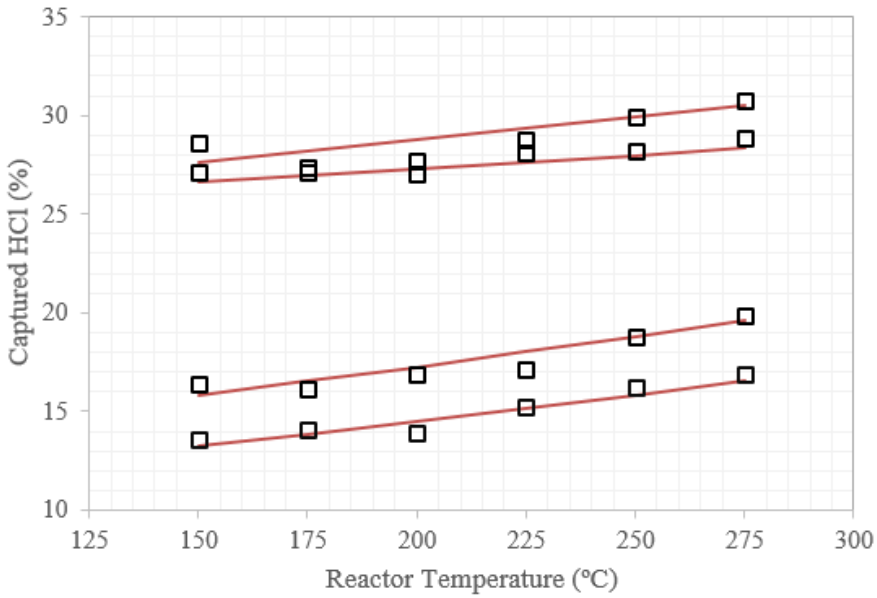

Figure 6.30 Validation of the model with the experimental results.

Here it can be observed that the highest contributions is possibly made by the pH meter uncertainties since this parameter appears to have a strong influence on the experimental results.

The experimental results and the corresponding model show that HCl capture can be succeeded safely at 275ºC reactor temperature at its highest level by 30.8 ∓ 0.36%. The horizontal semi-batch setup can be modified into a continuous-type reactor for higher amounts of HCl capture. The reactor temperature is limited to 280ºC due to possible formation of MgO particles from the dehydration of $Mg(OH)_2$ and the hydrolysis of possible $MgCl_2$ content.

XRD and SEM Results

The experimental results superimpose that there is a slight increase in the amount of captured HCl at elevated temperatures. However, these results do not provide useful information on which reaction occurred at a specific condition to capture HCl gas. The DTA/TGA analyses provide useful information on conditions of the reactions and their approximate amounts to make a quantitative determination. Since the reaction for the TGA sample is conducted at ambient temperature, TGA results would be misleading to verify what reaction is occurring at what specific condition. Thus, XRD measurements are necessary to observe the intensity of the substances which can be a very useful tool to

decide on the reaction temperature for better thermodynamics and for prevention of unwanted side reactions. For the XRD measurements, a Rigaku Ultra IV type phase analysis and texture measurement device is used. Continuous scanning is conducted at a scan range of 10-90º at 4000 deg/min. Scanned substances are limited to Mg- based compounds and all possible hydrates of $MgCl_2$. XRD measurements are made for 5 samples which are collected from the reactor at various temperatures. A final XRD measurement is conducted for the sample taken from 275ºC experiment, which is further heated up to 400ºC and kept at this rate for 30 minutes, in order to obtain a preliminary estimation for dehydration of $Mg(OH)_2$.

Figure 6.31 shows the XRD result of the sample from experiment at 150ºC reactor temperature. At this rate, the dominant substance is still $MgCl_2$ hydrates, as expected. Existence of Mg(OH)Cl and $Mg(OH)_2$ are lower with traces of unreacted MgO particles. Reaction at this temperature leads to production of high amounts $MgCl_2$ which needs elevated temperatures with high energy requirement to recycle MgO. Furthermore, it can be noted that steam is required to recycle MgO from $MgCl_2$, which would result in liberation of HCl in mixture with steam. Thus, higher reactor temperatures can be a better option to prevent $MgCl_2$ production.

The traces of Mg(OH)Cl and $Mg(OH)_2$ are observed at the 225ºC sample, where $MgCl_2$ hydrates are still dominant products of the reaction. At this rate, amount of Mg hydrates are also at a relatively high level, therefore, the resulting process to recycle steam from this substance would be energy intensive. The XRD result for this sample is presented in Figure 6.32 with major substances indicated. There are also unreacted MgO particles observed at relatively lower intensities, which shows that not all of the sample is reacted with the gas.

The predominant substance at 250ºC is now Mg(OH)Cl with large amounts of $MgCl_2$ hydrates, as shown in Figure 6.33. At this rate, it is not possible to see hydrates of $MgCl_2$ at high stoichiometric rates but it is highly possible to observe $MgCl_2 \cdot 2H_2O$ and $MgCl_2 \cdot H_2O$, where a possible side reaction to produce Mg(OH)Cl from $MgCl_2 \cdot H_2O$ occurs. Comparing with the 150ºC sample, amount of target products are significantly higher than that of 150ºC sample. At this temperature, expected products of the MgO chlorination are still mixture of various Mg compounds even if the predominant substance

is the target substance (MgOHCl). Thus, a higher temperature reactor can still be a good option for elimination of side reactions and increases the ratio of the target product.

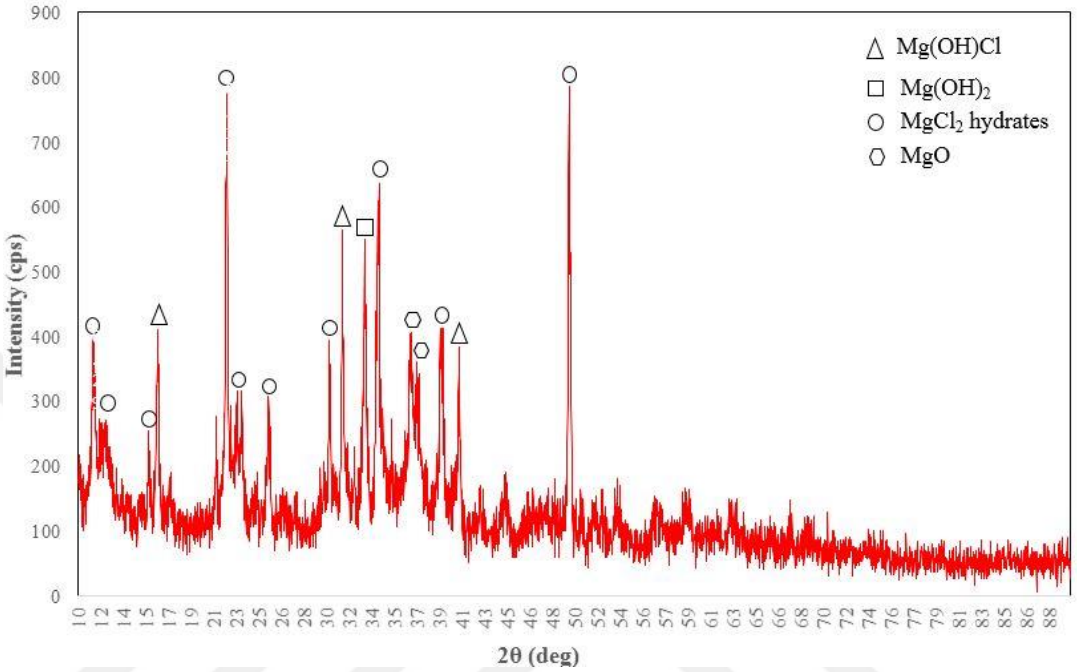

Figure 6.31 XRD results for the sample from 150ºC experiments.

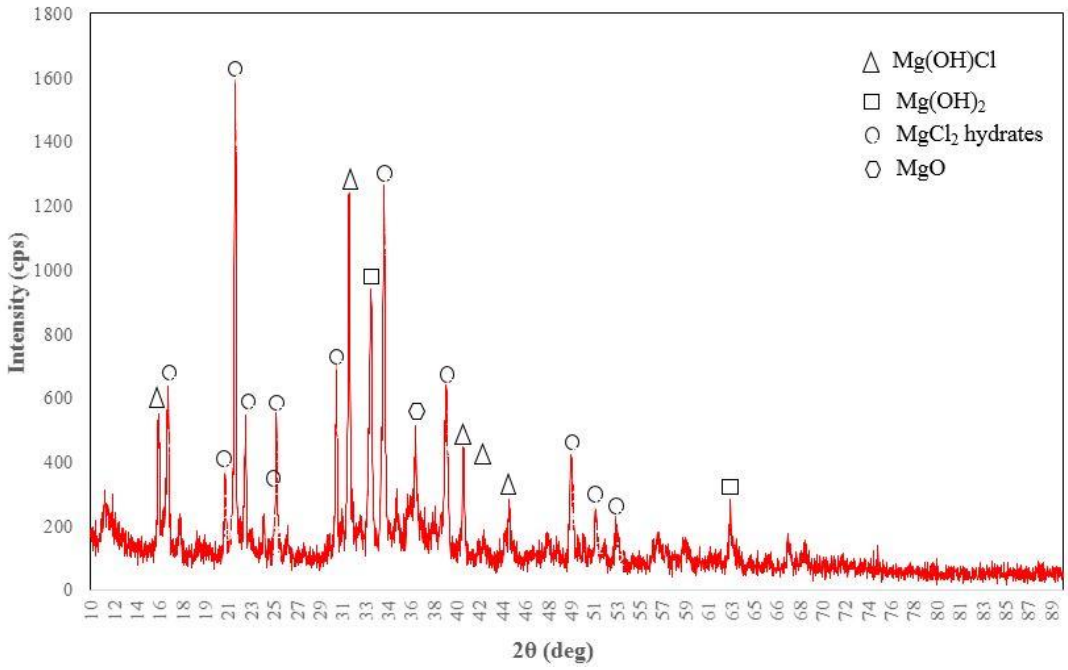

Figure 6.32 XRD results for the sample from 225ºC experiments.

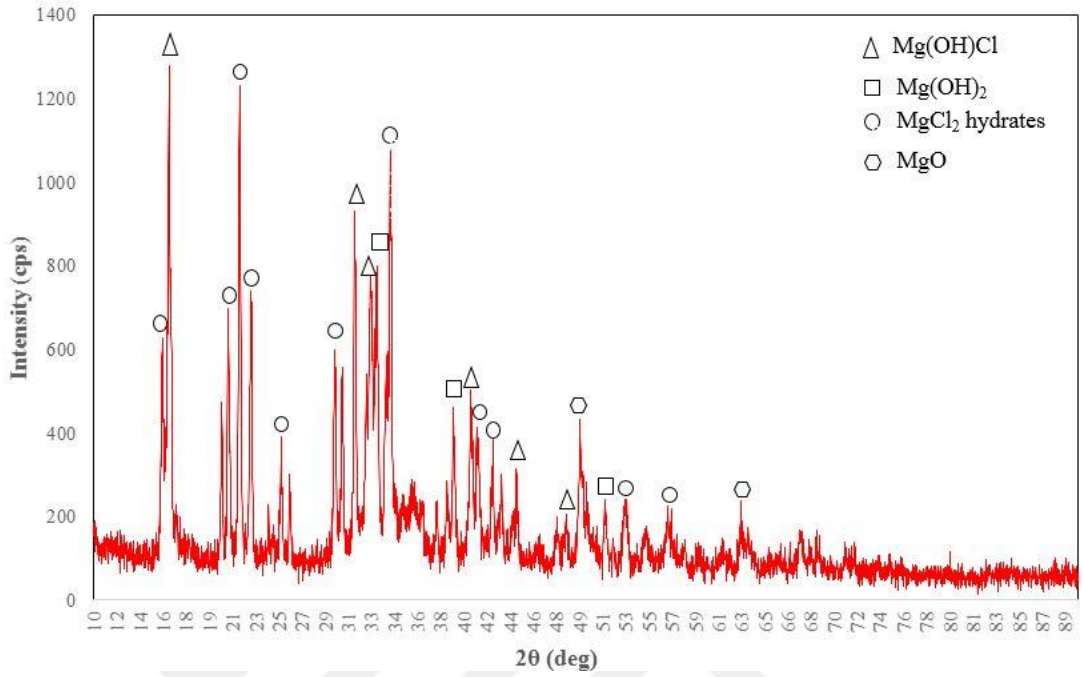

Figure 6.33 XRD results for the sample from 250ºC experiments.

The highest temperature of the reactor is set to 275ºC due to limitation of $Mg(OH)_2$ dehydration temperature (~280ºC). Thus an upper limit for this reaction should be set at this rate, and any XRD or texture measurement results might be misleading for this specific reaction due to recycling of MgO at elevated temperatures. The XRD result for the 275ºC sample is presented in Figure 6.34. At this temperature, almost all of the $MgCl_2$ hydrates are liberated compared to that of 250ºC sample. This is an expected outcome, considering controlled dehydration thermodynamics of the $MgCl_2$ hydrates (Kipouros and Sadoway, 2001). Here, the predominant substance is found to be MgOHCl at reasonable rates where a considerable amount of $Mg(OH)_2$ is also observed. In terms of the reactions through the reactor, the 275ºC reaction temperature is more favorable than that of lower temperature reactions due to formation of unwanted products.

The experimental measurements show that HCl is captured with a slight increase starting from 150ºC to 275ºC, however these results did not provide useful information on how it is captured. XRD measurement results show that, keeping the temperature of the reaction under 225ºC is not a feasible option due to side reactions and unwanted formation of HCl adsorbents. The temperature range of this reaction should be kept at a specific

temperature range, due to the tendency of MgO to react with both steam and HCl resulting in various formations of Mg Compounds.

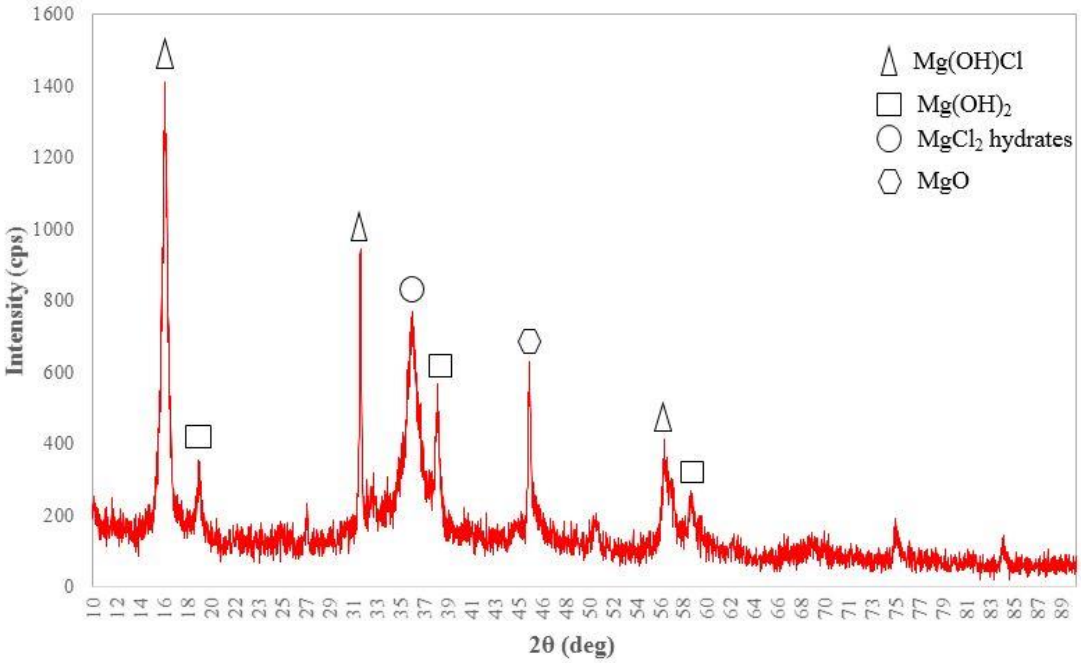

Figure 6.34 XRD results for the sample from 275ºC experiments.

A final XRD measurement is made for the sample from 275ºC experiments, where this sample is further heated up to 400ºC and kept at this temperature for 30 minutes in order to investigate the content of the solid sample at this rate. The only species at this temperature are found to be MgO, $MgCl_2$ and remaining Mg(OH)Cl. The intensity of Mg(OH)Cl is still at a relatively higher level which shows that decomposition of this substance is not completed yet, and HCl adsorption is succeeded at a reasonable rate. XRD result for 400ºC sample is illustrated in Figure 6.35. The three reactor configuration (Figure 3.5) for HCl capture by recycling MgO can be applied with minimum amount of interruptions due to side reactions.

An SEM image of the 275ºC sample is also provided in Figure 6.36. A Carl Zeiss Gemini Fesem type imaging equipment is used with the sample coated by Au-Pd. Imaging is made at 10K, 20K and 30K zoom at 5 kV. At 30K zoom, it is possible to differentiate the porous surface of the MgO particles holding HCl at its surface with denser and more

homogenous structure at the background. A final evaluation can be made for the overall experiments and measurements, and can be sorted as follows:

- TGA/DTA results show that lower temperature reaction of MgO with 5.5 M HCl is not recommended due to several unwanted reactions at lower temperatures.
- Experimental results show a slight increase in amount of captured HCl at 125ºC increase. An equation is correlated for HCl capture rate related to all studied parameters with a reasonable uncertainty result ($\mp$1.17%).
- Although lower temperature reactions seem to be favorable for further internal heat utilization within the Mg-Cl cycle, XRD results show that there are too many side reactions due to $MgCl_2$ hydrates which would jeopardize the recycling process of MgO.
- A three-step process at different temperatures can be considered to capture HCl as follows:
    - HCl capture process (250-280ºC)
    - $Mg(OH)_2$ dehydration process (330-350ºC)
    - MgOHCl decomposition (450ºC)

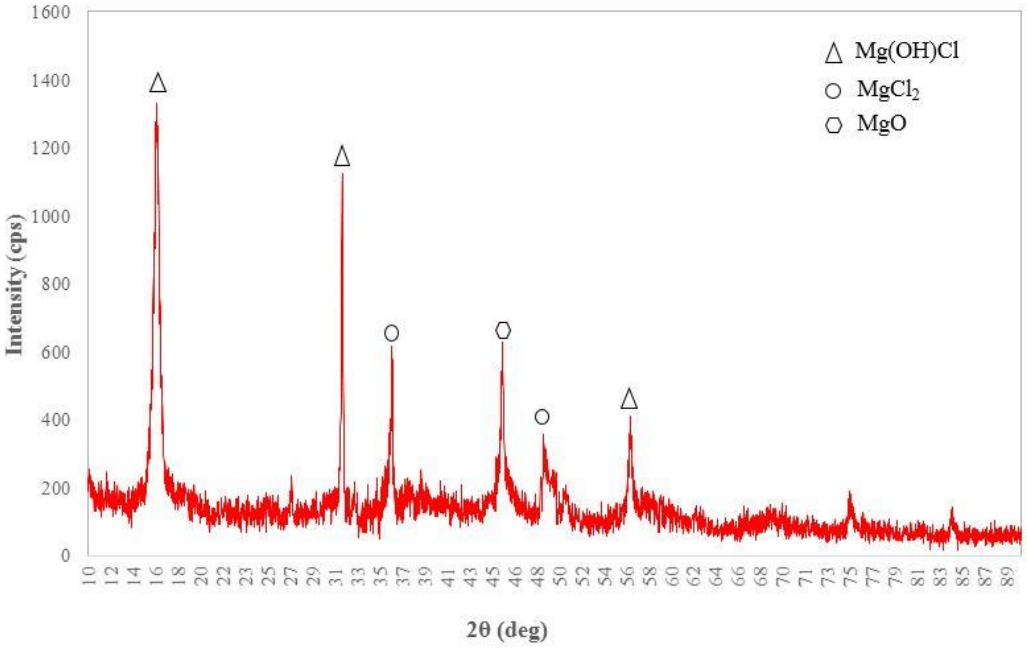

Figure 6.35 XRD results for the sample from rapid heating up to 400ºC.

Above findings are included in the final design of the Mg-Cl cycle through the Aspen Plus simulations and adapted to the system. Further assessment of the cycle with the HCl capture process is discussed in section 6.3 with thermodynamic analysis, and various comparisons are made with aforementioned options.

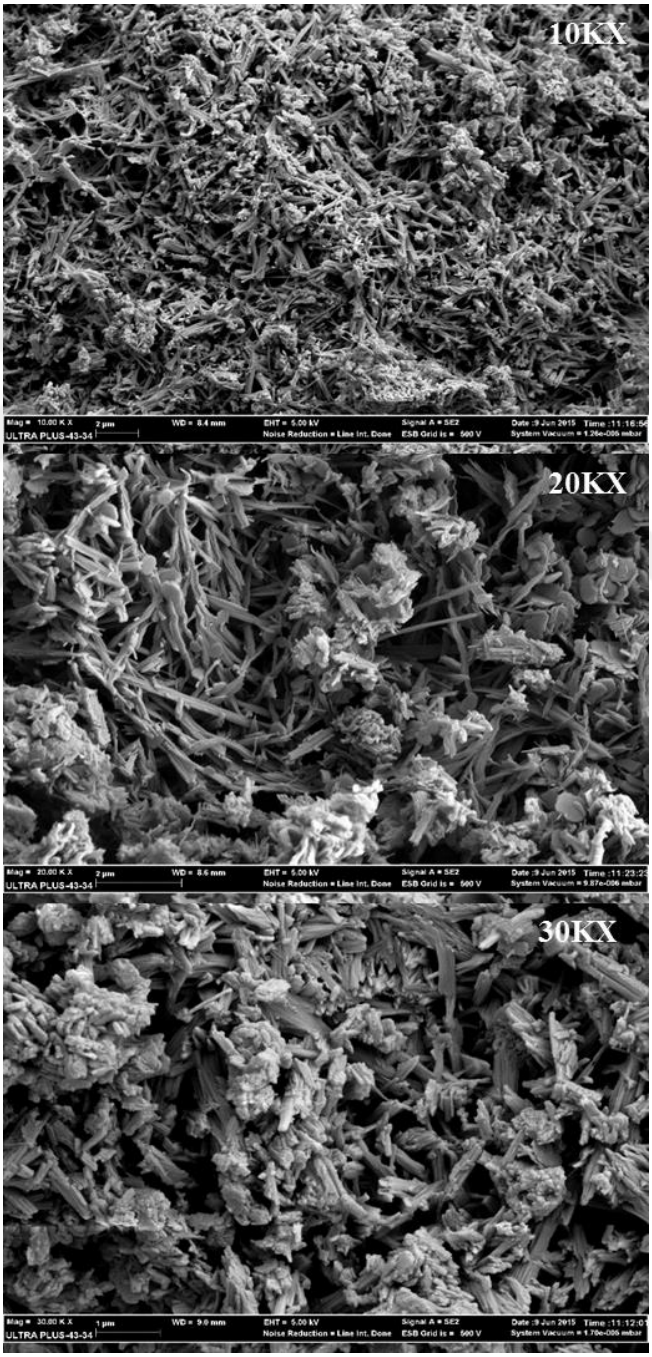

Figure 6.36 SEM images of the sample from 275ºC reactor temperature conditions at different zoom values.

6.3 Results of the Final Configuration

Three flow-sheet options with their thermodynamic results are presented in Section 6.1. The final design is similar to that of four-step Mg-Cl cycle where an additional HCl capturing process integration is made. The HCl capture process is one of the most crucial reactions throughout the cycle for decreased electrical work requirement. For the HCl capturing process, experimental results are adapted in connection with recycling of the solid particles with dehydration and decomposition of the products.

Table 6.8 Energy balance calculations of the four-step Mg-Cl cycle with HCl capture.

Component	Process	T (°C)	$\Delta\bar{H}$ (MJ/kmol H_2)	$\dot{W}$ (MW)
Hydrolysis	$MgCl_2$ hydrolysis	280	-17.82	-
Decomposition	MgOHCl decomposition	450	118.1	-
Chlorination	MgO chlorination	500	-31.51	-
HCl Separation*	See Table 3	280, 350, 450	17.77	-
Electrolysis (aq)	Aqueous HCl electrolysis	70	-	121.57
Electrolysis (dry)	Anhydrous HCl electrolysis	70	-	175.6
HEX-1	Steam superheating	280	546.8	-
HEX-2	MgOHCl heating	450	7.8	-
HEX-3	$HCl_{(aq)}$ cooling	70	-483.8	-
HEX-4	$HCl_{(dry)}$ cooling	70	11.2	-
HEX-5	Hydrogen cooling	25	-0.65	-
HEX-6	Hydrogen cooling	25	-0.65	-
HEX-7	Chlorine heating	500	15.61	-
HEX-8	Oxygen cooling	25	-7.46	-
HEX-9	$MgCl_2$ cooling	280	-17.8	-
Auxiliary	Water pumping, inert gas compression	-		1.1
Total heat**		-	283.47	
Total work		-		298.27

* Details of the energy balance of this process is provided in Table 8.9.
** The total heat is calculated based on 85% of heat exchanger effectiveness, and exothermic reactions are not included in the calculation.

A thermodynamic analysis of the four-step Mg-Cl cycle with HCl capture is conducted for 1 kmole/s hydrogen producing plant. Table 6.8 summarizes the endothermic and the exothermic reactions, as well as heat exchanger loads. The practical voltage requirement of the aqueous and anhydrous HCl electrolysis is taken to be 1.8 V, and 1.4 V, respectively. The highest heat requiring component is the Hex-1, where phase change and superheating of large amounts of water (11 kmole/s) are required. However, the Hex-3 recovers most of this heat with its high heat load. The total heat requirement for the

overall cycle with a more practical approach is around 283.5 MW, which is higher than previously evaluated values for stoichiometry. For 30.8% HCl capture as seen in the experiments, electrical energy requirement is 297.2 MW. This is almost 14.5% lower than direct aqueous HCl electrolysis, and 6.7% lower than water electrolysis (considering 1.65 V).

The energy requirement of the HCl capture process is also presented in Table 6.9. HCl capturing reaction is at the hydrolysis outlet temperature and shows relatively high exothermic behaviour. Dehydration and decomposition reactions are endothermic and it is possible to utilize the exothermic reaction heat for individual endothermic reactions, as well as heat exchangers in the HCl capture unit. Assuming the same heat exchanger effectiveness value (85%), the total heat requirement for the HCl capture process results in 17.77 MW for 1 kmol/s MgO feed. State point information with enthalpy, entropy and exergy values are presented in Table 6.10.

Table 6.9 Energy balance calculations of the HCl capturing process.

Component	Process	T (°C)	$\Delta\bar{H}$ (MJ/kmol H_2)
Capture	MgO hydration and hydrochlorination	280	-36.87
Dehydration	$Mg(OH)_2$ dehydration	350	11.4
Decomposition	MgOHCl decomposition	450	35.42
HEX-1	Heating at dehydration temperature	350	4.14
HEX-2	Heating at decomposition temperature	450	4.7
HEX-3	Cooling to HCl capture temperature	280	-8.11
Total*			17.77

* Total heat is calculated based on 85% of heat exchanger effectiveness. Total conversion of MgO is based on experimental results.

A total assessment of the cycle can be made by evaluating total performance of the system. Energy and exergy efficiencies of this cycle correspond to 41.7%, and 50.6%, respectively. The amount of steam required for hydrolysis step is one of the main reasons for the higher heat requirement. At stoichiometric conditions efficiency of the conventional cycle is evaluated as 55.2%. However, it is not appropriate to further assess the three-step cycles due to the aqueous HCl electrolysis. Figure 6.37 summarizes the efficiency comparison of the four-step Mg-Cl cycle with and without HCl capture. Dry HCl capture increases the energy and exergy efficiencies of the system by 5.46% and 8%, respectively. Considering a wider point of view, production of power is less efficient than production of heat. Thus, less power requirement is expected to bring a more feasible integrated system

in terms of performance, when energy supplying systems are taken into account. The maximum achievable energy and exergy efficiency values are 43.7%, and 53.66%, respectively with full HCl capture from the proposed reaction sets.

Table 6.10 State point information for the four-step Mg-Cl cycle with HCl capture.

State	Stream	$\dot{n}$ kmol/s	T (°C)	$\bar{h}$ (kJ/kmol)	$\bar{s}$ kJ/kmolK	$\overline{ex}_{ph}$ (kJ/kmol)	$\overline{ex}_{tot}$ (kJ/kmol)	$\dot{E}x$ (MW)
1	H_2O	1.0	25	-285820	-163.14	-33.77	3086.23	3.09
2	H_2O	11.0	66	-282750	-153.47	154.30	3274.30	36.02
3	H_2O	11.0	280	-233040	-23.00	2433.74	14143.74	155.58
4	$MgCl_2$	1.0	280	-621940	-119.42	5438.50	157298.50	157.30
5	Mix	12.0	280	-266930	-31.12			
6	HCl/H_2O	11.0	280	-219570	-15.81	13762.50	25472.50	280.20
6-I	HCl	0.3	450	-79813	36.14	4729.49	90679.49	27.20
6-II	HCl/H_2O	10.55	275	-223380	-17.90	10572.95	22282.95	235.09
6-III	H_2O	0.15	350	-230500	-18.68	3685.76	15395.76	2.31
7	HCl/H_2O	10.55	70	-268720	-138.31	1116.02	12826.02	135.31
8	Mix	10.55	70	-262800	-139.12			
9	$H2/H_2O$	10.2	70	-272040	-145.16			
10	H_2O	9.85	70	-282440	-152.57	195.50	3315.50	32.66
11	H_2	0.35	70	1302	4.17	57.39	238547.39	83.49
12	H_2	0.35	25	1	0.11	-32.63	238457.37	83.46
13	MgOHCl	1.0	280	-787930	-199.46	3209.71	148329.71	148.33
14	MgOHCl	1.0	450	-780160	-187.20	7326.02	152446.02	152.45
15	Mix	2.0	450	-331050	-16.41	-	-	-
16	HCl	1.0	450	-79813	36.14	4729.49	90679.49	90.68
16-I	HCl	1.3	450	-79813	36.14	4729.49	90679.49	117.88
17	HCl	1.3	70	-91028	14.18	60.20	86010.20	111.81
18	H_2/Cl_2	1.3	70	1406	10.28	-	-	-
19	Cl_2	0.65	70	1485	4.82	75.88	117595.88	76.44
20	H_2	0.65	70	1302	4.17	57.39	238547.39	155.06
21	H_2	0.65	25	1	0.11	-32.63	238457.37	155.00
22	Cl_2	0.35	70	1485	4.82	75.88	117595.88	41.16
23	Cl_2	1.0	70	1485	4.82	47.45	117567.45	117.57
24	MgO	1.0	450	-582290	-68.96	7459.28	66629.28	66.63
25	Cl_2	1.0	500	17098	34.20	6906.16	124426.16	124.43
26	Mix	1.5	500	-397800	-51.69	-	-	-
27	$MgCl_2$	1.0	500	-604170	-92.40	15155.30	167015.30	167.02
28	O_2	0.5	500	14927	29.72	6072.70	10042.70	5.02
29	O_2	0.5	25	-8	0.09	-32.59	3937.41	1.97

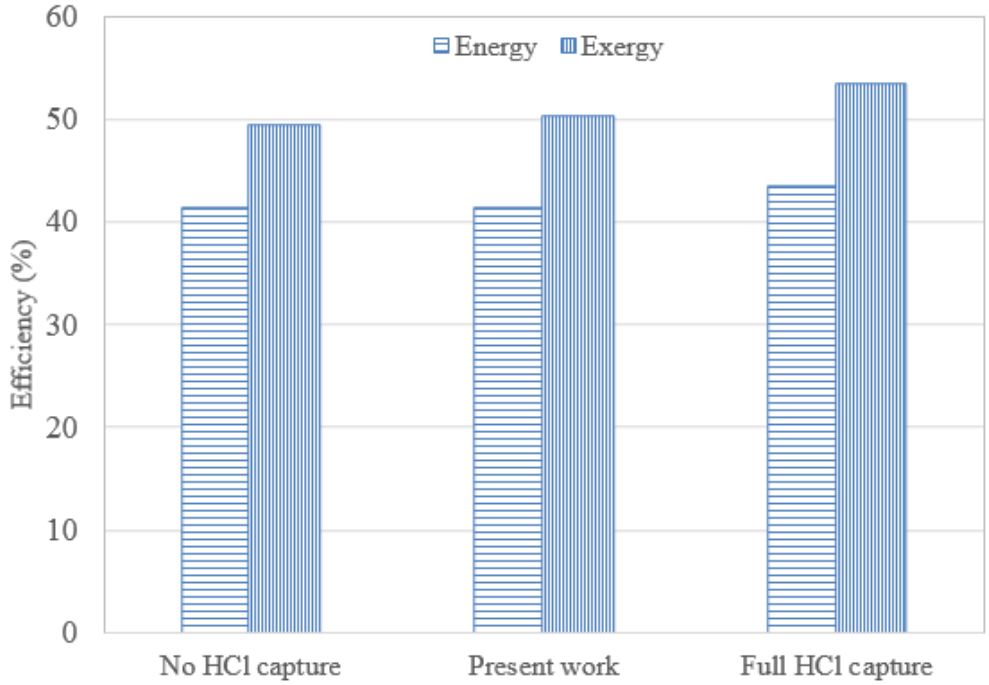

Figure 6.37 Comparison of energy and exergy efficiencies of the modified four-step cycle with and without HCl capture (No HCl capture option corresponds to the MgCl-C cycle).

The newly developed four-step Mg-Cl cycle with HCl capture is a good candidate and an alternative to produce hydrogen from moderate temperature energy sources with feasible reactions, competitive thermodynamic performance values, and mature electrolysis technology.

Both endothermic and exothermic heat exchangers are coupled for internal heat recovery with a simple assumption of 85% heat exchanger effectiveness for all options. However, it is of importance to conduct a proper pinch point analysis in order to evaluate maximum possible heat recovery, as well as the amount and grade of the required heat. As for the final design, 10ºC of approach temperature is assumed for the pinch point analysis and all heat exchangers through the cycle are included in the calculation. Specific heats of the streams are taken from Aspen Plus simulation results and calculation is made by multiplication of the mass flow rates and average specific heats of the corresponding streams. The required information to build the composite curves of the cycle are given in Table 6.11.

Table 6.11 Heat exchanger information to build composite curves.

	Component	Supply Temperature (ºC)	Target Temperature (ºC)	Duty (MW)	Cp (MW/ºC)
Cold	Hex-1	66	280	546.8	2.55
	Hex-2	280	450	7.8	0.045
	Hex-4	70	450	11.2	0.029
	Hex-7	70	500	15.61	0.036
	Hex-1c	275	350	4.14	0.055
	Hex-2c	350	450	4.7	0.047
Hot	Hex-3	275	70	483.8	2.36
	Hex-5	70	25	0.65	0.014
	Hex-6	70	25	0.65	0.014
	Hex-8	500	25	7.46	0.016
	Hex-9	500	280	17.8	0.081
	Hex-3c	450	280	8.11	0.048

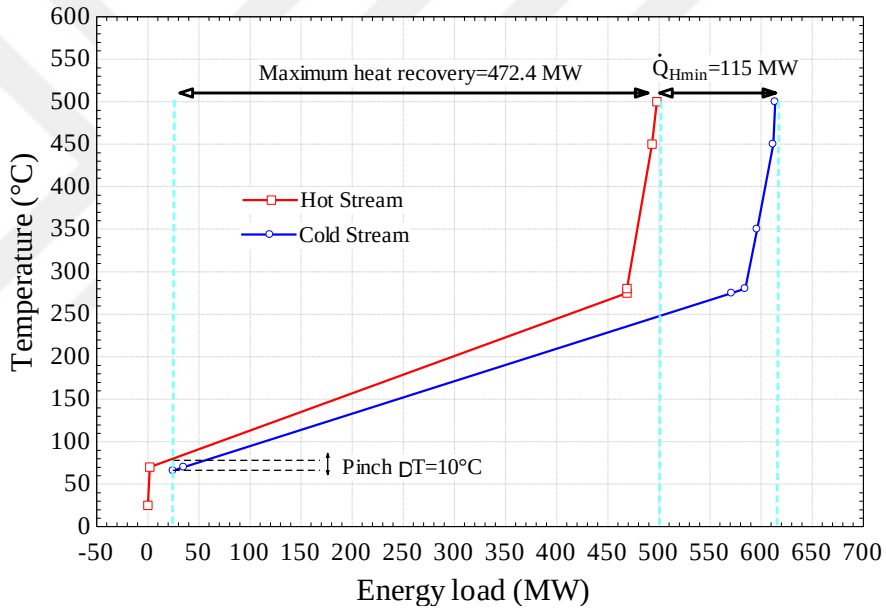

Figure 6.38 Composite curves of the modified MgCl-C cycle.

The pinch point analysis results show that the cycle shows lower external heat requirement than that of previous calculation based on Hex effectiveness factor. 115 MW of energy is required from an external source to heat cold streams, and the rate of heating should be higher than 250ºC as presented in Figure 6.38. The total heat requirement of the cycle now becomes 248.58 MW for 1 kmol/s hydrogen production which is 12.3% lower than previous value in Table 6.8. Using the result from pinch point analysis, energy and exergy efficiencies of the cycle becomes 44.3% and 53%, respectively. Further investigation can be made by applying various heat exchanger networks for a more efficient heat recovery within the system.

The final configuration of the Mg-Cl cycle is a more practical application of this cycle with many applications throughout the system thermodynamics and thermochemistry analysis. Heat and power requirements, as well as system efficiencies are important outcomes for the system integration. Thus, these values are presented in Table 6.12, and comparison of the final design with the previous designs are illustrated in Figure 6.39, respectively.

Table 6.12 Thermodynamic analysis results of the final configuration.

Definition	Unit	Range
Maximum temperature	ºC	450-500
Hydrogen production	kmol/s	1
Heat requirement	MW	248.58
Work requirement	MW	297.14
Thermal exergy of heat	MW	152.75
Total energy input	MW	545.77
Total exergy input	MW	449.9
Energy efficiency	%	44.3
Exergy efficiency	%	53

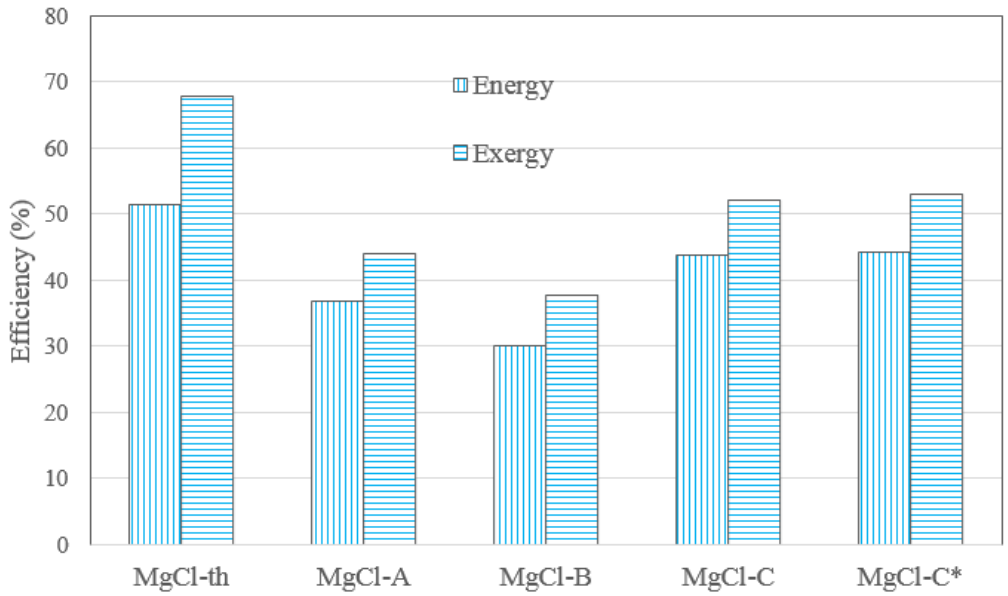

Figure 6.39 Efficiency comparison of the MgCl cycle options revisited (* Final design).

6.4 Exergoeconomic Analysis Results

Exergy based economic assessment of the four step Mg-Cl cycle with HCl capture process is conducted and compared with other hybrid thermochemical cycles. The exergy values of streams are used to analyse cost rate of the streams and component based cost rates of

destruction. For the base case assumptions, cost rate of the produced hydrogen is found to be \$1.861/s and \$1.319/s for hydrogen streams at states 12 and 21, respectively, as presented in Table 6.13. Since 0.69 kg/s of hydrogen is produced from aquaeous HCl electrolysis and 1.31 kg/s hydrogen is produced from dry HCl electrolysis, and total cost of the cycle becomes \$3.67 per kg of H_2. Since this cycle is a newly developed one, and no cost assessment of the conventional Mg-Cl cycle is performed before, a cost comparison with other hybrid thermochemical cycles is conducted. Cost of hydrogen from four-step Cu-Cl cycle has been conducted by ANL and was found to be \$3.30/kg H_2 (Levis et al., (2009)). Another cost assessment of the Cu-Cl cycle has been conducted by Ozbilen, (2013) for a modified four-step cycle with heat exchanger network, cost of this plant was found to be \$3.36/kg H_2. Cost assessment of the Westinghouse HyS cycle has been found to be \$3.85/kg H_2 in a study performed by Jeong and Kazimi (2006). These costs belong corresponding years of studies conducted, which are than updated to 2014 values using the CEPCI. Cost comparison of the Mg-Cl with aforementioned cycles are shown in Figure 6.40. Cost of hydrogen production from the four-step Mg-Cl cycle is lower than that of HyS cycle and slightly higher than the Cu-Cl cycle. Contribution of the separation process and comparatively higher electrical work consumption of the Mg-Cl cycle carry the major effect on hydrogen cost. However, cost of the cycle is in a feasible range and can be competitive among other hybrid cycles.

Table 6.13 Cost rates and specific costs of streams for the final design on Mg-Cl cycle.

State	$\dot{E}x$ (MW)	$\dot{C}$ (\$/s)	c (\$/MJ)	State	$\dot{E}x$ (MW)	$\dot{C}$ (\$/s)	c (\$/MJ)
1	3.09	0	0	**16**	90.68	0.650	0.00717
2	36.02	0.728	0.02023	**16-I**	117.88	1.234	0.01046
3	155.58	3.147	0.02023	**17**	111.81	1.170	0.01046
4	157.30	3.965	0.02521	**19**	76.44	0.651	0.00850
6	280.20	3.023	0.01079	**20**	155.06	1.319	0.00850
6-I	27.20	0.583	0.02144	**21**	155.00	1.319	0.00850
6-II	235.09	5.041	0.02144	**22**	41.16	0.865	0.02100
6-III	2.31	0.325	0.1408	**23**	117.57	1.515	0.01288
7	135.31	2.902	0.02144	**24**	66.63	1.840	0.02762
10	32.66	0.728	0.02231	**25**	124.43	1.603	0.01288
11	83.49	1.862	0.02231	**27**	167.02	4.066	0.02435
12	83.46	1.861	0.02230	**28**	5.02	3.382	0.67370
13	148.33	1.600	0.01079	**29**	1.97	3.340	1.69500
14	152.45	1.645	0.01079				

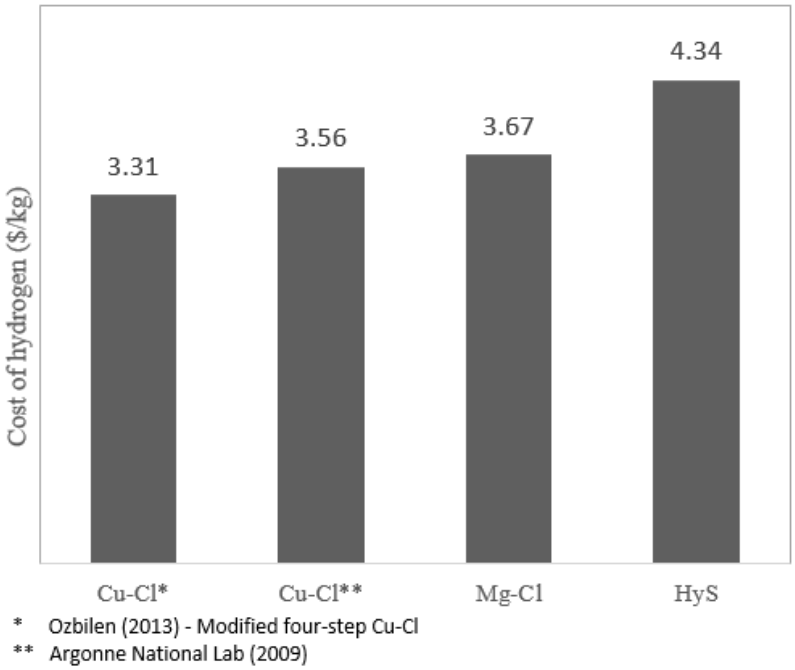

Figure 6.40 Cost comparison of the present study with other hybrid thermochemical cycles.

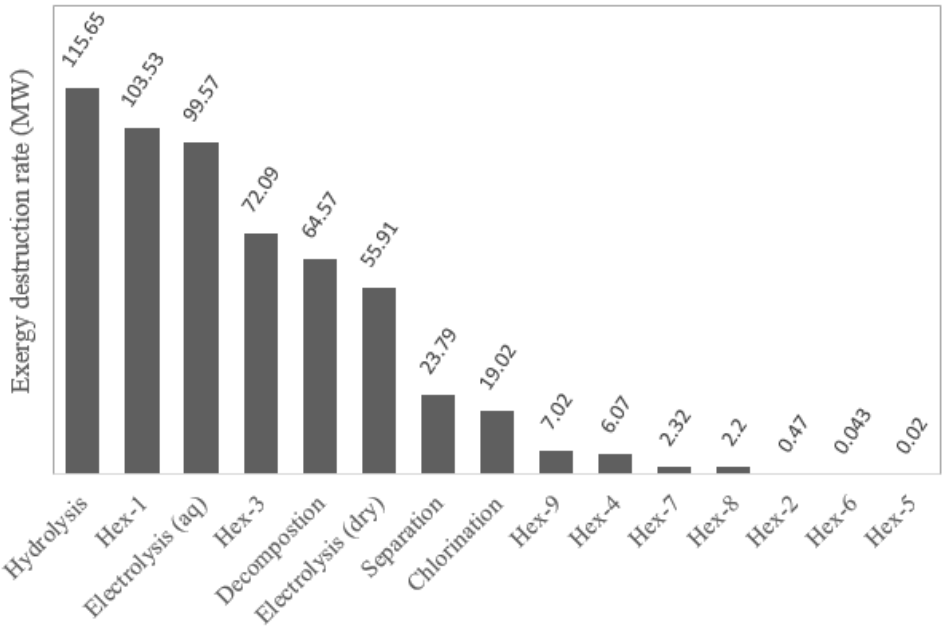

Figure 6.41 Exergy destruction rates of the Mg-Cl cycle components.

The main findings of the exergoeconomic assessment is based on stream exergy rates and corresponding exergy destruction ratios. Thus, exergy destruction rates of the cycle is illustrated in Figure 6.41. The hydrolysis reactor and the first heat exchanger for

water evaporation and superheating are main contributors of total losses. High exergy destruction of the hydrolysis reactor is due to isothermal conditions assumption in the reactor. The heat released from this reactor is not used for internal heat recovery and thermodynamically considered as a waste heat. The latent heat of high amounts of water vaporization is the main reason for exergy destruction in the superheating heat exchanger. Other major exergy destruction contributors can be sorted as; the electrolysis step, the Hex-3, the decomposition step, and the separation process.

The component based costs of capital cost rates and costs of exergy destructions are illustrated in Table 6.14. The highest capital cost belongs to hydrolysis reactor which is due to inlet of very high amount of steam into reactor, resulting in a large volume requirement. The total contribution of capital costs is 9.98 $/s which consist of 68.45% of the total cost rate. The remaining is the cost rate due to exergy destruction, which is found to be 4.56$/s. The exergoeconomic factor is observed to be lowest for heat exchangers 1 and 3 which are used for boiling water and condensing HCl/steam mixture, respectively. Heat exchangers for hydrogen and chlorine gases also show relatively lower exergoeconomic factors. Low values are due to low capital cost rates and high exergy destruction rates of these components.

Table 6.14 Exergoeconomic analysis results for the components of the cycle.

Component	$\dot{Z}_k$ (¢/s)	$\dot{C}_d$ ($/S)	f (%)
Hydrolysis	302.40	1.109	73.2
Decomposition	18.01	0.619	22.5
Chlorination	391.70	0.183	95.5
HCl Separation	284.80	0.228	92.5
Electrolysis (aq)	0.0761	0.452	0.30
Electrolysis (dry)	0.0937	0.254	0.21
HEX-1	0.0925	0.878	0.11
HEX-2	0.0492	0.004	9.94
HEX-3	0.0872	0.691	0.13
HEX-4	0.0402	0.058	0.68
HEX-5	0.0481	0.001	59.3
HEX-6	0.0481	0.007	6.24
HEX-7	0.0419	0.022	1.85
HEX-8	0.0402	0.021	1.84
HEX-9	0.0506	0.067	0.74

The cost rate distribution of exergy destruction of all components is shown in Figure 6.42. Compared to exergy destruction rates, the hydrolysis reactor is still the highest

cost contributor, where cost rate of the Hex-3 and the decomposition reactor show higher values than that of the aquaeous HCl electrolysis. Contribution of low mass flow rated heat exchangers are almost negligibly lower than the major cost producing components.

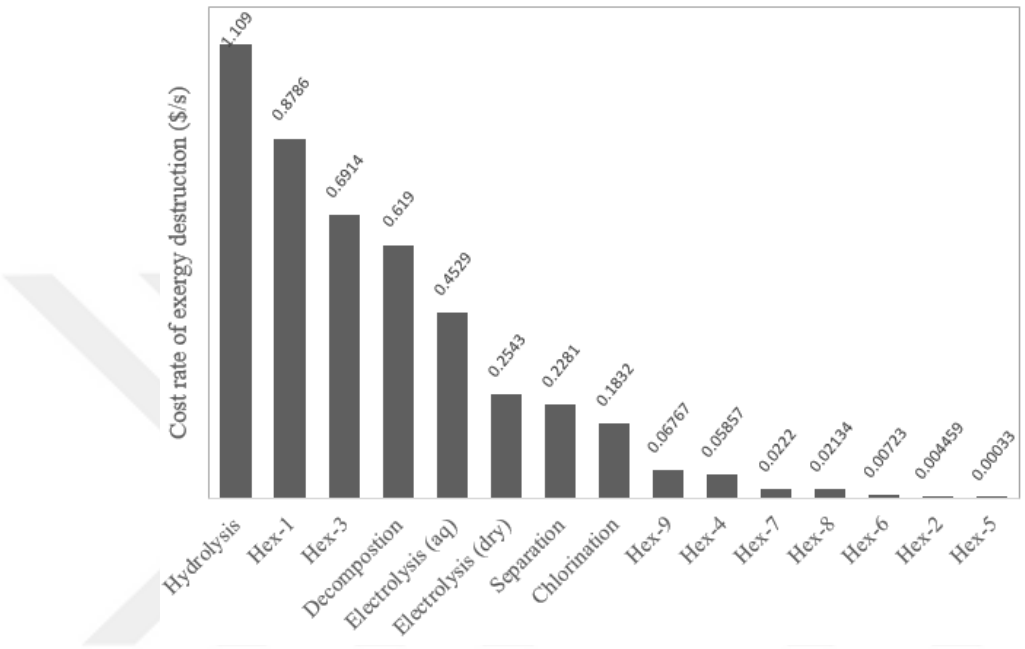

Figure 6.42 Comparison of exergy destruction costs for cycle components.

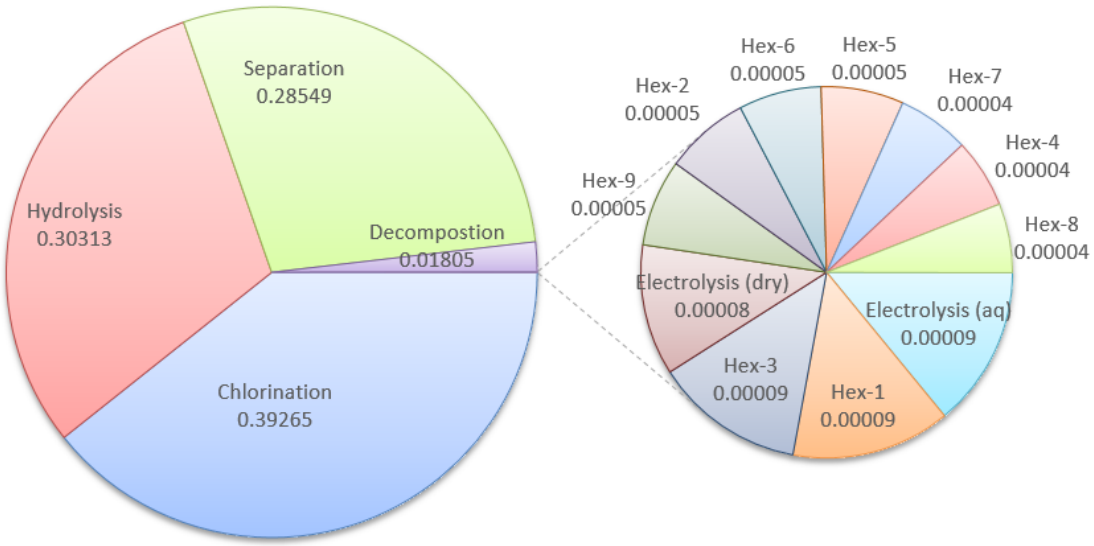

Figure 6.43 Share of capital cost investment rates of Mg-Cl cycle components.

The share of capital investment cost rates are also illustrated in Figure 6.43. Here, share of chlorination reactor is the highest due to higher residence time requirement for MgO chlorination as adapted from literature. Reason for high capital investment cost rates of hydrolysis and separation reactors are high vapor requirement for the reactions, resulting in high volume requirements. Here, one interesting outcome is the low capital cost contribution of electrolysis steps. Since the PEC of these steps are not based on residence time, relatively low contribution is observed. Plant life time, interest rates, and cost of thermal energy are some constant inputs for the exergoeconomic analysis. Effects of these parameters on exergoeconomic factor and total plant cost rate are illustrated in Figs 6.44 and 6.45.

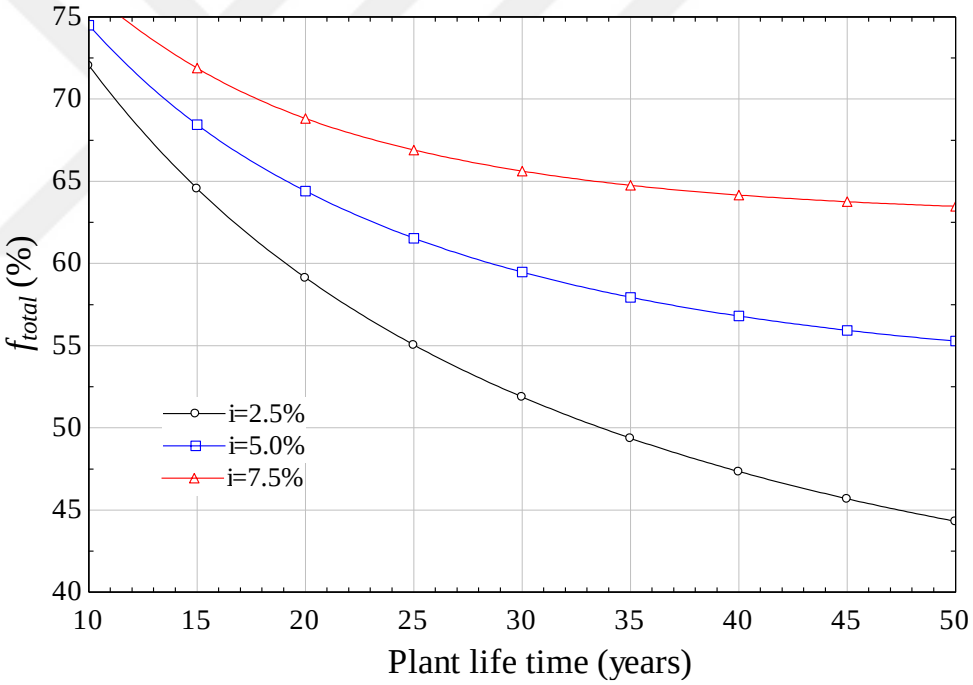

Figure 6.44 Effect of plant life time and interest rate on exergoeconomic factor.

The exergoeconomic factor of the cycle decreases at higher plant life time. This is due to decreased unit cost of components at higher plant life time. Since the cost of thermal energy can be obtained from various energy sources from coal fired plants to nuclear plants, impact of this parameter is also investigated. Higher thermal energy cost has a major effect on both cycle cost rate and exergoeconomic factor. Thus, selection of the heat source is

also a very important factor on assessment of hydrogen cost. For the base model, solar thermal energy is selected as the heat source.

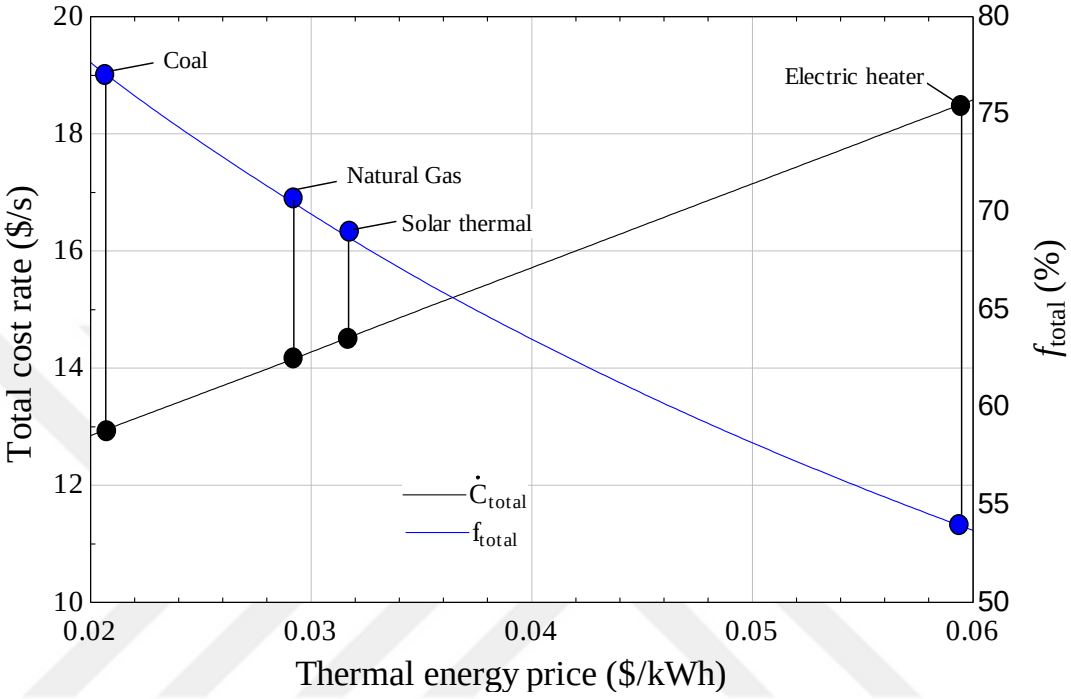

Figure 6.45 Effect of thermal energy cost on total cost and exergoeconomic factor of the Mg-Cl cycle.

6.5 Optimization Results

Optimization of the Mg-Cl cycle is performed by considering the aforementioned decision variables in order to maximize the exergy efficiency, and to minimize the total cost rate of the cycle. The economic assessment of the cycle superimposes that the hydrolysis and the decomposition reactors, and heat exchanger 1 are main contributors to the total cycle costs, which are due to high steam input to the system, and the reaction conditions. Thus, decision variables are selected based on this information. Objective functions for the multi-objective optimization are formed using parametric studies for corresponding decision variables. The Artificial Neural Networks (ANN) application of the MATLAB software is utilized to train the existing data from parametric studies to form objective functions which are functions of the selected decision variables. 70% of all samples are used for training, where 15% are randomly selected as samples, and remaining 15% are selected to be for testing the network performance. The training is selected to be the Levenberg-Marquart algorithm as a default

option. Regression results are illustrated in Figure 6.46 where obtained results are suitable for forming objective functions.

Decision variables for optimization are defined as T_{hyd}, T_{dec}, S/Mg, and $\dot{n}_{ar}$ for hydrolysis temperature, decomposition temperature, steam to Magnesium ratio, and Argon gas mole flow rate into decomposition reactor, respectively. Relation of the objective functions with decision variables are formed as follows:

$$\eta_{ex} = 0.004468T_{hyd} - 0.00000803T_{hyd}^2 + 0.0003252T_{dec} - 2.074 \cdot 10^{-7}T_{dec}^2 + 0.008618SMg - 0.0007442SMg^2 - 0.01624\dot{n}_{ar} + 0.01048\dot{n}_{ar}^2 - 0.1924 \quad (6.12)$$

$$\dot{C}_{tot} = 0.06759T_{hyd} - 0.0001049T_{hyd}^2 + 0.006337T_{dec} - 0.000005778T_{dec}^2 + 0.6341SMg - 0.0001637SMg^2 + 0.3294\dot{n}_{ar} + 0.01444\dot{n}_{ar}^2 - 4.878 \quad (6.13)$$

Above definitions are set as the objective functions and decision variables are defined in matrix form with upper and lower bounds. Decision on the upper and lower bounds are based on several constraints such as commercial availability of components, thermodynamic and material limits. It is now aimed to find out the best possible value of every decision variable for minimized total cost and maximized cycle exergy efficiency.

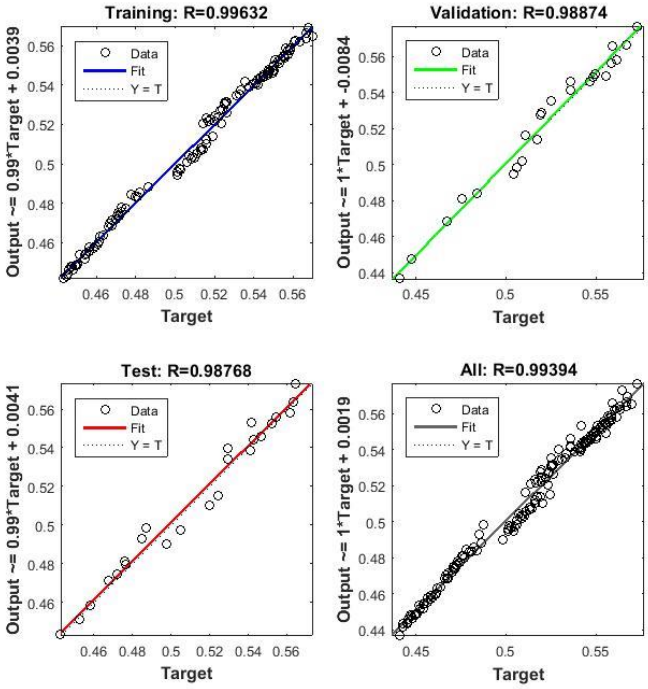

Figure 6.46 Regression results for the trained data.

A multi-objective optimization of the cycle is performed using the Genetic Algorithm option of the MATLAB software. For this purpose, a function is formed for determination of objective functions, and it is transferred to the GA in connection with upper and lower bounds of decision variables. The MATLAB code for the optimization process is provided in Appendix B. Since the multi-objective optimization allows only minimization of all objectives, a negative sign is assigned to the exergy efficiency. Population size of the parents is set to 120, Pareto fraction is set to 0.8, and number of generations are kept above 1000. Figure 6.47 shows the Pareto front of the optimization with optimal solution, best cost, and best efficiency values. The optimum cost and efficiency of the cycle if found to be 12.98 $/s, and 56.25% after several runs. These results does not change in a significant way at different runs. Table 6.15 represents initial decision variables and their values for best exergy efficiency, best total cost rate, and optimal solution. Average spread of particles are also plotted in Figure 6.48. Decision of the Pareto fraction is made based on the average spread of particles, which is a measure of movement of the Pareto front and decides on time of stopping the algorithm.

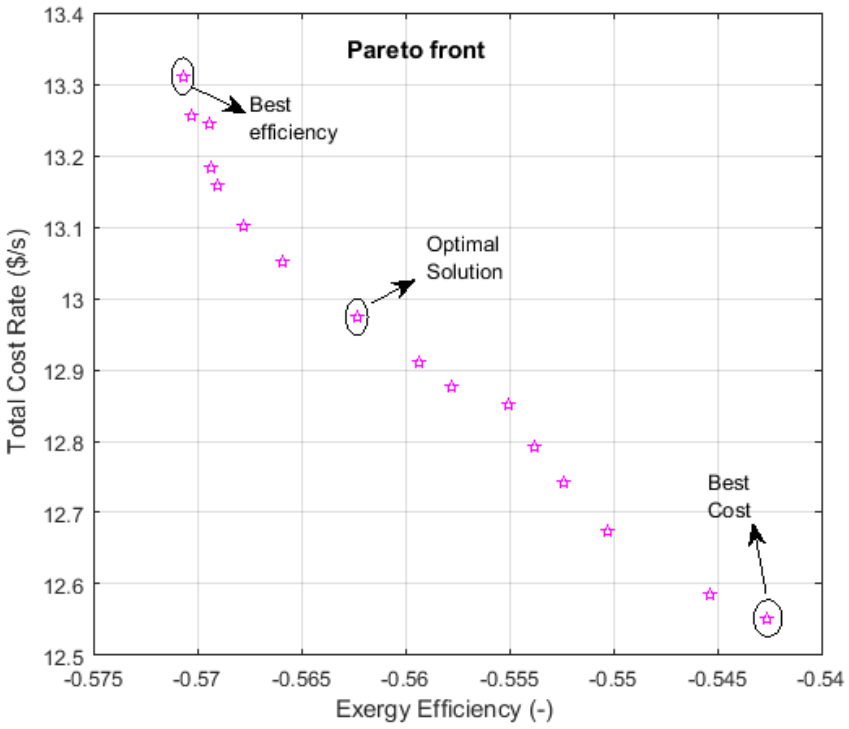

Figure 6.47 Pareto front of the multi-objective optimization.

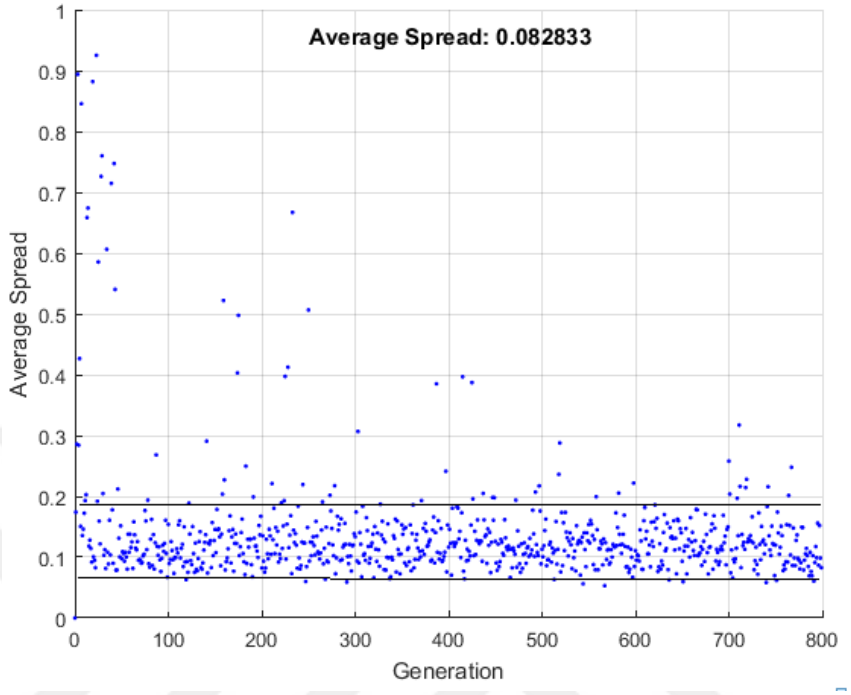

Figure 6.48 Average spread of particles through the optimization.

Lower maximum temperature and lower water use are seen to be thermodynamically favorable for better exergy efficiency, as mentioned earlier in the thermodynamic analysis results. However, higher decomposition temperature results in higher decomposition rate of MgOHCl into useful products, providing higher amount of HCl for electrolysis. Low reaction temperature and steam inlet values are also favorable for lower total cost rate of the system. Optimized values of decision variables are in agreement with other options with steam flow into cycle, however, lower hydrolysis reaction temperature, higher decomposition temperature, and a reasonable rate of inert gas flow is required for the optimal solution.

Table 6.15 Initial and optimum values of decision variables.

	Unit	**Base Case**	**Best exergy efficiency**	**Best total cost rate**	**Optimum value**
Hydrolysis Temperature	ºC	280	287	250	251.8
Decomposition temperature	ºC	450	500	450	485.8
Steam/Magnesium ratio	-	11	8	8	8.01
Gas mass flow rate	kmol/s	1	2	1,83	1.57

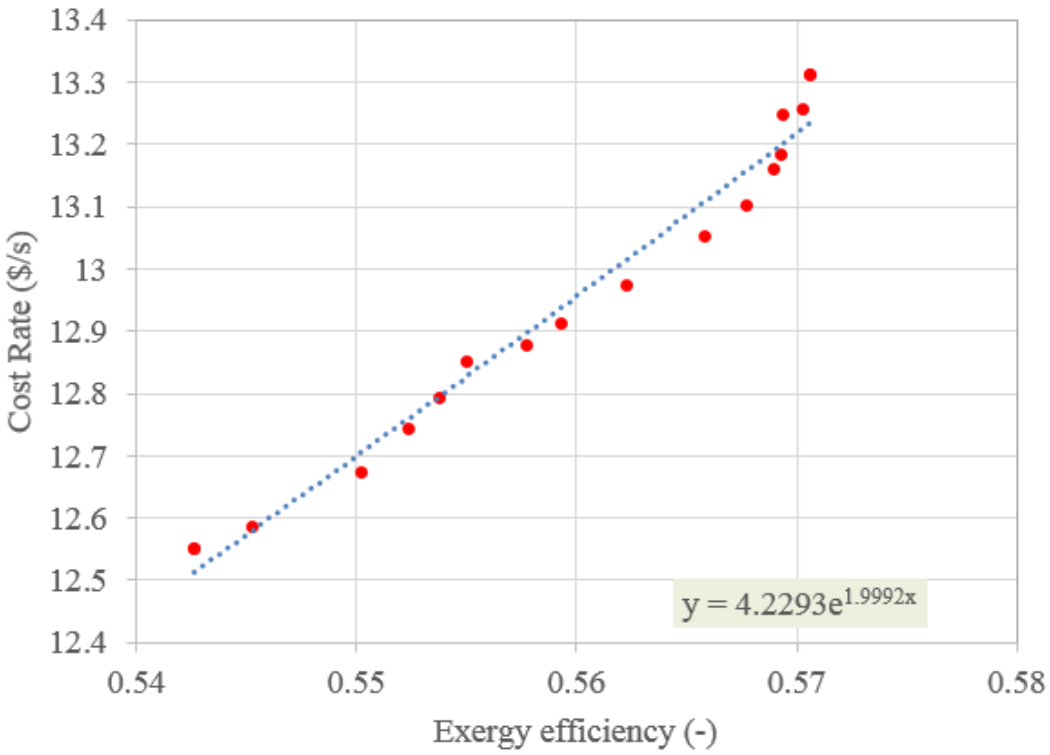

Figure 6.49 Relation between exergy efficiency and total cost rate.

A final correlation between the total cost rate and the exergy efficiency can be made by forming a trend line for results from the multi-objective optimization. Figure 6.49 shows the polynomial correlation between the total cost rate and the exergy efficiency with a reasonable R-squared value. It should be noted that this correlation is limited to the lower and higher bounds of the exergy efficiency values in the tabulated data from Pareto front results.

6.6 Thermodynamic Analysis Results of Integrated Systems

A final design of the Mg-Cl cycle is developed using Aspen Plus simulations and experimental procedures. Since the cycle requires external heat and work to produce hydrogen, and the resulting hydrogen from the cycle is at ambient conditions, a proper selection of power and heat producing systems as well as a hydrogen treatment plant selection are of importance. In this section, thermodynamic analysis and various sensitivity analysis results are presented here for the proposed integrated systems.

6.6.1 Results for System I

The thermodynamic analysis results of the first proposed system are presented by individual subsystem analysis. Since the thermodynamic analysis of the modified Mg-Cl-C cycle is already conducted, and required energy of this cycle is the decision maker for size of the remaining subunits, all the subsystems are sized and analysed based on the thermodynamic information taken from final design of the Mg-Cl cycle.

The hydrogen compression subsystem utilizes the produced hydrogen with several steps of compression where it needs electrical energy to drive the compressors. Thus, the first assessment is conducted for the hydrogen compression plant followed by the gas turbine and solar subsystems.

Hydrogen Compression Subsystem

A five-stage hydrogen compression plant is considered to compress hydrogen from ambient conditions to a desired pressure for storage purposes. Density of hydrogen can be increased from 0.08 kg/m^3 to 38.93 kg/m^3 by compressing this substance up to 700 bar. A pressure-enthalpy diagram of the compression process is illustrated in Figure 6.50 with state point information given in the integrated system figure. Intercooling after all compression steps is considered for less power consuming compressors, where the outlet streams of the compressors are cooled down to ambient temperatures. Compression process at a constant pressure ratio (3.7) results in a 150ºC increase in the stream temperature. The state point information of the plant is given in Table 6.16 for five-stage compression option.

Table 6.16 State point information for the five-stage hydrogen compression plant.

State	T (K)	P (bar)	$\bar{s}$ (kJ/kmolK)	$\bar{h}$ (kJ/kmol)	$\dot{Ex}$ (MW)
46	298	1	107.7	7922	238.5
47	453.5	3.707	109	12453	242.64
48	298	3.707	96.79	7924	241.75
49	453.5	13.74	98.12	12467	245.90
50	298	13.74	85.88	7933	245.00
51	453.5	50.94	87.21	12519	249.20
52	298	50.94	74.92	7967	248.31
53	453.5	188.8	76.26	12720	252.66
54	298	188.8	63.83	8114	251.77
55	453.5	700	65.3	13517	256.73
56	298	700	52.63	8828	255.82

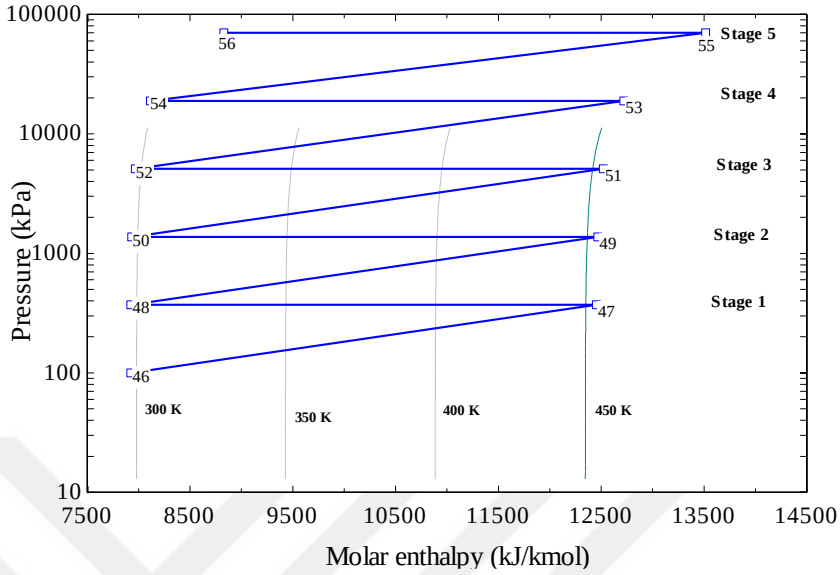

Figure 6.50 P-h diagram of the hydrogen compression plant.

Figure 6.51 illustrates the effect of inlet pressure on the exergy efficiency of the hydrogen compression plant where this parameter carries a dominant influence on the system performance. However, outlet pressure of hydrogen after electrolysis pressure is at ambient conditions and it corresponds to 62%, for a five-stage compression option. This value decreases down to 53% for two-stage compression. The plant shows the potential to be as high as 72% exergy efficient at higher compression stages with higher inlet pressure rates. Considering the energy efficiency of the plant, higher compression stages are not considered favorable with relatively lower performances values. A five-stage plant shows 90.2% energy efficiency where this value is higher at two stage compression. This is due to higher compression power requirement and lower enthalpy change of hydrogen at elevated pressures and ambient temperature. One should also note that the same pressure ratio is applied to the system regardless of the number of stages. Thus, lower stage options result in a lower pressure for the compressed hydrogen. High amounts of heat release at intercooling stages are efficiency decreasing factors and released heat is not considered to be a useful output from the overall system due to lower temperature energy content. However these values are lower when exergy is defined as a performance indicator and does not affect the exergetic efficiency as much as it does to energetic performance. The

effect of hydrogen inlet temperature is also shown in Figure 6.52, and it has a slight impact on the performance.

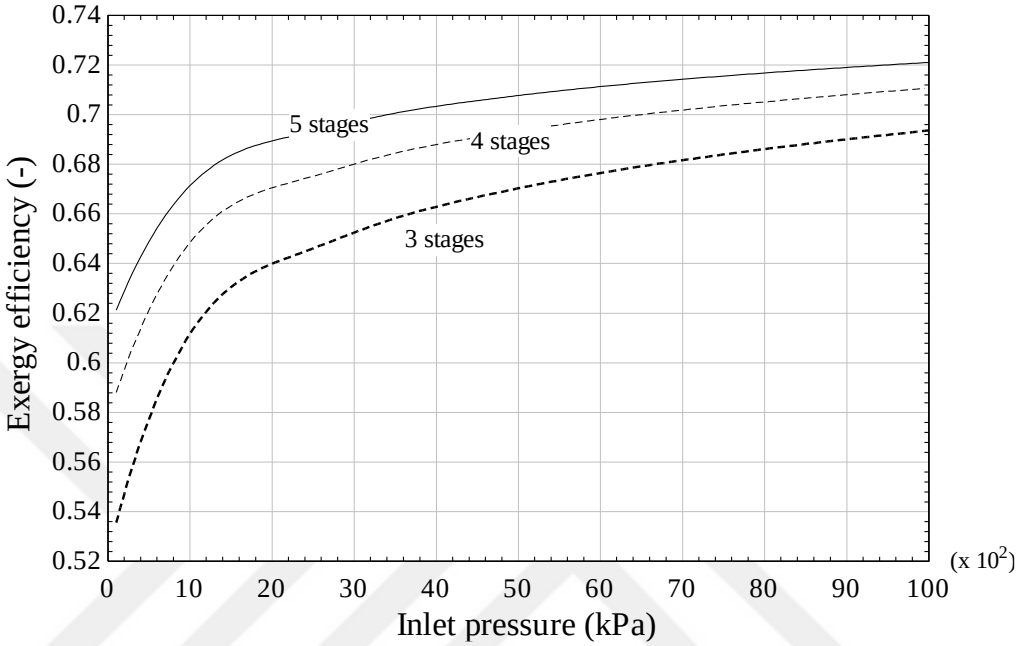

Figure 6.51 Effect of hydrogen inlet pressure on the exergy efficiency of the hydrogen compression plant subsystem.

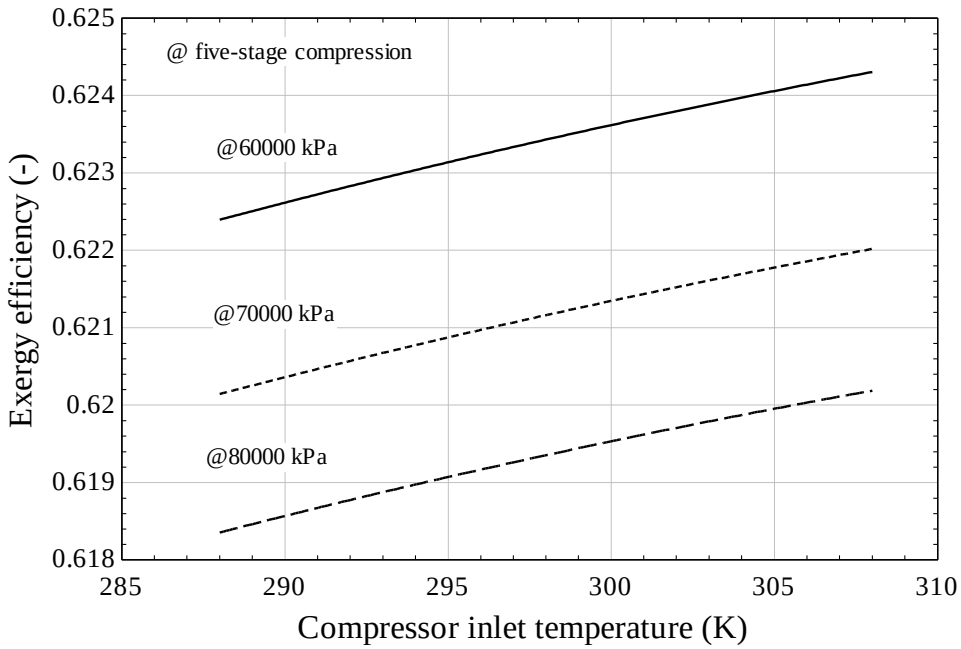

Figure 6.52 Effect of hydrogen inlet temperature on the exergy efficiency at various storage pressure values.

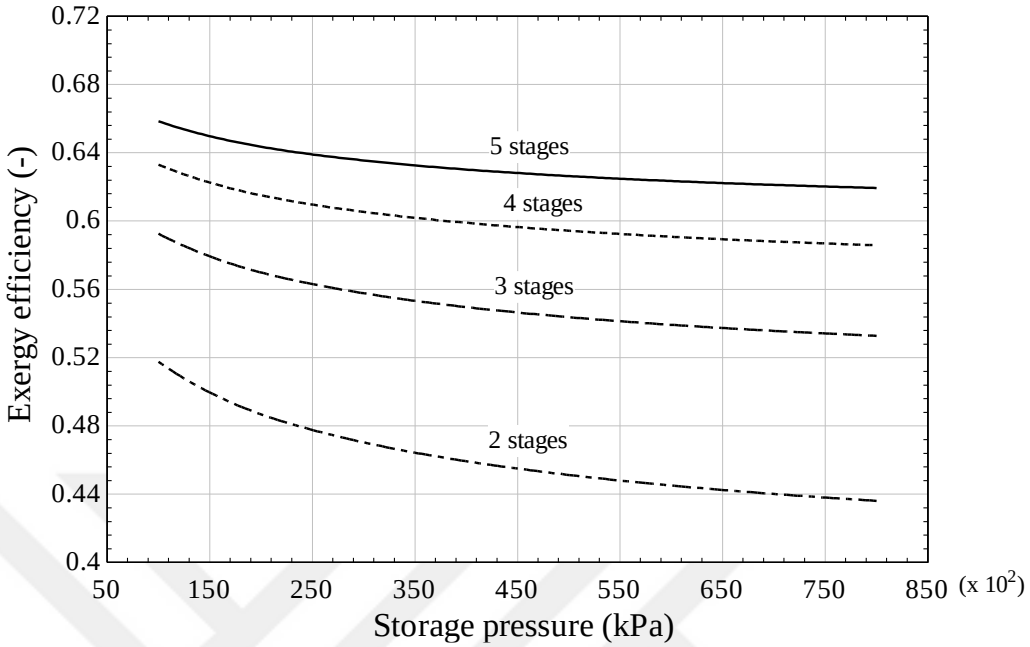

Figure 6.53 Effect of storage pressure on system exergy efficiency at various compression stages.

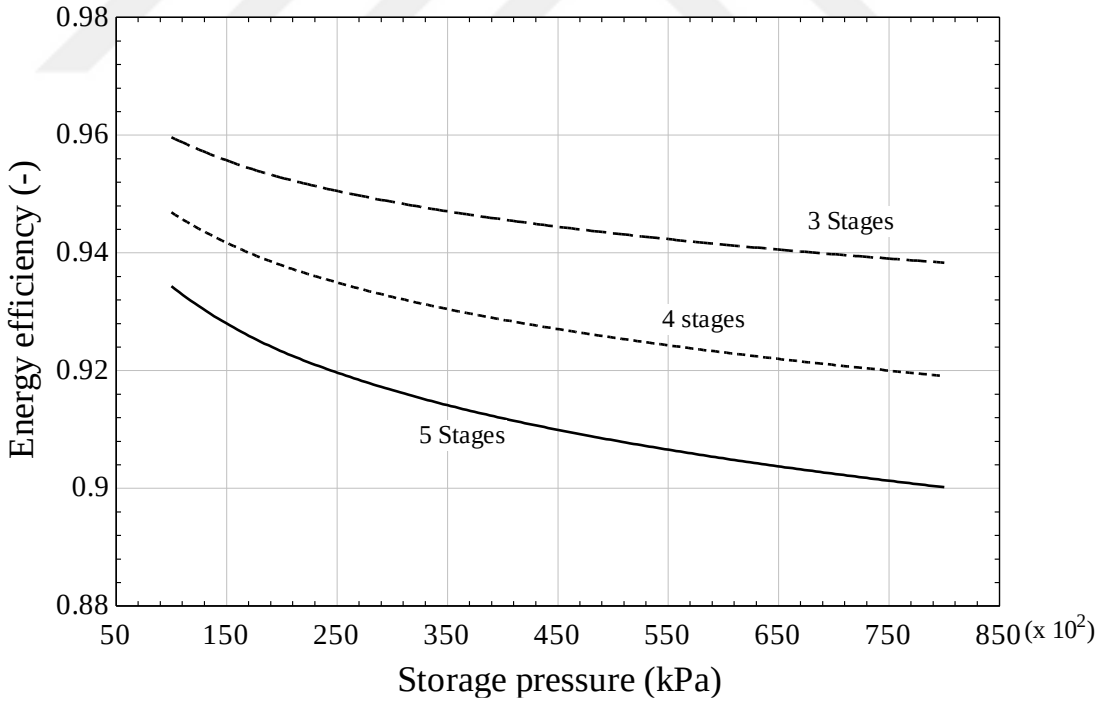

Figure 6.54 Effect of storage pressure on system energy efficiency at various compression stages.

Pressure is an assumed value and the higher it is, the higher the density of hydrogen. However, this energy intensive process drastically effects the performance of the hydrogen

compression plant both in terms of energy and exergy efficiencies. Figures 6.53 and 6.54 show the effect of storage pressure on system performances at various compression stages. Higher storage pressure requirements slightly decrease the exergy and energy performances with the same trend. Although increased storage pressure decrease the energy efficiency of the subsystem, higher pressure storage is recommended for the sake of increased energy density of hydrogen to favor transportation costs.

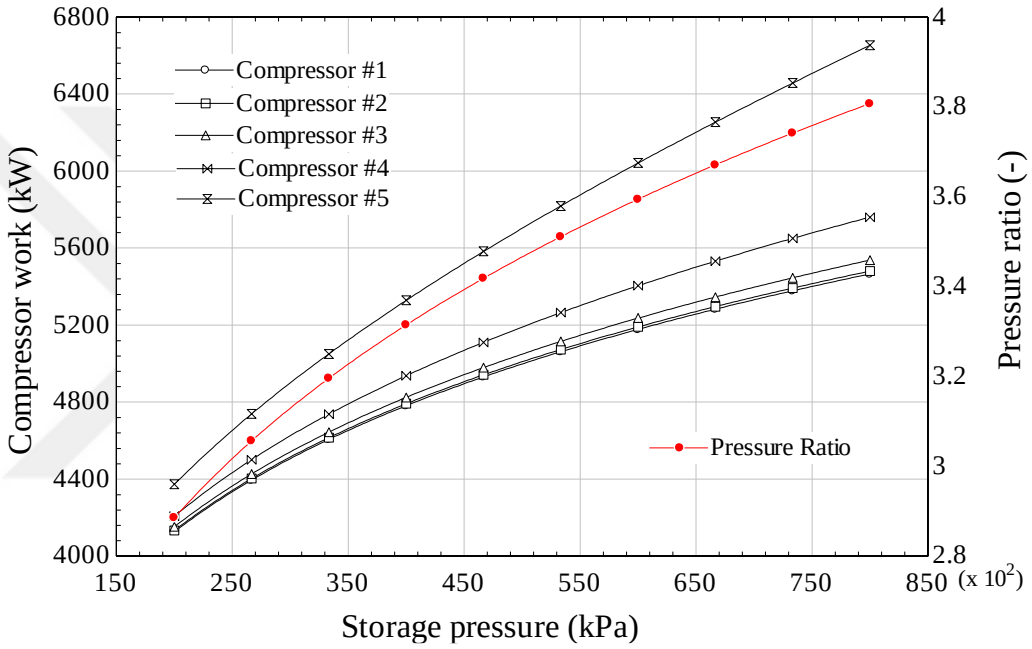

Figure 6.55 Power consumption of compressors at various storage pressure values.

A final representation can be made by comparing power consuming devices (Figure 6.55). The first four compressors show similar power consumption values where the pressure is increased up to 190 bar. After this step, compression is applied at the same pressure ratio from 200 bar to around 700-800 bar with a higher power consuming compressor, where this component consumes around 14% more power than that of compressor at stage 4. The total power consumption of the system is 28.02 MW to compress 1 kmol/s hydrogen to 700 bar in the five-stage option.

Supercritical CO_2 GT Cycle Subsystem

The supercritical CO_2 gas turbine cycle is a promising alternative to conventional gas turbine cycles with higher performance characteristics at lower maximum temperatures. A

recuperative cycle is considered for internal heat recovery within the system. The state point information and the T-s diagram are presented in Table 6.17 and Figure 6.56, respectively. Effects of the pressure ratio, the approach temperature, and the turbine inlet temperature are investigated, where these parameters have slight to strong influence on the cycle performance.

Table 6.17 State point information for the supercritical CO_2 gas turbine system.

State	T (K)	P (bar)	s (kJ/kgK)	h (kJ/kg)	ex (kJ/kg)	$\dot{Ex}$ (MW)
34	828	222	-0.01289	532.9	537.7	1657.19
35	694.9	74	0.005537	374	386.8	1192.12
36	354.9	74	-0.777	-6.866	225.7	695.61
37	318	74	-0.9692	-71.13	218.7	674.03
38	363.3	128.2	-0.9587	-45.71	241	742.76
39	318	128.2	-1.411	-198.4	223.1	687.59
40	334.9	222	-1.404	-183.2	236.3	728.27
41	644.9	222	-0.3223	306.1	403.2	1242.66

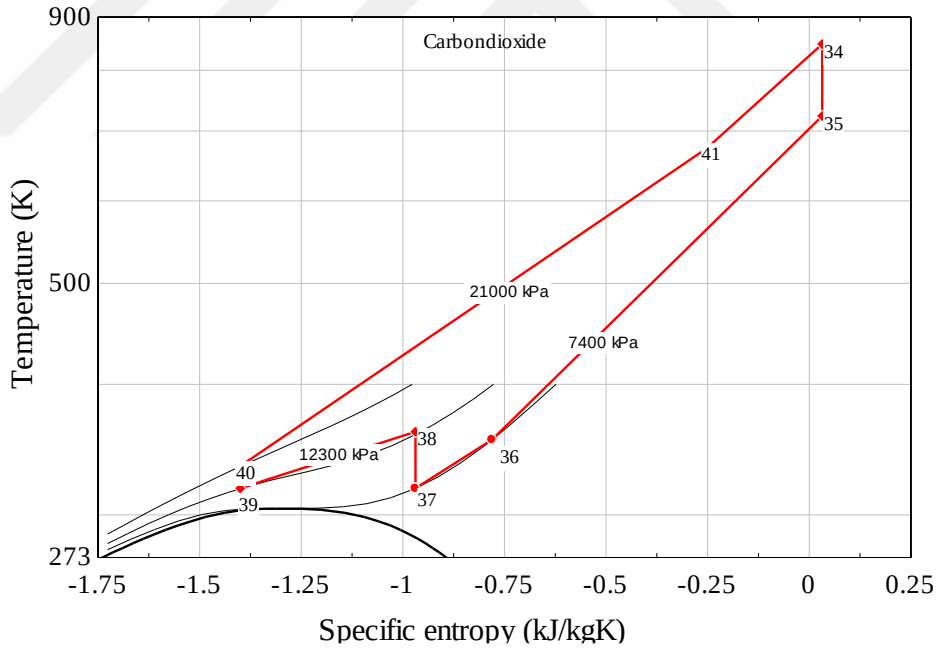

Figure 6.56 T-s diagram of the supercritical CO_2 gas turbine cycle.

The low pressure side of the cycle is set to 74 bar which is slightly above the critical pressure of CO_2. The high pressure side is not set as constant, but is instead decided by the pressure ratio. The effect of pressure ratio on power producing and consuming devices as well as the mass flow rate of the cycle is illustrated in Figure 6.57. A slight decrease at both power consuming and producing devices are observed until a pressure ratio of 2,

where a linear increase is than observed above 2. The mass flow rate of the cycle shows a significant decrease at higher pressure ratios, resulting in a more compact system. Even if higher pressure ratio seems to be favorable for the system size, the system performance should also be analysed at this range.

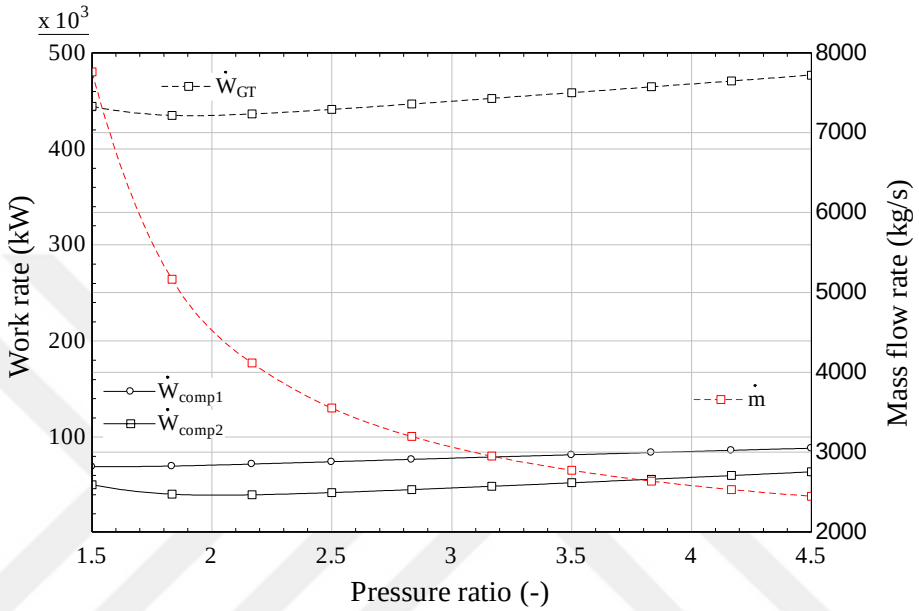

Figure 6.57 Effect of pressure ratio on the power producing and consuming devices and mass flow rate of the cycle.

The effect of pressure ratio on the cycle efficiencies and the back work ratio (BWR) is illustrated in Figure 6.58. The results show that higher pressure ratio enhances the system performances until 3.05, and a slight decrease is observed above this value. It should also be noted that the work consumption of compressors significantly increases at higher pressure ratios which would contribute to lower system performances. An optimum pressure ratio for both energy and exergy efficiencies is found to be 3.02. The internal heat recovery is one of the most crucial mechanisms within the GT cycle, where a reasonable assumption is made for the approach temperature. For the base case model, 20K assumption is made, where a parametric study is conducted to observe its influence on the system performance, and illustrated in Figure 6.59. A 20K difference in the approach temperature decreases the system exergy efficiency by 31.5%, and the energy efficiency by 32.1%. Best performing heat exchangers show low approach temperature values, however, heat exchanger technology for CO_2 is not yet a mature technology. Thus, 20K approach temperature is selected for more realistic results.

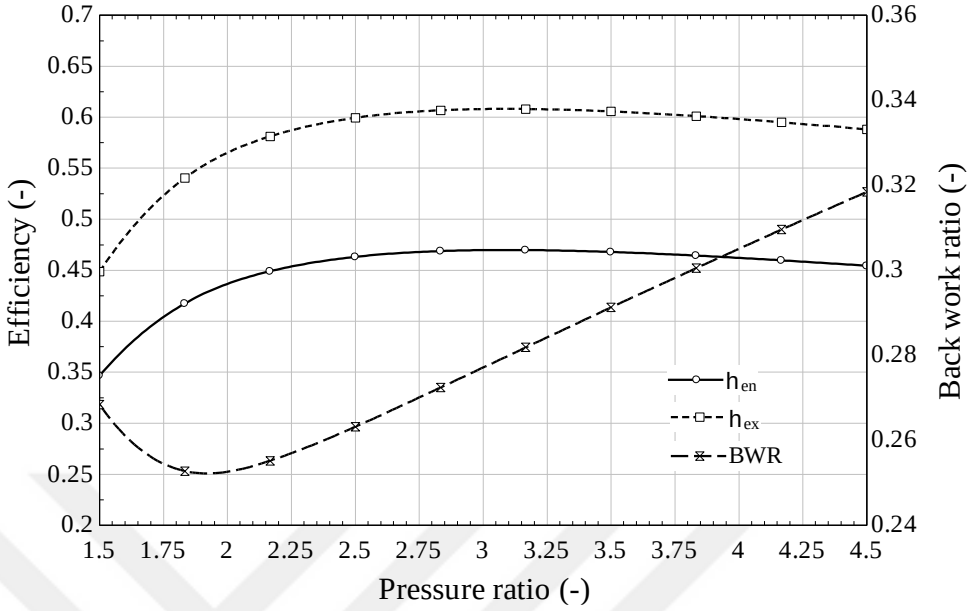

Figure 6.58 Effect of pressure ratio on the system efficiencies and back work ratio.

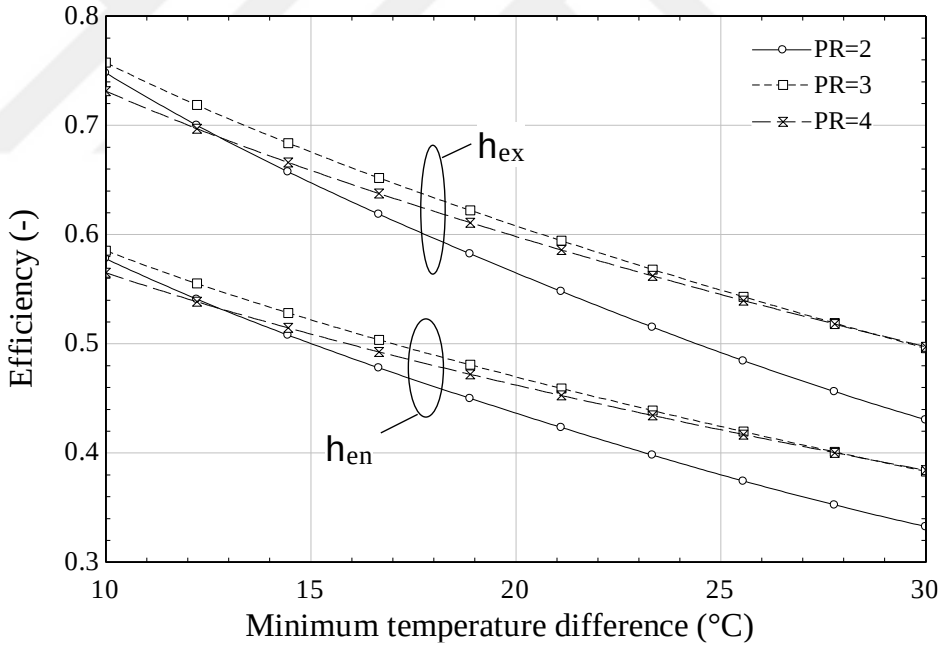

Figure 6.59 Effect of minimum temperature difference on the system efficiencies at various pressure ratios.

Since the maximum temperature from the solar subsystem can be up to 565ºC, a higher limit for maximum temperature is set as a constraint for the system. This maximum temperature can be higher than the mentioned value, however it should be noted that molten salt is considered for the solar subsystem in order to store energy for night time use.

Although it is not as effective as pressure ratio and approach temperature, higher turbine inlet temperature slightly increases both energy and exergy efficiencies within the system as shown in Figure 6.60. The base case model is based on the maximum temperature of the heat exchanger, for higher performance parameters.

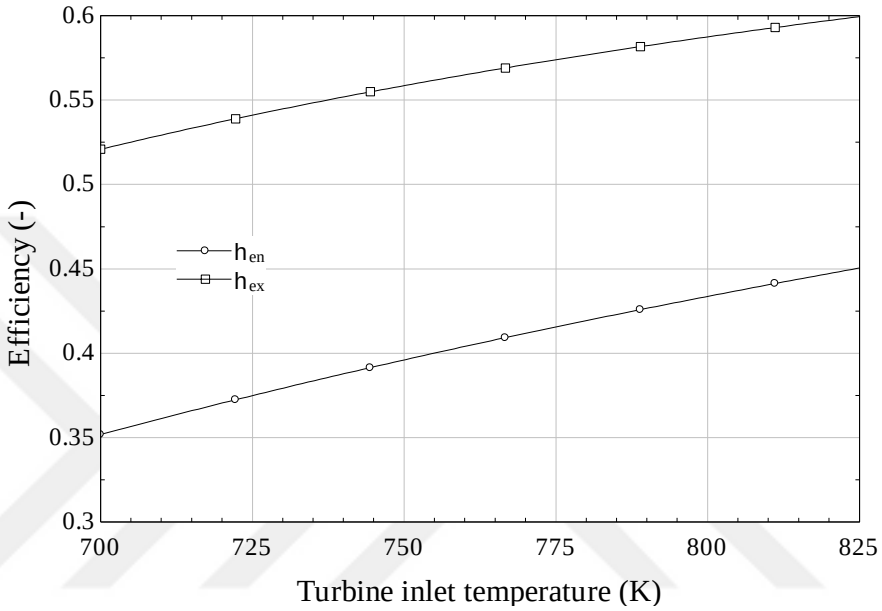

Figure 6.60 Effect of turbine inlet temperature on GT cycle efficiencies.

The modeled sCO_2-GT cycle consumes ~699 MW energy to produce the required power for the electrolysis of HCl in the Mg-Cl cycle and the compression of hydrogen by five-stage compressors. The parametric optimization results show that higher turbine inlet temperature and approach temperature increase system performances at a specific pressure ratio (3.02). The system energy and exergy efficiencies are found to be 46.5% and 60.9%, respectively. Use of supercritical CO_2-GT system is superior to conventional air gas turbine systems and shows the potential to perform at high performances at lower maximum temperature ranges. Even if this cycle shows relatively higher performance results, almost 208 MW energy is calculated as a total irreversibility within the cycle. A higher performing cycle with lower irreversibilities can be obtained by higher performing system components and proper selection and optimization of system parameters.

Solar Cycle Subsystem

The solar cycle subsystem is the main energy input for the first integrated system, where it provides high grade thermal energy for the Mg-Cl cycle and the sCO_2-GT cycle. As mentioned before, total heat requirement for the Mg-Cl cycle is found to be 248.58 MW and total heat input for the GT cycle is 698.9 MW. The solar cycle is designed by selecting GTA as the location and average values for Month of July are considered. State point information for the solar subsystem is given in Table 6.18. Energy load from the receiver is transferred to the Mg-Cl and the sCO_2-GT cycles' heat exchangers by splitting the energy stream. The total mass flow rate of the system is found to be 2644.2 kg/s, where 29.7% of this mass is transferred to supply heat for the Mg-Cl heat exchanger.

Table 6.18 State point information for the solar cycle.

State	T (ºC)	P (bar)	$\dot{m}$ (kg/s)	s (kJ/kgK)	h (kJ/kg)	$\dot{Ex}$ (MW)
1	565	1	2644.2	0.9394	532.9	668.87
2	565	1	1859	0.9394	532.9	668.87
2'	565	1	1859	0.9394	532.9	470.20
2''	565	1	785.2	0.9394	532.9	198.58
3	290	1	785.2	0.371	157.5	36.79
4	290	1	1859	0.371	157.5	87.16
5	290	1	2644.2	0.371	157.5	123.91

High and low temperature energy storage range for the molten salt (60% $NANO_3$, 40% KNO_3) is 565ºC and 290ºC, and this range is in perfect agreement with both GT and MgCl cycles. The System Advisory Model (SAM) software is utilized to determine daily, monthly, and annual solar energy information for the GTA. Irradiance values and dry bulb temperature for the GTA are shown in Figure 6.61, and layout of the heliostat field is given in Figure 6.62. Considering the amount of required heat, one field is not adequate to produce the desired amount of hydrogen (7.2 t/h). Thus, a ratio called 'Solar Multiple' is considered, which means the number of fields to produce required energy for hydrogen production. It is also possible to consider the energy production of one field, and size the hydrogen production cycle. However, existing thermodynamic results already provide a good information on the amount hydrogen production from a given energy source input.

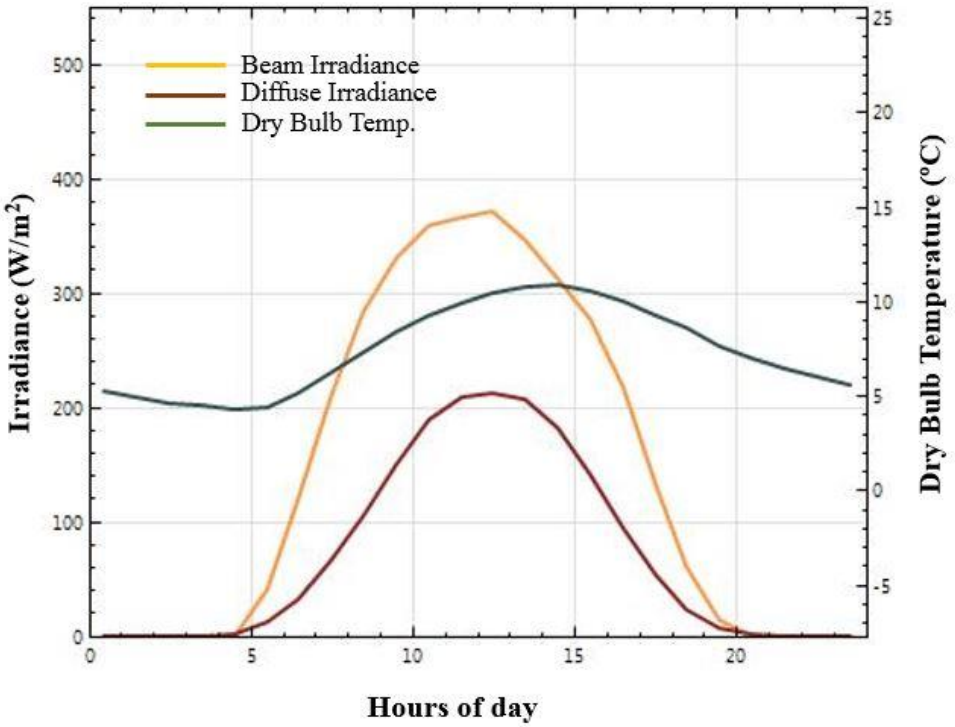

Figure 6.61 Annual environmental parameters for GTA.

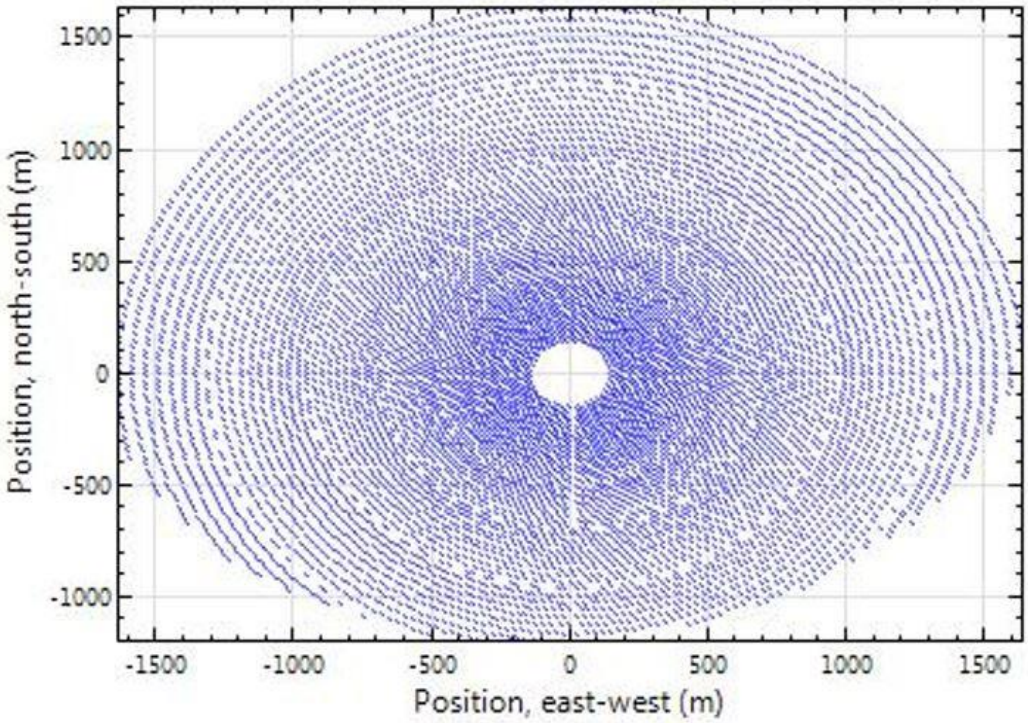

Figure 6.62 Layout of the heliostat field.

A variations of the absorbed thermal energy from the field and receiver efficiency is presented in Figure 6.63. Average values of the absorbed energy is adequate to run the system with the corresponding 'Solar Multiple' value, and efficiency of the receiver is up to 65% energy efficient. Temperature of the heat transfer fluid (HTF) from the receiver and to HEXs of the subsystems are illustrated in Figure 6.64 with the storage mode on and off. A possible issue is that the HTF temperature from storage might be too low for the decomposition reaction of the Mg-Cl cycle, jeopardizing the recycling throughout the system. Thus, one of the most crucial factors is to keep the maximum temperature above 450ºC at all times. Another option can be considered as utilizing the heat to produce only power from sCO_2-GT cycle, when the temperature from the solar field is not favorable for the Mg-Cl cycle.

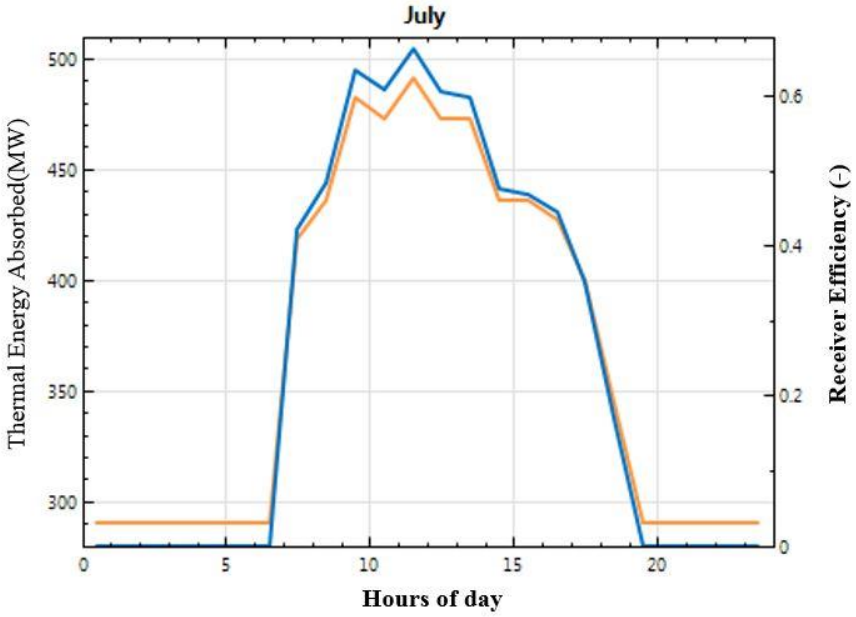

Figure 6.63 Variations of average absorbed thermal energy and reciever efficiency for the month of July.

The effect of irradiance, which is also related to time of the day, on the total field efficiency and the thermal energy of the cycle is plotted in Figure 8.65 using a scatter graph for various measurements in SAM software. Higher irradiance values result in higher system efficiency and higher useful thermal energy at higher temperatures. For the base case mode, irradiance values are taken as the average values from the month of July in GTA and adapted into the integrated system. Considering the required energy for the

subsystems, total energy from the field is calculated as 1535 MW where the exergy content corresponds to 1454 MW. Exergy efficiency of the field is calculated as the ratio of receiver exergy to solar exergy of the field, and it is found to be 44.2%.

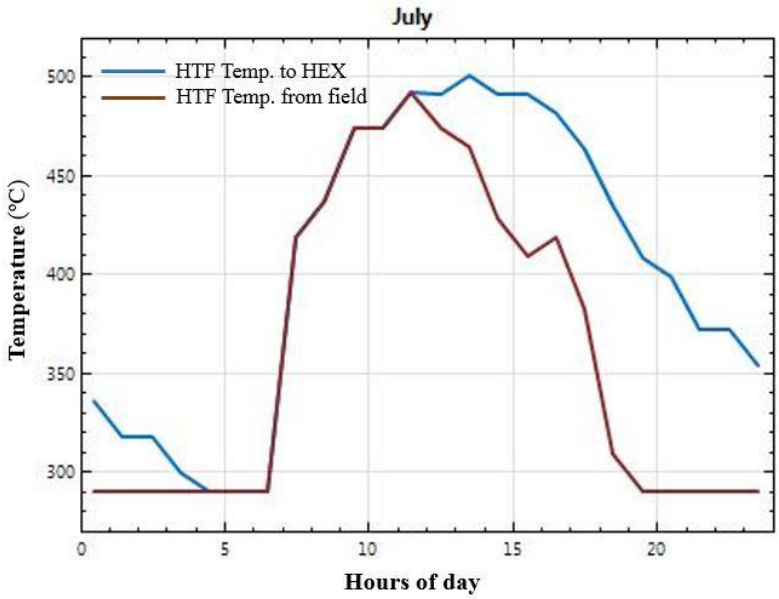

Figure 6.64 Temperature variations of the working fluid at when storage mode is on and off at the month of July.

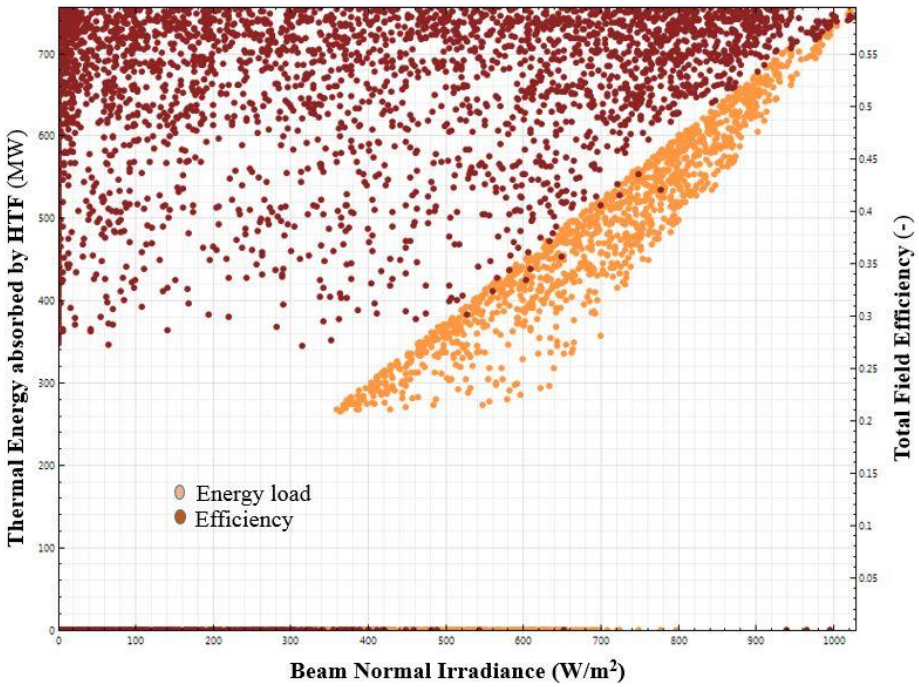

Figure 6.65 Energy Efficiency and energy load at various irradiance values.

A thermodynamic assessment of the overall system can now be comparatively evaluated using the obtained information from the subsystems. Energy and exergy efficiency comparisons of the system are illustrated in Figure 6.66, and irreversibility ratios are illustrated in Figure 6.67. The unique product of the integrated system is hydrogen at 700 bar, where its energy and exergy contents are calculated as 250.28 MW and 255.82 MW, respectively.

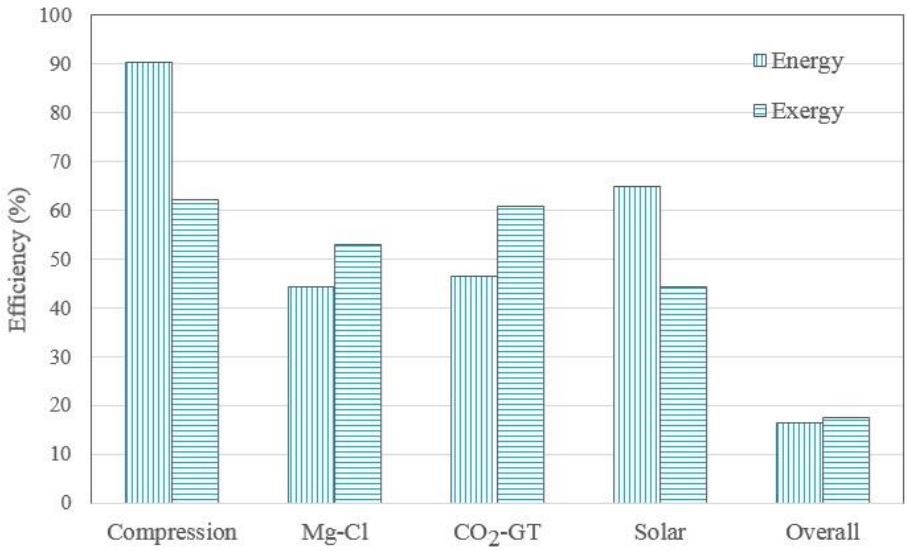

Figure 6.66 Energy and exergy efficiency comparison of the subsystems.

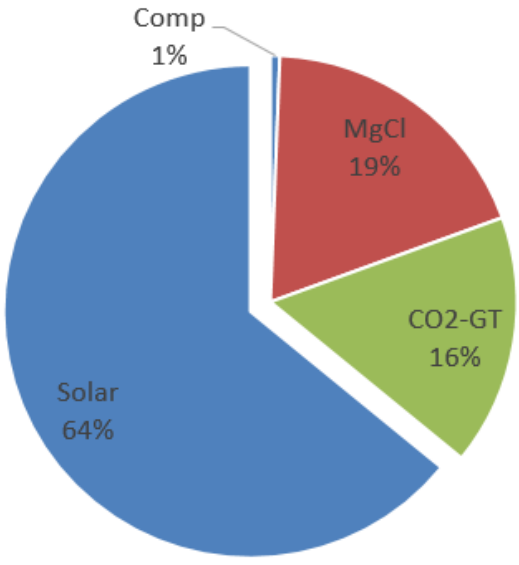

Figure 6.67 Irreversibility shares of subsystems in system I.

The total energy and exergy content of the energy input to the integrated system are calculated as 1535 MW and 1454 MW, respectively. Energy and exergy efficiencies of the overall system are calculated as 16.31% and 17.6%, respectively. When the energy and exergy loads of the receiver are taken into account as the main inputs, energy and exergy efficiencies become 25.1% and 39.8%, respectively. Total exergy destruction within the system is found to be 1265 MW where the solar field contains almost 64% of the total irreversibility with a value of ~811 MW.

6.6.2 Results for System II

The second integrated system proposed has common subsystems with the first integrated system using the same hydrogen production method only. Produced hydrogen is liquefied using Linde-Hampson liquefaction cycle, and power requirement is compensated by a steam Rankine cycle energized by CANDU SCW reactor. With known heat and power requirements of the Mg-Cl cycle, power consumption of the liquefaction cycle can be determined.

Liquefaction Cycle Subsystem

The cmpression of hydrogen gas up to 700 bar with the H_2 compression storage method increases the density of hydrogen to ~38 kg/m^3. Liquefied hydrogen shows an 1121 kg/m^3 density value at 23 K which is almost 30 times higher than for storage at high pressure. This option would make the transportation easier and cost effective. Thus, a Linde-Hampson type hydrogen liquefaction plant is considered for hydrogen storage for the second integrated system. The state point information and the T-s diagram of the cycle are presented in Table 6.19 and Figure 6.68, respectively. The chemical exergy content of hydrogen is the dominant factor in the total exergy, thus, the physical exergy content only slightly influences the overall evaluation. An isothermal compression of hydrogen is made and individual heat exchangers are internally utilized to cool down the high pressure hydrogen to its critical point. Liquid nitrogen is used to decrease the temperature to 50 K, where an expansion valve is used to liquefy hydrogen at 23 K. Liquid hydrogen is collected at the bottom of separator, and the remaining gas is utilized for internal cooling, before being fed back to the compressor at ambient conditions.

Table 6.19 State point information for the Linde-Hampson hydrogen liquefaction plant.

State	T (K)	P (kPa)	h (kJ/kg)	s (kJ/kgK)	Ex (MJ/kg)	$\dot{E}x$ (MW)
43	298	101	3815	52.99	238.500	238.5
44	298	101	3815	52.99	238.500	1591
45	298	101	3850	34.84	243.799	1662
46	146.2	8080	1826	25.24	244.558	1672
47	77.5	8080	904	16.7	246.113	1693
48	71.81	8080	820.1	15.57	246.356	1700
49	65	8080	714.1	14.02	246.699	1701
50	45.36	8080	381.4	7.924	248.136	1720
51	20.36	8080	381.4	18.73	245.001	1678
52	20.36	101	448.6	22.04	244.110	1417
53	56.81	101	840	33.16	241.277	1387
54	66.22	101	938.8	34.76	240.909	1379
55	288	101	3320	52.99	238.005	1343
60	20.36	101	381.4	18.73	245.001	251.5

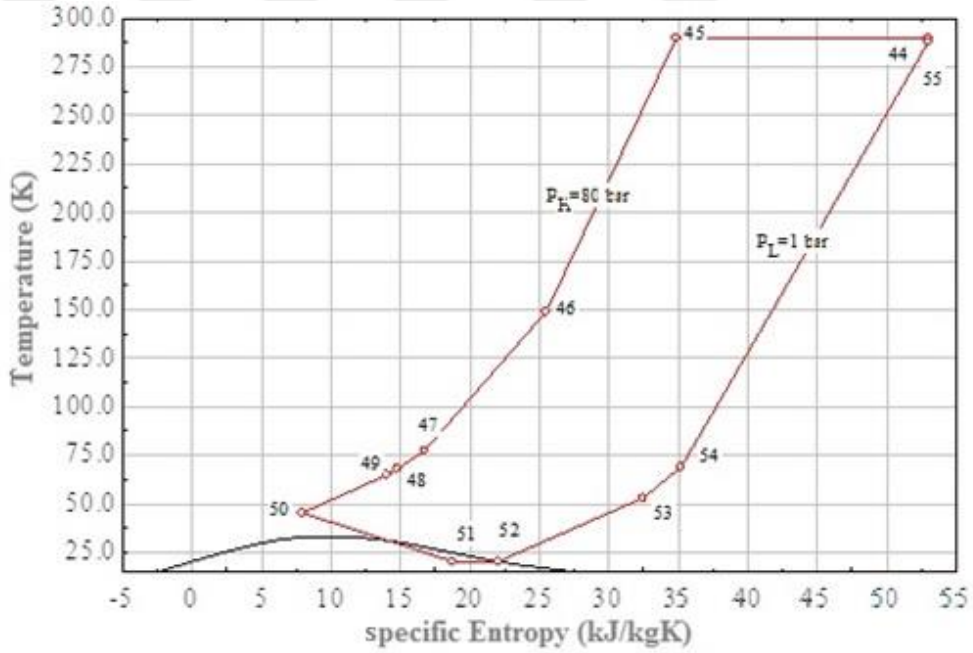

Figure 6.68 T-s diagram of the precooled Linde-Hampson hydrogen liquefaction plant.

Heat exchangers play a crucial role on liquefaction, and compression pressure is another influential factor. Effects of these two parameters are studied for enhanced system performance. An initial assumption is made on the cycle where the produced liquid hydrogen is 1 kmole/s. Thus, yield of this cycle corresponds to 1 kmol/s and the remaining amount is recirculated in the plant. This cycle shows an 11.56% yield, corresponding to liquid H_2 output. Effects of the compressor outlet pressure on liquid hydrogen yield and the specific work are illustrated in Figure 6.69. Higher outlet pressure is favorable for both

H_2 yield and the specific work of the system. It is expected that higher pressure would result in higher work consumption, however, power consumption of nitrogen liquefaction is also strongly manipulated by this parameter.

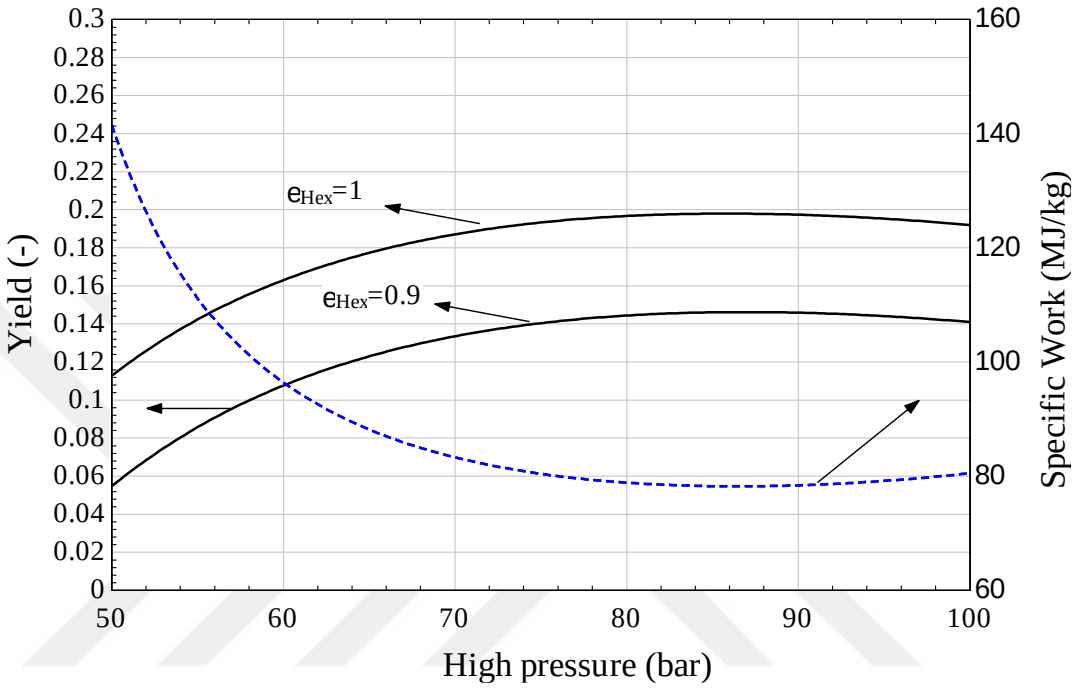

Figure 6.69 Effects of the compression pressure on liquid hydrogen yield and specific work consumption of the cycyle.

A general efficiency assessment of the precooled liquefaction cycle is made based on the liquid H_2 yield from the cycle. However, energy and exergy efficiencies are calculated based on main inputs and outputs to and from the system. Since the chemical exergy of hydrogen is very high, its physical exergy content does not influence the system performance as much as its chemical exergy content. However, all values related to physical exergy change of hydrogen are included in the efficiency assessment. Effect of compression pressure on system performances is illustrated in Figure 6.70. All performance parameters show a decreasing trend after 85 bar, due to relatively higher work consumption of the cycle. Thus, the compression pressure is set to 85 bar, and the heat exchanger effectiveness is kept at 85% in order to keep the cycle performance characteristics at a reasonable rate.

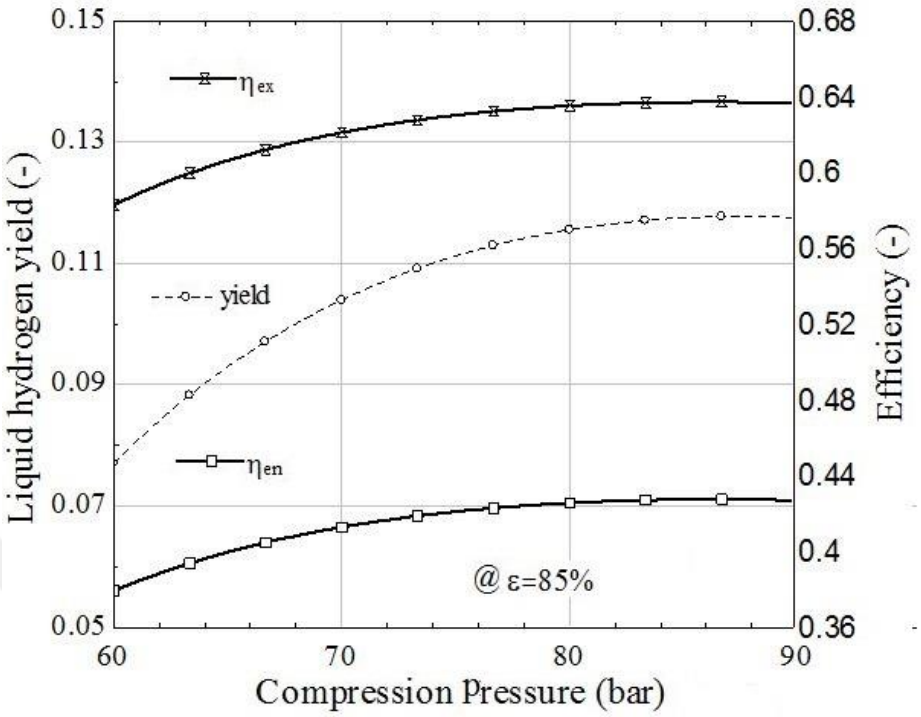

Figure 6.70 Effect of compression pressure on energy and exergy efficiencies.

The overall energy efficiency of the plant for the base case is found to be 42.7%, where the exergy efficiency is 63.7%. The total electrical work requirement to run the cycle including nitrogen liquefaction is found to be 156.46 MW to liquefy 1 kmole/s hydrogen. The total exergy destruction of the system is found to be 144.38 MW where the highest contribution is made by heat exchangers in the system. Compared to hydrogen compression plant, liquefaction cycle shows very high work requirement. However, transportation of hydrogen is costly, and higher volume requirement of compressed hydrogen may not be feasible for use in mobile applications.

Nuclear Rankine Cycle Subsystem

A reheat and regeneration type steam Rankine cycle (SRC) is considered for enhanced cycle performance, where the nuclear reactor is used as the boiler of the cycle. Total energy input of the nuclear reactor is based on total heat requirements of the Mg-Cl cycle and the SRC plant. Initially, the SRC plant is modeled and analysed based on total power requirement of liquefaction and the Mg-Cl cycle which is found to be 453.6 MW. The state point information and T-s diagram of the cycle are illustrated in Table 6.20 and Figure

6.71, respectively. The SRC cycle shows relatively higher performance results than that of conventional SRC plants with reheating and regeneration. Net power output is set to a constant number which is sum of power requirements of the Mg-Cl cycle and liquefaction plant, where the mass flow rate of the system is calculated based on this constant number.

Table 6.20 State point information for the SRC subsystem.

State	$\dot{m}$ (kg/s)	T (°C)	P (bar)	h (kJ/kg)	s (kJ/kgK)	ex (kJ/kg)	$\dot{E}x$ (MW)
17*	354.8	224.1	100	964.3	2.541	211.6	75.061
2	354.8	500	100	3374	6.597	1413	50.1154
3	45.06	341.9	34.18	3086	6.638	1112	50.097
4	309.7	198.7	10	2824	6.687	836.2	25.8985
5	309.7	500	10	3479	7.762	1170	362.348
6	42.7	399.5	5.029	3271	7.789	953.9	46.661
7	267	35.23	0.057	2463	8.017	78.62	20.504
8	267	35.23	0.057	147.6	0.5081	0.645	0.1682
9	267	35.28	5.029	148.2	0.5085	1.149	0.299.8
10	309.7	152.1	5.029	641.3	1.863	90.58	28.055
11	309.7	153.7	100	654.3	1.869	101.7	31.503
12	309.7	221.2	100	951.4	2.515	239.3	74.107
13	45.06	241.2	34.18	1043	2.713	239.3	10.781
14	45.06	243.2	100	1053	2.717	248.2	11.184

* Mass flow for the MgCl cycle HEX is not included.

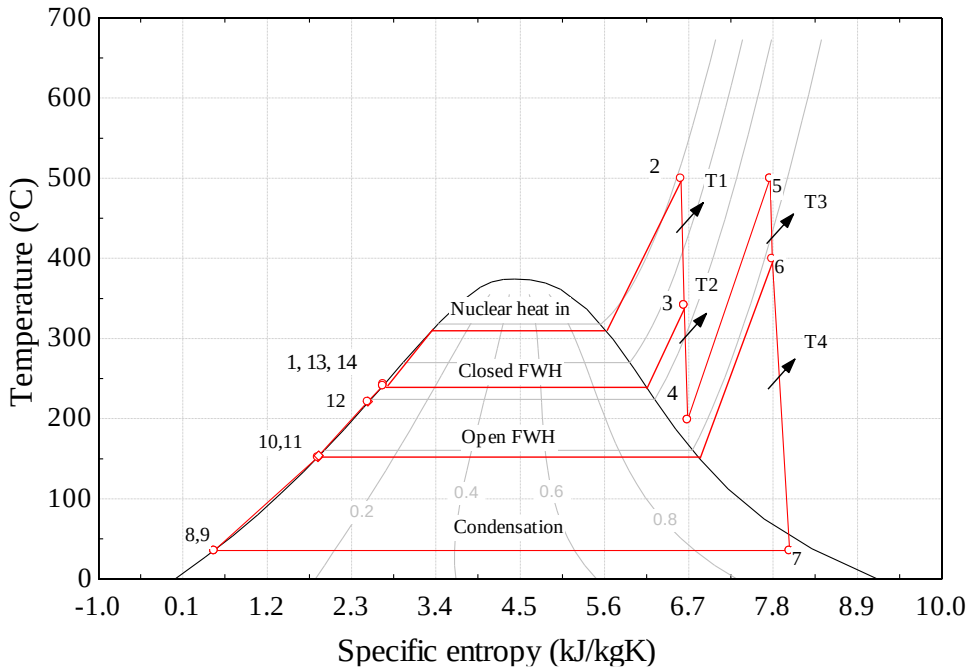

Figure 6.71 T-s diagram of the SRC plant.

Parametric studies are conducted to decrease the heat requirement of the cycle by manipulating various system and environmental parameters. Fractions of the turbine leaks (*f1* and *f2*) are calculated by writing an energy balance for open and close feed water heaters, where fraction of state 3 and 6 correspond to 12.7% and 15.8%, respectively.

Extraction pressures are initially assumed to be constant numbers within the high and low pressure values, and an optimization method is applied to enhance the energy performance of the cycle using the EES software. Energy and exergy efficiencies of the SRC system results in 42.9% and 62.8%, respectively, for the base model. Energy efficiency of the plant is superior to those of conventional plants. The total heat requirement to produce the desired power is found to be 1058 MW.

Effect of the boiler pressure on system mass flow rate, exergy efficiency, and plant input and output are illustrated in Figures 6.72 and 6.73. Higher boiler pressure influences all parameters with a similar trend except for the mass flow rate. For a more compact design, 85-90 bar range can be a feasible selection, even if it does not show as promising performance values. Both the heat input and the net power output decrease at higher boiler pressures, where decrease in heat input is higher resulting in higher exergy efficiency.

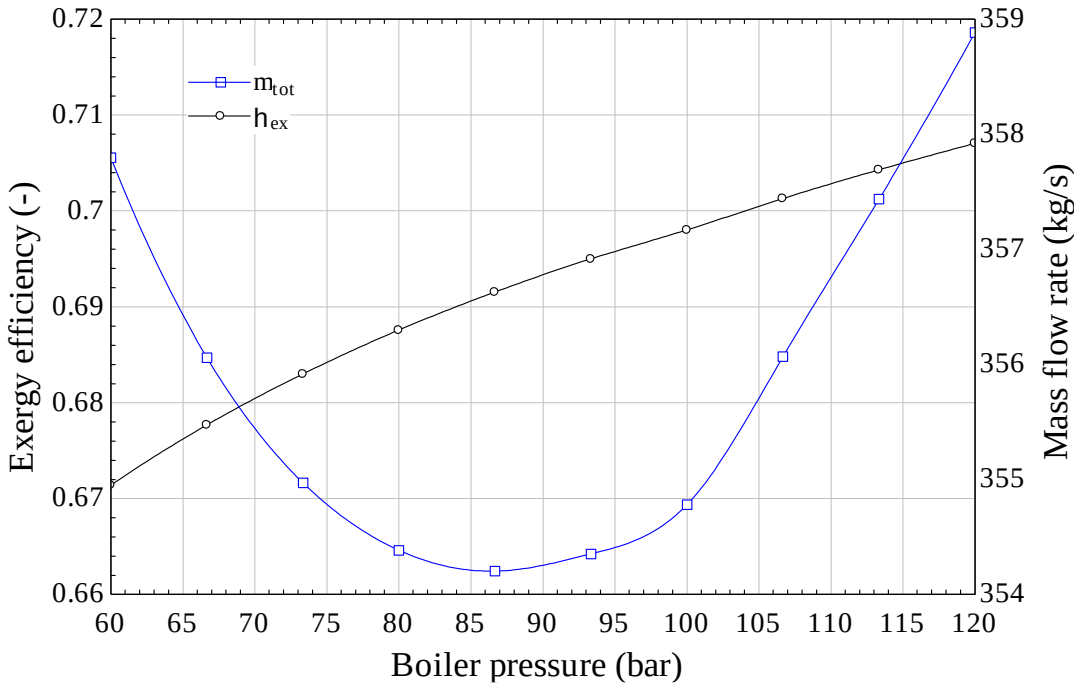

Figure 6.72 Effect of boiler pressure on mass flow rate and exergy efficiency of the SRC plant.

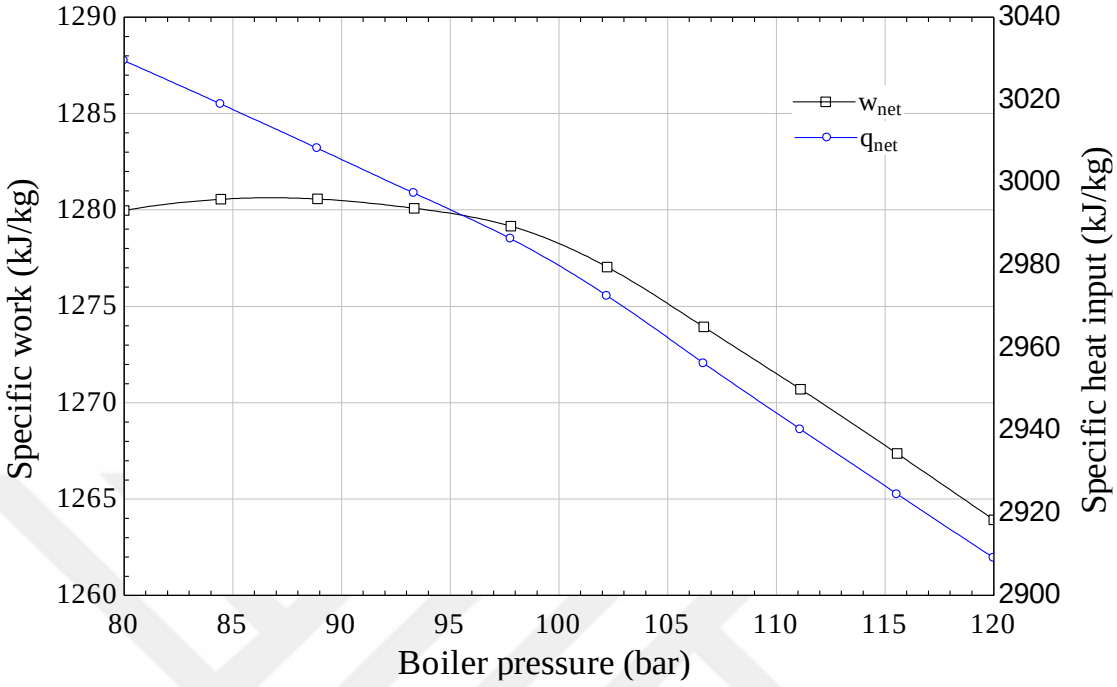

Figure 6.73 Effect of boiler pressure on the net specific work and heat.

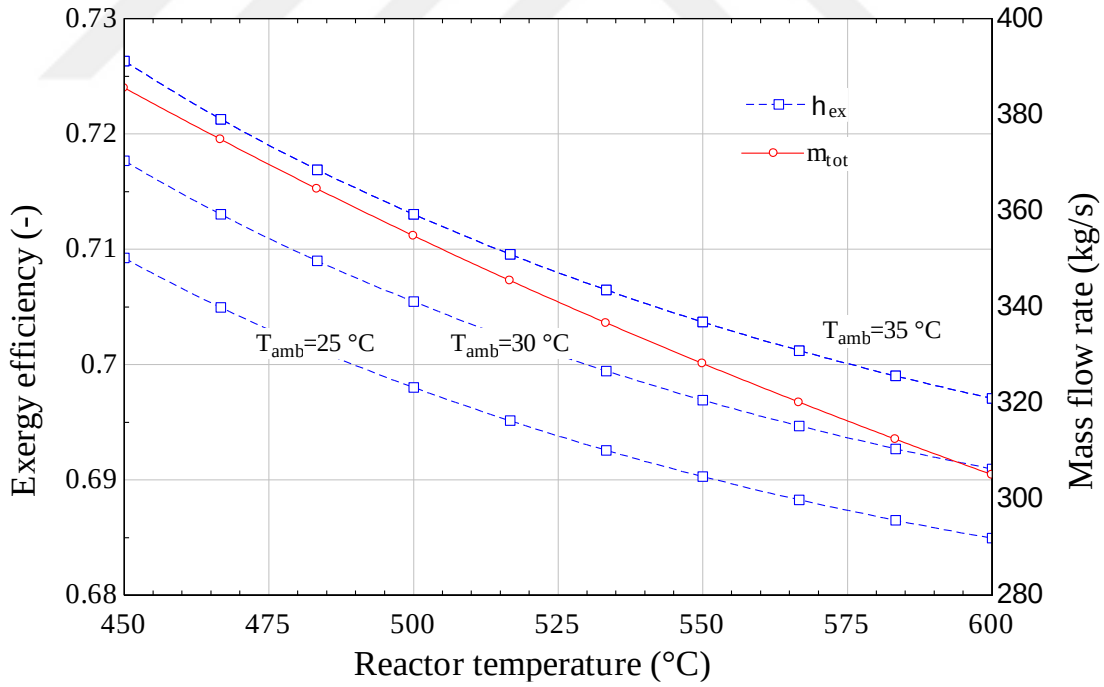

Figure 6.74 Effect of turbine inlet temperature and ambient temperature on system exergy performance and mass flow rate.

Effect of the turbine inlet temperature and ambient temperature on exergy performance of the system and mass flow rate is also illustrated in Figure 6.74. Higher

turbine inlet temperature at lower ambient temperatures are not favorable for system exergy performance, but it is highly effective on lower mass flow rate within the system. Lower exergy efficiency values are due to higher thermal exergy of the input energy at elevated temperatures. A more compact design of the system can be made by higher turbine inlet temperature and boiler pressure, where it is not much effected by the environmental parameters.

The heat requirement of the Mg-Cl cycle is also compensated by the nuclear reactor by providing 248.58 MW of energy to HEX of the cycle. The grade of the heat is kept higher than 320 ºC, and steam is used as the heat transfer fluid. Total heat provided by the nuclear cycle to run the integrated system is found to be 1306.58 MW. Efficiency assessment of the integrated system can now be made by calculating efficiencies based on main inputs and outputs to and from the system.

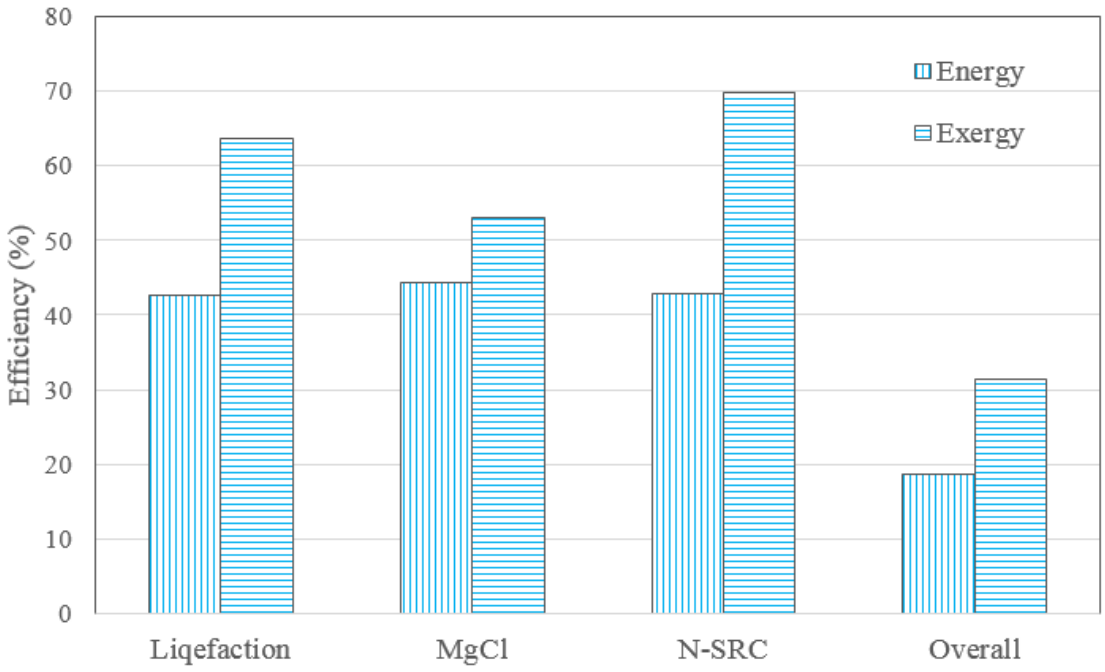

Figure 6.75 Energy and exergy efficiency comparisons of system II.

Total energy and exergy efficiencies of the plant are found to be 18.6% and 31.35%, respectively. It should be noted that energy and exergy efficiencies of uranium processing are 33%, and 26.7%, respectively (Ozbilen, 2013). When both efficiencies associated with the uranium processing process is taken into account, energy and exergy efficiencies of the second system become 6.14% and 8.37%, respectively. However, nuclear performance

assessments are in general made without taking the uranium processing into account. Thus, it is more appropriate to present existing calculated values. However, the efficiency calculations for the solar field is calculated by considering the energy input from solar radiation, therefore, one can claim that the solar energy from heliostat field can be a more efficient option than the nuclear based operation.

The comparisons of the subsystem efficiencies and total exergy destructions are illustrated in Figures 6.75 and 6.76. Here, highest irreversibility ratio belongs to the Mg-Cl cycle by 41%. Liquefaction system also contributes to total irreversibilities with a high ratio compared to that of System I (H_2 compression). When the uranium processing is taken into account, nuclear rankine cycle would show the highest share of the total irreversibility rate.

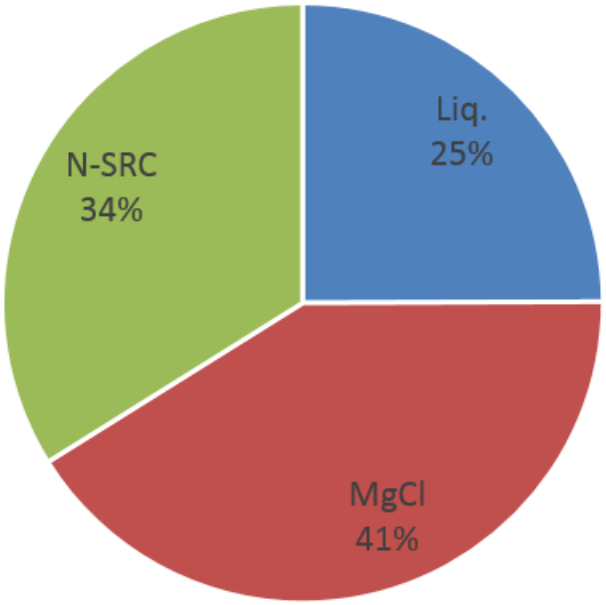

Figure 6.76 Exergy destruction ratios of system II subsystems.

A final comparison of the integrated systems are tabulated in Table 6.21. Even if hydrogen is the unique output from both systems, the physical exergy and energy of hydrogen varies with the storage method. System II is more efficient than that of system I with both efficiency parameters, and shows lower total exergy destruction. This is due to very high exergy destruction of the heliostat field in the first system.

Table 6.21 Performance comparison of integrated systems.

	Unit	System I	System II
Energy input	MW	1535	1306
Exergy input	MW	1454	802.3
Energy output	MW	250.3	242.8
Exergy output	MW	255.8	251.5
Exergy destruction	MW	1199	550.8
Energy Efficiency	%	16.3	18.6
Exergy Efficiency	%	17.6	31.4

CHAPTER 7: CONCLUSIONS AND RECOMMENDATIONS

7.1 Conclusions

The Mg-Cl hybrid thermochemical cycle is one of the promising methods to split water into hydrogen and oxygen by utilizing intermediate temperature heat to decrease the relatively high electrical input of conventional methods such as water electrolysis. This thesis provides a comprehensive investigation of the Mg-Cl cycle for its ideal and practical characteristics, several configuration developments, thermodynamic and economic assessments, and cycle integration for sustainable hydrogen production. This thesis is organized in five main steps as follows; (i) investigation of the ideal and practical cases of the conventional three-step cycle, (ii) configuration developments of the conventional cycle by considering reaction thermochemistry for a better performing system, (iii) experimental investigation of developed configurations to validate their feasibility, (iv) thermodynamic and thermoeconomic assessment, and optimization of the cycle to investigate its feasibility by comparing with other hybrid thermochemical cycles, (v) integration and thermodynamic assessment of the cycle for a sustainable hydrogen production and storage.

Some of the key conclusions from this thesis can be summarized as follows:

- The ideal three-step Mg-Cl cycle shows 51.6% energy, and 67.6% exergy efficiency values at stoichiometry conditions.
- The Mg-Cl-A cycle has lower energy and exergy efficiencies by 36.8% and 44.1%, respectively, than that of the ideal cycle, leading to an infeasible cycle with high heat and power consumption which cannot compete with other methods for water splitting.
- The Mg-Cl-B cycle is also an infeasible configuration due to high steam requirement of the hydrolysis step and high reaction heat of the chlorination reactor. Energy and exergy efficiencies of this configuration are 30% and 37.7%, respectively.
- The newly developed four-step Mg-Cl-C cycle is a more feasible option that that of previous configurations in terms of efficiency and power consumption. Energy

and exergy efficiencies of the Mg-Cl-C cycle are 43.7% and 52%, respectively, where the electrical energy consumption is 3.1% lower than that of water electrolysis.

- The four-step cycle recovers half of the HCl in dry form, where the remaining HCl is still in mixture with steam. Therefore, a separation process is considered to capture HCl in dry form from the HCl/steam mixture. An experimental procedure is developed to validate the hydrochlorination of MgO with aqueous HCl.
- Mixing of the aqueous HCl with MgO at ambient conditions results in several side products, especially hydrates of $MgCl_2$. Therefore, experiments are conducted from 150ºC to 275ºC by manipulating various other parameters.
- The HCl capture is accomplished safely at 275ºC reactor temperature at its highest level by 30.8 ∓ 0.36%. The reactor temperature is limited to 280ºC due to possible formation of MgO particles from the dehydration of $Mg(OH)_2$ and the hydrolysis of possible $MgCl_2$ content.
- Although lower temperature reactions are thermodynamically favorable for further internal heat utilization within the Mg-Cl cycle, there are too many side reactions due to $MgCl_2$ hydrates which jeopardize the recycling process of MgO. Thus, the reaction temperature should be above 250ºC for better MgOHCl formation.
- The energy and exergy efficiencies of the modified four-step Mg-Cl-C cycle are 44.3% and 53%, respectively, after adaptation of experimental results. The modified cycle is more efficient than all other configurations.
- The electrical power requirement of the final configuration is 14.5% lower than direct aqueous HCl electrolysis, and 6.7% lower than the water electrolysis.
- The cost of hydrogen production from the four-step Mg-Cl cycle is $3.67/kg of H_2. Cost of hydrogen production is lower than that of HyS cycle and slightly higher than the Cu-Cl cycle. Contribution of the separation process and comparatively higher electrical work consumption of the Mg-Cl cycle carry the major impact on the hydrogen cost. However, cost of the cycle is in a feasible range and can be competitive among other hybrid cycles.
- The optimized annual cost of the modified four-step Mg-Cl cycle is $ 409.3 million which is 10.73% lower than that of base case. The maximum achievable exergy

efficiency of the modified Mg-Cl cycle is 56.24%, and 5.8% higher than the base case.

- The energy and exergy efficiencies of system I are 16.31% and 17.6%, respectively. When the energy and exergy loads of the receiver are taken into account as the main inputs, energy and exergy efficiencies become 25.1%, and 39.8%, respectively. The total exergy destruction ratio belongs to the solar field by ~64%.
- The overall energy and exergy efficiencies of system II are found to be 18.6%, and 31.35%. The highest irreversibility ratio belongs to the Mg-Cl cycle by 41%.
- System II is more efficient than system I in terms of efficiency values, and shows lower total exergy destruction. This is due to very high exergy destruction of the heliostat field in system I.

7.2 Recommendations

Several recommendations can be made for future research on the Mg-Cl cycle, and they are listed as follows:

- A comprehensive experimental investigation should be conducted to study the characteristics of chlorination of MgO particles produced from decomposition of MgOHCl as in the four-step Mg-Cl cycle.
- A fluidized bed type reactor should be used to increase the HCl capture ratio which would result in further enhancement of the four-step Mg-Cl cycle.
- A kinetics study should be performed to further determine the rate of the hydrochlorination reaction.
- An extensive research should be performed for a less steam requiring hydrolysis reactor in order to decrease the energy requirement of the Mg-Cl cycle.
- Renewable energy sources, ranging from solar to biomass, should be considered to supply the necessary heat and electricity for the overall Mg-Cl cycle and its integrated systems.
- Feasibility of the Mg-Cl cycle based integrated systems should be further investigated by co-, tri- and multi-generation of various energy forms.

REFERENCES

Alkan, M., Oktay, M., Kocakerim, M. M., Çopur, M. (2005). Solubility of chlorine in aqueous hydrochloric acid solutions. *Journal of Hazardous Materials*, 119(1), 13-18.

Al-Sulaiman, F. A., Atif, M. (2015). Performance comparison of different supercritical carbon dioxide Brayton cycles integrated with a solar power tower. *Energy*, 82, 61-71.

Anderson, E. B., Taylor, E. J., Wilemski, G., Gelb, A. (1994). A high performance hydrogen/chlorine fuel cell for space power applications. *Journal of Power Sources*, 47(3), 321-328.

Aramendía, M. A., Borau, V., Jiménez, C., Marinas, J. M., Ruiz, J. R., & Urbano, F. J. (2003). Influence of the preparation method on the structural and surface properties of various magnesium oxides and their catalytic activity in the Meerwein–Ponndorf–Verley reaction. *Applied Catalysis A: General*, 244(2), 207-215.

Ashrafizadeh, S. N., Mohammadi, F., Sattari, A., Shojaikaveh, N. (2010). Prediction of Cell Voltage and Chlorine Current Efficiency of Aqueous HCl Electrolysis Utilizing an Oxygen Reducing Cathode Based on Artificial Neural Network. *ECS Transactions*, 25(33), 27-42.

Aspen Plus user guide (2003). *Aspen Technology Limited*, Cambridge, Massachusetts, United States.

Atif, M., Al-Sulaiman, F. (2014). Performance analysis of supercritical CO_2 Brayton cycles integrated with solar central receiver system. In *Renewable Energy Congress (IREC)*, 2014 5th International (pp. 1-6). *IEEE*.

Balat, M. (2009). Gasification of biomass to produce gaseous products. *Energy Sources, Part A*, 31(6), 516-526.

Balko, E. N. (1981). *U.S. Patent No. 4,294,671*. Washington, DC: U.S. Patent and Trademark Office.

Ball, M., Wietschel, M. (2009). The future of hydrogen–opportunities and challenges. *International Journal of Hydrogen Energy*, 34(2), 615-627.

Balta, M. T., Dincer, I., & Hepbasli, A. (2012). Energy and exergy analyses of magnesium-chlorine (Mg-Cl) thermochemical cycle. *International Journal of Hydrogen Energy*, 37(6), 4855-4862.

Barbir, F., Veziroğlu, T. N. (1992). Effective costs of the future energy systems. *International Journal of Hydrogen Energy*, 17(4), 299-308.

Baker, C. R., Shaner, R. L. (1978). A study of the efficiency of hydrogen liquefaction. *International Journal of Hydrogen Energy*, 3(3), 321-334.

Barmashenko, V., Jörissen, J. (2005). Recovery of chlorine from dilute hydrochloric acid by electrolysis using a chlorine resistant anion exchange membrane. *Journal of Applied Electrochemistry*, 35(12), 1311-1319.

Bartling, J., Winnick, J. (2003). Chlorine recovery from anhydrous hydrogen chloride in a molten salt electrolyte membrane cell. *Journal of the Electrochemical Society*, 150(6), D99-D107.

Biniwale, R. B., Mizuno, A., Ichikawa, M. (2004). Hydrogen production by reforming of iso-octane using spray-pulsed injection and effect of non-thermal plasma. *Applied Catalysis A: General*, 276(1), 169-177.

Brown, R. N. (1997). Compressors: Selection and sizing. *Gulf Professional Publishing.*

Bulan, A., Hansen, W., Gestermann, F., Grossholz, M., Pinter, H. D. (2006).*U.S. Patent No. 7,128,824*. Washington, DC: U.S. Patent and Trademark Office.

Call, D., Logan, B. E. (2008). Hydrogen production in a single chamber microbial electrolysis cell lacking a membrane. *Environmental Science & Technology*, 42(9), 3401-3406.

Carmo, M., Fritz, D. L., Mergel, J., Stolten, D. (2013). A comprehensive review on PEM water electrolysis. *International Journal of Hydrogen Energy*, *38*(12), 4901-4934.

Chachuat, B., Mitsos, A., Barton, P. I. (2005). Optimal design and steady-state operation of micro power generation employing fuel cells. *Chemical Engineering Science*, 60(16), 4535-4556.

Christensen, N. C. (1946). *U.S. Patent No. 2,413,292*. Washington, DC: U.S. Patent and Trademark Office.

Collado, F. J. (2009). Preliminary design of surrounding heliostat fields. *Renewable Energy*, 34(5), 1359-1363.

De Bakker, J., Peacey, J., Davis, B. (2012). Thermal decomposition studies on magnesium hydroxychlorides. *Canadian Metallurgical Quarterly*, 51(4), 419-423.

Deb, K. (2001). Multi-objective optimization using evolutionary algorithms (Vol. 16). *John Wiley & Sons.*

Department of Energy, (2010). *Annual Energy Outlook*. Washington, D.C.

Dincer, I. (2000). Renewable energy and sustainable development: a crucial review. *Renewable and Sustainable Energy Reviews*, 4(2), 157-175.

Dincer, I. (2012). Green methods for hydrogen production. *International Journal of Hydrogen Energy*, 37(2), 1954-1971.

Dincer, I., Kanoglu, M. (2011). Refrigeration Systems and Applications. *John Wiley & Sons*.

Dincer, I., Rosen, M. A. (2012). Exergy: energy, environment and sustainable development. *Newnes*.

Dincer, I., Zamfirescu, C. (2012). Sustainable hydrogen production options and the role of IAHE. *International Journal of Hydrogen Energy*, 37(21), 16266-16286.

Dincer, İ., Zamfirescu, C. (2014). Advanced Power Generation Systems. *Academic Press*.

Dincer, I., Acar, C. (2015). A review on clean energy solutions for better sustainability. *International Journal of Energy Research*, 39(5), 585-606.

Dokiya, M., Kotera, Y. (1976). Hybrid cycle with electrolysis using Cu Cl system. *International Journal of Hydrogen Energy*, 1(2), 117-121.

Eames, D. J., Newman, J. (1995). Electrochemical Conversion of Anhydrous HCl to Cl2 Using a Solid-Polymer-Electrolyte Electrolysis Cell. *Journal of the Electrochemical Society*, 142(11), 3619-3625.

Eberle, U., Arnold, G., Von Helmolt, R. (2006). Hydrogen storage in metal–hydrogen systems and their derivatives. *Journal of Power Sources*, 154(2), 456-460.

El-Emam, R. S., Ozcan, H., Dincer, I. (2015). Comparative cost evaluation of nuclear hydrogen production methods with the Hydrogen Economy Evaluation Program (HEEP). *International Journal of Hydrogen Energy.*

Eom, H. C., Park, H., Yoon, H. S. (2010). Preparation of anhydrous magnesium chloride from ammonium magnesium chloride hexahydrate. *Advanced Powder Technology*, 21(2), 125-130.

Ferrandon, M. S., Lewis, M. A., Tatterson, D. F., Nankanic, R. V., Kumarc, M., Wedgewood, L. E., Nitsche, L. C. (2008, March). The hybrid Cu–Cl thermochemical cycle. I. Conceptual process design and H2A cost analysis. II. Limiting the formation of CuCl during hydrolysis. In *NHA Annual Hydrogen Conference, Sacramento convention center*, CA (Vol. 10, pp. 3310-3326).

Funk, J. E. (1976). Thermochemical production of hydrogen via multistage water splitting processes. *International Journal of Hydrogen Energy*, 1(1), 33-43.

Generation IV International Forum (GIF), (2014). *Annual Report*. Retrieved from https://www.gen4.org/gif/upload/docs/application/pdf/201505/gif_2014_annual_report_final.pdf

Gooding, C. H. (2009). Analysis of alternative flow sheets for the hybrid chlorine cycle. *International Journal of Hydrogen Energy*, 34(9), 4168-4178.

Gorensek, M. B., Summers, W. A. (2009). Hybrid sulfur flowsheets using PEM electrolysis and a bayonet decomposition reactor. *International Journal of Hydrogen Energy*, 34(9), 4097-4114.

Grimes, C. A., Varghese, O. K., Ranjan, S. (2008). *Hydrogen generation by water splitting* (pp. 35-113). Springer US.

Guide, M. U. S. (1998). *The Mathworks. Inc*., Natick, MA, 5, 333.

Haag, G. L. (1977). Kinetics of the hydrolysis of $MgCl_2$ and the chlorination of magnesia (No. IS-T-742). *Ames Lab.*, IA (USA).

Hesson, R. N. (1979). Kinetics of the chlorination of magnesium oxide (No. IS-T-823). *Ames Lab.*, IA (USA).

Holladay, J. D., Hu, J., King, D. L., Wang, Y. (2009). An overview of hydrogen production technologies. *Catalysis Today*, 139(4), 244-260.

Holland, J.H. (1975). Adaptation in natural and artificial systems. Ann Arbor: *University of Michigan Press.*

Hotta, Y., Kuboki, T., Morita, T. (2014). *U.S. Patent* 14/210,747.

Huskinson, B., Rugolo, J., Mondal, S. K., Aziz, M. J. (2012). A high power density, high efficiency hydrogen–chlorine regenerative fuel cell with a low precious metal content catalyst. *Energy & Environmental Science*, 5(9), 8690-8698.

Ino, S., & Ochiai, Y. (1961). *Tokyo Kogyo Shikensho Hokoku*, 56 (3), 81–89.

Jeong, Y. H., Kazimi, M. S. (2007). Optimization of the hybrid sulfur cycle for nuclear hydrogen generation. *Nuclear Technology*, 159(2), 147-157.

Jianu, O.A. (2013). Mass transfer and particle dissolution in liquid-gas and solid-liquid flows: Application to hydrogen production processes (Doctoral dissertation, *University of Ontario Institute of Technology*).

Johnson, J., Winnick, J. (1999). Electrochemical membrane separation of chlorine from gaseous hydrogen chloride waste. *Separation and Purification Technology*, *15*(3), 223-229.

Kalinci, Y., Hepbasli, A., Dincer, I. (2009). Biomass-based hydrogen production: a review and analysis. *International Journal of Hydrogen Energy*, *34*(21), 8799-8817.

Kanari, N., Gaballah, I. (1999). Chlorination and carbochlorination of magnesium oxide. *Metallurgical and Materials Transactions B*, *30*(3), 383-391.

Kashani-Nejad, S. (2005). Oxides in the Dehydration of Magnesium Chloride Hexahydrate (Doctoral dissertation, *McGill University*).

Kashani-Nejad, S., Ng, K. W., Harris, R. (2004). Preparation of MgOHCl by controlled dehydration of $MgCl_2 \cdot 6H_2O$. *Metallurgical and Materials Transactions B*, *35*(2), 405-406.

Kashani-Nejad, S., Ng, K. W., Harris, R. (2005). MgOHCl thermal decomposition kinetics. *Metallurgical and Materials Transactions B*, *36*(1), 153-157.

Kelley, K. K. (1945). Energy requirements and equilibria in the dehydration, hydrolysis, and decomposition of magnesium chloride (Vol. 676). *US Government. Printing Office.*

Kipouros, G. J., Sadoway, D. R. (2001). A thermochemical analysis of the production of anhydrous MgCl 2. *Journal of Light Metals*, *1*(2), 111-117.

Kipouros, GJ, Sadoway, DR (1987). The chemistry and electrochemistry of magnesium production. *Advances in Molten Salt Chemistry*, *6*, 127-209

Kirsh, Y., Yariv, S., Shoval, S. (1987). *Kinetic* analysis of thermal dehydration and hydrolysis of $MgCl_2 \cdot 6H_2O$ by DTA and TG. *Journal of Thermal Analysis*, *32*(2), 393-408.

Klein, S. A., Alvarado, F. L. (2002). Engineering equation solver. *F-Chart Software*, Madison, WI.

Klein, S.A., Nellis, G. (2011) Thermodynamics. *Cambridge University Press*, Cambridge, UK.

Klein, S. A. (2008). Engineering Equation Solver (EES), *Academic Commercial V8*. 208, F-Chart Software.

Konak, A., Coit, D. W., Smith, A. E. (2006). Multi-objective optimization using genetic algorithms: A tutorial. *Reliability Engineering & System Safety*,*9*1(9), 992-1007.

Kotas, T. J. (2013). The exergy method of thermal plant analysis. *Elsevier*.

Kovács, K. L., Maroti, G., Rákhely, G. (2006). A novel approach for biohydrogen production. *International Journal of Hydrogen Energy*, *31*(11), 1460-1468.

Kuwertz, R., Martinez, I. G., Vidaković-Koch, T., Sundmacher, K., Turek, T., Kunz, U. (2013). Energy-efficient chlorine production by gas-phase HCl electrolysis with oxygen depolarized cathode. *Electrochemistry Communications*, *34*, 320-322.

Lamy, M., Ng, K. W., Harris, R. (2004). Mechanism of chlorination of MgO by HCl gas injection. *Canadian Metallurgical Quarterly*, *43*(4), 555-560.

Lazzaretto, A., Tsatsaronis, G. (2006). SPECO: a systematic and general methodology for calculating efficiencies and costs in thermal systems. *Energy*, 31(8), 1257-1289.

Levin, D. B., Pitt, L., Love, M. (2004). Biohydrogen production: prospects and limitations to practical application. *International Journal of Hydrogen Energy*, 29(2), 173-185.

Lewis, M. A., Masin, J. G. (2009). The evaluation of alternative thermochemical cycles–Part II: The down-selection process. *International Journal of Hydrogen Energy*, *34*(9), 4125-4135.

Lewis, M. A., Masin, J. G., O'Hare, P. A. (2009). Evaluation of alternative thermochemical cycles, Part I: the methodology. *International Journal of Hydrogen Energy*, 34(9), 4115-4124.

Li, Y., Song, P., Xia, S., Li, W., Gao, S. (2006). Solubility prediction for the HCl–$MgCl_2$–H_2O system at 40°C and solubility equilibrium constant calculation for HCl· $MgCl_2$· $7H_2O$ at 40°C. *Calphad*, *30*(1), 61-64.

Lyke, S. E., Tatapudi, P. (2000). *U.S. Patent No. 6,066,248*. Washington, DC: U.S. Patent and Trademark Office.

Martin, C. (2007). *The ASPEN user manual*.

Messner, G. (1974). *U.S. Patent No. 3,855,104*. Washington, DC: U.S. Patent and Trademark Office.

Minz, F-.R. (1988). *U.S. Patent No. 4,725,341*. Washington, DC: U.S. Patent and Trademark Office.

Mohammadi, F., Ashrafizadeh, S. N., Sattari, A. (2009). Aqueous HCl electrolysis utilizing an oxygen reducing cathode. *Chemical Engineering Journal*, 155(3), 757-762.

Moldenhauer, W. (1906). Über die Einwirkung von Sauerstoff und Wasserdampf auf Chlormagnesium. *Zeitschrift für Anorganische Chemie*, 51(1), 369-390.

Motupally, S., Becker, A. J., Weidner, J. W. (2002). Water Transport in Polymer Electrolyte Membrane Electrolyzers Used to Recycle Anhydrous HCl I. Characterization of Diffusion and Electro-osmotic Drag. *Journal of the Electrochemical Society*, *149*(5), D63-D71.

Muradov, N. (2003). Emission-free fuel reformers for mobile and portable fuel cell applications. *Journal of Power Sources*, *118*(1), 320-324.

Nandi, T. K., Sarangi, S. (1993). Performance and optimization of hydrogen liquefaction cycles. *International Journal of Hydrogen Energy*, *18*(2), 131-139.

Naterer, G. F., Dincer, I., Zamfirescu, C. (2013). Hydrogen production from nuclear energy. *Springer*.

Naterer, G. F., Suppiah, S., Stolberg, L., Lewis, M., Wang, Z., Daggupati, V., Avsec, J. (2010). Canada's program on nuclear hydrogen production and the thermochemical Cu–Cl cycle. *International Journal of Hydrogen Energy*,*35*(20), 10905-10926.

Ng, K. W., Kashani-Nejad, S., Harris, R. (2005). Kinetics of MgO chlorination with HCl gas. *Metallurgical and Materials Transactions B*, *36*(3), 405-409.

Nieminen, J., Dincer, I., Naterer, G. (2010). Comparative performance analysis of PEM and solid oxide steam electrolysers. *International Journal of Hydrogen Energy*, *35*(20), 10842-10850.

Ozbilen, A. Z. (2013). Development, analysis and life cycle assessment of integrated systems for hydrogen production based on the copper-chlorine (Cu-Cl) cycle (Doctoral dissertation, *University of Ontario Institute of Technology*).

Ozcan, H., Dincer, I. (2014). Energy and exergy analyses of a solar driven Mg–Cl hybrid thermochemical cycle for co-production of power and hydrogen. *International Journal of Hydrogen Energy*, *39*(28), 15330-15341.

Ozcan, H., Dincer, I. (2014). Performance investigation of magnesium–chloride hybrid thermochemical cycle for hydrogen production. *International Journal of Hydrogen Energy*, *39*(1), 76-85.

Ozcan, H., Dincer, I. (2015). Thermodynamic and environmental impact assessment of steam methane reforming and magnesium–chlorine cycle-based multigeneration systems. *International Journal of Energy Research*.

Ozcan, H., El-Emam, R. S., Dincer, I. (2014). Comparative Assessment of Nuclear Based Hybrid Sulfur Cycle and High Temperature Steam Electrolysis Systems Using HEEP. In *Progress in Sustainable Energy Technologies: Generating Renewable Energy* (pp. 165-180). Springer International Publishing.

Ozsaban, M., Midilli, A., Dincer, I. (2011). Exergy analysis of a high pressure multistage hydrogen gas storage system. *International Journal of Hydrogen Energy*, 36(17), 11440-11450.

Pacheco, J. E., Dunkin, S. R. (1996). Assessment of molten-salt solar central-receiver freeze-up and recovery events (No. SAND--96-0331C; CONF-9603117--1). *Sandia National Labs*. Livermore, CA.

Partanen, J., Backman, P., Backman, R., Hupa, M. (2005a). Absorption of HCl by limestone in hot flue gases. Part I: the effects of temperature, gas atmosphere and absorbent quality. *Fuel*, 84(12), 1664-1673.

Partanen, J., Backman, P., Backman, R., Hupa, M. (2005b). Absorption of HCl by limestone in hot flue gases. Part II: importance of calcium hydroxychloride. *Fuel*, 84(12), 1674-1684.

Pérez-Ramírez, J., Mondelli, C., Schmidt, T., Schlüter, O. F. K., Wolf, A., Mleczko, L., Dreier, T. (2011). Sustainable chlorine recycling via catalysed HCl oxidation: from fundamentals to implementation. *Energy & Environmental Science*, 4(12), 4786-4799.

Pitzer, K. S. (1998). Aqueous electrolytes at near-critical and supercritical temperatures. *International Journal of Thermophysics*, 19(2), 355-366.

Pope, K. (2012). Multiphase Flow and Chemical Reactor Thermodynamics for Hydrolysis and Thermochemical Hydrogen Production (Doctoral dissertation, *University of Ontario Institute of Technology*).

Rappold, U., Luft, G. (1999). New dry process for separating HCl from flue gases by adsorption on MgO. *Chemical Engineering & Technology*, 22(10), 843-846.

Rugolo, J., Huskinson, B., Aziz, M. J. (2011). Model of performance of a regenerative hydrogen chlorine fuel cell for grid-scale electrical energy storage. *Journal of the Electrochemical Society*, 159(2), B133-B144.

Seader, J.D., & Henley, E.J. (2006). Separation Process Principles. *John Wiley & Sons*.

Simpson, M. F., Herrmann, S. D., Boyle, B. D. (2006). A hybrid thermochemical electrolytic process for hydrogen production based on the reverse Deacon reaction. *International Journal of Hydrogen Energy*, 31(9), 1241-1246.

Sukhatme, S. P., Nayak, J. K. (2008). Principles of thermal collection and storage. Solar Energy, 3rd Edition, *Tata McGraw Hill Publishing Company, New Delhi*.

Talbi, E. G. (2009). Metaheuristics: from design to implementation (Vol. 74). *John Wiley & Sons.*

Taylor, J. D., Herdman, C. M., Wu, B. C., Wally, K., Rice, S. F. (2003). Hydrogen production in a compact supercritical water reformer. *International Journal of Hydrogen Energy*, 28(11), 1171-1178.

Thomassen, M. S. (2005). Hydrogen-chlorine fuel cell for production of hydrochloric acid and electric power: chlorine kinetics and cell design. PhD Thesis, *Norvegian University of Science and Technology*, Trondheim.

Thomassen, M., Børresen, B., Scott, K., Tunold, R. (2006). A computational simulation of a hydrogen/chlorine single fuel cell. *Journal of Power Sources*, 157(1), 271-283.

Tolmachev, Y. V. (2014). Hydrogen-halogen electrochemical cells: A review of applications and technologies. *Russian Journal of Electrochemistry*, *50*(4), 301-316.

Tsatsaronis, G., Moran, M. J. (1997). Exergy-aided cost minimization. *Energy Conversion and Management*, 38(15), 1535-1542.

Turner, J., Sverdrup, G., Mann, M. K., Maness, P. C., Kroposki, B., Ghirardi, M., Blake, D. (2008). Renewable hydrogen production. *International Journal of Energy Research*, *32*(5), 379-407.

Turton, R., Bailie, R. C., Whiting, W. B., Shaeiwitz, J. A. (2008). Analysis, synthesis and design of chemical processes. *Pearson Education*.

U.S. Department of Energy (2007). Annual Report for the DOE Hydrogen Program. Washington, DC: *Government Printing Office*.

Urwongse, L., Sorrell, C. A. (1980). The System MgO-$MgCl_2$-H_2O at 23°C. *Journal of the American Ceramic Society*, 63(9-10), 501-504.

Vatavuk, W. M. (2002). Updating the CE plant cost index. *Chemical Engineering*, 109(1), 62-70.

Vidakovic-Koch, T., Gonzalez Martinez, I., Kuwertz, R., Kunz, U., Turek, T., Sundmacher, K. (2012). Electrochemical membrane reactors for sustainable chlorine recycling. *Membranes*, 2(3), 510-528.

Wang, W., Chen, S. (2011). Theoretical Study on the Thermolysis Mechanism of Monohydrate Magnesium Chloride. *Journal of Computational Science & Engineering*, 2, 79-84.

Wilhelm, D. J., Simbeck, D. R., Karp, A. D., Dickenson, R. L. (2001). Syngas production for gas-to-liquids applications: technologies, issues and outlook. *Fuel Processing Technology*, *71*(1), 139-148.

Wu, Y. L., Huang, X. F., Yang, M. D., Zou, S. P., Dang, J., Hu, H. S. (2008). Study on the mechanisms and kinetics of complex's thermal decomposition getting anhydrous magnesium chloride. *Journal of Analytical and Applied Pyrolysis*, *81*(1), 133-135.

Ya-Hong, L., Peng-Sheng, S., Shu-Ping, X., Wu, L., Shi-Yang, G. (2005). Application of the Ion-interaction Model to the Solubility Prediction of LiCl-HCl-MgCl2-H2O System at 20° C. *Chinese Journal of Chemistry*, 23(8), 953-956.

Yildiz, B., Kazimi, M. S. (2006). Efficiency of hydrogen production systems using alternative nuclear energy technologies. *International Journal of Hydrogen Energy*, 31(1), 77-92.

Zeng, D., Liu, H., Chen, Q. (2007). Simulation and prediction of solubility phase diagram for the separation of MgCl 2 from LiCl brine using HCl as a salting-out agent. *Hydrometallurgy*, 89(1), 21-31.

Zhang, H. L., Baeyens, J., Degrève, J., Cacères, G. (2013). Concentrated solar power plants: Review and design methodology. *Renewable and Sustainable Energy Reviews*, 22, 466-481.

Zhang, Z., Lu, X., Yang, S., Pan, F., Wang, Y. (2012). Preparation of Anhydrous Magnesium Chloride from Ammonium Carnallite. *Materials and Manufacturing Processes*, 28(1), 5-9.

Zhou, N., Chen, B., He, X., Li, Y. (2006). Preparation of anhydrous magnesium chloride in a gas-solid reaction with ammonium carnallite. *Frontiers of Chemistry in China*, 1(4), 384-388.

Zimmerman, W. H., Trainham, J. A., Law Jr, C. G., Newman, J. S. (2001).U.S. Patent No. 6,203,675. Washington, DC: *U.S. Patent and Trademark Office*.

APPENDIX A: MATLAB CODE FOR UNCERTAINTY ASSESSMENT

This code is modified to calculate the uncertainty of the hydrochlorination experiment by considering all necessary information from existing Bias and precision error values of required measurement devices. This code is adapted from an open source provided by Jianu, 2013.

```
%--------------------------------
%-----Uncertainty Assessment------
%--------------------------------
clear all; close all; clc; format short;
Temperature=[150 175 200 225 250 275];
flowrate = [10 20]';
cmratio = [1 2]';
Temp = Temperature(1,1);
flow = flowrate(1,1);
cmrat = cmratio (1,1);
Variables = 'Temp flow cmrat';
Eq = '20.29*exp(-
flow^(0.1766)+cmrat^(0.1688*exp(flow^(0.1766)))+1.433*10^(-
3)*exp(flow^(0.0683)-cmrat^(0.1259*exp(flow^(0.2701))))*Temp)';
Conversion = 1;
string.Eq = ' +-';
%-------------------------------------------------
%  bias and precision errors in matrix form
%-------------------------------------------------
Variable_Values = [Temp 0.0011 0.0004;
Temp 0.016 0.005
flow 0.0013 0.00034;
cmrat 0.0014 0];
index = 0;
string.old = [];
for i = 1:length(Variables)
if ~isspace(Variables(i)) && i ~= length(Variables)
string.new = sprintf('%c',Variables(i));
string.old = strcat(string.old,string.new);
elseif i == length(Variables)
index = index + 1;
string.new = sprintf('%c',Variables(i));
string.old = strcat(string.old,string.new);
Symbolic_Variables(index) = sym(string.old);
string.old = [];
else
index = index + 1;
Symbolic_Variables(index) = sym(string.old);
string.old = [];
end
end
%Calculation and display of Partial Derivatives
string.Initial_Eq = sprintf('Initial
Equation%s:\n%s\n',string.Eq,char(Eq));
```

```
disp(string.Initial_Eq)
for i = 1:length(Symbolic_Variables)
string.Partial = sprintf('Partial wrt %s:',char(Symbolic_Variables(i)));
Partial(i) = diff(Eq,Symbolic_Variables(i));
if Partial(i) ~= 0
disp(string.Partial)
disp(Partial(i))
end
end
% Uncertainty computation
uncertainty = 0;
for i =
1:length(Symbolic_Variables)uncertainty_b=(eval(Partial(i))*Variable_Val
ues(i,2))^2 + uncertainty;
end
for i = 1:length(Symbolic_Variables)uncertainty_p
=(eval(Partial(i))*Variable_Values(i,3))^2 + uncertainty;
end
uncertainty = sqrt(uncertainty_p+uncertainty_b)*Conversion;

string.Answer = sprintf('The uncertainty is
%.4f%s%s',uncertainty,string.Eq);
disp(string.Answer)
```

APPENDIX B: MATLAB CODE FOR MULTIOBJECTIVE OPTIMIZATION

The Multi-objective optimization code consists of two parts. The first part is simply creating a function to calculate the objective functions, which are functions of decision variables, using the correlated equations taken from ANN training of the data. Second part is setting up the lower and upper bounds of all decision variables and utilizing the created function by the multi objective optimization function of MATLAB software (Deb, 2001; The MathWorks, 2007).

```
%--------------The first m-script------------------
%------------Creating the function---------------
%------------------------------------------------
function y = kur_multiobjective(x)
%
%   Reference: Kalyanmoy Deb, "Multi-Objective Optimization using
%   Evolutionary Algorithms", John Wiley & Sons ISBN 047187339
%   Copyright 2007 The MathWorks, Inc.

y = zeros(2,1);

% Maximizing efficiency—(multiplied by negative one)
for i = 1
  y(1) = -1*(y(1)-1.92447884E-01+4.46814815E-03*x(i)-8.02962963E-
06*x(i)^2+3.25185185E-04*x(i+1)-2.07407407E-07*x(i+1)^2+8.61832011E-
03*x(i+2)-7.44212963E-04*x(i+2)^2-1.62407407E-02*x(i+3)+1.04814815E-
02*x(i+3)^2) ;
end

% Minimizing the total cost rate--
for i = 1
   y(2) = y(2) -4.87779101E+00+6.75851852E-02*x(i)-1.04888889E-
04*x(i)^2+6.33703704E-03*x(i+1)-5.77777778E-06*x(i+1)^2+6.34070767E-
01*x(i+2)-1.63690476E-04*x(i+2)^2+3.29444444E-01*x(i+3)+1.44444444E-
02*x(i+3)^2 ;

end


%--------------The second m-script------------------
%---------Multi-objective optimization------------
%------------Courtesy of MathWorks, 2007----------

FitnessFunction = @kur_multiobjective;
numberOfVariables = 4; % Number of decision variables
lb = [250 450 8 1]; % Lower bound
ub = [300 500 18 2]; % Upper bound
A = []; % No linear inequality constraints
```

```
b = []; % No linear inequality constraints
Aeq = []; % No linear equality constraints
beq = []; % No linear equality constraints
options=gaoptimset;
options = gaoptimset('populationsize',120);
options = gaoptimset('ParetoFraction',0.8);
options = gaoptimset('Display','iter')

% Below functions can be separately used to plot a desired graph to
observe.
%options = gaoptimset('PlotFcns',{@gaplotpareto})
%options = gaoptimset('PlotFcns',{@gaplotbestindiv})
%options = gaoptimset('PlotFcns',{@gaplotrange})
%options = gaoptimset('PlotFcns',{@gaplotgenealogy})
%options = gaoptimset('PlotFcns',{@gaplotscores})
%options = gaoptimset('PlotFcns',{@gaplotbestindiv})
options = gaoptimset('PlotFcns',{@gaplotparetodistance});
%options = gaoptimset('PlotFcns',{@gaplotspread});
options = gaoptimset(options,'TolFun',1e-4,'StallGenLimit',1000);
[x,Fval,exitFlag,Output] =
gamultiobj(FitnessFunction,numberOfVariables,A, ...
    b,Aeq,beq,lb,ub,options);
fprintf('The number of points on the Pareto front was: %d\n',
size(x,1));
fprintf('The number of generations was : %d\n', Output.generations);
Fval
x
```

DISSEMINATION OF THESIS

Journal Papers

H. Ozcan, I. Dincer. Performance evaluation of a nuclear energy based integrated system for hydrogen production and liquefaction. *ASME Journal of Nuclear Engineering and Radiation Science*, under review, 2016.

H. Ozcan, I. Dincer. Modeling of a new four-step magnesium-chlorine cycle with dry HCl capture for more efficient hydrogen production. *Int. J Hydrogen Energy*, in press, corrected proof, 2016.

H. Ozcan, I. Dincer. Comparative performance assessment of three configurations of magnesium-chlorine cycle, *Int. J Hydrogen Energy*, in press, corrected proof, 2016.

H. Ozcan, I. Dincer. Thermodynamic and environmental impact assessment of steam methane reforming and magnesium-chlorine cycle based multigeneration systems, *Int. J Energy Research*, Vol. 39(13), pp. 1778-1789, 2015.

H. Ozcan, I. Dincer. Energy and exergy analysis of a solar driven Mg-Cl hybrid thermochemical cycle for cogeneration of hydrogen and electricity, *Int. J Hydrogen Energy*, Vol 39, pp. 15330-15341, 2014.

H. Ozcan, I. Dincer. Performance investigation of magnesium-chloride hybrid thermochemical cycle for hydrogen production, *Int. J. Hydrogen Energy*, Vol 39, pp. 76-85, 2014.

Conferences

H. Ozcan, I. Dincer. The four-step Magnesium Chlorine cycle with dry HCl capture for decreased electrical work consumption, *6th International Conference on Hydrogen Production*, pp. 913, 3-6 May 2015, Oshawa, Canada.

H. Ozcan, I. Dincer. Energetic and Exergetic Performance Comparisons of Various Flowsheet Options of Magnesium-Chlorine Cycle, *7th International Energy, Exergy, and Environment Symposium*, 27-30 April 2015, Valenciennes, France.

H. Ozcan, I. Dincer. Comparative exergy based environmental impact assessment of two integrated renewable energy based systems for multigeneration, *Global Conference on Global Warming*, pp. 25-29, 25-29 May 2014. Beijing, China.

H. Ozcan, I. Dincer. Performance assessment of a solar driven Mg-Cl hybrid thermochemical cycle for co-production of power and hydrogen, 5th *International Conference on Hydrogen Production*, pp. 65-67, 2-5 February 2014, pp. 65. Fukuoka, Japan.